INSTITUT POLYTECHNIQUE DE PARIS

NNT : 2026IPPAX007

Thèse de doctorat

Magnetic Geometry Impact on the Edge Radial Electric Field in Tokamaks

Thèse de doctorat de l'Institut Polytechnique de Paris
préparée à l'École polytechnique et IRFM Cadarache

École doctorale n°626 École doctorale de l'Institut Polytechnique de Paris (EDIPP)
Spécialité de doctorat : Optique, Laser et Plasma

Thèse présentée et soutenue à Cadarache, Saint-Paul-Lez-Durance, le 09 Mars 2026, par

SASCHA RIENÄCKER

Composition du Jury :

Guido Ciraolo Directeur de recherche, CEA (IRFM)	Président
Teresa Estrada Professeur, CIEMAT (Laboratorio Nacional de Fusión)	Rapporteure
Gregor Birkenmeier Professeur chargé de cours, Max-Plank-Institut für Plasmaphysik	Rapporteur
Benoît Labit Directeur de recherche, EPFL (SPC)	Examinateur
Laure Vermare Directrice de recherche, CNRS (LPP)	Directrice de thèse
Pascale Hennequin Directrice de recherche, CNRS (LPP)	Codirectrice de thèse
Branka Vanovac Chargée de recherche, MIT (Plasma Science and Fusion Center)	Invitée
Yann Camenen Directeur de recherche, Aix Marseille Univ., CNRS (PIIM)	Invité

Contents

Abstract **5**

Résumé **7**

Chapter 1 – Introduction **9**
1.1 Magnetic Confinement Fusion 9
1.1.1 Toroidal confinement devices 10
1.1.2 Description of the tokamak equilibrium 11
1.1.3 Limitations of confinement and turbulent transport 14
1.1.4 Lawson criterion 16
1.1.5 Importance of sheared flows 17
1.1.6 Confinement transition and H-mode 19
1.2 Scope of the Thesis 20
1.2.1 Motivations and research aim 20
1.2.2 Scientific approach and focus 21
1.2.3 Investigated magnetic geometry effects 21
1.2.4 Overview of the considered tokamaks 23
1.3 Thesis outline 28

Chapter 2 – Radial Electric Field and Flow Generation in Tokamaks . **29**
2.1 Introduction on E_r and chapter outline 29
2.2 Radial Force Balance 31
2.3 Neoclassical description 32
2.3.1 Basic elements of neoclassical theory 32
2.3.2 Rotation within Standard Neoclassical Theory 33
2.3.3 Neoclassical E_r approximation 34
2.3.4 Case of strong magnetic ripple 35
2.4 Ion Orbit Losses 36
2.5 Turbulent Reynolds stress and Zonal flows 38
2.6 Magnetic shear induced Reynolds stress 39
2.7 Radial Electric Field in the SOL 40
2.8 Phenomenological review of the edge E_r 42
2.8.1 E_r and ion profiles at the L-H transition 42
2.8.2 Sensitivity of edge E_r and turbulence velocity to magnetic configuration 50
2.9 Chapter summary 52

Chapter 3 – Doppler backscattering at TCV: setup, methodology and first E_r studies **53**
3.1 Principles of DBS 54
3.1.1 Brief description 54
3.1.2 Scattering condition and radial localization 55
3.1.3 $E_r \times B$ velocity measurement 57
3.1.4 Proxy for density fluctuation level 57
3.2 Signal detection and analysis 58
3.2.1 Signal detection scheme 59
3.2.2 Doppler shift estimation 60
3.2.3 Beamtracing 64
3.3 Launcher and operating range 67
3.4 Overview of main TCV diagnostics and quantities used 68
3.5 Comparison of DBS and GPI measurements 72
3.6 Comparison of DBS and C^{6+} radial force balance 72
3.7 Mapping $v_\perp$ to the OMP 74
3.8 Survey of the edge E_r in TCV 78
3.8.1 Density scan 78
3.8.2 Auxiliary heating scan 80
3.8.3 Magnetic field helicity 82
3.9 Chapter summary 85

Chapter 4 – Sensitivity of E_r to Magnetic Drift Configuration **86**
4.1 Review of FAV/UNFAV studies and proposed mechanisms 87
4.2 FAV/UNFAV comparison in L-mode TCV discharges 92
4.2.1 Discharge parameters and edge profiles 92
4.2.2 Toroidal rotation 94
4.2.3 Density fluctuation properties 95
4.2.4 Oscillations of the $E_r \times B$ flow 97
4.2.5 Discussion 99
4.3 Influence of plasma current in WEST, TCV and AUG 100
4.3.1 Review of I_p scans in WEST and Tore Supra 100
4.3.2 Confirmation of WEST trend in stationary conditions 102
4.3.3 I_p sensitivity under auxiliary heating in WEST 103
4.3.4 Comparison with I_p scans in TCV 105
4.3.5 Comparison with a restricted I_p scan in AUG 107
Method and discharge design 110
Results of the I_p scan in AUG (UNFAV drift only) 111
4.4 Density scans in TCV 113
4.5 Power scans in TCV 117
4.5.1 NBI 117
4.5.2 ECRH 120
4.5.3 Confinement analysis 123
4.5.4 Discussion 125
4.6 `GENE-X` simulations of TCV experiments 125
4.7 Chapter summary and discussion 131

Chapter 5 – Influence of Shaping: E_r in Positive versus Negative Triangularity TCV Plasmas **134**
5.1 Review of NT (edge) studies 136
5.2 NT/PT comparison in USN 138
5.2.1 Ohmic case 138
5.2.2 Shape variations 141
5.2.3 Auxiliary Heating 144
5.2.4 Comparison of DBS power 148
5.3 NT/PT comparison in LSN 150
5.4 Limited configuration 153
5.5 Towards higher performance in fully NT shape 156
5.6 Chapter summary and discussion 161

Chapter 6 – Conclusion and Outlook **164**

Bibliography **168**

Appendix A: Supplementary comparisons between radial force balance DBS **183**

Appendix B: Definition of triangularity **186**

Appendix C: Results of linear `GENE` simulations in NT and PT **187**

Abstract

Mitigating plasma turbulence is a major objective of magnetic confinement fusion research, as the resulting transport of heat and particles largely determines confinement quality—and thus the performance and cost of future fusion power plants.

Central to this PhD thesis are plasma edge flows associated with the $E_r \times B$ drift in the presence of a radial electric field (E_r). Their radial gradients produce velocity shear that regulates turbulent transport. Strong velocity shear can lead to a local suppression of turbulence, as observed during confinement bifurcations such as the transition from the low (L-mode) to the high confinement mode (H-mode). This (L–H) transition is accompanied by a sharp deepening of the negative E_r "well" located just inside the plasma boundary. The resulting gain in thermal confinement is considered essential for achieving reactor-relevant fusion performance.

While several neoclassical or turbulent transport processes can generate a negative E_r, the mechanisms predominantly shaping its edge structure remain uncertain, particularly in L-mode. Notably, the sensitivities of E_r to plasma conditions, such as magnetic configuration, shape, or proximity to the L–H threshold, remain poorly understood and difficult to capture using existing models or numerical tools. This PhD work investigates these dependencies experimentally, to help disentangle the dominant E_r sources in L-mode and clarify their role in confinement improvement or transitions.

To this end, E_r is measured using Doppler backscattering (DBS), a non-intrusive microwave diagnostic that detects the signal backscattered by density fluctuations. The Doppler shift yields the perpendicular velocity ($v_\perp \approx E_r/B$), thereby enabling radially localized measurements of E_r.

Experiments are conducted on the tokamaks WEST, AUG and TCV—with a particular focus on the latter. TCV's unique flexibility makes it ideal for complementing the E_r investigations on WEST and AUG—already equipped with DBS systems—by allowing both cross-machine comparisons and exploration of otherwise inaccessible magnetic configurations. The commissioning of a DBS system on TCV enabled the first detailed edge E_r studies on this device, that form a central part of this thesis.

This work focuses on magnetic geometry effects on E_r, distinguishing between two aspects: magnetic drift configuration and plasma shaping.

The first topic examines the impact of the ion magnetic drift direction—toward or away from the X-point—termed *favorable* and *unfavorable* in reference to their propensity for H-mode access. Comprehensive parameter scans are performed on TCV in both drift configurations. Consistent with AUG and WEST, the favorable drift case features a deeper L-mode E_r well. Approaching the L-H transition enhances the difference in E_r,

which supports a connection with the long known, yet unresolved, drift-dependent H-mode access. Further, plasma current has little influence—in contrast to WEST results, while higher density reduces the favorable/unfavorable asymmetry in E_r.

The second line of research explores how triangularity—which gives the plasma its typical "D"-shape—influences E_r. While conventional tokamak plasmas usually have positive triangularity (PT), negative triangularity (NT) shapes have recently gained interest for their superior L-mode performance and avoidance of ELMs (harmful edge instabilities). Matched PT/NT experiments on TCV reveal, for the first time, a stronger E_r well and $E_r \times B$ shear in NT compared to PT.

Overall, the findings support a link between the edge E_r shear and the impact of magnetic geometry on confinement properties. The experiments provide a strong basis for edge transport modelling in view of disentangling the dominant E_r drives. Combined with recent first-principles simulations, the observations point to the importance of turbulence-driven flow generation for explaining sensitivities of E_r to magnetic geometry.

Résumé

La réduction de la turbulence plasma est un objectif majeur de la recherche sur la fusion par confinement magnétique, car le transport de chaleur et de particules qui en résulte détermine largement la qualité du confinement — et donc les performances ainsi que le coût des futures centrales de fusion.

Cette thèse porte sur les écoulements au bord du plasma, associés à la dérive $E_r \times B$ en présence d'un champ électrique radial (E_r). Le gradient de celui-ci génère un cisaillement de vitesse, régulant le transport turbulent. Un cisaillement fort peut conduire à une suppression locale de la turbulence, comme observé lors des bifurcations de confinement telles que la transition du mode de faible (mode L) au mode de haut confinement (mode H). Cette transition (L–H) s'accompagne d'un creusement du « puits » de E_r négatif situé au bord du plasma et d'un gain de confinement essentiel pour atteindre des performances de fusion pertinentes pour un réacteur.

Bien que plusieurs effets (d'origine néoclassique ou turbulente) puissent générer un E_r négatif, les principaux mécanismes qui déterminent sa structure au bord restent incertains; En particulier, la sensibilité de E_r aux conditions plasma en mode L demeure mal comprise et difficile à reproduire avec les modèles ou outils numériques actuels. Cette thèse examine expérimentalement ces dépendances, afin d'éclairer les sources de E_r et leur rôle dans l'amélioration du confinement.

E_r est mesuré par rétrodiffusion Doppler (DBS), un diagnostic micro-onde qui détecte le signal rétrodiffusé par les fluctuations de densité. Le décalage Doppler fournit la vitesse perpendiculaire ($v_\perp \approx E_r/B$), permettant ainsi une mesure localisée de E_r.

Les expériences sont menées sur les tokamaks WEST, AUG et surtout TCV, dont les études de E_r complètent celles de WEST et AUG en offrant à la fois des comparaisons multi-machines et l'accès à des configurations magnétiques autrement inaccessibles. L'installation d'un système DBS sur TCV a permis les premières études détaillées de E_r sur cette machine, qui constituent une partie majeure de cette thèse.

Ce travail se focalise sur les effets de la géométrie magnétique sur E_r, en distinguant deux aspects : l'orientation de la dérive magnétique ainsi que la forme du plasma.

Le premier volet étudie l'impact du sens de la dérive magnétique des ions — vers ou à l'opposé du point X — configurations dites *favorable* et *défavorable* selon leur facilité d'accès au mode H. Des scans paramétriques étendus sont réalisés sur TCV pour les deux configurations. En accord avec AUG et WEST, le cas favorable présente un puits de E_r en mode L plus profond. À l'approche de la transition L–H, l'écart de E_r s'accentue, renforçant l'hypothèse d'un lien avec la dépendance du seuil de transition à la dérive magnétique. Par ailleurs, le courant plasma influence peu le puits de E_r — contraire-

ment aux observations de WEST — tandis qu'une densité plus élevée réduit l'asymétrie favorable/défavorable de E_r.

Le second axe de recherche s'intéresse à l'influence de la triangularité — qui confère au plasma sa forme en « D » — sur E_r. Alors que les plasmas de tokamak adoptent généralement une triangularité positive (PT), les configurations à triangularité négative (NT) suscitent un intérêt croissant en raison de leurs bonnes performances en mode L et de l'absence d'ELMs (instabilités de bord nuisibles). Des comparaisons NT/PT sur TCV mettent en évidence, pour la première fois, un puits de E_r plus prononcé en NT qu'en PT.

Dans l'ensemble, ces résultats soutiennent un lien entre le cisaillement de E_r et l'influence de la géométrie magnétique sur les propriétés de confinement. Les expériences fournissent une base solide pour la modélisation dans l'objectif de discriminer les mécanismes d'écoulement au bord. Combinées à de récentes simulations premiers principes, ces observations soulignent l'importance de la génération d'écoulement induite par la turbulence pour expliquer la sensibilité de E_r à la géométrie magnétique.

Chapter 1

Introduction



Contents

1.1 Magnetic Confinement Fusion 9
1.2 Scope of the Thesis 20
1.3 Thesis outline 28

1.1 Magnetic Confinement Fusion

The ultimate goal of controlled thermonuclear fusion is to harness the nuclear energy released when light atoms (typically hydrogen isotopes) undergo fusion. Magnetic confinement inside a toroidal reactor chamber constitutes one of the two main pathways to controlled fusion[1]. In this approach, the fusion fuel—a gas composed of light atoms, typically hydrogen isotopes such as deuterium (D) and tritium (T)—is heated to temperatures on the order of 10 keV (or $\sim 10^8$K), whereby the atoms become fully ionized. These extreme temperatures are required to overcome the repulsive Coulomb force, which tends to keep nuclei apart, preventing their fusion. The hot mixture of charged ions and electrons, called plasma, must be isolated from solid materials; This is achieved through confinement by strong magnetic fields within a toroidal chamber.

The fundamental principle underlying this *magnetic confinement* is that in the presence of a magnetic field $\boldsymbol{B}$, charged particles gyrate around field lines with a cyclotron frequency $\omega_c = qB/m$ and Larmor radius $\rho_L = \mathsf{v}_\perp/\omega_c$, where $B \equiv |\boldsymbol{B}|$, $\mathsf{v}_\perp$ is the velocity perpendicular to $\boldsymbol{B}$, q denotes the charge, m the mass, and T the temperature of the particle. This constrains the particle motion in the transverse direction to $\boldsymbol{B}$, while leaving the parallel motion unhindered. Bending the magnetic field lines into a torus provides a suitable solution for containing the parallel motion within a similarly toroidal reactor chamber, while preventing contact between the hot core of the plasma column and the walls. This allows the plasma core to retain sufficient density and temperature to reach fusion conditions. This is, in simple terms, the foreseen principle of toroidal fusion devices, of which the "tokamak" (introduced below) is the most studied and the one considered in this work.

The D-T reaction is the preferred option for such a fusion reactor, owing to the higher cross-section compared to other conceivable fuels [1, § 1.2]. It releases 17.6 MeV carried as

[1] The second approach being inertial confinement fusion which is not addressed in this thesis.

kinetic energy by a neutron (n) and a helium ion (He, or α-particle):

$$ {}^{2}_{1}\mathrm{D} + {}^{3}_{1}\mathrm{T} \rightarrow {}^{4}_{2}\mathrm{He}\,(3.5\,\mathrm{MeV}) + {}^{1}_{0}\mathrm{n}\,(14.1\,\mathrm{MeV})\ . $$

The fusion neutrons escape the chamber and are captured by a blanket, where their heat can be extracted to generate electricity. The α-particles, on the other hand, remain confined by the $\boldsymbol{B}$ field, and their energy is deposited in the plasma. This "α-heating" helps to sustain the fusion reactions, combined with external heating and fueling.

In the following, basic elements of plasma physics relevant to magnetic confinement fusion are assumed to be known to the reader. These include the kinetic, (multi-) fluid, and magnetohydrodynamic (MHD) plasma descriptions, as well as charged particle motions in straight and toroidal magnetic fields and the leading order guiding centre drifts; in particular the electric ("$E\times B$") drift, and the combined magnetic drifts from the curvature and gradient of B—hereafter denoted as the "$B \times \nabla B$" drift. For readers unfamiliar with these concepts, we refer to the introductory literature [1, 2].

1.1.1 Toroidal confinement devices

The leading designs for magnetic confinement fusion reactors are based on either the "stellarator", or the "tokamak" principle (Fig. 1.1). Of the two toroidal machine types proposed in the 1950s, the tokamak remains the dominant one in terms of currently operating devices and accumulated experimental and theoretical knowledge. Nevertheless, stellarators have gained considerable attention in recent years through promising advances in theory and experiments.

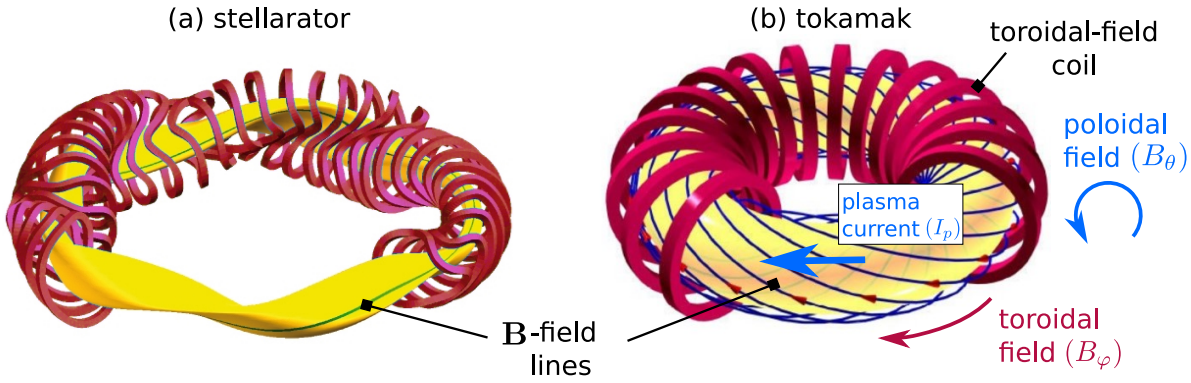

Figure 1.1: *Cartoon illustration of (a) stellarator and (b) tokamak devices. A powerful helical magnetic field ($\boldsymbol{B}$) provides the common basis for magnetic toroidal confinement. Adapted figures, with credits to: (a) Max-Planck Institut für Plasmaphysik, CC BY 3.0, via Wikimedia Commons. (b) Institut de Recherche sur la Fusion Magnétique (IRFM), CEA Cadarache.*

Tokamaks and stellarators share in common that their $\boldsymbol{B}$-field consists of a powerful toroidal (B_φ) combined with a weaker poloidal (B_θ) component, generating helically "twisted" magnetic field lines that wind around the torus (Fig. 1.1). The helicity of the field lines is necessary to compensate for the—nearly vertical—$B\times\nabla B$ drifts, which are of opposite signs for electrons and ions. It ensures that, along their parallel motion, particles alternate between the upper and lower sides of the torus. This cancels the

net cross-field drift, thereby preventing vertical charge separation that would otherwise promptly deconfine the plasma through an outward $E \times B$ drift.

The machines notably differ in how these field components are generated; Stellarators use a complex structure and arrangement of (often non-planar) magnetic coils, wrapped around the chamber, to generate the total (toroidal and poloidal) B-field. In tokamaks, B_φ is produced by an array of identical, vertically-positioned coils, shown in Fig. 1.1 (b). Besides these *toroidal-field* coils, horizontal, ring-shaped auxiliary coils (not shown) produce a weaker, vertical (or poloidal) field for plasma stability and shaping. However, in contrast to stellarators, tokamaks, primarily rely on an externally-driven, large toroidal plasma current (I_p) to produce the B_θ component. In most present-day tokamaks, I_p is mainly driven inductively by a central solenoid, akin to a transformer where the plasma acts as the secondary circuit.

Tokamaks thus benefit from a simpler, nearly toroidally symmetric geometry, at the significant cost of requiring active current drive[2].

Hereafter, we focus exclusively on the tokamak device, which is the one addressed in this study. Before further outlining the context and scope of this work, the tokamak equilibrium is introduced along with the relevant terminology.

1.1.2 Description of the tokamak equilibrium

The geometry in a tokamak is conveniently described using the right-handed cylindrical (R,Z,φ) and toroidal coordinates (r,θ,φ), as represented in Fig. 1.2. Here, r are R are

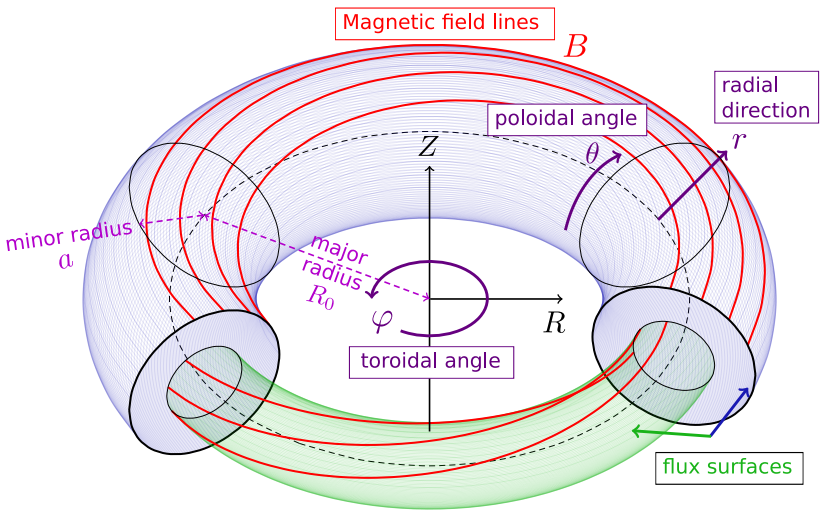

Figure 1.2: *Notations and coordinate conventions for describing the tokamak geometry. Courtesy of R. Varennes.*

respectively the coordinates along the minor and major radius, Z is the vertical coordinate,

[2] This constitutes a major drawback compared to stellarators, since the strong current required in tokamaks makes the plasma prone to instabilities that can cause its disruption. Moreover, for steady-state operation, a tokamak reactor must rely also on non-inductive current drives, whereas magnetic confinement in a stellarator is inherently steady-state.

and φ and θ denote the toroidal and poloidal angles. This work adopts the standard COCOS17 [3] toroidal coordinates convention. It implies that, as indicated in Fig. 1.2, φ is positive in the counter-clockwise direction when viewed from above, and θ is positive in the clockwise direction when considering a cross-section in which the vertical symmetry axis ($R = 0$) is on the left.

The helical field lines trace out nested toroidal surfaces, called "magnetic flux surfaces". Flux surfaces can be labelled by the poloidal magnetic flux $\psi = \frac{1}{2\pi} \int_S B_\theta \mathrm{d}S$ lying within that surface, where the integration surface S spans an annulus between flux surfaces.

The innermost surface, which corresponds to a circular line at $r = 0$, is the "magnetic axis". The magnetic field at this location is denoted B_0 and is purely toroidal. The toroidal field (B_φ), which is the dominant component of B, scales as $1/R$. This leads to a weaker B on the outboard than on the inboard side of the plasma. They are thus referred to as low- and high-field sides (LFS and HFS), respectively.

The so-called "safety factor" q measures the average field line helicity (related to the pitch angle) on a given flux surface. Its value corresponds to the number of toroidal turns a field line traces before completing a poloidal turn. In case of a large aspect ratio ($R/a \gg 1$) plasma with circular cross-section, as illustrated in Fig. 1.2, it may be approximated as $q = rB_\varphi/(R_0 B_\theta)$ [1, § 3.4].

The ideal MHD equilibrium relation [1, § 3.2], $\boldsymbol{j} \times \boldsymbol{B} = \boldsymbol{\nabla} p$, where $\boldsymbol{j}$ is the current density and p the radial plasma pressure, states that to leading order, the magnetic (Lorentz) force balances the pressure gradient. This implies that $\boldsymbol{B} \cdot \boldsymbol{\nabla} p = 0$ and therefore, magnetic surfaces are also surfaces of constant pressure, $p = p(\psi)$. This reflects the fast parallel transport of particles along field lines, which quickly homogenizes plasma quantities—including the pressure—on a given flux surface.

In the common approximation of an "axisymmetric" tokamak equilibrium, which does not vary in the toroidal direction ($\partial/\partial\varphi = 0$), the geometrical description reduces to 2D, and the plasma cross-sectional shape is determined by (R, Z) contours of constant ψ. The possible flux functions $\psi(R, Z)$ are given by solutions of the Grad-Shafranov equation [4]. This nonlinear equation is obtained from $\boldsymbol{j} \times \boldsymbol{B} = \boldsymbol{\nabla} p$ using an axisymmetric representation of $\boldsymbol{B}$ [5, § 7.2]. It links the flux surfaces to the profiles of plasma pressure and current density, along with boundary conditions that include the currents in the external coils.

The plasma shape can be controlled and, to some extent, varied in experiments using the aforementioned auxiliary coils, which produce an external B_θ component that modifies the poloidal flux in their vicinity. This tends to expand or compress flux surfaces, depending on whether the coil current is in the same or opposite direction as the plasma current, respectively.

Flux surface geometries that depart significantly from a circular cross-section are referred to as *shaped*. The most common shaping parameters include the "elongation" κ and "triangularity" δ, see Fig. 1.3. The triangularity parameter is of particular importance to this work; Positive δ (b) tends to confer the plasma a "D"-shaped cross-section, whereas the "D" is flipped horizontally in case $\delta < 0$ (c).

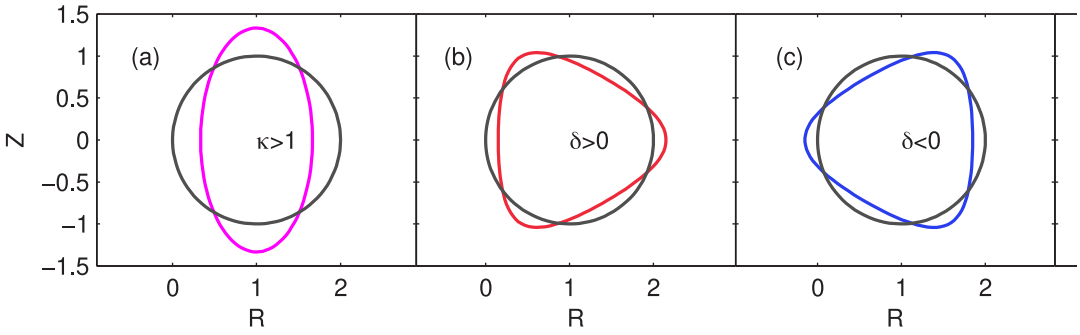

Figure 1.3: *Illustration of flux surface shaping via (a) elongation $\kappa > 1$, (b) positive triangularity, $\delta > 0$ and (c) negative triangularity, $\delta < 0$. Figure adapted from [6].*

Beyond the plasma boundary, field lines are intercepted by plasma facing components, resulting in open field lines, as illustrated by the poloidal cross-sections in Fig. 1.4. This defines a "Last Closed Flux Surface" (LCFS), separating the region of closed flux surfaces from the region of open field lines. The latter is denoted as the "scrape-off layer" (SOL).

In a *limited* configuration, Fig. 1.4 (a), the plasma is bound by a limiter, which can be the device wall or a dedicated material surface. In the case of a *diverted* plasma (b), a magnetic X-point (or poloidal-field null) separates the confined plasma from the SOL.

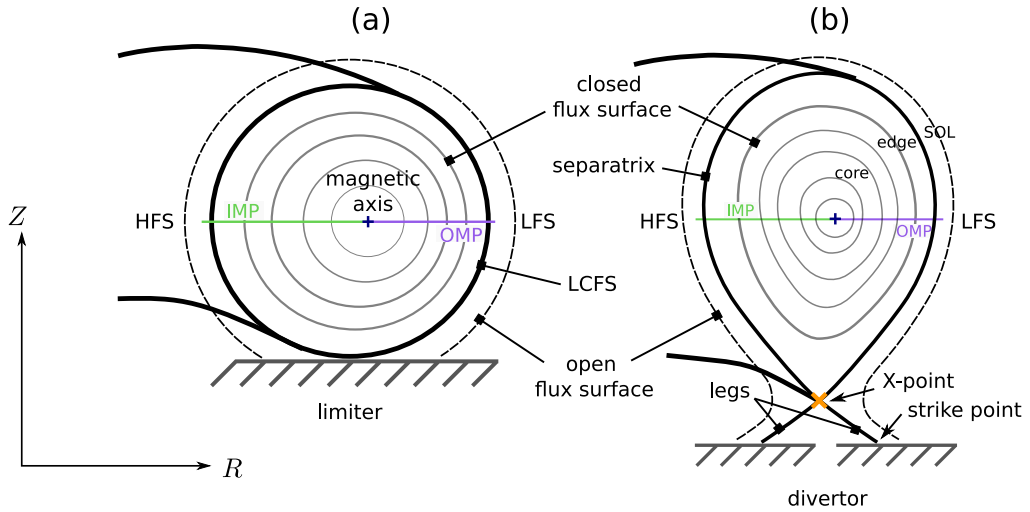

Figure 1.4: *Poloidal cross-section illustrations of (a) limited and (b) diverted, lower single-null (LSN) magnetic configurations.*

The LCFS is then referred to as the "separatrix". The X-point is formed by controlling the external current of a poloidal-field coil near the divertor. The divertor refers to the region between the X-point and the intersections—called "strike points"—between the outgoing divertor "legs" and the wall.

A diverted "single-null" discharge has one active X-point, which is the standard case. In this configuration, the active X-point is typically found either at the bottom of the plasma—as shown in Fig. 1.4—or at the top. These configurations are known as "lower single-null" (LSN) and "upper single-null" (USN), respectively. A secondary X-point

outside of the confined plasma can, nonetheless, be present in the vacuum chamber. Although not studied in this work, the case in which both X-points lie on the same separatrix is called a "double-null" (DN) shape.

It is worth noting also in Fig. 1.4 the definitions of the inboard midplane (IMP) and outboard midplane (OMP). The IMP spans the horizontal plane from the magnetic axis to the high-field side (HFS), and the OMP spans from the magnetic axis to the low-field side (LFS).

It is convenient to introduce a dimensionless effective radial coordinate ρ_ψ, which can be thought of as a normalized minor radius adapted for arbitrary magnetic geometries. It is defined as the square root of the normalized poloidal flux (ψ_N),

$$\rho_\psi = \sqrt{\psi_N}\,, \qquad \psi_N = (\psi - \psi_0)/(\psi_{\mathrm{LCFS}} - \psi_0)\,, \tag{1.1}$$

where ψ_0 and ψ_{LCFS} are the poloidal magnetic fluxes at the magnetic axis and at the last closed flux surface (LCFS), respectively. Hence, $\rho_\psi = 0$ at the magnetic axis, and $\rho_\psi = 1$ at the LCFS, while $\rho_\psi > 1$ corresponds to the SOL.

In this work, radial plasma profiles are always expressed in terms of ρ_ψ, with special focus on the plasma edge region. As shown in Fig. 1.4, this region lies between the plasma core and the LCFS. We further distinguish between the *inner* and *outer* core. The transition between these regions is continuous, and their radial extent, therefore, loosely defined. For reference, however, they may roughly be separated as follows:

- inner core: $0 \leq \rho_\psi \lesssim 0.7$
- outer core: $0.7 \lesssim \rho_\psi \lesssim 0.9$
- edge: $0.9 \lesssim \rho_\psi \leq 1$
- SOL: $1.0 < \rho_\psi$.

1.1.3 Limitations of confinement and turbulent transport

Above we have introduced the geometry of a tokamak, which—to first approximation—provides an axisymmetric magnetic equilibrium in which the plasma ions and electrons are bound to their respective flux surface, providing the basic requirement for magnetic confinement.

However, this confinement is not perfect. Thermal energy can escape the plasma through radiation (especially in the presence of heavy impurities), and particles and heat can also be transported radially (across field lines) via different processes. These transport processes have in common that they are fundamentally driven by radial gradients in equilibrium quantities, such as pressure, that are inherent to magnetically confined hot plasmas (as developed below).

An intrinsic transport channel is the diffusion associated with Coulomb collisions. Describing the collision-driven transport in toroidal geometry is the subject of "neoclassical theory", to which we will return later. In present-day tokamaks, the observed transport is often found to largely exceed neoclassical predictions. This discrepancy, which historically

led to the term "anomalous" transport, is believed to stem from a dominant transport channel associated with plasma *turbulence*.

The turbulent nature of the plasma is linked to the extreme conditions necessary for fusion. As mentioned above, the confined plasma necessarily develops strong pressure gradients between the hot core and the cooler edge region. This, among other perpendicular gradients (including in B and in the current density) keep the plasma far from thermodynamic equilibrium. They constitute a reservoir of free energy that can drive a variety of modes unstable. These include large-scale MHD instabilities that may cause significant perturbations to the equilibrium and even lead to plasma disruptions.

At smaller spatial scales, so-called "micro-instabilities" are nearly ubiquitous in these plasmas. They are less of a concern for macroscopic (MHD) stability. Instead, they grow and interact with each other, and eventually reach a saturated state, underlying plasma turbulence. This turbulence is characterized by a disordered mix of perturbations spanning a broad range of spatial scales, as illustrated in Fig. 1.5.

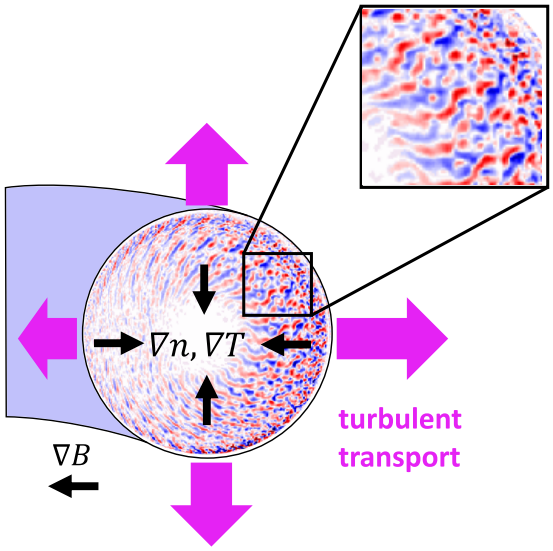

Figure 1.5: *Sketch of the main gradients driving micro-instabilities in hot magnetized plasmas. The resulting turbulence, illustrated using a snapshot of the potential perturbations obtained from a gyrokinetic* `GYSELA` *simulation [7], usually accounts for most of the radial transport in tokamaks.*

Turbulent perturbations (e.g., of the electrostatic potential, density, temperature, ...) vary predominantly in the transverse direction to $\boldsymbol{B}$, and only slowly in the parallel direction along field lines. This is a consequence of the transport anisotropy in tokamaks, characterized by much faster parallel transport (and therefore faster perturbation relaxation) than across field lines. Such perturbations are commonly referred to as "eddies", or "vortices", reflecting the rotating plasma motion caused in particular by the $E_r \times B$ advection associated with potential fluctuations.

Owing to the nonlinear character of the turbulence, its 2D spatial structure in the plane perpendicular to $\boldsymbol{B}$ tends to be anisotropic, forming, for example, radially elongated eddies, also called "streamers", as shown in the zoom inset of Fig. 1.5. Ballistic transport events, associated e.g. with "avalanches"[8, § 2.3.2], are another form of what can generally

be referred to as turbulent "structures".

Turbulent eddies, especially those that are large and radially stretched, tend to mix neighboring regions of different density and temperature. This process generates outward radial transport of particles and heat away from the hot, dense plasma core. This turbulent energy loss decisively deteriorates the confinement in a tokamak, limiting its fusion performance when extrapolated to a reactor.

1.1.4 Lawson criterion

In the previous section, we have seen that magnetic confinement is inherently limited by radiation and transport losses—of which turbulence is a major contributor. However, perfect confinement is not necessary for operating a fusion reactor. Instead, the fundamental requirement is that of a positive power balance. That is to say, the plasma must be maintained in steady-state at temperatures and densities that yield a fusion power (P_{fus}) much larger than the auxiliary heating power (P_{aux}). The auxiliary heating is necessary—at least initially—to compensate for the aforementioned thermal losses (P_{loss}) and keep the plasma in steady-state. In a power plant, the plasma will partly self-sustain its fusion reactions by the α-heating. "Scientific breakeven" is achieved if the energy gain factor $Q = P_{\mathrm{fus}}/P_{\mathrm{aux}}$ exceeds one, whereas an economically viable power plant must have a significantly greater Q-factor, on the order of 30 or higher. A common metric in this context is the energy confinement time (τ_E), which in steady state reads $\tau_E = W/P_{\mathrm{loss}}$. It represents the characteristic decay time of the confined thermal energy (W) set by its loss rate P_{loss} through transport and radiation from the confined plasma. In other terms, τ_E measures the confinement quality of the device.

In a fusion reactor, τ_E must be on the order of seconds, such that the "triple product" of plasma density n, temperature T and confinement time reaches values well above the threshold related to the breakeven condition ($Q > 1$). A common formulation of this "Lawson criterion" [9] reads:

$$nT\tau_E \gtrsim 3 \times 10^{21}\,\mathrm{m}^{-3}\,\mathrm{keV\,s}\,.$$

The fundamental difficulty of reaching this threshold with current devices is the combination of high transport losses (often dominated by turbulence) and the small plasma volume. For a given B-field strength (mainly set by technological and engineering constraints), increasing the plasma size tends to increase τ_E, as confirmed by empirical scaling laws [10]. Conversely, a reduction of cross-field transport also enhances the energy confinement, allowing the Lawson criterion to be reached at smaller device size and cost. Thus, the control of plasma turbulence, which sensitively determines the overall transport, is a central objective of magnetic confinement fusion research. A major breakthrough in this endeavor came in 1982 with the discovery of the "H-mode", a confinement regime marked by an improvement in τ_E due to locally suppressed turbulent transport. It will be introduced in more detail below in the context of turbulence reduction via sheared plasma flows—a key focus of this work.

1.1.5 Importance of sheared flows

We have seen that the energy confinement in tokamaks is largely set by turbulent transport, driving the size and cost of future fusion power plants. Radially sheared plasma flows represent an effective mechanism for reducing turbulent transport, and they form the central focus of this PhD thesis.

More specifically, the focus lies on *edge* flows associated with the mean radial electric field (E_r). The resulting "$E_r \times B$" drift, $v_{E\times B} = |\boldsymbol{E_r} \times \boldsymbol{B}/B^2| = E_r/B$, gives rise to a mean flow, or plasma rotation. Here, "mean" refers to the temporal average over millisecond time scales that are typical of experimental measurements, and long with respect to turbulence correlation times (microseconds).

The $E_r \times B$ drift is perpendicular to both $\boldsymbol{B}$ and the radial direction (r), and thus approximately—but not exactly—aligned with the poloidal direction (θ). Near the plasma edge, E_r is generally negative and forms a characteristic well-like structure just inside the separatrix (Fig. 1.6). Radial gradients of E_r—such as those associated with the E_r

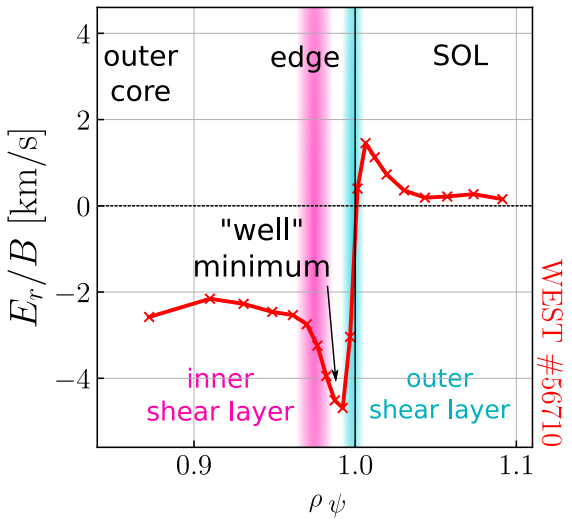

Figure 1.6: *E_r "well" measured at the edge of a typical (L-mode) plasma discharge on WEST. The regions of significant negative and positive E_r gradients around the well minimum are referred to as the inner and the outer shear layers.*

"well"—produce velocity shear that is widely believed to stabilize microinstabilities and the turbulent cross-field transport caused by them.

A prominent physical picture underlying this effect is the shear-decorrelation mechanism proposed by Biglari, Diamond and Terry [11]. It is illustrated in Fig. 1.7. A radially sheared flow velocity distorts turbulent eddies, stretching and tearing them apart into smaller structures. The resulting decorrelation of eddies reduces their radial mixing length and thus their ability to drive radial transport. Beyond this *nonlinear* decorrelation effect, $E_r \times B$ shear can also linearly stabilize a range of instabilities [12], limiting their growth rate and intensity.

The general tendency of flow shear to reduce turbulent transport is well-established theoretically. Global turbulent simulations largely support the relevance of the phenomenon

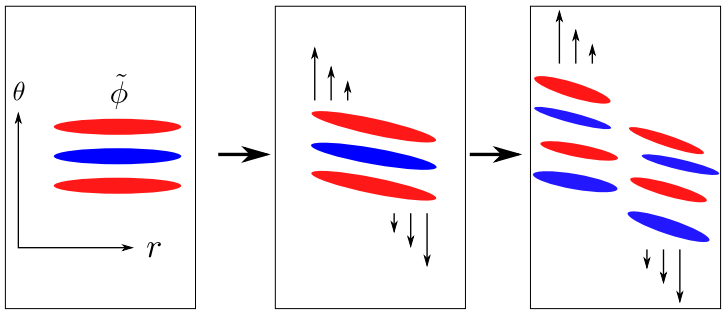

Figure 1.7: *Cartoon of the shear-decorrelation mechanism: Turbulent fluctuations ($\tilde{\phi}$) are represented by radially elongated structures. Time increases from left to right. The sheared flow, indicated by vertical arrows, distorts and eventually breaks the fluctuations into smaller structures that cause less transport.*

and provide a good illustration of it. The comparison between cases with sheared flows suppressed and included[3] reveals a pronounced reduction in fluctuation levels in the latter [13]. Such an exercise was performed also using the `GYSELA` code [7], with the turbulence snapshots shown in Fig. 1.8. Supporting evidence for the impact of flow shear on

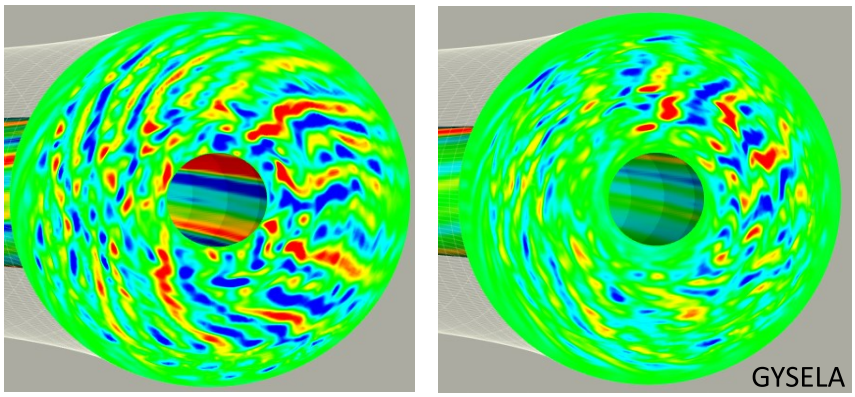

Figure 1.8: *Turbulence snapshots from `GYSELA` [7] simulations with suppressed sheared flows (a) versus the case where they are included (b). Turbulent fluctuations are reduced in the latter. Courtesy of G. Dif-Pradalier. A similar figure can be found in Ref. [13] based on a different turbulence code.*

transport also comes from experiments: The H-mode and its associated edge transport barrier are iconic examples that will be discussed below.

A second type of shear, intrinsic to the magnetic equilibrium, is the *magnetic* shear. This mechanism can also stabilize instabilities and reduce turbulent transport, in a way that is broadly analogous to $E_r \times B$ shear. In particular, *negative* magnetic shear is thought to facilitate *internal* transport barriers. While this work focuses on the $E_r \times B$ shear, the interplay between magnetic and velocity shear is central to the concept of "magnetic-shear-induced Reynolds stress", introduced in Sec. 2.6 and relevant to the discussions in Chapter 4.

[3] Here, the suppressed or included flows are turbulence-driven "zonal flows", introduced later in Sec. 2.5.

1.1.6 Confinement transition and H-mode

As already hinted, strong enough flow shear can lead to a local suppression of turbulent transport. Such events are associated with confinement bifurcations, the most prominent being the transition from the low (L-mode) to the high confinement mode (H-mode). This (L-H) transition can be readily triggered in most present-day tokamaks by exceeding a certain threshold of injected heating power.

The transition is accompanied by the abrupt formation of an edge "transport barrier", along with a sharp deepening of the negative E_r well (Fig. 1.9). The transport barrier

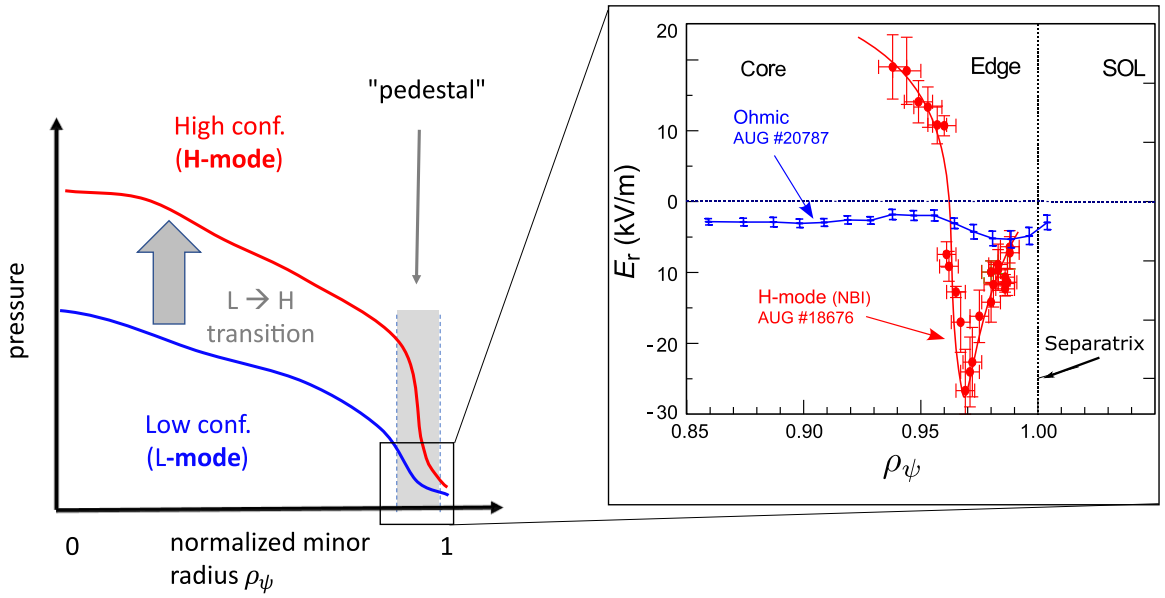

Figure 1.9: *Schematic illustration of the radial pressure profile in L- versus H-mode. The edge transport barrier—where the H-mode pressure pedestal forms—coincides with a sharp E_r well, as indicated by the inset with experimental data from the AUG tokamak. Figure adapted from [14], courtesy of G.D. Conway.*

formation is marked by a steepening of the edge pressure gradient—reflecting the reduced particle and heat diffusivity. Moreover, turbulent fluctuation levels are drastically reduced in this region.

The H-mode pressure "pedestal"—indicated in Fig. 1.9—tends to rigidly raise the pressure profile up to the core. This significantly increases the overall thermal energy content—and therefore, the energy confinement time—typically by a factor 2 compared to L-mode. H-mode-level confinement is considered essential for achieving reactor-relevant fusion performance. Notably, the large international ITER tokamak, currently under construction in France, is foreseen to operate in this regime [15]. However, typical H-modes also come with a decisive drawback: the onset of edge MHD instabilities, known as "edge localized modes" (ELMs), which pose a serious challenge for power exhaust in future reactors. We later return to this point when discussing negative triangularity plasmas, which could represent an attractive ELM-free L-mode alternative to H-mode.

Although the L-H transition was discovered over 40 years ago on the ASDEX tokamak [16] and has since been reproduced on many devices—demonstrating its universality, a deep

understanding of its physics is still lacking. As no robust, predictive physics-based model of the transition exists yet, estimates of the L-H power threshold continue to rely on empirical scaling laws.

1.2 Scope of the Thesis

The key terminology and general context relevant to tokamaks and the physics addressed in this PhD thesis have been introduced above. We now proceed to state the objective of this work and outline its methodology and specific focus.

1.2.1 Motivations and research aim

The phenomenon of the H-mode and the associated L-H transition provide strong indications that the E_r well—and the mean flow shear it generates—play a fundamental role in suppressing turbulent transport and, thereby, enhancing confinement.

More generally, an E_r well is also observed in L-mode—even without external heating and well below the L-H transition threshold. Although less pronounced than in H-mode, the L-mode E_r well still produces a narrow radial layer with relatively strong mean velocity shear.

It is therefore reasonable to expect that this shear may also contribute, at least to some extent, to the general regulation of transport—not just in H-mode. In addition, the L-mode velocity shear *prior* to confinement bifurcations might be a crucial ingredient in triggering the latter, thereby determining the access conditions to improved confinement regimes such as the H-mode. However, a clear understanding of the role of the E_r well in setting the L-mode confinement properties and in providing access to high confinement regimes remains to be established.

Moreover, the tightly related question of what primarily *drives* the negative E_r well at the plasma edge remains longstanding and unresolved. In particular, the sensitivities of E_r to plasma conditions—such as magnetic configuration, plasma shape, or proximity to the L-H transition threshold—are still poorly understood and remain difficult to capture with existing models and numerical tools.

In summary, there is broad consensus that sheared flows play a central role in suppressing turbulent transport in tokamaks and in achieving high confinement (in particular, though not exclusively, via access to H-mode). This provides strong motivation to clarify the origin and parametric sensitivities of the E_r well, and to determine how they connect to confinement properties.

Within this context, the overarching objective of this PhD thesis may be formulated as follows:

The aim is to experimentally isolate the influence of specific parameters to elucidate the mechanisms underlying the formation of the E_r well and its relevance to plasma confinement.

To address this objective, advanced diagnostics are combined with systematic E_r studies in

carefully designed tokamak experiments. The study thereby focuses on magnetic geometry effects, laid out below along with the experimental approach.

1.2.2 Scientific approach and focus

The general methodology of this experimental study consists of the following key elements, with more explanations provided thereafter:

(1) E_r measurements are obtained via Doppler backscattering.

(2) Experiments are performed on the WEST, AUG and—primarily—TCV tokamaks.

(3) The analysis of E_r focuses on its sensitivities to magnetic geometry in L-mode.

(1) Doppler backscattering (or DBS, for short) is a non-intrusive microwave diagnostic. It detects the signal backscattered by density fluctuations. The Doppler shift yields the perpendicular velocity ($v_\perp \approx E_r/B$), thereby enabling radially localized measurements of E_r. Radial profiles of $v_\perp$ (or E_r) are obtained by stepping the probing frequency. More details are provided in the dedicated chapter (Chapter 3).

(2) The European tokamaks WEST, AUG, and TCV are complementary in terms of machine geometry and size, wall material, as well as diagnostics, heating, and magnetic configuration capabilities. These devices will be presented briefly in Sec. 1.2.4. Particular focus is thereby placed on the TCV tokamak, where the recent commissioning of a DBS system enabled the first detailed edge E_r studies on this device, and provided the basis for addressing the above research questions. TCV's versatility makes it ideal for complementing the E_r investigations on WEST and AUG—already equipped with DBS systems—by allowing both multi-machine comparisons and exploration of otherwise inaccessible magnetic geometries. The comparison of E_r across different machine conditions is instructive to disentangle universal from machine-specific effects, which, in turn, may help pinpoint key physics ingredients.

(3) This work uses externally controlled magnetic geometry variables (introduced further below) to study their influence on the E_r well. Magnetic geometry can strongly affect confinement in tokamaks—including in L-mode or in the absence of auxiliary heating—through mechanisms that remain insufficiently understood. Given these considerations, the magnetic geometry effects examined here serve as an effective actuator for investigating the link between mean E_r shear and confinement. Moreover, such a research focus makes efficient use of TCV's unique magnetic shaping and configuration flexibility. The focus on *L-mode* is justified by the fact that the dominant E_r drives remain particularly unclear in this confinement regime. In addition, the L-mode phase *preceding* the L-H transition is key to elucidating the possible role of the E_r well in triggering the bifurcation. L-mode experiments also allow for a cleaner isolation of parameter influences. In fact, measurements of E_r and other key plasma quantities are considerably easier to obtain in L-mode than in H-mode, thanks to more reproducible and controllable plasma conditions.

1.2.3 Investigated magnetic geometry effects

Two distinct magnetic geometry aspects are considered in this work:

(A) magnetic drift configuration,

(B) plasma shaping—specifically via the "triangularity" parameter.

Below we provide a brief introduction to these topics, which are further developed in their dedicated Chapters 4 and 5.

(A) Favorable and unfavorable drift configurations

The first line of research examines the influence of the (mainly vertical) ion magnetic drift direction, hereafter simply referred to as "$B\times\nabla B$ drift". The $B\times\nabla B$ drift is termed *favorable* when it points toward the X-point and *unfavorable* when it points away from it, as illustrated in Fig. 1.10.

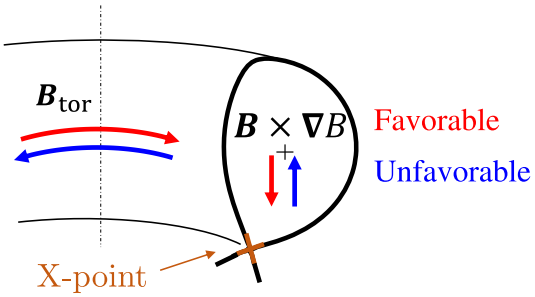

Figure 1.10: *Sketch showing the distinction between the favorable and unfavorable magnetic drift directions in a diverted tokamak plasma.*

The terminology originates from their differing ease of H-mode access, with the unfavorable configuration requiring a significantly higher power for triggering the L-H transition, than the favorable configuration.

Although the impact of the $B\times\nabla B$ drift direction on the L-H power threshold has been known for four decades and widely investigated, its origin remains unresolved. This magnetic geometry effect stands as a clear example of fundamental gaps that persist in our understanding of high confinement access.

As will be illustrated later in this manuscript, several experiments find a marked influence of drift configuration also on the L-mode edge E_r profile. Such a pronounced sensitivity presents a valuable opportunity: It may help clarify the dominant mechanisms driving the E_r well formation, and illuminate how these mechanisms relate to H-mode access. This will be the focus of Chapter 4.

(B) Negative and positive triangularity shaping

The second research axis explores how the triangularity shaping parameter affects the edge E_r. As introduced in Sec. 1.1.2, triangularity (δ) is responsible for the characteristic "D"-shaped plasma cross-section. Whereas conventional tokamak plasmas typically operate with positive triangularity (PT, Fig. 1.11 a), negative triangularity (NT) has recently attracted growing interest for its superior L-mode performance and intrinsic avoidance of ELMs—large-scale edge MHD instabilities that must be avoided or mitigated in future reactors.

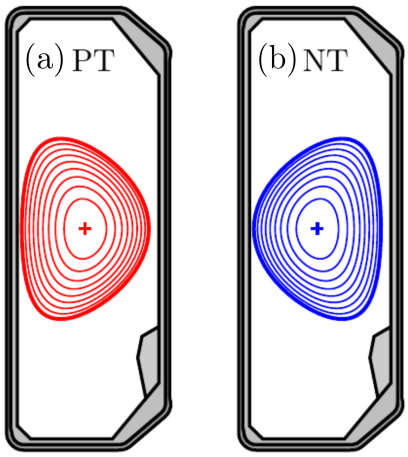

Figure 1.11: *Illustration of plasma cross-sections with a (a) positive and (b) negative triangularity shape.*

Given its favorable properties, NT is increasingly viewed as a promising alternative configuration for future tokamak reactors. Following the pioneering and sustained studies on TCV [17–20], the confirmation on the DIII-D tokamak of robust ELM-free, high L-mode performance [21–25] has driven intensified experimental and modelling efforts to further assess the potential of NT as a reactor concept.

While these results from NT experiments are promising, the exceptional L-mode confinement observed in NT is not fully understood yet. As will be elaborated later, several indications point to reduced turbulence in NT compared to PT, with recent studies emphasizing also the key role of the plasma edge—where the E_r well is located. A possibly enhanced edge E_r shear in NT could plausibly contribute to the reduced turbulence and, therefore, to the improved confinement. Yet, prior to the present work, the systematic characterization of the E_r well in NT has been very limited. The present study addresses this experimental gap in Chapter 5.

1.2.4 Overview of the considered tokamaks

To conclude the outline of the present scope, we provide a brief overview of the experimental tokamak devices—WEST, AUG, and TCV—used in this work. A more detailed description is thereby reserved for TCV, the primary device used in this study.

These tokamaks are three out of the four participating in the EUROfusion Medium-Sized Tokamak program[4]. Accordingly, this work's research activities were directly and indirectly promoted by the EUROfusion Consortium and the associated Work Package for Tokamak Exploitation (WPTE). The experiments were carried out both within the internal campaign programs (managed by the devices' host lab) and/or through the WPTE programme. Part of the analysis also draws on prior discharges from WEST's predecessor, Tore Supra.

A tabular overview of the tokamak's main geometrical and operational features is given in Tab. 1.1. The list should serve only as an approximate reference, as it is neither exhaustive,

[4] https://euro-fusion.org/devices/medium-sized-tokamaks/

Table 1.1: *Overview of main characteristics of the tokamaks considered in this work. The data are largely based on the World Survey of Fusion Devices 2022 [26] and references therein; [27–29], in addition to [30].*

Device	**Tore Supra**	**WEST**	**TCV**	**AUG**
Major radius, R_0 [m]	2.4	2.5	0.88	1.65
Minor radius, a [m]	0.8	0.5	0.25	0.5
On-axis field, B_0 [T]	$\leq$4.5	$\leq$3.7	$\leq$1.5	$\leq$3.2
Plasma current, I_p [MA]	$\leq$2	$\leq$1	$\leq$1	$\leq$1.4
Installed aux. heating [MW]	21	15	7	32
Magnetic config.	limiter, circular	divertor	divertor	divertor
Wall material	carbon	tungsten	carbon	tungsten
Operation period	1988-2011	2016-present	1992-present	1991-present

nor does it reflect the complexity of operational limitations[5].

Except for Tore Supra, which operated only in limited, circular-shaped discharges, the other tokamaks WEST, AUG, and TCV, are primarily operated in diverted configurations (though limited plasmas are still possible), ranging from LSN to USN shapes, including DN.

To better illustrate machine and plasma dimensions, Fig. 1.12 compares the cross-sections of typical LSN plasmas (to scale), as well as the inner contours of the vacuum chamber in these tokamaks. It highlights their complementarity in terms of plasma size and/or aspect ratio.

WEST (formerly **Tore Supra**)

The *tungsten (W) Environment in Steady-state Tokamak* (WEST) [27, 31, 32] is run by the French *Institut de Recherche sur la Fusion par confinement Magnétique* (IRFM), based at the CEA Cadarache Centre. It was developed as part of a major upgrade of its predecessor Tore Supra, from a limiter to a divertor-compatible, full-tungsten device. WEST has an ITER-grade lower divertor, designed to withstand 10 MW/m^2 in steady-state. It is equipped with superconducting toroidal field coils, actively cooled plasma-facing components, and non-inductive current drive systems. As such, WEST is designed to sustain long discharges, and currently holds the world record with a duration of over 22 min, established in early 2025. Such long pulses enable addressing key challenges associated with steady-state heat exhaust, plasma-wall interaction, and tungsten erosion under large (cumulated) particle and heat flux exposures, in preparation for ITER and next-generation devices.

The installed heating capacity in WEST consists of lower hybrid (LH) wave heating and current drive (6 MW), and ion cyclotron resonance heating (ICRH, 9 MW). Additional gyrotrons (3×1 MW) for electron cyclotron resonance heating (ECRH) and current drive (ECCD) are planned for commissioning in 2026.

AUG

The *Axially Symmetric Divertor EXperiment (ASDEX) Upgrade* [28, 33], AUG for short,

[5] For instance, the installed heating power is typically much larger than the actual maximum power that can realistically be delivered to a discharge.

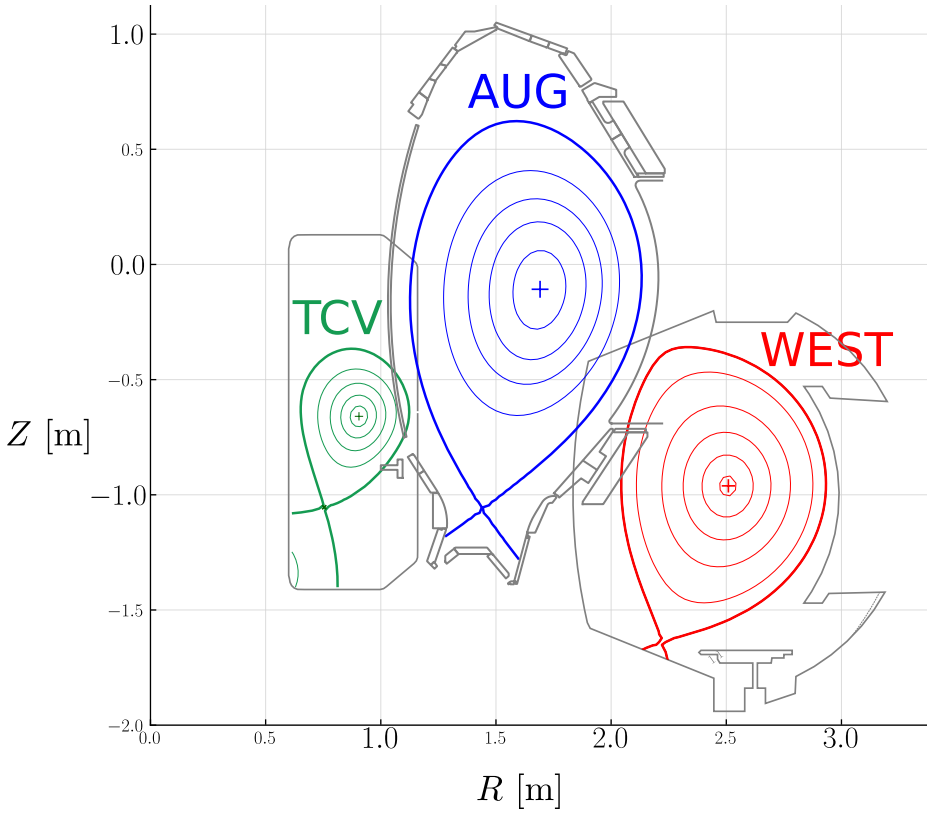

Figure 1.12: *Typical plasma cross-sections and inner vessel contours for the different tokamaks.*

is operated by the Max Planck Institute for Plasma Physics in Garching, Germany. The design of AUG is based on its predecessor, the ASDEX tokamak—in which the H-mode was discovered [16], with adaptations towards reactor-relevant requirements, such as an optimized ITER-like divertor and magnetic geometry [34]. Like WEST, AUG's plasma facing components are made of, or coated with tungsten. AUG features a powerful auxiliary heating capacity, comprising neutral beam injection (NBI, 20 MW), ECRH (6 MW) and ICRH (6 MW), delivering up to 27 MW [28]. Together with an extensive suite of diagnostics, this capability has enabled a productive experimental program with a wealth of results obtained over its ≈ 35 years of operation. Among the notable historic contributions of AUG is the work demonstrating tungsten as a suitable reactor first wall material, following a step-wise transition from carbon to full tungsten between 1999 and 2007. A central focus of the experiments at AUG is related to power and particle exhaust physics under reactor-relevant H-mode conditions.

TCV

The *Tokamak à Configuration Variable* (TCV) [29, 35–37] of the Swiss Plasma Center (EPFL-SPC) in Lausanne, Switzerland, is the main device considered in this work. An illustration of the TCV vessel and of the ring-shaped (poloidal field and inductive, or Ohmic) coils system is provided in Fig. 1.13.

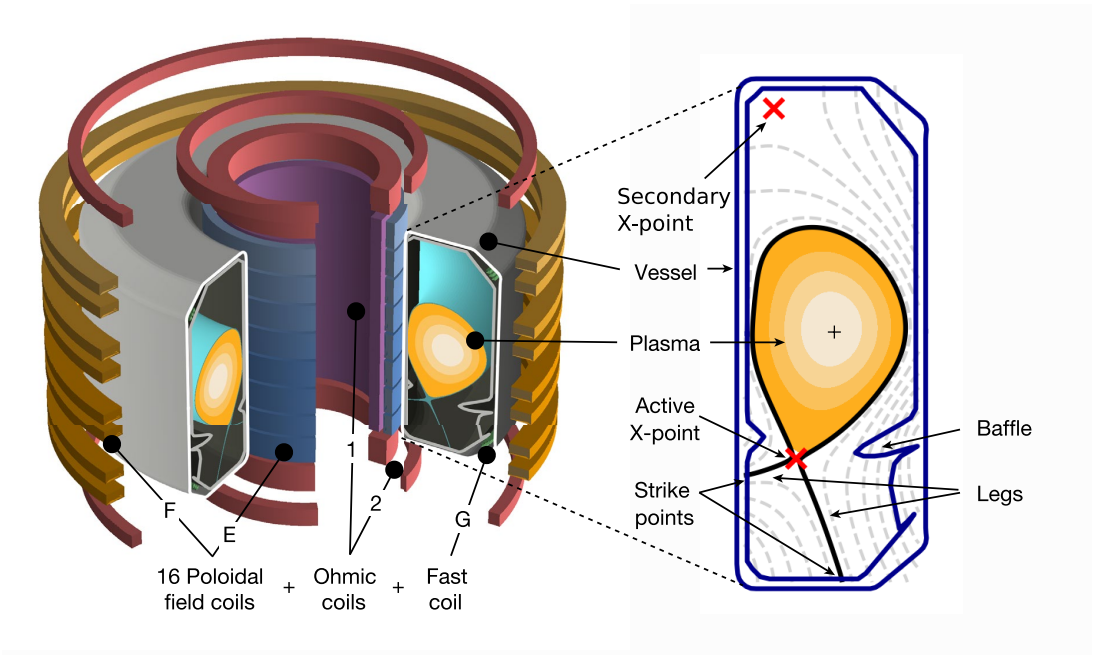

Figure 1.13: *Sketch of the TCV tokamak adapted from [38], showing the vacuum vessel and a subset of the magnetic coil system (left), and a poloidal cross-section of the vessel with a typical diverted plasma geometry (right).*

It highlights some important features of TCV: a vertically elongated vacuum vessel (1.5 m high by 0.5 m wide), and an ample set of auxiliary coils, of which 16 are independently powered, poloidal field coils used in particular for shaping. This provides TCV with outstanding flexibility in terms of shaping and vertical positioning of the plasma—an important asset for the experiments conducted in this work.

The poloidal-field coils in Fig. 1.13 are surrounded by 16 toroidal field coils (not shown). All coils are made of copper. This limits the inductive discharge duration to about 2 s. The signs of B_0 and I_p can be chosen arbitrarily and changed between shots. The time delay between discharges is about 12 min. TCV operates with hydrogen (H), deuterium (D), or helium (He) as the main plasma species. However, all experiments in this work use D plasmas.

The TCV auxiliary heating system comprises both second and third harmonic (X2 and X3) ECRH (6 gyrotrons with up to 0.5–1 MW each [37]). TCV is also equipped with two neutral beams for NBI heating [39]. The beams (denoted NBI-1 and NBI-2) are injected horizontally in the midplane, each with nearly toroidal, but opposite, incidence (Fig. 1.14). They deliver up to 1.3 and 1 MW, respectively. The beam properties differ in particular

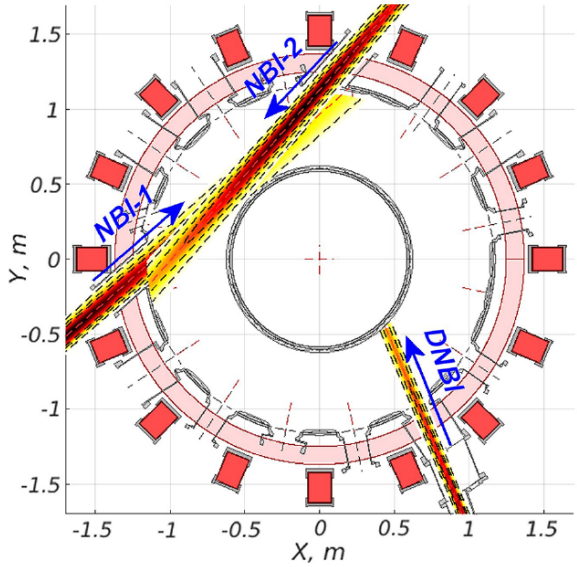

Figure 1.14: *Top view of the diagnostic (DNBI) and heating (NBI-1 and NBI-2) neutral beams in TCV. Figure from [39].*

in the energy per injected neutral, which is lower for NBI-1 (7–28 keV) than NBI-2 (25–51 keV) [39]. Auxiliary heating by NBI is usually delivered in the co-current direction, since counter-I_p injection leads to significant prompt (first-orbit) ion losses. There is, however, also active research at TCV into intrinsic toroidal rotation physics through balanced NBI experiments [40, 41].

In addition to the heating beams, TCV has a diagnostic neutral beam (DNBI [42]), also shown in Fig. 1.14. The DNBI provides the neutral donors required for charge exchange recombination spectroscopy (CXRS [43]), a diagnostic used—in particular in this work—to measure kinetic profiles of impurity ions. Unlike heating beams, which are widely used on other devices also for CXRS applications, the low power ($\leq$ 80 kW) and the radial injection of TCV's DNBI minimize the heat and torque deposition, thereby making it largely non-perturbative. The specificities of the CXRS and other diagnostics used in this work will be presented in Chapter 3.

1.3 Thesis outline

With the scope of the present study established, we now outline the structure of the remainder of this manuscript.

First, Chapter 2 lays out the theoretical and experimental context relevant to the discussions of E_r results in the subsequent chapters.

Chapter 3 is dedicated to the description of the Doppler backscattering diagnostic (DBS, introduced above) and its implementation on TCV. The chapter also presents a broad survey of E_r well sensitivities in TCV L-mode plasmas, which contextualizes the more targeted E_r studies discussed in the subsequent chapters.

Chapter 4 addresses the favorable/unfavorable drift configuration effect on E_r, drawing primarily on new measurements from the TCV tokamak, and their comparison with results from WEST and AUG.

The influence of triangularity on the E_r well is explored in Chapter 5 through carefully matched PT/NT experiments in TCV.

The work is summarized in Chapter 6, with outlooks and suggestions.

Chapter 2

Radial Electric Field and Flow Generation in Tokamaks



Contents

2.1 Introduction on E_r and chapter outline 29
2.2 Radial Force Balance 31
2.3 Neoclassical description 32
2.4 Ion Orbit Losses 36
2.5 Turbulent Reynolds stress and Zonal flows 38
2.6 Magnetic shear induced Reynolds stress 39
2.7 Radial Electric Field in the SOL 40
2.8 Phenomenological review of the edge E_r 42
2.9 Chapter summary 52

This chapter presents elements from theory and experiments on the formation of the edge radial electric field (E_r) in tokamaks. They are meant to better place the present work and the interpretation of its results in context.

2.1 Introduction on E_r and chapter outline

We begin with a few remarks to frame this chapter: In a tokamak equilibrium, within the region of closed flux surfaces, a mean radial electric field (E_r) is generally present as it balances the sum of the pressure gradient and the Lorentz forces associated with the poloidal and toroidal rotation. This is described by the radial force balance equation (that will be introduced in Sec. 2.2). Yet, by itself, the force balance does not provide intuition about the underlying physics processes that lead to a given equilibrium E_r state.

Fundamentally, a radial electric field arises in response to a radial current, as follows from Maxwell's equations:

$$\epsilon_\perp \epsilon_0 \frac{\partial E_r}{\partial t} = -j_r \,,$$

where $\epsilon_\perp$ is an appopriate relative dielectric constant for magnetized toroidal plasmas [44], and $j_r = \sum_a q_a \Gamma_{a,r}$ is the radial current density expressed in terms of a sum of radial particle fluxes $\Gamma_{a,r} = n_a V_{a,r}$, where a denotes the species (electron, main ion, and possibly other impurity ions) and q_a its charge. An imbalance between electron and ion currents causes a finite j_r, which may be associated to different non-ambipolar transport processes that will be layed out below.

The ambipolarity condition requires that $j_r = 0$, so that E_r always quickly adjusts to compensate for any radial charge separation. This reasoning can be visualized as follows. An initial radial charge separation gives rise to a $\boldsymbol{j}_r \times \boldsymbol{B}$ force acting on all plasma species. Any force $\boldsymbol{F}$ perpendicular to $\boldsymbol{B}$ produces a guiding-center drift with velocity $\boldsymbol{V}_{a,d} = \boldsymbol{F} \times \boldsymbol{B}/(q_a B^2)$. Consequently, the $\boldsymbol{j}_r \times \boldsymbol{B}$ force (or $q_a \boldsymbol{V}_{a,r} \times \boldsymbol{B}$ force at the species level) induces oppositely directed radial drifts for ions and electrons, which act to oppose—and ultimately cancel—the radial current j_r. Thus, as pointed out in Refs. [45, 46], the $E_r \times B$ velocity (or E_r) can be regarded as resulting from a competition of transverse forces—representing momentum sources and sinks, or equivalently from non-ambipolar radial transport mechanisms.

Sticking to the latter representation, the radial current may contain various contributions [44, §5.3.3 and references therein],

$$j_r = j_{\mathrm{CX}} + j_{\mathrm{NC}} + j_{\mathrm{IOL}} + j_{\mathrm{RS}} + \dots \ ,$$

such as charge exchange friction with neutrals (j_{CX}), or neoclassical effects (j_{NC}) associated with parallel viscosity, toroidal magnetic ripple [47–50], and higher-order neoclassical effects such as gyroviscosity. Other contributions that will be discussed in more detail, as they are important for the subsequent discussions in this thesis, are linked to ion orbit losses (j_{IOL}) and turbulence-driven Reynolds stress (j_{RS}). A discussion of the neutral friction term (j_{CX})—although potentially relevant at the edge where neutrals can penetrate the plasma [51–55]—is beyond the present scope. In experimental devices, E_r may also be driven externally, via electrically biased probes that impose an additional radial current [56, 57], magnetic field perturbations [58, 59], or through the toroidal torque associated in particular with neutral beam injection.

With these general considerations in mind, the remainder of this chapter is structured as follows. After introducing in Sec. 2.2 the radial force balance, Sec. 2.3 summarizes elements from neoclassical theory for the description of E_r and rotation in the confined plasma.

Going beyond the framework of standard neoclassical theory, the aforementioned ion orbit loss and Reynolds stress drives are introduced in Sec. 2.4 and 2.5, respectively.

The above considerations and the experiments in this thesis focus on the E_r profile within the *confined* edge region, just inside the separatrix. For completeness, Sec. 2.7 also provides a description of the E_r profile outside of it, in the near scrape-off layer (SOL).

The chapter concludes with a phenomenological perspective on the E_r profile (Sec. 2.8), compiling observations across various devices as context for this work's research.

2.2 Radial Force Balance

The radial force balance decribes the relation between E_r and the equilibrium plasma profiles of pressure and rotation. It is obtained from the fluid momentum conservation equation, which describes the evolution of the fluid velocity $\boldsymbol{V}_a$ for of a given plasma species a. The latter reads [5, § 2]:

$$m_a n_a \left(\frac{\partial}{\partial t} + \boldsymbol{V}_a \cdot \boldsymbol{\nabla} \right) \mathbf{V}_a = -\boldsymbol{\nabla} p_a - \boldsymbol{\nabla} \cdot \boldsymbol{\pi}_a + q_a n_a \left(\mathbf{E} + \mathbf{V}_a \times \mathbf{B} \right) + \mathbf{R}_a \,. \tag{2.1}$$

Here, m and q are respectively the mass and charge of the species, n the density, p the pressure, $\boldsymbol{\pi}$ the viscous stress tensor, and $\boldsymbol{R}$ represents the influence of collisions with other plasma species.[1] Taking the radial projection of Eq. (2.1) at steady state ($\partial/\partial t = 0$), and neglecting small terms[2] yields the *radial force balance equation*:

$$E_r = \underbrace{V_{a,\varphi} B_\theta - V_{a,\theta} B_\varphi}_{-V_a \times B \text{ (Lorentz)}} + \underbrace{(\nabla_r p_a)/n_a q_a}_{-V_a^* B \text{ (diamag.)}} \,. \tag{2.2}$$

In this expression, the index a denotes the considered species, $V_{a,\varphi}$ and $V_{a,\theta}$ are its fluid toroidal and poloidal velocities, respectively, $p_a = n_a T_a$ its pressure and q_a its charge. The first term on the right-hand side represents the Lorentz force, the second is referred to as the "diamagnetic" contribution as it is proportional to the diamagnetic fluid drift velocity (V_a^*). Eq. (2.2) states that at equilibrium, the sum of the leading-order radial forces (electric, Lorentz and pressure) must cancel. This holds individually for each species.

From a practical perspective, Eq. (2.2) offers a way to determine E_r experimentally by measuring V_φ, V_θ, n and T simultaneously for a given plasma species. This is commonly done via charge exchange recombination spectroscopy (CXRS) [43], using an impurity instead of the main ion species. The method will be used also in this work, complementing some of the E_r measurements obtained by Doppler backscattering (more details in Chapter 3). However, as pointed out in [60], note that the *main* ion species carries most of the plasma momentum and ion thermal energy. The impurity radial force contributions—especially from rotation—may deviate substantially from those of the main ion [61, 62]. Yet, according to Eq. (2.2), E_r remains the same regardless of the considered species, as confirmed also in experiments [62].

Next, we consider elements from neoclassical theory that provide predictions for the main ion $V_{i,\theta}$, and—within certain conditions—for $V_{i,\varphi}$ which then determines E_r through Eq. (2.1) as a function of n and T_i only.

[1] The collision term for species a can be expressed as $\boldsymbol{R}_a = \int m_a \mathbf{v} C_a(f_a) d^3v$, where $C_a = \sum_a C_a b(f_a, f_b)$ is a collision operator (usually the right-hand side of the kinetic Fokker-Planck equation), summing over contributions from all species b. [5, § 2]

[2] Assuming usual transport orderings, the contributions from collisions and viscosity are small compared to the pressure gradient in the transverse direction to B. Furthermore, the inertial term on the left-hand side of Eq. (2.1), $mn(\boldsymbol{V} \cdot \boldsymbol{\nabla})\boldsymbol{V}$ is negligible if the flow velocity is much smaller than the thermal speed [5, § 4.7].

2.3 Neoclassical description

We recall that in present-day tokamaks, transport is largely *anomalous* [63], meaning that it often exceeds neoclassical levels, most likely as a consequence of turbulent transport. Nevertheless, the framework of neoclassical theory is important as it provides the foundation for describing the "baseline" transport in tokamaks, including mechanisms that are generally relevant to the understanding of confinement and rotation—in particular (although not exclusively) in regimes where turbulence is suppressed. We first outline key concepts of neoclassical theory, thereby introducing the relevant terminology used thereafter.

2.3.1 Basic elements of neoclassical theory

Neoclassical theory [5, 64] describes the collision-driven transport in toroidal geometry. Compared to classical transport, which is associated with cross-field diffusion owing to Coulomb collisions in a straight magnetic field (the cylindrical geometry limit), neoclassical theory captures additional effects inherent to toroidicity and the resulting B-field inhomogeneity and magnetic drifts. Notably, these effects include particle trapping [1, § 3], which significantly enhances the transport compared to classical diffusion [5, § 1.3].

Trapped particles refer to ions and electrons which, owing to a relatively low parallel velocity, undergo magnetic mirror reflections on their parallel motion towards the inboard, higher B-field side. When projected to a poloidal plane, trapped particles trace out so-called "banana"-trajectories between bounce points and the outboard, weaker B-field side of the plasma[3]. The frequency of this bounce motion is $\omega_b = \sqrt{\epsilon} v_\mathrm{T}/qR$, where $\epsilon = r/R$ is the inverse aspect ratio and $v_\mathrm{T} = \sqrt{T/m}$ the thermal velocity.

Passing particles, on the other hand, have sufficient parallel velocity to overcome the magnetic mirror force and, if not scattered by collisions, therefore execute a full poloidal orbit with a transit frequency $\omega_t = v_\mathrm{T}/qR$.

A crucial quantity in the context of neoclassical transport is the collisionality parameter ν^*, defined as [5, § 8.2]:

$$\nu^* = \epsilon^{-3/2} \frac{\nu}{\omega_t} \,, \tag{2.3}$$

where ν is the (ion or electron) collision frequency, as defined in [1, § 2.15]. For a pure plasma with singly-charged ions ($Z = 1$), the ion and electron collisionalities (ν_i^* and ν_e^*) are similar if $T_i \simeq T_e$.

Thus, collisionality measures the relative magnitude of collisions (which tend to detrap particles) over transit/bounce frequencies. Neoclassical theory distinguishes three main regimes according to collisionality [5, § 8.2]:

- Pfirsch-Schlüter (high-collisionality) regime: $\nu^* > \epsilon^{-3/2}$,

[3] More generally, beyond standard neoclassical theory, B is also inhomogeneous in the toroidal direction owing to magnetic ripple. This causes analogous (local) trapping by the toroidal mirror force, with implications discussed in Sec. 2.3.4.

- plateau regime (intermediate-collisionality): $1 < \nu^* < \epsilon^{-3/2}$,
- banana (low-collisionality) regime: $\nu^* < 1$.

In the high-collisionality regime, particles are scattered out of their orbits by collisions before the latter are completed, while in the opposite, banana regime, both passing and trapped orbits can be completed before de-trapping occurs. In the intermediate, plateau regime, only passing orbits tend to be completed. Collisionality regimes correspond to different transport regimes (in terms of neoclassical diffusion coefficients), and, as will be mentioned below, collisionality also affects the ion momentum balance.

2.3.2 Rotation within Standard Neoclassical Theory

Within the approximations of standard neoclassical theory for tokamaks, the magnetic equilibrium is considered axisymmetric, that is, invariant in the toroidal direction, or $\partial/\partial\varphi = 0$. The fluid particle flux of species a on a given flux surface ψ can then be expressed in its most general form for an incompressible (divergence-free) flow as [5, Eq. 8.24]:

$$n_a \mathbf{V}_a = \omega_a(\psi) n_a(\psi) R\hat{\boldsymbol{\varphi}} + K_a(\psi)\mathbf{B}\,, \tag{2.4}$$

with

$$\omega_a(\psi) = -\frac{d\Phi}{d\psi} - \frac{1}{n_a q_a}\frac{dp_a}{d\psi}\,. \tag{2.5}$$

The first term in Eq. (2.4) corresponds to a rigid body rotation with toroidal angular velocity ω_a, where Φ is the electrostatic potential (such that $E_r = -\nabla_r\Phi$). The second term in Eq. (2.4) contains the poloidal component of the flow since $V_{a\theta} = K_a(\psi)B_\theta$. The proportionality factor $K_a(\psi)$ must be calculated from kinetic theory. In the case of a circular, large aspect ratio plasma with a single ion species (i) with charge $q_i = Ze$, the ion poloidal velocity reads

$$V_{i\theta} = -\frac{k_{\theta 1}}{ZeB}\nabla_r T_i\,, \tag{2.6}$$

with T_i the ion temperature and $k_{\theta 1}$ a coefficient depending on the collisionality regime ($k_{\theta 1} = -1.17$ in the banana regime, $k_{\theta 1} = 0.5$ in the plateau and $k_{\theta 1} = 1.7$ in the Pfirsch-Schlüter regime) [5, § 13]. In the absence of other flow driving forces, the poloidal rotation relaxes to this neoclassical prediction on a fast (ion-ion collision) time scale[4]. This poloidal flow damping is a consequence of the so-called "neoclassical parallel viscosity", which fundamentally arises from the B-field variation (due to its $1/R$ dependence) experienced by the particles along their parallel motion[5].

Analytically tractable solutions can also be derived for the case of an impure plasma with one trace impurity [61]. While the main ion poloidal velocity remains roughly the same as

[4] The deuterium ion-ion collision time is $\tau_{ii} \sim 200\,\mu s$ at $T = 100\,eV$ and $n = 10^{19} m^{-3}$, see [1, § 2.15] for a handy formula.

[5] As summarized in [65, §3.4.2], this neoclassical poloidal flow damping is related to dissipative processes including magnetic pumping [66] and—in the banana regime—friction between passing and trapped ions (the latter carrying no bulk poloidal momentum) [67, §13.1]. The ion poloidal velocity at equilibrium is obtained from the system of parallel momentum and heat flow balance equations, which relate parallel viscosity and friction forces for momentum and heat, see [61] [67, §13.1].

in Eq. (2.6), that of the impurity contains additional dependencies—in particular on the main ion pressure gradient. As discussed in [61], the impurity velocity can thus deviate significantly from the main ion one—even having opposite signs, as observed for instance in the H-mode edge pedestal region [62].

Perhaps surprisingly, the neoclassical poloidal velocity (of main ions, Eq. (2.6), and impurities [61, Eq. 34]) is independent of the radial electric field. In fact, neoclassical transport in an axisymmetric system is largely insensitive to the radial electric field [67]. While $E_r = -\nabla_r \Phi$ is linked to the toroidal velocity through Eq. (2.5), at leading order it does not enter the (classical and neoclassical) transport, which is automatically ambipolar at steady state.[6] That is, in case of toroidal symmetry, collisional particle diffusion does not lead to radial charge separation and therefore does not need to be balanced by E_r to maintain ambipolarity. As a consequence, the plasma can rotate freely in the toroidal direction. In other terms, toroidal symmetry implies a form of degeneracy that prevents E_r and the toroidal rotation from being determined separately within standard neoclassical theory.

Breaking the toroidal symmetry introduces an additional constraint through the toroidal component of the parallel viscosity (which enters the toroidal projection of the momentum conservation equation). It lifts the degeneracy and allows to uniquely determine E_r and the toroidal velocity [68, § 7.8]. This will be discussed below for the case of axisymmetry breaking by magnetic ripple.

2.3.3 Neoclassical E_r approximation

A common approximation of E_r (see [69, § 2.2]) consists of neglecting the main ion toroidal rotation contribution ($V_{i\varphi} B_\theta$) and replacing $V_{i\theta}$ in Eq. (2.2) by its neoclassical prediction, Eq. (2.6). Splitting up the ion diamagnetic contribution to E_r into the components proportional to the logarithmic gradients of temperature and density, the "neoclassical" E_r approximation reads:

$$E_r^{\mathrm{NC}}(V_{i,\varphi} \approx 0) = \frac{T_i}{Ze} \left(\frac{\nabla_r n}{n} + (1 - k_{\theta 1}) \frac{\nabla_r T_i}{T_i} \right) . \tag{2.7}$$

In the particular case of the AUG tokamak, typical edge conditions correspond to a small value of $k_{\theta 1} \approx 0$ [69, § 2.2 and references therein]. Eq. (2.7) then further simplifies to

$$E_r^{\mathrm{NC}} \approx (\nabla_r p_i)/(Zen_i) , \quad \text{or equivalently: } v_{E\times B}^{\mathrm{NC}} = -V_i^* . \tag{2.8}$$

Note that Eq. (2.8) implies that the ion fluid is nearly at rest, since the leading-order (electric and diamagnetic) perpendicular drifts cancel and toroidal rotation is assumed to be small. As pointed out in [45], this may be viewed as resulting from the ambipolar E_r required to maintain the balance between the electron and ion viscous forces (akin to the classical transport in cylindrical geometry where the role of the viscous force is replaced by neutral friction).

[6] On time scales shorter than the poloidal rotation damping to its neoclassical value given by Eq. (2.6), neoclassical diffusion is not automatically ambipolar [68, § 7.5].

As will be illustrated in Sec. 2.8, experimental evidence from AUG [70, 71] indicates that this "neoclassical" E_r approximation may be valid in certain plasma conditions, such as at the edge of H-mode plasmas where the $(\nabla_r p_i)/(Zen_i)$ contribution dominates. However, several observations show that it is not generally appropriate for L-mode. This implies that either $V_{i,\theta}$ can depart substantially from Eq. (2.6) and/or that $V_{i,\varphi}$ is not negligible. Next, we consider the case where $V_{i,\varphi}$ is retained and described by neoclassical theory in the case of toroidal symmetry breaking by magnetic ripple.

2.3.4 Case of strong magnetic ripple

As previously mentioned, neoclassical theory cannot determine E_r independently from V_φ except when accounting for toroidal symmetry-breaking effects. An example is magnetic ripple, which refers to the toroidal modulation of magnetic field strength associated with the discrete number of coils. Even small non-axisymmetric perturbations can substantially influence toroidal rotation [72, 73] and, by extension, E_r. This has possibly relevant implications for ITER plasmas where external toroidal rotation drives will be limited. High ripple tokamaks such as Tore Supra, or—albeit to a lesser extent—its successor WEST provide an opportunity for testing the neoclassical prediction of E_r derived in the limit of strong ripple. We provide a brief account of this prediction and how it compares to experimental measurements.

Magnetic ripple causes toroidal (or "local") particle trapping between consecutive coils. Unlike poloidally trapped ("banana orbits"), locally trapped particles experience uncompensated magnetic $(B\times\nabla B)$ drifts—since they are locked within a narrow toroidal and therefore also poloidal section—until they are de-trapped by collisions or escape the confined region. Viewed as a random walk process, thermal ions and electrons diffuse radially at a rate that would be higher for ions due to their lower collisional de-trapping frequency [47, 74] if not compensated by a decrease of E_r to maintain ambipolarity. Alternatively, the effect of ripple may be described in terms of a toroidal force entering the momentum balance. This force is referred to as "magnetic braking" [49, and references therein], or "neoclassical toroidal viscosity". Its origin may be understood in an analogous way to that of the parallel visocosity (which constrains the ion poloidal rotation as a consequence of the modulation of B in the poloidal plane). The ripple-induced toroidal modulation of B has a similar impact on the toroidal rotation.

Accounting for thermal ripple losses within a thermodynamical framework [48], analytical expressions for the neoclassical mean E_r and ion rotation have been derived in the case of a circular, large aspect ratio tokamak. Their general form is given by:

$$\begin{aligned}\frac{ZeE_r}{T_i} &= \nabla_r \ln n - k_E \nabla_r \ln T_i,\\ V_{i\theta} &= -k_{\theta 1}\frac{\nabla_r T_i}{ZeB},\\ V_{i\varphi} &= -k_\varphi \frac{\nabla_r T_i}{ZeB_\theta},\end{aligned} \tag{2.9}$$

with numerical coefficients k_E and k_φ depending on the regime of collisionality and ripple

amplitude; $k_E \in [-3.37, -1.5]$ and $k_\varphi \in [-1.67, -3.54]$, and a poloidal velocity coefficient, $k_{\theta 1}$, that remains close to its standard neoclassical value (Eq. (2.6)) in the absence of ripple. Note that $-k_\varphi$ is positive in all regimes (for realistic levels of ripple), implying that the neoclassical ripple-induced toroidal torque is counter-current, consistent with Tore Supra measurements at high ripple amplitudes [73].

In the limit of strong ripple, where local trapping is important, the model yields $k_E = -3.37$ [48], in line with the expression for E_r derived earlier by Connor and Hastie [74]:

$$E_r = \frac{T_i}{Ze}\left(\frac{\nabla_r n}{n} + 3.37\frac{\nabla_r T_i}{T_i}\right). \tag{2.10}$$

In the circular, large aspect ratio plasmas of Tore Supra, where the ripple amplitude reaches up to 7 %, the prediction by Eq. (2.10) was found to be in reasonable agreement with DBS measurements in the outer core [47].

Note that both the approximation, Eq. (2.7), and the more general neoclassical expression for E_r given by Eq. (2.9) have the same form. They predict a negative (inward-pointing) E_r, as usually observed in particular at the edge and in the absence of strong co-current momentum injection.

Thus, in this neoclassical framework, for a given collisionality and ripple regime, E_r should be determined by the equilibrium n and T_i profiles (with their gradients).

As will be discussed throughout this manuscript, a simple relation of this form, Eq. (2.9), does not appear to capture certain experimental observations in which the edge E_r profile varies significantly in the absence of notable changes in n or T_i. This, together with numerical results from turbulence codes, are strong indications that additional non-ambipolar mechanisms, beyond those captured by standard neoclassical theory, contribute to setting the edge E_r well in tokamaks. Two such mechanisms—ion orbit losses and turbulence-driven Reynolds stress—are introduced in the following sections.

2.4 Ion Orbit Losses

Close to the plasma boundary, ions may escape and hit the divertor or vessel wall as a result of their finite orbit width. These ion orbit losses (IOL) possibly contribute to the formation of a negative radial electric field at the tokamak plasma edge. IOL may be driven in particular by collisional cross-field transport, although as a boundary effect, they are not described by neoclassical theory.

The mechanism underlying IOL may be pictured as follows. Guiding center orbits (of trapped or passing) confined particles form closed loops when projected on a poloidal plane. They have a radial excursion from their flux surface that stems from the (mainly vertical) magnetic $B \times \nabla B$ drift. The excursion width can be substantial for ions (especially trapped ones with "banana" orbits), whereas it is much smaller for electrons. As illustrated by the red trajectory in Fig. 2.1 (from [75]), edge ion orbits extend radially into the SOL and may therefore connect to a vessel component such as a limiter or the divertor targets. Initially confined ions are continuously scattered (e.g. through collisions

or turbulence) into such "loss orbits", which constitute an effective particle sink at the edge (and in a certain region of velocity space).

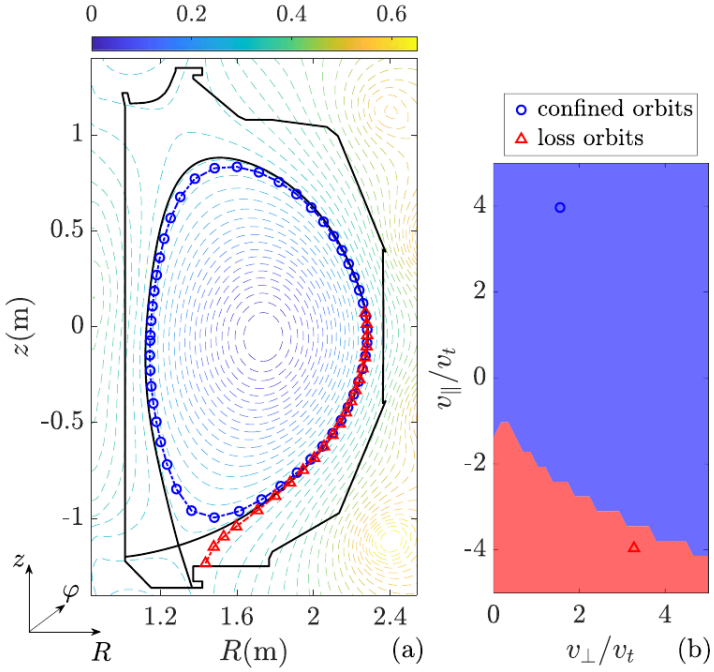

Figure 2.1: *Figure from [75]: (a) Illustration of a confined and unconfined (loss) orbit for ions both located close to the separatrix but emanating from different velocity space regions (b).*

Since the loss rate is negligible for electrons owing to their small orbit width, IOL constitute a non-ambipolar radial transport mechanism that tends to enhance the negative radial electric field inside the LCFS. Furthermore, IOL can drive toroidal momentum (e.g. [76] and references therein) as escaping ions tend to carry a velocity in the counter-current direction.

IOL have been invoked in early studies on the L-H transition [77–80] shortly after its discovery, followed by several other IOL-based bifurcation models (see [81, p. 4.1.1] for a review). Since then, the study of IOL—both for L-mode and in the context of the L-H transition—has seen continued development. Various models have been developed to address in particular the impact of IOL on E_r and intrinsic rotation [82] (and references therein). It remains an active research topic [75, 82–87]; Simulations using the gyrokinetic particle-in-cell code `XGC` suggest that E_r is not very sensitive to IOL in H-mode [85], where E_r remains close to its standard neoclassical value, mainly balancing the $(\nabla p_i)/en_i$ force balance contribution (in line with some experimental evidence [70]). A corresponding study in L-mode [75] finds indications that collisional IOL may shift the edge toroidal rotation in the co-current and E_r in the negative direction.

Further, the IOL mechanism is predicted to be sensitive to the magnetic geometry; This includes plasma shaping and the X-point geometry [84, 88, 89], as well as the $B \times \nabla B$ drift direction [78, 82, 83, 90–92]. Accordingly, IOL are among the candidate mechanisms for explaining the effect of magnetic drift configuration on the power threshold and on the edge E_r profile, as will be elaborated in Chapter 4. The role of IOL in the context negative versus positive triangularity shaping will be discussed as well, in Chapter 5.

2.5 Turbulent Reynolds stress and Zonal flows

Turbulent Reynolds stress has been suggested as another major drive of $E_r \times B$ rotation [93, 94]. This mechanism, explained below, underlies the generation of "zonal flows" [95]. Zonal flows are perturbations in the electrostatic potential that are constant on a flux surface but may vary rapidly in the radial direction and may thus contribute to the overall $E_r \times B$ flow shear. They arise from a nonlinear energy transfer from small-scale fluctuations to larger scale flows through the radial flux of momentum conveyed by turbulent fluctuations, the so-called "Reynolds stress". Physically, Reynolds stress can be viewed as a measure of "the degree of anisotropy in the structure of the fluctuations" [96]. Its divergence can redistribute plasma momentum from small to large scales.

To see where Reynolds stress originates from the momentum balance, consider the contribution of the advective nonlinearity $mn(\mathbf{V}\cdot\boldsymbol{\nabla})\mathbf{V}$ in the fluid momentum equation Eq. (2.1). Denoting $\tilde{\boldsymbol{V}}$ the fluctuating part of the fluid velocity, and taking the flux surface average (represented by $\langle\cdot\rangle$), we write the mean acceleration due to the fluctuating advective term as

$$\frac{\partial}{\partial t}\langle \boldsymbol{V}\rangle \,|_{\text{fluct.}} = -\left\langle(\tilde{\mathbf{V}}\cdot\boldsymbol{\nabla})\tilde{\mathbf{V}}\right\rangle \equiv -\boldsymbol{\nabla}\cdot\boldsymbol{\mathcal{R}} \tag{2.11}$$

where incompressibility ($\boldsymbol{\nabla}\cdot\tilde{\boldsymbol{V}} = 0$) has been assumed and $\mathcal{R}_{jk} = \langle\tilde{V}_j\tilde{V}_k\rangle$ is the turbulent Reynolds stress tensor. The plasma can thus be accelerated in the perpendicular direction if there is a radial gradient in the Reynolds stress component $\mathcal{R}_{r\perp} = \langle\tilde{V}_r\tilde{V}_\perp\rangle$. The velocity fluctuations in V_r and $V_\perp$ may both arise from the $E\times B$ advections caused by electrostatic perturbations, although the importance of the diamagnetic contribution to the overall Reynolds stress has also been pointed out [97].

The turbulence anisotropy, or average correlation between $\tilde{V}_r$ and $\tilde{V}_\perp$, that is required for $\mathcal{R}_{r\perp}$ to be non-vanishing, can be achieved if the eddies are elongated and poloidally tilted. Such eddy tilting may arise from $E_r \times B$ velocity shear, as well as from magnetic shear (as discussed in more detail below).

Evidence for Reynolds stress driven flow has been provided by experiments [98] and simulations [13, 99]. It is suggested as a possible reason for the discrepancy between observed poloidal velocities and neoclassical predictions (e.g. [100–102]). Turbulence-generated flows are among the leading proposed mechanisms for providing the necessary $E_r \times B$ enhancement to convey the L- to H-mode transition [103–106]. Their role in driving intrinsic toroidal rotation has also been discussed [107, 108].

Remark on the terminology used for distinguishing flow types. Turbulence-driven zonal flows are often considered to form meso-scale structures, that is to say, they occur on radial scales large compared to turbulence correlation lengths, but shorter than equilibrium profile variations. However, the distinction may not be straightforward close to the edge where equilibrium quantities may vary on relatively short scales. Therefore, this work does not distinguish between the terms "zonal flows" and turbulence-driven $E_r \times B$ flows. They include both the average component to the mean flow, and finite-frequency $E_r \times B$ oscillations excited by the turbulence, including the high-frequency branch of zonal flows associated with the geodesic acoustic mode (GAM) [109, 110]. Note that, experimentally, it is difficult to distinguish between the various (turbulence, neoclassical

or other) contributions to the measured mean flow due to the tight interdependence of turbulence, flow shear and equilibrium profiles.

2.6 Magnetic shear induced Reynolds stress

The magnetic shear, $\hat{s} = (r/q)\partial_r q$, is the logarithmic radial gradient of the safety factor $q(r)$. As the safety factor usually increases towards the edge, $\hat{s} > 0$. A radially elongated eddy will therefore experience a spatial tilt, when tracking the eddy's transverse projection along field lines (Fig. 2.2a). This is because of the higher pitch angle (or lower q) on the

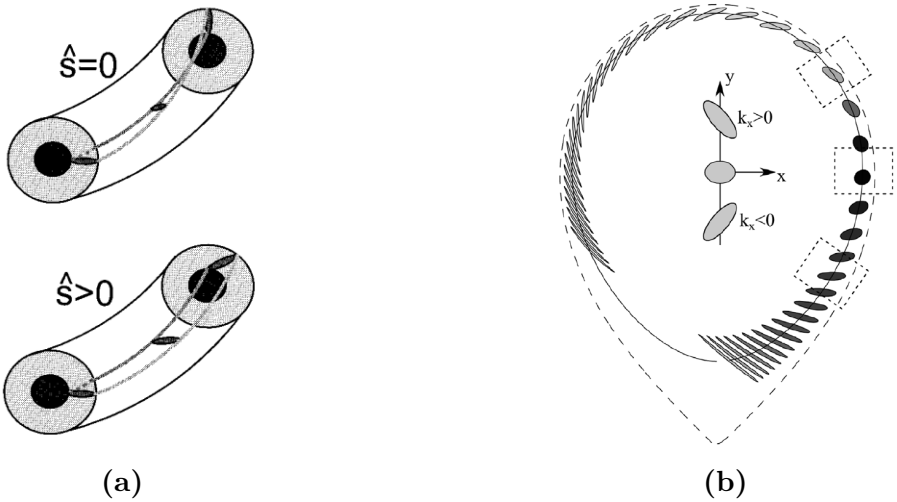

Figure 2.2: *Illustrations of eddy tilting by magnetic shear: (a) When following field lines in the absence of shear ($\hat{s} = 0$), the transverse projection of an eddy simply moves poloidally. In the presence of magnetic shear ($\hat{s} > 0$), the eddy is additionally tilted. Figure from [111]. (b) Similar schematic of the same effect; Starting from the OMP, the eddy is tilted in opposite direction when following field lines towards the bottom or top side of the plasma cross-section. Figure from [112].*

inner compared to the outer side of the eddy. For eddies located at the OMP, the direction of the tilt tends to be anti-symmetric with respect to the OMP, as shown in Fig. 2.2b.

Magnetic shear is relevant to this work in the context of the "magnetic-shear-induced Reynolds stress" introduced by Fedorczak *et al.* [112, 113]. This concept has been proposed as a possible symmetry-breaking mechanism that might explain the favorable/unfavorable asymmetry (the focus of Chapter 4).

The idea relies on the net residual stress associated with (up-down asymmetric) tilting of turbulent eddies by magnetic shear. The theory of Refs. [112, 113] assumes a ballooning-like turbulence intensity, that is,the underlying dominant modes are most unstable and their intensity thus peaked around the OMP. This is modeled using a Gaussian envelope, centered around the OMP, which modulates the poloidal contribution from eddy tilting to the Reynolds stress. Owing to the up-down anti-symmetric pattern of the shear-induced eddy tilting (Fig. 2.2b), the associated residual stress vanishes on a poloidal average unless the equilibrium and/or the turbulence envelope is up-down asymmetric.

In a realistic geometry, the poloidal symmetry of the equilibrium is always perturbed at its boundary, either by the plasma contact with a limiter, or by an X-point in case of a diverted plasma. Such a boundary effect is accounted for in Refs. [112, 113] by truncating the turbulence envelope around the poloidal location of the limiter or X-point. In the case of a single-null configuration with an X-point located at the bottom or top of the plasma, as considered in [112], the truncated envelope creates an imbalance between lower and upper eddy tilting contributions, resulting in a finite stress. The latter tends to amplify the $E_r \times B$ shear if $B \times \nabla B$ points toward the X-point (the favorable drift case), or competes with it in the opposite (unfavorable) case. This turbulence-driven mechanism is one of the hypotheses to explain the stronger edge E_r well observed in the favorable configuration, to which we will return in Chapter 4.

2.7 Radial Electric Field in the SOL

So far, we have concentrated on the edge region, that is, in the outermost part of the confined plasma with closed magnetic flux surfaces. There, equilibrium quantities such as density, temperature and potential remain—to leading order—flux functions. Outside the separatrix, in the "scrape-off layer" (SOL) region, this is not necessarily valid and the radial force balance Eq. (2.2) is not applicable.

Instead, a relation for the mean E_r may be obtained from the parallel electron momentum conservation equation neglecting electron inertia [114, §9.5]:

$$E_\parallel = \frac{j_\parallel}{\sigma_\parallel} - \frac{1}{en_e}\nabla_\parallel p_e - \frac{0.71}{e}\nabla_\parallel T_e\,, \tag{2.12}$$

where notation conventions were adopted from Ref. [115]. In the first term on the right hand side, $j_\parallel = en(V_{i\parallel} - V_{e\parallel})$ denotes the parallel current density and $\sigma_\parallel = e^2 n/m_e\nu_{ei}$ the electric conductivity. The second term is the thermal (pressure gradient) force, and the third is a collisional thermal force, caused by a favored direction of electron-ion friction in the presence of a temperature gradient. Eq. (2.12) is also referred to as Ohm's law for the SOL.

Integrating Eq. (2.12) along magnetic field lines from the outer target (OT) to the outboard midplane (OMP), assuming local ambipolarity ($j_\parallel = 0$) and a pressure dependence such that $p_e/p_{e,\mathrm{OT}} = (T_e/T_{e,\mathrm{OT}})^\alpha$, yields the following equation for the potential at the OMP (see [116] and references therein):

$$\phi_{\mathrm{OMP}} = \underbrace{\frac{2.85}{e}T_{e,\mathrm{OT}} + V_{\mathrm{fl}}}_{\phi_{\mathrm{OT}}} + \frac{0.71+\alpha}{e}\left(T_{e,\mathrm{OMP}} - T_{e,\mathrm{OT}}\right), \tag{2.13}$$

where the first term accounts for the sheath potential drop and V_{fl} is the floating potential of the divertor (assumed here to be constant, so it can be ignored). Eq. (2.13) determines the OMP profile of the radial electric field through $E^{\mathrm{SOL}}_{r,\mathrm{OMP}} = -\nabla_r \phi_{\mathrm{OMP}}$.

We consider the two regimes of interest[114, §16.3]:

(I) Sheath-limited (or low recycling): Occurring at low upstream density, this regime is characterized in particular by a constant T_e along field lines in the SOL.

(II) Conduction-limited (or high recycling): At higher upstream density, while pressure is still conserved, significant parallel T_e gradients develop in this regime.

In the sheath-limited case, we have $T_{e,\mathrm{OMP}} \approx T_{e,\mathrm{OT}} \approx T_e$ so that

$$E_r^{\mathrm{SOL}} \approx -3\nabla_r T_e/e. \tag{2.14}$$

It was noted in [116] that $\alpha(T_{e,\mathrm{OMP}} - T_{e,\mathrm{OT}})$ converges to a finite value $\approx 0.5T_{e,\mathrm{OT}}$, only slightly modifying the numerical coefficient in front of $\nabla_r T_e$.

In the conduction-limited regime, the sheath contribution can be neglected since $T_{e,\mathrm{OMP}} \gg T_{e,\mathrm{OT}}$, which leads to:

$$E_{r,\mathrm{OMP}}^{\mathrm{SOL}} \approx -(0.71+\alpha)\nabla_r T_{e,\mathrm{OMP}}/e\,. \tag{2.15}$$

where $(0.71+\alpha)$ is of order unity, see [116, Fig. 5].

We have thus established that, both in the sheath and conduction limited regime, E_r satisfies a relatively simple relation in the outboard midplane SOL, of the form:

$$E_r^{\mathrm{SOL}}(r) \approx -C\nabla_r T_e(r)/e\,. \tag{2.16}$$

with a coefficient $C > 0$ of order unity. It describes a positive (outward-pointing) E_r since $T_e(r)$ decreases with r.

Consequently, E_r typically changes sign across the separatrix, as exemplified in Fig. 2.3 which shows DBS measurements in AUG. The characteristic peak, or E_r "hill" in the

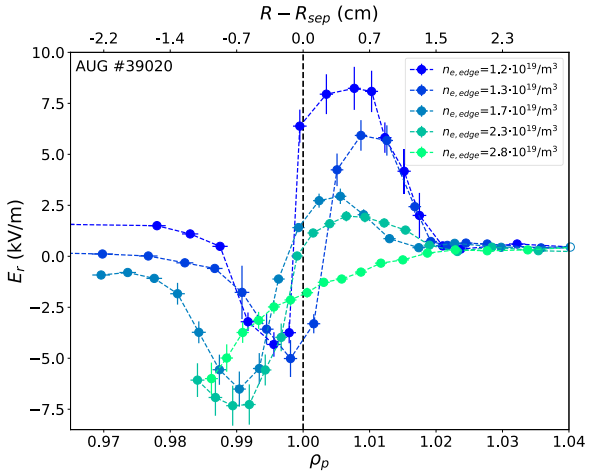

Figure 2.3: *Figure from [116]. E_r profiles measured via DBS in AUG for an L-mode discharge; the E_r "hill" in the SOL decreases with increasing edge density ($n_{e,edge}$).*

SOL, decreases sharply with increasing density. Qualitatively, it can be understood as resulting from the cooling effect of increased density, reducing T_e and its radial gradient in the SOL and at the outer target. Ref. [116] showed that this trend in AUG is successfully captured by a model based on Eq. (2.13). More precisely, the empirical scaling of the

$E_r^{\max}$ over an L-mode database in AUG was found to be approximately described by $E_r^{\max} \propto (n_G/n_e^{\text{edge}})^2$, where $n_G = I_p/(\pi a^2)$ is the Greenwald density limit [117] and n_e^{edge} the edge electron density [116].

2.8 Phenomenological review of the edge E_r

This section aims to provide a phenomenological perspective on the edge E_r behavior in tokamaks. It will illustrate the difficulty of obtaining a conclusive picture from past experiments concerning, in particular, its role at the L-H transition. Partly, this is due to the diversity of observations across different devices and the variety of diagnostics employed. Despite substantial advances in diagnostic techniques over the past decades, limitations persist for accessing and interpreting edge E_r data within the required spatial and temporal resolution—especially close to the L-H transition, where transients or MHD modes can additionally complicate the analysis. Moreover, measurements of E_r are still relatively scarce compared to more routinely diagnosed plasma profiles, such as density and temperature, and often lack redundancy from independent diagnostics.

After reviewing E_r observations near the L-H transition and their interpretation, we turn to experiments that uncovered pronounced sensitivities of the edge E_r profile to magnetic geometry, which forms the primary focus of this PhD thesis.

2.8.1 E_r and ion profiles at the L-H transition

DIII-D. To begin with, some early observations from DIII-D are reviewed on the behavior of E_r and ion rotation profiles at the L-H transition. Ref. [118] presents the *main* ion kinetic profiles collected by CXRS in helium plasmas, from which E_r is computed using the radial force balance. The main results are summarized in Fig. 2.4; It compares the L-mode phase just prior to the L-H transition (open blue circles) to the later H-mode phase (filled magenta circles). Panel (b) shows the edge ion diamagnetic ($(\nabla_r p_i)/Zen_i$) and the Lorentz ($-V_i \times B$) contributions to E_r. The corresponding E_r profiles, obtained from the helium radial force balance, are shown in panel (a).

We first focus on the L-mode curves in (b). Ref. [118] specifies that the $-V_i \times B$ term is dominated by the ion poloidal rotation ($V_{i\theta}$) contribution. Note that $-V_i \times B$ and $(\nabla_r p_i)/Zen_i$ have opposite signs, in both L- and H-mode phases. The positive $-V_i \times B$ contribution to E_r, which implies that $V_{i\theta}$ is in the ion diamagnetic direction, dominates the diamagnetic one in the L-mode phase. This results in a positive edge E_r (a).

Shortly after the L-H transition (filled circles), E_r becomes negative and forms a well that tends to be dominated by the diamagnetic term. However, $-V_i \times B$ remains significant, including during the later, established H-mode phase (as shown in [118, Fig. 4]).

Ref. [119] presents a more detailed analysis of the temporal sequence of E_r and other quantities across an L-H transition on DIII-D. It finds that, a few mm inside the separatrix, E_r starts to evolve from slightly positive towards negative values *prior* to the L-H transition. This behavior is inferred from the E_r data obtained by CXRS as well as from Langmuir probes. The floating potential measured by the probes indicates an increase in E_r shear prior to the sharp drop in fluctuation levels marking the bifurcation [119, Fig. 7].

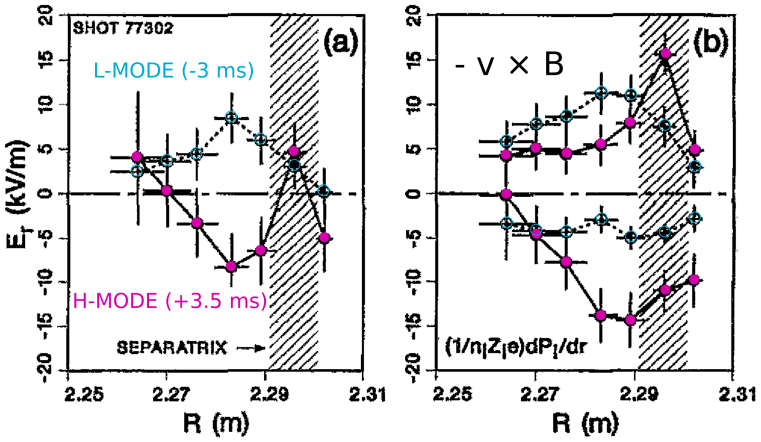

Figure 2.4: *Radial profiles of (b) the main ion contributions that sum up to (a) E_r, measured by CXRS in a DIII-D discharge right before (open circles) and after (filled circles) the L-H transition. The $-v \times B$ term is dominated by $V_{i,\theta}$, which is in the ion diamagnetic direction. Figure adapted from [118].*

This lead to the conclusion that mean $E_r \times B$ shear is a key player at the L-H transition in DIII-D.

Moreover, considering the radial profiles shown in Fig. 2.5 (which uses a similar representation as Fig. 2.4), it appears that the decrease of E_r in H-mode is not accompanied by a

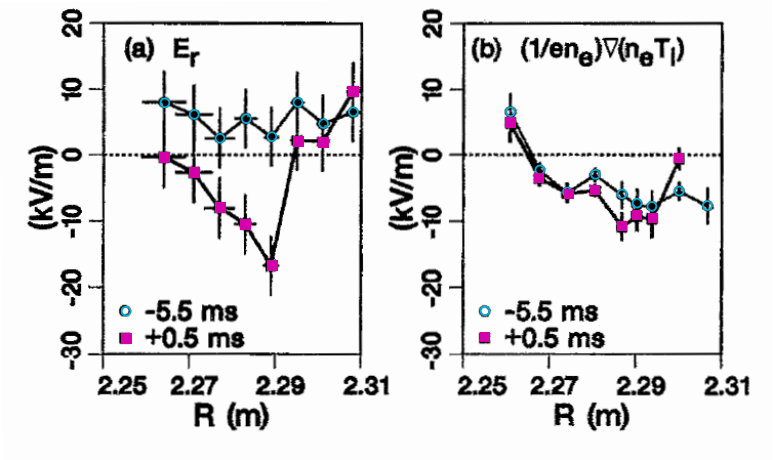

Figure 2.5: *Radial profiles of (a) E_r and of the (b) diamagnetic contribution before and shortly after the L-H transition. The latter does not track the E_r change across the transition. Figure adapted from [119].*

change in the diamagnetic contribution (b) that could account for the magnitude of the E_r variation (Fig. 2.5). This suggests that the shear associated with the $V_i \times B$ term (and not the diamagnetic one) plays the dominant role at the transition.

It should be noted, however, that these historic findings do not appear to have been substantiated by more recent studies on DIII-D, despite upgraded E_r diagnostic capabilities [120].

AUG. A comprehensive review of L-H transition experiments at AUG [69] highlights the

importance of mean E_r shear in the H-mode access on this tokamak. A notable finding is the apparently consistent magnitude of the $E_r \times B$ velocity in the well, observed shortly before the L-H transition [121], namely $|v_{E\times B}| \approx 7\,\mathrm{km/s}$, which suggests a threshold behavior. The supporting data for this conclusion are shown in Fig. 2.6, where the

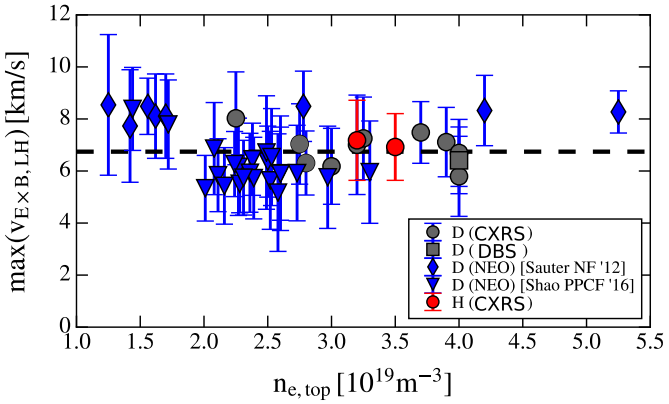

Figure 2.6: *Maximum of $|v_{E\times B}|$ just prior to the L-H transition over a set of AUG discharges with fixed magnetic geometry (favorable $B\times\nabla B$ drift) but different toroidal magnetic field strengths and edge densities ($n_{e,\mathrm{top}}$). Blue triangles and diamonds are neoclassical approximations rather than E_r measurements. Figure adapted from [121].*

maximum of $|v_{E\times B}|$ remains constant over a wide range of densities. This dataset also covers different magnetic field strengths and $P_{\mathrm{L}\to\mathrm{H}}$, for a fixed magnetic geometry. This suggests a critical threshold in $v_{E\times B}$ (or its shear) for H-mode access. It is reminiscent of a turbulence suppression criterion involving the mean $E_r \times B$ shearing rate, as described by L-H theories based on the shear flow paradigm [81, § 2.3 and references therein].

It should be noted, however, that in Fig. 2.6, only circles and squares correspond to direct E_r measurements (mostly via CXRS), while all other (blue) symbols represent an approximation by the diamagnetic term according to Eq. (2.8), namely $v_{E\times B} \approx -V_i^*$. Here, it appears that both measurements and approximations of $|v_{E\times B}|$ align around a common threshold value of $\approx 7\,\mathrm{km/s}$, which tends to support the validity of the "neoclassical" E_r approximation under these plasma conditions.

Furthermore, note that Fig. 2.6 includes two data points for hydrogen (H) in addition to the deuterium (D) discharges. The values appear consistent for both isotopes, suggesting a common critical value of $|v_{E\times B}|$, even though $P_{\mathrm{L}\to\mathrm{H}}$ is usually higher in hydrogen. This observation was corroborated by more recent and detailed edge E_r measurements [69, 115], acquired via DBS and He II spectroscopy (HES [115]). The HES diagnostic detects the line emission of singly ionized helium (He^+) to infer its kinetic profiles and reconstruct E_r from the He^+ radial force balance. Fig. 2.7 (a,b) shows edge E_r profiles for D and H discharges acquired just before their respective L-H transitions. The E_r wells and their associated shear are similar for the two species, despite the large difference (by a factor 3) in auxiliary ECRH power—annotated in Fig. 2.7. Taken together, the above results support the idea of a critical threshold in $|v_{E\times B}|$ (or its shear) for accessing H-mode in AUG, that is robust to variations in density, B-field, heating power, and isotope mass.

Further, on AUG, the neoclassical approximation was found to be accurate in the established pedestal of H-mode plasmas [70, 71]. There, the E_r well indeed follows the main

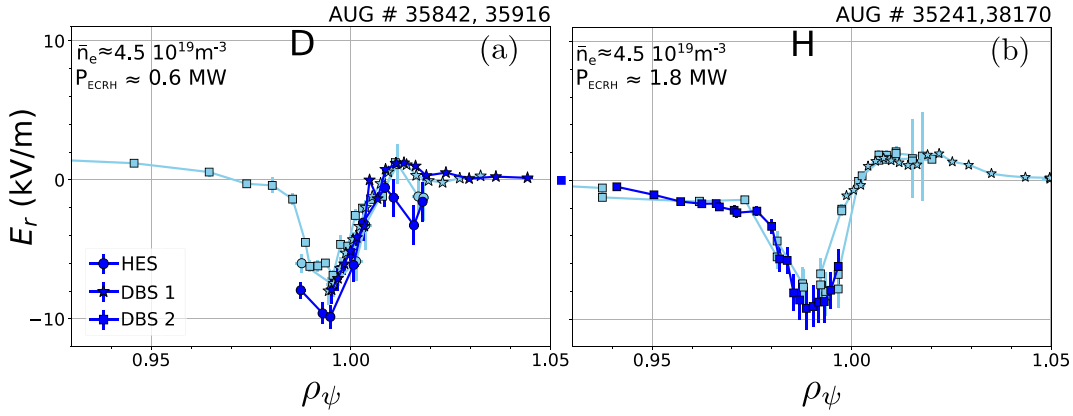

Figure 2.7: *Edge E_r mesurements by DBS and helium spectroscopy (HES) in (a) deuterium and (b) hydrogen plasmas, at their respective L-H transitions. The E_r well profiles are similar for the two species. Figure adapted from [69].*

ion $(\nabla p_i)/en_i$ profile, as evidenced by high resolution CXRS measurements (Fig. 2.8b) in helium plasmas. In addition, the main ion rotation (V_θ) is weak (few km/s), in agree-

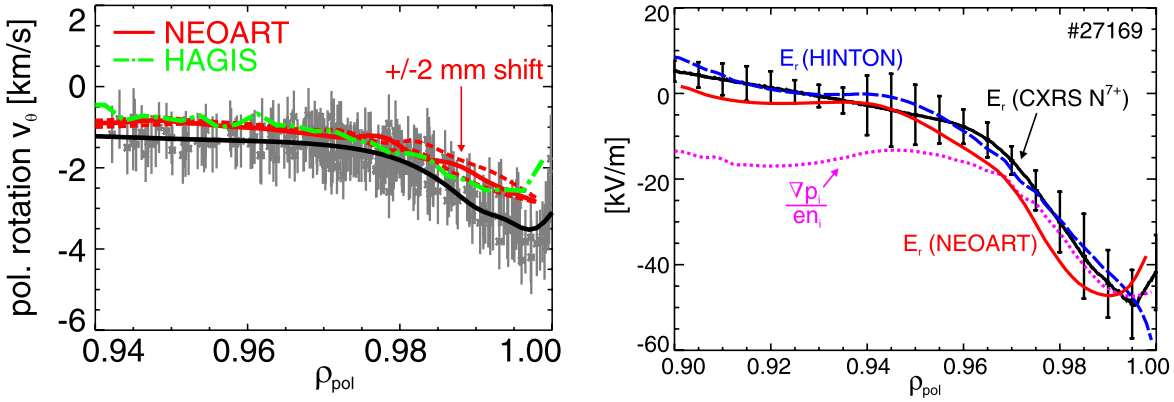

(a) **(b)**

Figure 2.8: *Radial profiles of (a) main ion poloidal rotation $V_{i\theta}$ and (b) E_r measured by CXRS in an AUG H-mode discharge. $V_{i\theta}$ is in good agreement with neoclassical predictions from different codes (NEOART and HAGIS), and the "neoclassical" approximation $E_r \approx (\nabla p_i)/en_i$ is accurate in the E_r well region. Figures from [71].*

ment with neoclassical predictions also shown in Fig. 2.8a. Note that $V_{i\theta}$ is in the electron diamagnetic direction, unlike the DIII-D case discussed above (Fig. 2.4).

In L-mode AUG plasmas, $(\nabla p_i)/en$ is not generally found to be a good approximation for E_r, despite earlier suggestions (see Fig. 2.6). As noted in [69, 122], it can differ substantially from the edge E_r measured at by DBS and HES. This discrepancy is particularly pronounced towards low densities [69, Fig. 3]. Furthermore, it is important to note that the diamagnetic velocity does not account for the E_r sensitivities observed in L-mode

with respect to the magnetic drift configuration [122]—a key focus of this work that will be further developed in 4.

JET. In contrast to AUG, the E_r well on JET remains shallow at the transition [123]. This is exemplified in Fig. 2.9a, for an ICRH power scan at a line-averaged density of $\overline{n}_l \approx 3.4 \times 10^{19}\,\mathrm{m}^{-3}$.

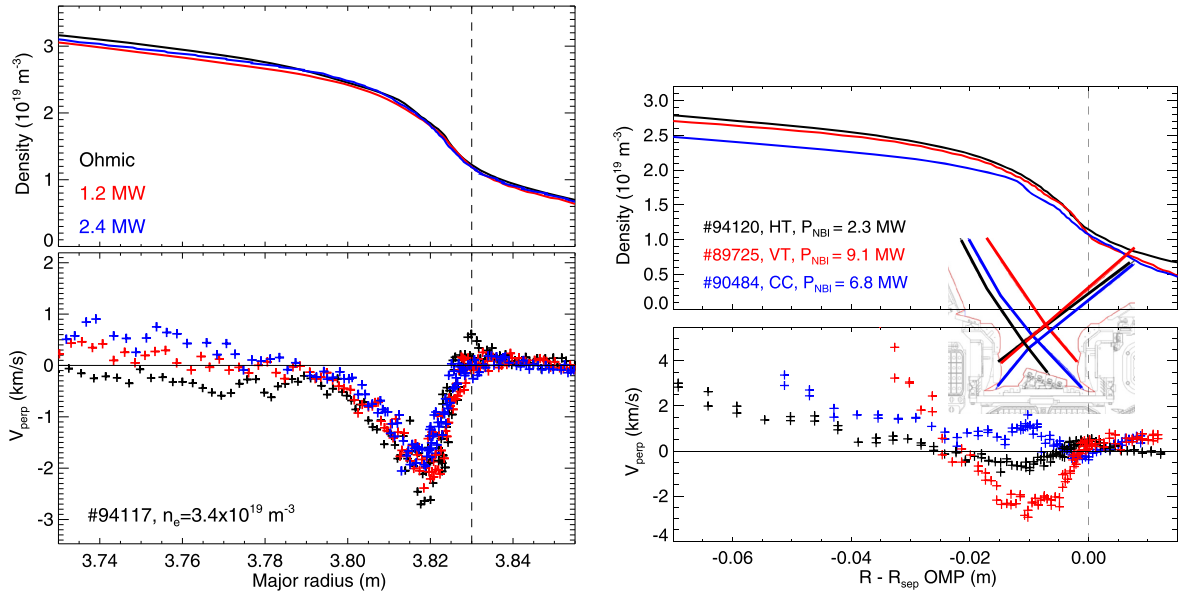

(a) **(b)**

Figure 2.9: *Density profile (top) and $v_\perp$ measurements from DBS (bottom) approaching the L-H transition via ICRH in JET. The well remains shallow up to $P_{\mathrm{ICRH}} = 2.4\,\mathrm{MW}$, while L-H transition dithers start to appear at 2.6 MW. Figure from [123]. (b) $v_\perp$ shortly before the L-H transition in JET discharges with different divertor strike point configurations; horizontal (HT), vertical (VT) and corner (CC) target. Figure adapted from [124].*

The $v_\perp \approx v_{E\times B}$ profiles measured by DBS show no appreciable evolution in the region of the well, even close to the L-H transition threshold around 2.6 MW. A similar behavior is also reported for a lower density ($2.7 \times 10^{19}\,\mathrm{m}^{-3}$), or when replacing ICRH by NBI heating [123]. Meanwhile, the magnitude of the diamagnetic term (estimated using T_e rather than T_i) increases during the power ramp. However, the authors of Ref. [123] point out the difficulty of assessing the $E_r \times B$ shear behavior on shorter time scales than $\sim 300\,\mathrm{ms}$ due to diagnostic limitations. Therefore, faster transient behaviors of E_r prior to the L-H transition cannot be excluded.

On the other hand, a subsequent study found that $v_\perp$ is highly sensitive to the detailed divertor configuration [124]. Specifically, modifying the outer strike point locations—which have a strong impact on $P_{\mathrm{L}\to\mathrm{H}}$ in JET—correlates with large variations of the edge flow profile (Fig. 2.9b). When the outer strike point is on the horizontal target (HT)—a configuration that comes with a significantly lower $P_{\mathrm{L}\to\mathrm{H}}$ compared to the vertical (VT) and corner (CC) target case, the edge $v_\perp$ profile just prior to the L-H transition is particularly flat, whereas the VT configuration shows a deeper well with a pronounced inner-side shear layer (negative $v_\perp$ slope). Note that the changes in $v_\perp$ are primarily observed in the confined region, whereas $v_\perp$ remains flat in the SOL regardless of the

strike point location. Interestingly, this suggests that the E_r "hill" in the SOL—that, depending on plasma conditions, can be very pronounced and enhance the *outer* E_r shear layer—is not a key player at the L-H transition.

Taken together, the findings from Refs. [123, 124] suggest that—unlike AUG—the L-H transition threshold on JET is not associated with a critical value of the mean $E_r \times B$ or its shear. Moreover, the strong modification of $v_\perp$ by the divertor configuration points to a high sensitivity to the boundary condition imposed by the magnetic equilibrium.

MAST. The structure of E_r was also measured in the spherical tokamak MAST, using spectroscopy on singly ionized helium (He^+) [125] (as the HES diagnostic in AUG). Similarly to JET, approaching the L-H transition, no significant variation of the well depth or the edge E_r shear is observed (Fig. 2.10) [126]. Ref. [126] further reports that sensitivities

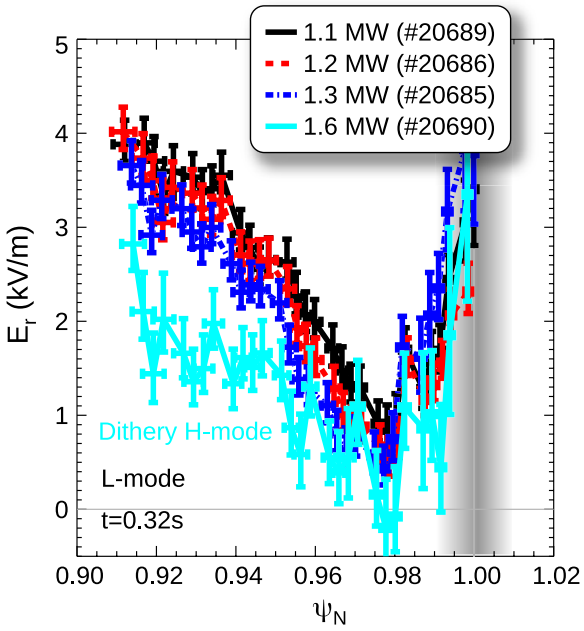

Figure 2.10: *E_r profiles measured by helium spectroscopy on MAST, approaching the L-H transition through an NBI power ramp. Figure from [126].*

of $P_{L\to H}$ on the elongation in double-null discharges are not reflected by notable changes in the mean E_r profile.

Taken together, the results from JET and MAST do not point towards a key role of mean $E_r \times B$ shear at the L-H transition. Instead, they might be taken as suggesting that the strong E_r shear observed in H-mode merely builds up as a *consequence* of the spontaneous turbulent transport suppression (without necessarily contributing to the latter).

TJ-II stellarator. While this work focuses on tokamak plasmas, it is instructive to also consider results from E_r studies in the TJ-II stellarator [127]. These observations complement the diverse phenomenology of E_r in magnetized toroidal plasmas and help reveal where its behavior is similar to, or differs from that seen in tokamaks. A notable analogy is the presence of a bifurcation reminiscent of the L-H transition, which can likewise be triggered by external heating. The transition is also accompanied by a deepening of the edge E_r well, as shown in Fig. 2.11a.

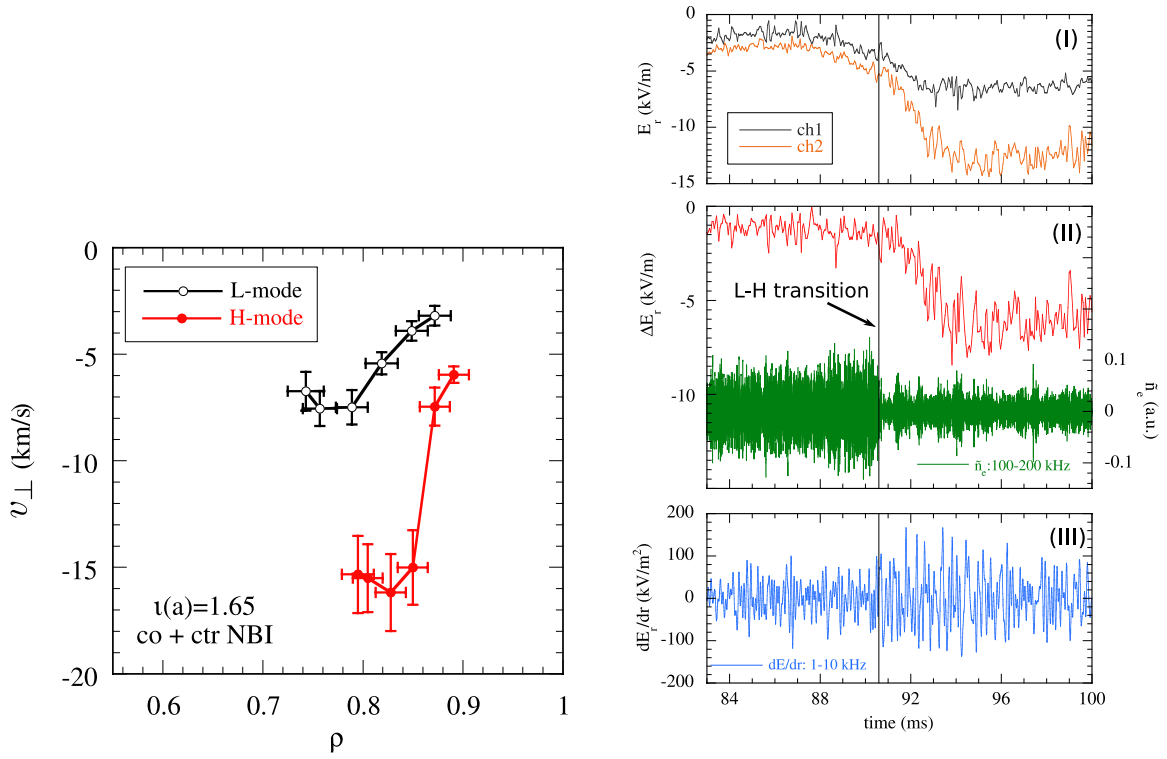

(a) **(b)**

Figure 2.11: *(a) Perpendicular velocity measured by DBS in the TJ-II stellarator, shortly before an L-H transition triggered by NBI in a standard magnetic configuration. (b) Evolution of E_r signals (panel I) from two adjacent radial probing locations, (II) their difference (ΔE_r) along with the high-frequency density fluctuations level ($\tilde{n}$), and (III) low-frequency fluctuations in the E_r shear. Figures adapted from [127].*

Ref. [127] reports that E_r is dominated by the diamagnetic term in L-mode, but departs from it in H-mode. This behavior appears qualitatively different from that in the AUG tokamak, where—as discussed above (Fig. 2.8)—E_r agrees well with $(\nabla p_i/n_i e)$ in H-mode, while pronounced discrepancies appear in certain L-mode conditions.

Another notable finding is that, unlike in DIII-D, the temporal sequence across the L-H transition in TJ-II indicates that the reduction in turbulence *precedes* the rise in mean E_r shear (Fig. 2.11b); The ΔE_r difference (upper curve in panel II) measured by a dual-channel DBS system at two radial locations provides a proxy for the instantaneous E_r shear, which increases only shortly *after* the high-frequency (turbulent) density fluctuations are reduced (lower curve in panel II).

This suggests that the mean $E_r \times B$ shear alone does not trigger the L-H transition in this experiment. However, low-frequency oscillations of the E_r shear appear simultaneously with the turbulence reduction (panel III). The authors of Ref. [127] interpreted this observation as a possible signature of zonal flows initiating the bifurcation, which would be consistent with L-H transition theories based on turbulence-enhanced zonal $E_r \times B$ flow shear [103, 104].

While this thesis concentrates on the *mean* E_r profile, we nonetheless include a brief account of related work that investigated the dynamical interplay between flows and turbulence.

Dynamic flow-turbulence interaction and LCOs. Following theoretical developments that emphasized the importance of zonal flows in the self-regulation of turbulence [95], several experimental studies investigated the flow-turbulence dynamics during the "limit-cycle oscillations" (LCOs) associated with "I-phase" bursts. The I-phase is an intermediate regime between L- and H-mode, often observed transiently during gradual L-H transitions. It is characterized by low-kHz bursts, for example in the D_α signal.

Such LCOs have been studied on various devices, including TJ-II [128], AUG [129], and DIII-D [130]. The dynamical coupling between DBS-inferred $v_\perp$ and fluctuation signals has been interpreted as supporting evidence for predator-prey models [104, 131] describing the interplay between equilibrium and zonal flows (the predators) and turbulence (the prey); see [106] for a review of the topic.

Note that other investigations of I-phase LCOs point to a small contribution by zonal compared to neoclassical flows, questioning the relevance of the former at the L-H transition [132]. Moreover, as reviewed in [69, § 5.2], some studies interpret the I-phase bursts as ELM-like oscillations rather than predator-prey interactions between turbulence and flows. In particular, a characterization of its magnetic structure on AUG [133] finds the I-phase LCOs to be similar in nature to type-III ELMs.

Thus, while I-phase LCOs provide a valuable opportunity to study the coupling between turbulence and flow shear, their interpretation—and the role of turbulence-driven (zonal) flows—remains inconclusive.

Having summarized the empirical E_r behavior in the broader context of the L-H transition, we now briefly review some key E_r observations that are more directly aligned with, and provide context for the focus of this work.

2.8.2 Sensitivity of edge E_r and turbulence velocity to magnetic configuration

One of the earliest reports of edge flow shear sensitivities to magnetic geometry in a tokamak is provided in [134]. This study compares lower single-null (LSN) to upper single-null (USN) discharges on DIII-D, with a fixed downward-pointing $B\times\nabla B$ drift. For the same NBI power, the kinetic profiles (n_e, T_e, T_i) are similar, yet the E_r profile inferred from CXRS shows a (modest) difference (Fig. 2.12a), with a lower E_r near and inside the separatrix in the LSN case—corresponding to a favorable $B \times \nabla B$ drift configuration according to the terminology introduced in Sec. 1.2. As will be seen, this early indication

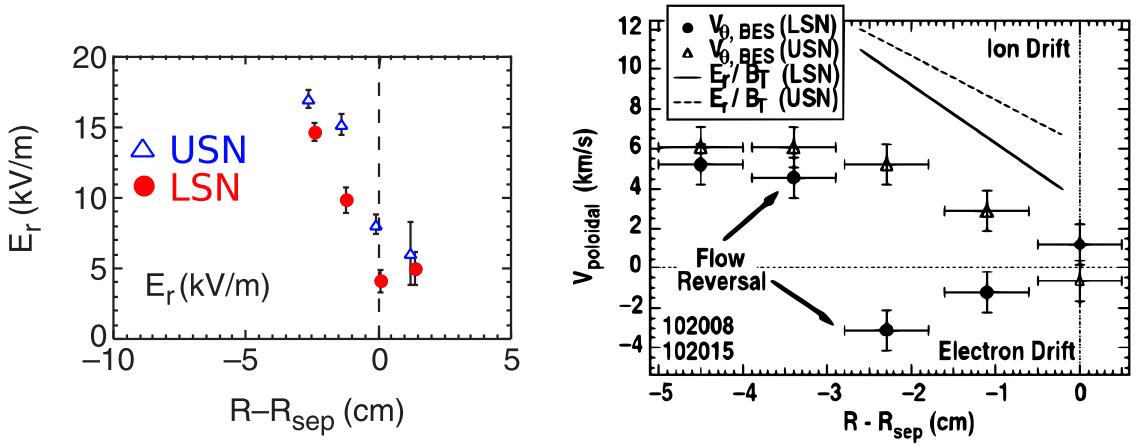

(a) **(b)**

Figure 2.12: *(a) E_r profiles measured by CXRS for similar LSN and USN L-mode discharges on DIII-D. Figure adapted from [134]. (b) Poloidal turbulence velocity from BES measurements, showing a flow reversal only in the LSN case. Figure from [135].*

of an E_r dependence on drift configuration was later confirmed on various other tokamaks and leveraging improved diagnostic capabilities.

Another, perhaps more apparent, discrepancy between the LSN and USN configurations in DIII-D was revealed by beam emission spectroscopy (BES) [134, 135]. The BES system on DIII-D [136] provides 2D images—within a radial-poloidal plane near the OMP—of the D_α line emission. Fluctuations in its intensity are proportional to long-wavelength $(k_r, k_\theta \lesssim 3\,\mathrm{cm}^{-1})$ density fluctuations. Their average poloidal velocity can be estimated from the time delay correlation between poloidally separated channels (see [136] and references therein).

A profile of this turbulence poloidal velocity is shown in Fig. 2.12b. It displays a sign reversal in the LSN case, indicating a stronger turbulence velocity shear than in the USN case. Note also the significant difference between the poloidal projection of the CXRS-derived $E_r \times B$ drift (solid and dashed lines in Fig. 2.12b) and the BES measurements[7].

[7] It is unclear why the $E_r \times B$ flow does not reflect the turbulence poloidal velocity in Fig. 2.12b. It might be a consequence of diagnostic limitations, or of a strong deviation of low-$k_\perp$ fluctuations velocity from background $E \times B$ flow, or a combination of both factors.

The findings from DIII-D of edge $E_r \times B$ and/or turbulence flow discrepancies depending on the magnetic configuration were later substantiated, particularly by DBS measurements on AUG, as shown in Fig. 2.13a. During the USN phase of the discharge (unfavorable $B \times \nabla B$), the E_r profile lacks the pronounced well that is observed in the double-null and lower single-null (favorable $B \times \nabla B$) case. The $E_r \times B$ shear is thus weaker in unfavorable compared to favorable $B \times \nabla B$ drift.

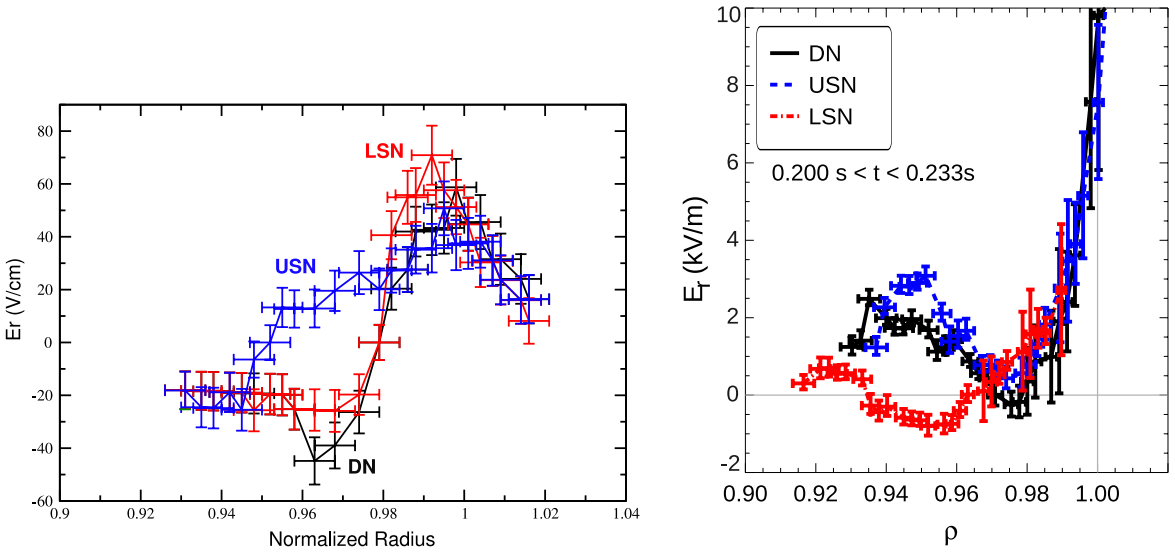

(a) **(b)**

Figure 2.13: *(a) L-mode E_r profiles measured by DBS on AUG for various shapes (with $B \times \nabla B$ pointing down). Figure adapted from [137]. (b) Similar study on MAST using He^+ diagnostics. Figure adapted from [125].*

An analogous comparison on MAST [125], where E_r profiles are inferred by He^+ spectroscopy, recovered a partly consistent trend; The E_r well is deeper in the LSN (favorable) than in the USN (unfavorable $B \times \nabla B$) or DN case. However, the edge E_r shear actually appears weaker in LSN, which constrast with the AUG observations.

Overall, experiments on DIII-D, AUG, and MAST revealed common features pointing to pronounced variations of the L-mode edge E_r (and turbulence velocity) profile with magnetic configuration. These historic indications have motivated more detailed investigations on WEST and AUG (reviewed in Chapter 4), and on TCV as part of this work.

On the other hand, concerning the impact of plasma *shaping*, on E_r, so far, little experimental data is available. In particular, no systematic studies have previously addressed the effect of triangularity on the E_r well—the focus of the TCV experiments that will be presented in Chapter 5. Nevertheless, previous impurity rotation measurements on TCV and DIII-D suggested a sensitivity of toroidal rotation to triangularity, which will be discussed in Chapter 5.

2.9 Chapter summary

This chapter has provided theoretical background as well experimental context concerning the edge E_r in tokamaks, to help interpret the results presented in the subsequent chapters.

The sources of E_r in the confined plasma region can be described as a competition of non-ambipolar transport mechanisms, associated with collisional or turbulence processes.

In axisymmetrical geometry, E_r remains undetermined within standard neoclassical theory as it cannot be separated from the unconstrained toroidal rotation—unlike the poloidal rotation, which is set by neoclassical parallel viscosity. Neglecting toroidal rotation leads to a so-called "neoclassical" approximation of E_r (Sec. 2.3.3). Further, the degeneracy between toroidal rotation and E_r is lifted by toroidal symmetry-breaking effects, such as magnetic ripple (Sec. 2.3.4). This provides an expression relating E_r to the equilibrium ion density and temperature profiles (Eq. (2.9)).

The edge E_r is likely influenced also by other non-ambipolar transport effects, not described by neoclassical theory. They include ion orbit losses (IOL), or the turbulent Reynolds stress that gives rise to zonal flows. As will be discussed later in this work, both IOL and turbulent $E_r \times B$ flow drives offer possible explanations for the magnetic geometry effects studied in this work, which do not appear to be captured by neoclassical predictions.

Experimental E_r studies highlighted differing edge E_r behaviors prior to the L-H transition, which have led to contrasting interpretations; DIII-D and AUG results provided evidence of a key role of mean $E_r \times B$ shear in triggering the transport barrier. This stands in contrast to observations on JET and MAST that do not show any substantial E_r shear evolution preceding the bifurcation. Furthermore, on the stellarator TJ-II, the initial turbulence suppression *precedes* the growth of mean E_r shear—as opposed to DIII-D.

Moreover, some experiments on AUG are consistent with an E_r that is mainly dictated by neoclassical physics at the edge, while others point to additional drives, such as turbulence-driven zonal flows. Both equilibrium and zonal flows remain prominent candidates, which, possibly through a complex interplay with the turbulence, provide the shear required for turbulence suppression at the confinement bifurcation.

Beyond the issue of causality at the L-H transition, the reviewed E_r studies also reveal a recurring feature: the L-mode E_r structure is sensitive to magnetic geometry. Examples include the dependences on divertor strike point location in JET and on magnetic drift configuration in DIII-D, AUG, and MAST. This is a central aspect studied in this work, and the subject of Chapter 4.

Overall, these diverse E_r observations highlight the importance of systematic E_r studies—such as those carried out in this work—combined with cross-device comparisons to establish robust experimental trends.

Chapter 3

Doppler backscattering at TCV: setup, methodology and first E_r studies



Contents

3.1 Principles of DBS 54
3.2 Signal detection and analysis 58
3.3 Launcher and operating range 67
3.4 Overview of main TCV diagnostics and quantities used 68
3.5 Comparison of DBS and GPI measurements 72
3.6 Comparison of DBS and C^{6+} radial force balance 72
3.7 Mapping $v_\perp$ to the OMP 74
3.8 Survey of the edge E_r in TCV 78
3.9 Chapter summary 85

This chapter describes the implementation of a Doppler backscattering (DBS) system on TCV—the essential diagnostic to access the edge E_r in this work, along with the methodology and first results.

The DBS system, which is on loan from the *Laboratoire de Physique des Plasmas* (LPP), has been installed on TCV in late 2023. DBS studies at TCV have been conducted in the past, using a similar predecessor [138], or with SPC's in-house DBS system [139]. E_r profiles have also been reconstructed from CXRS measurements [140, 141], but an extended characterization of the edge E_r had not been undertaken previously for this tokamak. The commissioning of the DBS system from LPP on TCV forms an integral part of this work, enabling the first systematic investigations into the edge E_r structure on this device.

This chapter first lays out the DBS working principles in Sec. 3.1. Then, Sec. 3.2 presents technical details related to the signal detection and analysis method. The DBS launcher and operational features are described in Sec. 3.3. Subsidiary information regarding TCV-related diagnostics and methodology is provided in Sec. 3.4. Then, as part of the commissioning process to validate the DBS measurements, consistency checks are carried out; A confrontation between DBS and GPI measurements is presented in Sec. 3.5, and another with the radial force balance in Sec. 3.6. A comparison of DBS data acquired at different poloidal tilt angles is discussed in Sec. 3.7. Finally, this chapter presents a first survey of

the E_r well in TCV, covering representative L-mode plasma conditions. Key elements of this chapter are reproduced in [142].

3.1 Principles of DBS

3.1.1 Brief description

Doppler backscattering (DBS) [143–145], also known as Doppler *reflectometry*, is a non-intrusive, lightweight diagnostic that is based on the scattering of an incident microwave beam to infer information on the plasma turbulence and flow. With a suitably chosen frequency and polarization (O-mode or X-mode), the incident probing beam encounters a reflecting cutoff layer in the plasma. By deliberately tilting the beam poloidally, the reflected wave is spatially separated from the one backscattered by density perturbations ($\tilde{n}$), see Fig. 3.1. The backscattered wave then travels back to the antenna, where it is

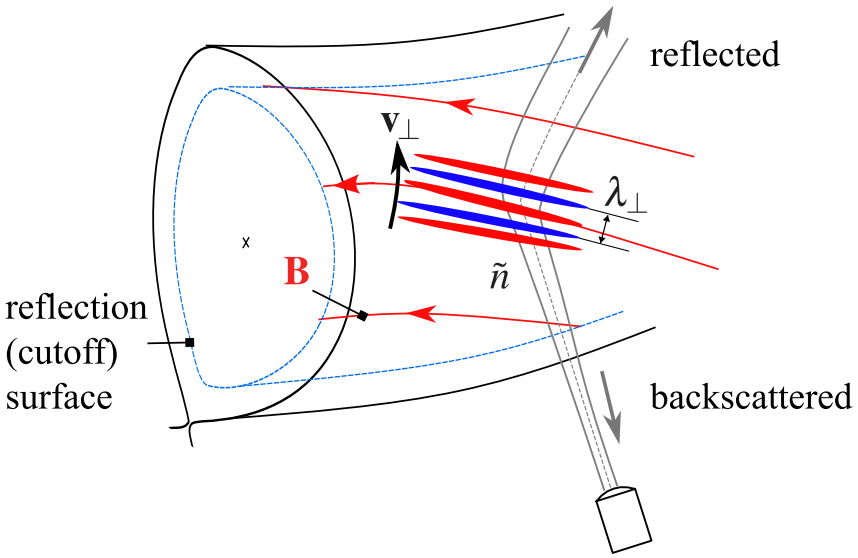

Figure 3.1: *Sketch of the DBS measurement principle; It detects the wave backscattered off density fluctuations ($\tilde{n}$) that are localized near the beam turning location and match the spatial scale $\lambda_\perp = 2\pi/k_\perp$ selected by the scattering geometry.*

detected. As will be explained subsequently, the scattering fluctuations are localized near the beam turning point and have a perpendicular wavenumber ($k_\perp = 2\pi/\lambda_\perp$) determined by the scattering geometry.

The Doppler shift (ω_{Dop}) introduced by the moving scatterers yields their lab frame velocity, $v_\perp = \omega_{\mathrm{Dop}}/k_\perp$, which corresponds to the $E_r \times B$ rotation if the turbulence intrinsic velocity can be considered negligible. $v_\perp$ is inferred by extracting ω_{Dop} from the power spectral density (PSD) of the DBS signal, combined with beamtracing to determine the radial location of the beam turning point and the selected $k_\perp$. Radial profiles of $v_\perp$ (or E_r) are obtained by stepping the probing microwave frequency, thereby varying the cutoff's radial location.

While the mean $v_\perp$ flow and its shear are the primary focus of this study, DBS can also provide access to the turbulence wavenumber spectrum [145, 146], and—using multi-

channel systems—to the instantaneous velocity shear [127, 137], turbulence radial correlation length [8, 147–149], or structure tilt angle [150, 151].

3.1.2 Scattering condition and radial localization

The principle of DBS may be illustrated using the analogy of periodic density fluctuations at the cutoff layer acting like a diffraction grating [143]. The probing beam is thus scattered into different diffraction orders. Backscattering corresponds—in this idealized picture[1]—to the -1st diffraction order, which satisfies the scattering condition, known as the "Bragg selection rule":

$$\boldsymbol{k} = -2\boldsymbol{k}_i \,, \tag{3.1}$$

where $\boldsymbol{k}$ and $\boldsymbol{k}_i$ are the local wavevectors of the density fluctuations and of the incident probing wave, respectively (Fig. 3.2).

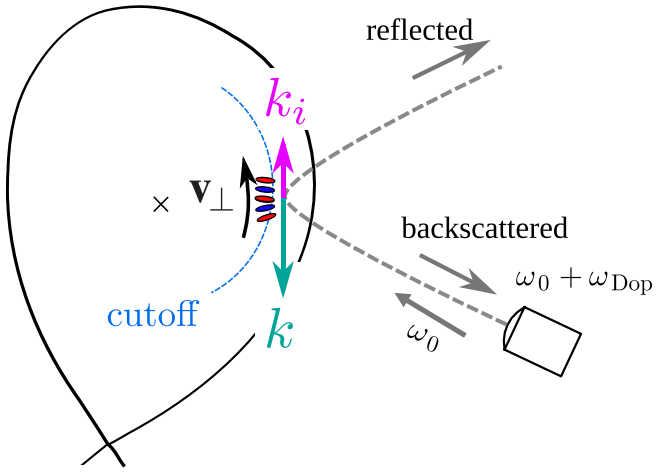

Figure 3.2: *Poloidal cross-section of a DBS probing geometry similar to the one in Fig. 3.1. Backscattering according to Eq. (3.1) occurs mostly near the beam turning point.*

In the following, the indices $(r, \perp, \|)$ denote the locally field-aligned coordinates, so that $k_\perp$ is the binormal component of $\boldsymbol{k}$ (locally orthogonal to both $\boldsymbol{B} = B\hat{\boldsymbol{e}}_\|$ and the radial direction $\hat{\boldsymbol{e}}_r$), and not the norm of the (2D) wavevector in the perpendicular plane to $\boldsymbol{B}$. We recall that the turbulence anisotropy leads to fluctuations that are highly elongated along field lines (as illustrated in Fig. 3.1) such that $k_r, k_\perp \ll k_\|$. Hence, the Bragg selection rule, Eq. (3.1), is only satisfied for incident wavevectors with $k_{i,\|} \approx 0$. Consequently, a beam incidence perpendicular to the local magnetic field, i.e., $\boldsymbol{k}_i \perp \boldsymbol{B}$, optimizes the scattering efficiency and therefore the DBS signal-to-noise ratio (SNR). This optimum is approached by tilting the beam also toroidally (as indicated in Fig. 3.1) to roughly match the field line pitch angle in the probing region.

Scattering occurs all along the beam path, but the combination of the Bragg rule, the turbulence spectral features and a wave electric field enhancement ensures the spatial

[1] A regular modulation of the refractive index by periodic density fluctuations corresponds to a single wave number (k) and therefore to a peaked diffraction response, whereas in the more realistic situation of a disordered (turbulent) medium, the response is spread over a k-spectrum and the diagnostic no longer selects a well-defined diffraction order.

localization of the measurement [145][152, § 4.1.2] close to the beam turning point, as explained below.

Far from the cutoff, where beam refraction is weak, $k_{i,r}$ is too high compared to the turbulence k_r spectrum [152, Fig. 4.5]. The latter is concentrated around small k_r values [145, 153, 154], as exemplified by Fig. 3.3. Hence, few fluctuations match the Bragg rule, and the backscattered power from that portion of the beam trajectory is low. Closer to the cutoff, $k_{i,r}$ decreases (and eventually vanishes at the turning point in case of O-mode polarization). The power density of fluctuations at these lower k_r values is much higher, resulting in a large contribution to the backscattered signal. At the same time, $k_{i,\perp}$ remains finite near the turning point, which is particularly adapted to the turbulence spectrum which—for the dominant ion-scale instabilities—tends to be peaked at finite $k_\perp \rho_s \sim 0.1$–1 values[2] ($k_\perp \rho_s \approx 0.2$–$0.3$ in the example of Fig. 3.3b).

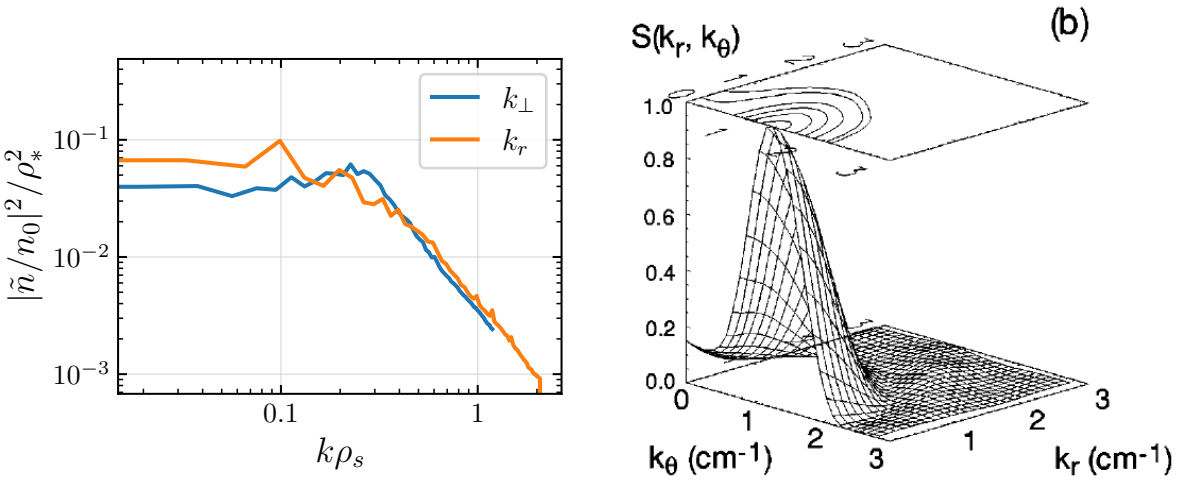

Figure 3.3: *Examples of radial (k_r) and perpendicular ($k_\perp$) wave number turbulence spectra, illustrating the dominance of low-k_r and finite $k_\perp$ density fluctuations. (a) Synthetic $(k_r, k_\perp)$ spectra generated by local nonlinear gyrokinetic simulations using the* GENE *code [155] based on a JT-60SA scenario [156]. Courtesy of O. Krutkin. A similar representation can be found in Ref. [153, Fig. 5] for a Tore Supra scenario. (b) Experimental 2D representation of (k_r, k_θ) spectra obtained from BES measurements on DIII-D, with $k_\theta \simeq k_\perp$ since $B_\theta/B \ll 1$ at the edge, and $k_\parallel \approx 0$. Figure from [136].*

In addition, the backscattered power is enhancend near the turning point by the swelling of the probing wave's electric field—a result of the decreasing refractive index[3]. Thus, combined with the above considerations, the DBS signal is expected to stem predominantly from a region radially localized near the beam turning point, with contributions dominated by ion-scale $k_\perp$ and low-k_r density perturbations.

For a given plasma equilibrium, density and magnetic field, the radial location of the turning point can be controlled by varying the vacuum probing frequency ($f_0 = 2\pi/\omega_0$),

[2] $\rho_s = \sqrt{T_e m_i}/eB$ is the ion Larmor radius at electron temperature T_e.

[3] In simplified cases, this swelling may be described analytically in terms of the Airy function, see e.g. [157].

since a higher f_0 corresponds to a deeper cutoff in the plasma. In addition, DBS systems like the ones used in this work come with a poloidally tiltable antenna. The poloidal beam inclination (θ_b) mainly determines the $k_\perp$ and poloidal location of the turning point, but in general it is the combination of parameters (f_0, θ_b, toroidal beam inclination, wave polarization, plasma density profile and magnetic geometry) that determines the precise scattering location and $k_\perp$. The latter are usually determined numerically via beamtracing, as described later in Sec. 3.2.3.

3.1.3 $E_r \times B$ velocity measurement

The velocity $\boldsymbol{v}$ of the scattering density fluctuations (in the lab frame) introduce a Doppler-shift in the backscattered signal, so that

$$\omega_\mathrm{Dop} = \boldsymbol{k} \cdot \boldsymbol{v} = k_r v_r + k_\perp v_\perp \,, \tag{3.2}$$

where the parallel component has been omitted due to the aforementioned alignment of turbulent structures along $\boldsymbol{B}$. Compared to $v_\perp$ which is on the order of a few km/s, the fluctuation's radial velocity v_r is usually negligible within the confined plasma. Moreover, as was established above, the dominant scattering contributions stem from low or vanishing k_r structures, such that $k_r \lesssim k_\perp$. Hence, the first term in Eq. (3.2) is negligible and the Doppler shift simplifies to:

$$\omega_\mathrm{Dop} \approx k_\perp v_\perp \,. \tag{3.3}$$

The scattering perturbations are carried by the local $v_{E\times B}$ flow, so that

$$v_\perp = E_r/B + v_\mathrm{turb} \,, \tag{3.4}$$

where v_turb represents the *intrinsic* velocity of the turbulence, which may also be regarded as an effective phase velocity. The v_turb contribution is usually neglected compared to the bulk $E_r \times B$ rotation. Such an approximation is supported by certain numerical [47, Fig .4] and experimental evidence [137, and references therein][127, 145]. Yet, certain cases are reported where DBS [146, 158, 159] or other diagnostics [134, 135] point to a discrepancy between $v_\perp$ and $v_{E\times B}$. Although beyond the present scope, the study and interpretation of a possible v_turb contribution to the DBS-inferred velocity remain the subject of ongoing research [160].

Here, $v_\perp \approx E_r/B$ will be used as a proxy for the local radial electric field. For the sake of generality, however, the results in this work will often be expressed in terms of $v_\perp$ rather than E_r. The method used to extract the Doppler shift will be explained in Sec. 3.2.2.

3.1.4 Proxy for density fluctuation level

The collected DBS signal intensity may be considered as a measure of the spatial Fourier transform of electron density fluctuations $\tilde{n}_e$, around a given scattering wavevector $\boldsymbol{k} = -2\boldsymbol{k_i}$:

$$\hat{n}_e(\boldsymbol{k},t) = \int_V \tilde{n}_e(\boldsymbol{r},t)\mathrm{e}^{\mathrm{i}\boldsymbol{k}\cdot\boldsymbol{r}}\mathrm{d}^3\boldsymbol{r}\,, \tag{3.5}$$

within a scattering volume V defined by the beam characteristics and radially localized near the cutoff [145]. The diagnostic response is then proportional to the convolution in wave number space of $n(\boldsymbol{k},t)$ with the Fourier transform of a weighting function representing the beam spatial distribution; In the simple case of laser scattering, the wavenumber resolution is inversely proportional to the beam waist [161]. However, the wavenumber response and resolution is more challenging to determine in the case of Doppler backscattering, owing to a much more complex weighting function [162, 163]. The latter generally requires advanced modelling, such as via 2D full-wave simulations [164, 165].

However, for a given probing frequency[4] and scattering geometry, the power of the DBS signal provides a measure of $|\hat{n}(k_\perp,t)|^2$, that will be used as a qualitative proxy for the density fluctuation level at a given radial location and perpendicular wavenumber $k_\perp$.

3.2 Signal detection and analysis

Having introduced the basic working principles of DBS, we now turn our attention to the signal processing and interpretation chain used in this work. As shown schematically in Fig. 3.4,

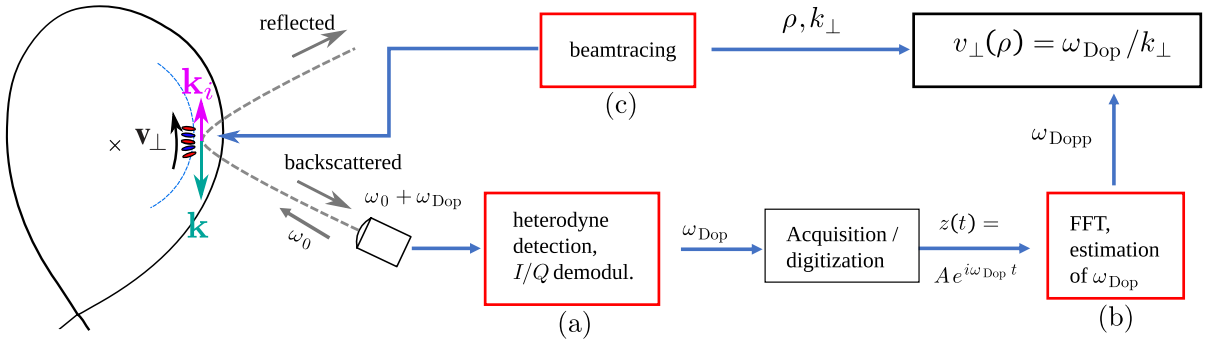

Figure 3.4

these steps consist of

(a) detecting the signal and acquiring it,

(b) extracting its Doppler shift $\omega_{\mathrm{Dop}} = 2\pi f_{\mathrm{Dop}}$,

(c) inferring ρ and $k_\perp$ at the beam turning point through beamtracing.

The details are provided below in that order.

[4] A relative calibration of the DBS signal power across different probing frequencies or channels is not straightforward and was not attempted in this work. Therefore, it is only meaningful to compare DBS signals of the same probing frequency and within the same channel.

3.2.1 Signal detection scheme

This section lays out the DBS signal detection method. It relies on a microwave scheme whose main components are explained using the example of the DBS system currently installed on WEST. The descriptions are largely applicable also to the system on TCV, both being developed by LPP with similar hardware. In principle, the microwave signal detection in the current system remains similar to the original implementation on Tore Supra [166], with significant hardware upgrades introduced since. A reduced diagram is shown in Fig. 3.5.

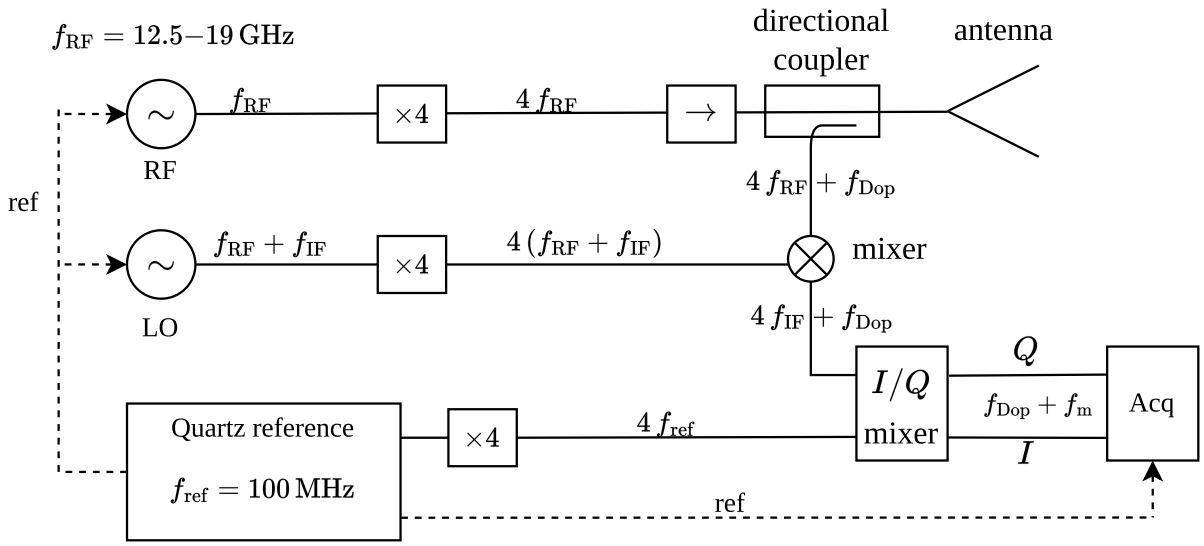

Figure 3.5: *Simplified diagram of the microwave scheme at the core of the DBS hardware on WEST and TCV.*

For simplicity, only one of the two equivalent V-band channels is represented. The DBS system at WEST has an additional W-band channel with 6x instead of 4x multipliers, while at TCV the system is composed of two equivalent V-bands.

The scheme is based on heterodyne detection which uses a reference signal, or "local oscillator" (LO), in addition to the probing radio frequency (RF) signal. The RF and LO sources originate from two separate synthesizers that share a common phase reference provided by a quartz oscillator[5]. The LO signal is frequency-shifted by f_{IF} (typically 100 MHz) with respect to the probing RF signal. 4-fold frequency multipliers raise the RF and LO signals to the V-band microwave range (50-75 GHz). The probing wave is then guided through a directional coupler—which separates the emitted from the received signals—to the antenna/launcher system.

The subsequent demodulation consists of two steps. First, the received (backscattered) signal is mixed with the LO signal, retaining the intermediate frequency component oscillating at $4\,f_{IF} + f_{Dop}$, where f_{Dop} represents the Doppler shift. Second, it is mixed with the quartz reference signal at $4\,f_{ref} = 400$ MHz through an in-phase and quadrature (I/Q)

[5] Alternatively, as explained below, a single source may be used as RF signal, and the LO is obtained from the RF signal using a single sideband modulator (SSBM [167]). This is the situation shown in Fig. 3.6.

mixer. The resulting I and Q signals are digitized and acquired with a 14 bits system at 10–100 MHz sampling rate. In the conventional case of *analog* I/Q demodulation, the quartz and LO frequency offset are set equal, $f_{\mathrm{ref}} = f_{\mathrm{IF}}$. The acquired I and Q signals are thus left without a modulation frequency other than caused by the Doppler shift (since $f_{\mathrm{m}} = |4f_{\mathrm{IF}} - 4f_{\mathrm{ref}}| = 0$).

An upgrade to this setup from *analog* to *digital* I/Q demodulation has been performed in 2024 for the DBS system on TCV, and subsequently also on WEST. It is a distinguishing feature of these DBS systems. The idea is to retain a finite modulation frequency (here $f_m = 6\,\mathrm{MHz}$) at the output of the second (I/Q) mixer and to digitize the I signal with sufficient sampling rate to perform the final demodulation step numerically, instead of through the analog I/Q mixer. The practical advantages of this approach are twofold. First, analog I/Q detection exhibits imperfections in amplitude balance and phase shift between the I and Q output signals, potentially distorting the resulting complex signal's power spectrum. Second, digital demodulation bypasses the effect of a notch filter causing a broad spectral gap ($\Delta f \sim 50\,\mathrm{kHz}$) around $f = 0$. Especially small Doppler shifts are thus better resolved.

To enable digital demodulation, the LO frequency is shifted with respect to the quartz oscillator, so as to retain a modulation frequency of typically $f_{\mathrm{m}} = |4\,f_{\mathrm{IF}} - 4\,f_{\mathrm{ref}}| = 6\,\mathrm{MHz}$ after the I/Q mixing. Only the I signal needs to be acquired, provided that the sampling rate (here 25 MHz) is high enough. From $I(t) = \cos(2\pi(f_{\mathrm{m}} + f_{\mathrm{Dop}})t)$ the complex signal can be computed directly as

$$Z(t) = I(t)\,\mathrm{e}^{-i2\pi f_{\mathrm{m}} t} \tag{3.6}$$

$$= \frac{1}{2}\mathrm{e}^{-i2\pi(2f_{\mathrm{m}}+f_{\mathrm{Dop}})t} + \frac{1}{2}\mathrm{e}^{i2\pi f_{\mathrm{Dop}} t}\ , \tag{3.7}$$

where the first (high-frequency) term is filtered out numerically to keep only the latter.

Another update was performed on both TCV and WEST systems in early 2025 and October 2024, respectively. These aimed to reduce the phase noise between the RF and LO sources. To illustrate the differences, the diagram above (Fig. 3.5) is reproduced in Fig. 3.6, with the main changes highlighted in red. The LO synthesizer is replaced with a single sideband modulator (SSBM [167])—as used in the original setup on Tore Supra [166]. The SSBM shifts the probing RF signal by the fixed reference frequency $f_{\mathrm{ref}} = 100\,\mathrm{MHz}$. An independent synthesizer with a lower frequency range than the RF sources provides a tunable intermediate frequency signal (typically $f_{\mathrm{IF}} = 394\,\mathrm{MHz}$[6]) for mixing with the received signal at $4\,f_{\mathrm{IF}} + f_{\mathrm{Dop}}$. This results in the finite modulation frequency—required for digital demodulation—$f_{\mathrm{m}} = 4f_{\mathrm{ref}} - f_{\mathrm{IF}} = 6\,\mathrm{MHz}$ after the final mixing stage.

3.2.2 Doppler shift estimation

During stationary, MHD-quiescent, L-mode discharges, and in the absence of dominant spurious contributions, the collected DBS signal mainly stems from the scattering by

[6] For the W-band channel on WEST, $f_{\mathrm{IF}} = 594\,\mathrm{MHz}$, owing to the 6x frequency multipliers (and not 4x).

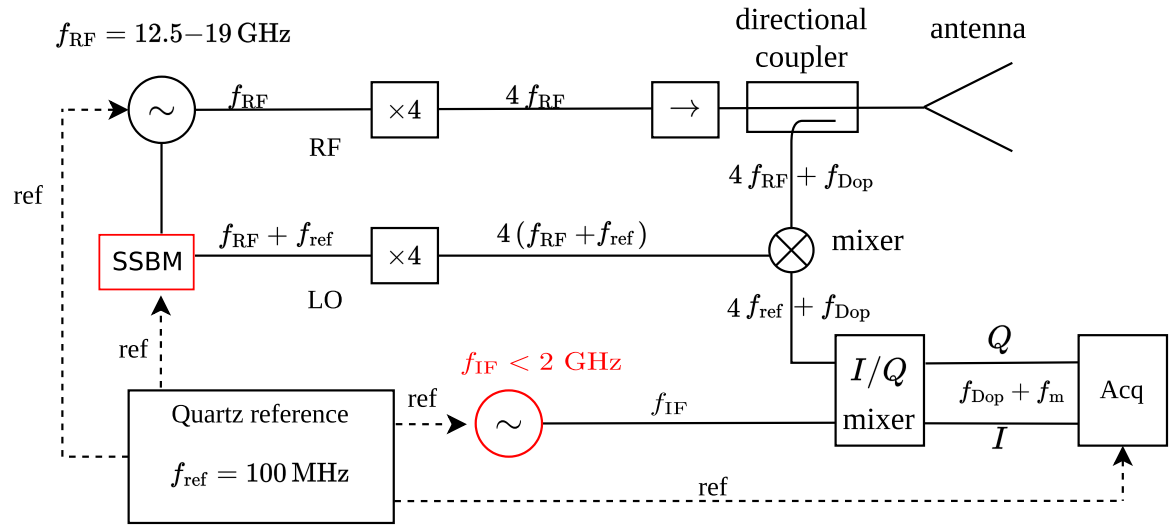

Figure 3.6: *Similar diagram to Fig. 3.5, reflecting updates made on both TCV and WEST systems over the course of this thesis.*

broadband turbulent density fluctuations. As was established in Sec. 3.1.3, the Doppler shift (f_{Dop}) reflects their perpendicular velocity $v_\perp$ at a given spatial scale $k_\perp$. The mean $v_\perp$ is then simply determined by the mean f_{Dop}, which can be extracted by combining standard FFT methods with an appropriate peak finding method. By contrast, more involved time-frequency analysis is necessary to study the dynamical properties of the flow [145]—including the $v_\perp$ oscillations associated with GAMs [168], or to infer its profile during H-mode, where density perturbations tend to be suppressed, or superseded by strong MHD activity [169].

In the following, we first focus on the former case, that is, the estimation of the mean $v_\perp$ in L-mode, which is applied to most of the results presented in this work. Then, the methods applied to H-mode and dynamic $E_r \times B$ flow studies are outlined, which serve only as complementary analyses in this work.

Mean Doppler shift in L-mode.

The mean f_{Dop} is extracted from the power spectral density (PSD) using the following peak finding method. The PSD is estimated for each frequency step (with a step duration of typically 5–10 ms) using Welch's method ($n_{FFT} = 2048$ with 50% overlap). A combination of Doppler peak estimations is used, from which the median value is retained. This includes Gaussian and Lorentzian curve fits, as well as the fit by a test function related to the statistical properties of turbulent motion [170]. The test function is denoted hereafter as the "T-spectrum". It can describe the transition between a Gaussian and a Lorentzian function, reflecting either the ballistic or diffusive character of the underlying turbulent motion, respectively. An example is shown in Fig. 3.7a.

By minimizing both linear and logarithmic squared residuals, the T-spectrum fit is usually well constrained. It captures both the peak and the wings of the distribution. This is generally not the case for Gaussian or Lorentzian fits. In practice, spurious components, e.g., associated with electronic noise or reflections, have to be discarded to ensure an

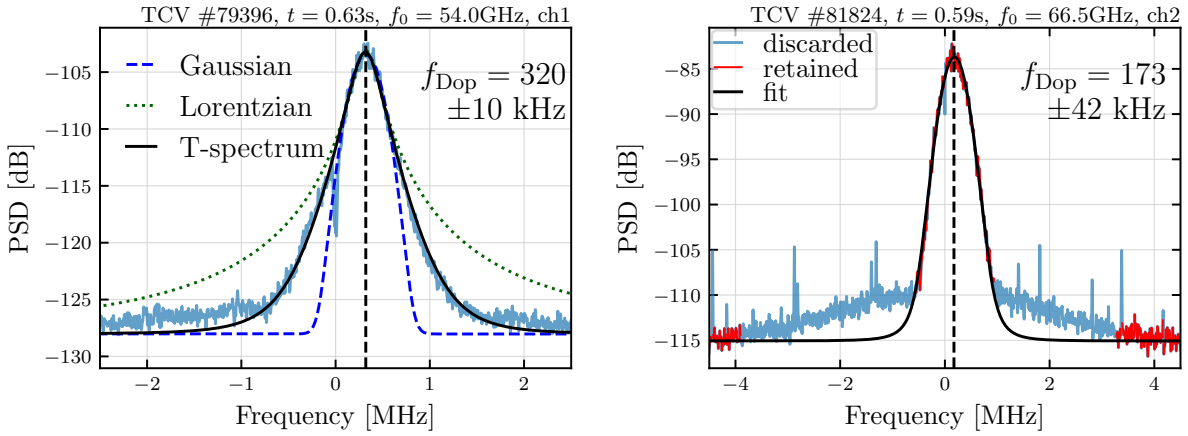

(a) **(b)**

Figure 3.7: *(a) Example PSD and corresponding fits by a Gaussian, a Lorentzian and the test function ("T-spectrum" [170]). (b) A mask is often applied to exclude spurious contributions while retaining the relevant parts of the PSD, ensuring an accurate fit of the Doppler peak.*

optimal fit, see Fig. 3.7b. Other spurious contributions are evident in Fig. 3.9, for the case of an H-mode plasma with low SNR (discussed below).

The uncertainty associated with this estimation of f_{Dop} can be obtained by taking the lower and upper bounds across the different estimations. However, their scatter tends to be small for well-pronounced Doppler peaks, resulting in an underestimation of the uncertainty. Reasonable conservative uncertainties are therefore evaluated manually, based on the data quality and the width of the distribution. They are indicated as error bars for representative data points in the $v_\perp$ profiles shown in this work.

Dynamical E_r analysis using MUSIC.

Although the primary focus of the present work is on the mean E_r profile, a subsidiary analysis in Chapter 4, Sec. 4.2.4, examines the dynamical properties of the edge E_r, for a selected pair of TCV discharges. The aim is to compare the amplitude of high-frequency oscillations in E_r (typically 5–100 kHz). The method relies on the MUltiple SIgnal Classification (MUSIC) algorithm [171]. In short, this time-frequency technique allows the Doppler shift $f_{\mathrm{Dop}}(t)$ to be extracted from MUSIC pseudo-spectra at a higher sampling rate than enabled by conventional FFT-based methods [145, 168]. An example pseudo-spectrum is shown in Fig. 3.8a. The $f_{\mathrm{Dop}}(t)$ signal is extracted by taking taking the maxima of the pseudo-spectra. Once extracted, the PSD of the resulting $v_\perp(t) = 2\pi f_{\mathrm{Dop}}(t)/k_\perp$ signal is then computed using a standard Welch estimation.

The DBS signal analyzed in Fig. 3.8b is an example that displays a pronounced coherent mode feature in the PSD of $f_{\mathrm{Dop}}(t)$ (Fig. 3.8b), with a peak frequency of ≈ 21 kHz. As described in Ref. [168], this technique is thus particularly suited for the detection of flow oscillations $\tilde{v}_\perp = \tilde{E}_r/B$, related for instance to the geodesic acoustic mode (GAM). As was mentioned in Sec. 2.5, GAMs [109, 110] are a high-frequency manifestion of turbulence-driven (zonal) flows. GAM studies based on the MUSIC algorithm were previously performed on Tore Supra [168, 172, 173], as well as TCV [138], where the GAM was characterized using a combination of fluctuation diagnostics, including DBS.

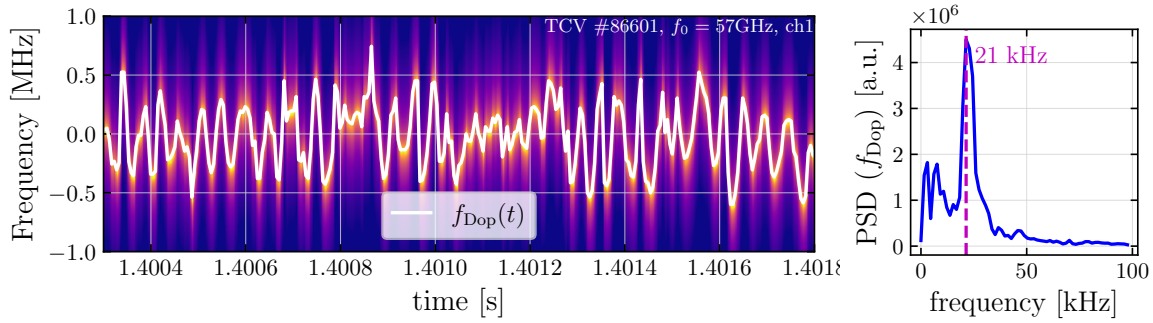

(a) **(b)**

Figure 3.8: *(a) Example pseudo-spectrum of the instantaneous Doppler shift obtained using the MUSIC algorithm. (b) Power spectral density of the extracted Doppler shift signal $f_{\mathrm{Dop}}(t)$, displaying a dominant coherent mode feature.*

Mean Doppler shift in H-mode.

H-mode discharges are not investigated systematically in this work, which focuses exclusively on L-mode, or the phase just prior to the L-H transition. For the sake of completeness, we nevertheless illustrate the approach that was used to obtain restricted E_r data in isolated TCV H-mode plasmas (an example is shown in Sec. 5.5).

In general, interpreting DBS data is significantly more complicated in H-mode, owing to the much lower broadband turbulence level compared to L-mode. Extracting the Doppler shift from an FFT-derived PSD, therefore, becomes more challenging. Depending on the specific H-mode behavior and, in particular, that of its edge-localized modes (ELMs), it sometimes becomes impossible, as the signal contributions from broadband turbulence fluctuations are statistically too low compared to those of macroscopic perturbations associated with ELMs or other MHD activity.

In that case, resorting to a finer time-frequency analysis, using for instance the MUSIC algorithm mentioned above, may enable the extraction of $v_\perp$ from the instantaneous Doppler shift associated with individual fluctuations (rather than from a time-integrated FFT frequency spectrum).

In this work, however, the restricted E_r analyses in TCV H-mode plasmas are limited to cases where the conventional extraction of the Doppler shift from the PSD is feasible. This is typically the case when the ELM frequency is low enough to allow for sufficient inter-ELM statistics. The DBS data collected during an H-mode phase are processed within ELM-free time intervals. The D_α signal from a vertical photodiode, along with the spectrogram of the DBS signal, are used for guidance to identify ELM-free phases within a considered time window. Representative examples of the PSDs obtained in such cases are displayed in Fig. 3.9.

We note that for typical TCV discharge parameters, the cutoff for the V-band range using X-mode polarization lies within the H-mode density pedestal, thereby limiting the accessible range to a narrow radial region around the separatrix. It is therefore hardly possible to access both outer and inner E_r shear layers simultaneously in a given H-mode plasma. Although challenging and not successfully attempted in this work, it might be

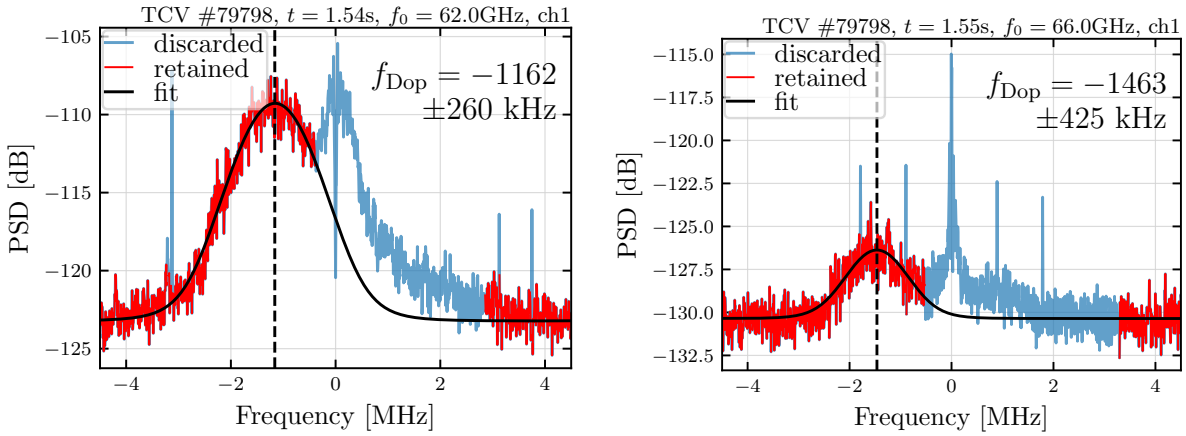

(a) **(b)**

Figure 3.9: *PSD obtained during ELM-free phases of a TCV H-mode discharge. (a) and (b) show representative signals corresponding to relatively good and low SNR, respectively.*

possible to probe the entire edge E_r well profile either using O-mode polarization, or a combination of X-mode and O-mode measurements acquired over repeated H-mode discharges.

3.2.3 Beamtracing

The interpretation of DBS data requires knowledge of the radial coordinate ρ and the wavenumber k_i of the probing beam at its turning point. As there are no generally applicable analytical solutions, the microwave ray trajectory is usually modeled numerically using beam- or raytracing algorithms.

Here, we use the beamtracing code `beam3d` [174], which was initially developed for DBS at Tore Supra (now WEST). It remains in use for DBS measurements in WEST, and is now used also in TCV with the recently installed DBS system on loan from LPP. In this work, `beam3d` has further been employed to process DBS data from AUG (Sec. 4.3.5).

The code propagates a set of interconnected rays representing a Gaussian probing beam in 3D geometry. It computes their trajectories within the Wentzel-Kramers-Brioullin (WKB, e.g. [175, §2.8.1]) approximation, which is valid in the case where the refractive index (and therefore the electric field amplitude) varies on spatial scales that are large compared to the local wavelength.

The probing location is defined here as the beam turning point[7], that is, the point corresponding to the minimum of the refractive index N^2 along the beam trajectory. In ordinary (O-mode) polarization, where the wave electric field is parallel to $\boldsymbol{B}$, N^2 depends only on the local density. Its minimum thus coincides with the innermost flux surface (or the minimum in ρ_ψ). In the extraordinary (X-mode) polarization—corresponding to a wave electric field that is perpendicular to $\boldsymbol{B}$, N^2 also depends on B and therefore on the major radius since $B \propto 1/R$. Then the cutoff layers do not correspond to flux surfaces in general, and, at the turning point, $\boldsymbol{k}_i$ therefore does not (exactly) lie on a flux surface. The expressions for N^2 in both polarization modes can be found e.g. in [173, § 2.1.5]

Because of refraction, the beam trajectory and turning point location are sensitive to the density profile prior to the turning point. Accurately estimating the density profile across the separatrix and into the scrape-off layer (SOL) is therefore crucial to reach the desired level of precision in localizing the edge measurements. This implies an inherent limitation of DBS: It relies on independent estimations of the edge density profile and of the magnetic equilibrium, subject to their own uncertainties. The localization capability of DBS is therefore limited by their accuracy.

Next, we provide the details regarding the interfacing of the beamtracing code with TCV. It requires in particular the beam properties (launch point, probing angles, and waist radius) associated with the launcher system. The latter will be presented subsequently in Sec. 3.3.

Beamtracing in TCV. The aforementioned beam properties are retrieved from inherited routines shared with the short-pulse reflectometer (SPR) diagnostic [176]. The magnetic equilibrium, Fig. 3.10a, is obtained from the free boundary equilibrium reconstruction code LIUQE [177]. The density profile, Fig. 3.10b, is estimated from raw Thomson scattering (TS) [178] data. This is achieved by fitting the edge TS data to a modified hyperbolic tangent (*mtanh*) function (similar to F_{ped} in [179]). A negative slope in the SOL ensures a smooth drop to zero to avoid any discontinuity in the refractive index. The core density profile, on the other hand, is taken from standard post-shot analysis (`proffit`) outputs. A smooth hyperbolic tangent transition between the core (`proffit`) and edge profile is imposed with a free parameter defining the transition point. To further improve the quality and robustness of the fit, TS measurements originating from regions close to the divertor legs or within the private flux region are excluded. These regions are shown in Fig. 3.10 (a) as shaded areas. The corresponding data points, grayed out in Fig. 3.10 (b), are systematically found to be outliers that would otherwise distort the pedestal fit. The output of the `beam3d` code is shown in Fig. 3.11 for a given probing frequency.

[7] Based on a comprehensive 2D full-wave modeling study [163], in typical edge probing conditions, the DBS beam turning point is expected to be a good proxy for the peak location of the spatial weighting function (W) defined by the beam pattern. This is the case for mirror-like beam incidence; that is, at close to normal beam incidence and/or when probing the plasma edge region where the gradient of the refractive index is stronger than in the core. In contrast, when probing at larger relative tilt angles or further in the core, beam refraction is more gradual and results in a "banana-shaped" trajectory. In this latter case, the peak of W is radially displaced outward and poloidally tilted compared to the expected cutoff layer, introducing errors in ρ_ψ and $k_\perp$. In this work, we are exclusively probing the edge region and use sufficiently shallow probing angles, so we consider the "mirror-like" case to be satisfied and assume systematic errors in ρ_ψ and/or $k_\perp$ from this approximation to be negligible.

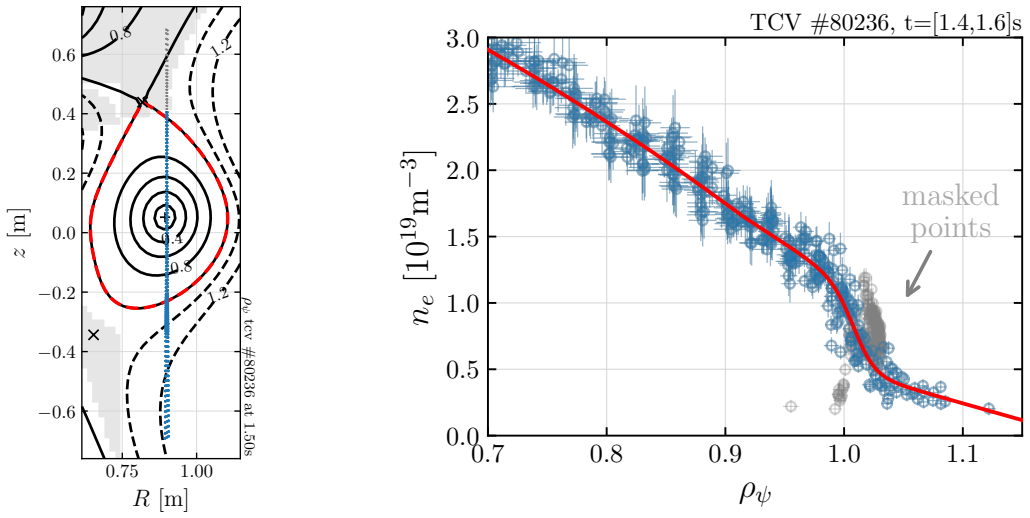

(a) **(b)**

Figure 3.10: *Beamtracing inputs for an example TCV discharge: (a) Magnetic equilibrium (with TS measurement locations indicated) and (b) density profile. The red curve represents a fit through the raw TS data, excluding spurious contributions (gray data points) stemming from the shaded regions in (a).*

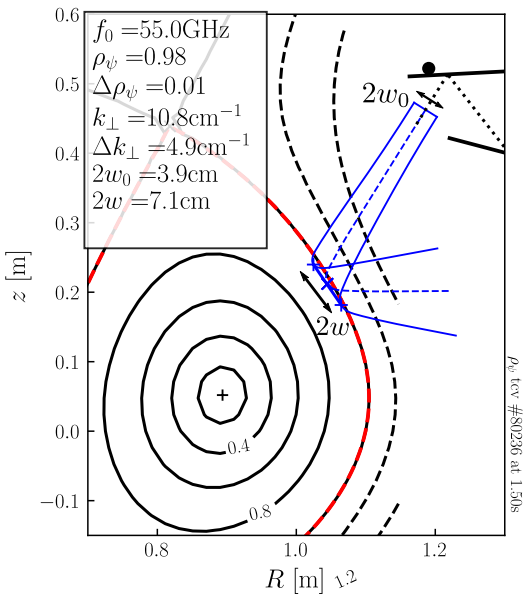

Figure 3.11: *Beamtracing result for the TCV equilibrium and density inputs of Fig. 3.10 and a given probing frequency (f_0). Annotated are the $(\rho_\psi, k_\perp)$ values at the turning point of the central ray, as well as the separation $(\Delta\rho_\psi, \Delta k_\perp)$ between the inner and outer rays representing the Gaussian beam amplitude e-folding radius. Moreover, the beam diameter at the waist (w_0) and at the turning point (w) are annotated.*

Following this procedure, there are no indications in TCV of striking or systematic inconsistencies in the radial alignment of the $v_\perp$ profiles with respect to the separatrix location. Accordingly, in this work, no corrections of the DBS or other kinetic profiles are performed after mapping the measurements onto ρ_ψ. It should be noted, however, that the available density data from TS typically does not reach beyond $\rho_\psi \gtrsim 1.1$ (see Fig. 3.10b). The density profile shape in this far-SOL region is thus poorly constrained, which might introduce errors in the precise values of ρ_ψ and $k_\perp$ when the turning point is near or just outside the separatrix[8].

3.3 Launcher and operating range

The dual channel V-band (50-75 GHz) DBS system is coupled to TCV's quasi-optical launcher antenna [139] shared with the short-pulse reflectometer (SPR) [176]. Hence, the DBS and SPR cannot operate simultaneously. The antenna allows for toroidal and poloidal steering with 0.2° precision [139]. Furthermore, poloidal angle sweeps can be performed at a (safe) speed of $\lesssim 30\,^\circ\,\mathrm{s}^{-1}$. The wave polarization can be switched flexibly between O- and X-mode. More technical details on the launcher can be found in [139] and references therein.

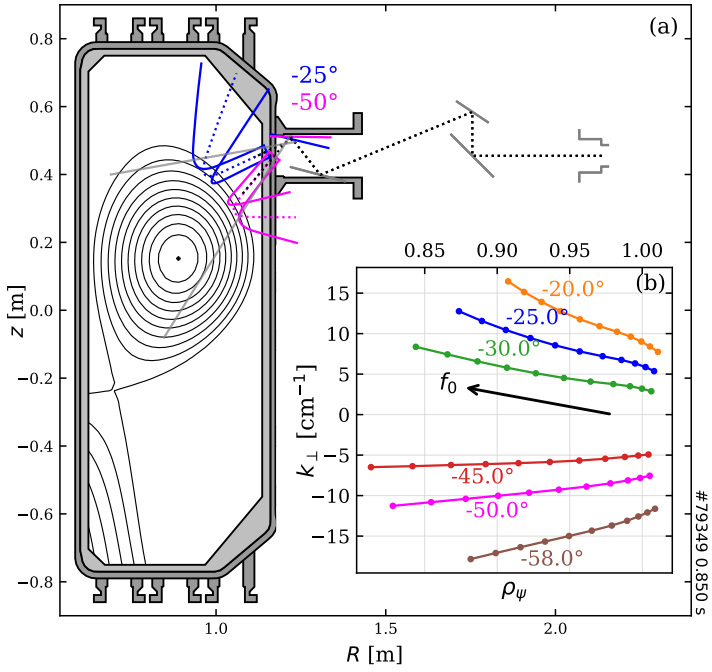

Figure 3.12: *(a) Illustration of the launcher geometry, showing two possible beam paths with opposite poloidal inclinations for an example TCV discharge. Gray solid lines indicate the tilt angle range limits, $\theta \in [-58, -10]^\circ$. The inset (b) shows the reasonably accessible $(k_\perp, \rho_\psi)$ space in this scenario. It is spanned by a set of 6 suitable poloidal angles and 11 equidistant probing frequencies (f_0) ranging from 48 to 68 GHz.*

The beam is launched diagonally downward from the upper low-field side, as shown in Fig. 3.12. Using X-mode in typical L-mode conditions, the radial probing range lies between the separatrix and $\rho_\psi = 0.7 - 0.9$, for low to high density scenarios at nominal B-field. The probed wavenumber is usually contained within $k_\perp \sim [4, 16]\,\mathrm{cm}^{-1}$. This

[8] A possible refinement of the density profile fit by including thermal helium beam (THB [180]) density data in the SOL is deferred to future work.

translates roughly to $k_\perp \rho_s \sim [0.5, 2]$, typical of ion-scale turbulence (ρ_s being the ion Larmor radius evaluated at sound speed). Typically, a sequence of 20 $\times$5 ms frequency steps is programmed separately on both channels, to obtain a well-resolved (up to 40-points) profile of the mean $v_\perp$ flow every 100 ms.

Operation of the DBS is ensured fully remotely, including off-site. Compared to the system on WEST, however, more careful supervision is required. This is due in parts to the larger variability of plasma scenarios in TCV, requiring frequent adjustments to the launcher settings (beam orientation and fast polarizers [139]).

The highly elevated position of the DBS launcher in TCV adds to the operational complexity. Indeed, for a typically centered TCV plasma ($z_{\text{axis}} \approx 0$), finding a suitable probing geometry is not straightforward. More particularly, access to the outboard midplane (OMP) edge region not guaranteed, even for the steepest downward tilt of the beam (58 °), unless the plasma is shifted upward. In principle, TCV provides the freedom to raise the plasma high enough for the DBS beam to reach the OMP. Yet, this comes at the cost of other constraints, especially in terms of coverage by other diagnostics, or neutral beam power deposition which is centered at $z = 0$. As an example, a reasonable compromise can be found in the scenario depicted in Fig. 3.12. There, with a $\sim$ 10 cm upward shift, the plasma cross-section remains sufficiently centered for neutral beam heating. At the same time, a large part of its first quadrant becomes accessible, almost up to the OMP edge region. This upward-shifted geometry was used in the early stages of the E_r studies presented in this work. However, it is not compatible high-quality edge CXRS measurements or in the very core, nor with complementary edge turbulence diagnostics such gas-puff imaging in the OMP (GPI, introduced below). For this reason, subsequent analyses relied on more centered plasma shapes ($z_{\text{axis}} \approx 0$), in both LSN and USN configurations.

Alternatively, the beam may be tilted in the opposite direction, towards the top region of the plasma, as indicated by the blue beam in Fig. 3.12 (a). Although the turbulence level is expected to be lower there compared to the OMP (assuming ballooned turbulence), the signal quality turns out to be satisfactory. However, collecting DBS data from the top instead of the OMP requires caution when interpreting the E_r measurements. First, it complicates the direct comparison with other tokamas such as WEST and AUG, where the DBS systems predominantly probe the OMP. Second, the variation of the flux expansion and of B with the poloidal location (and therefore R) of the turning point affect the local $E_r \times B$ velocity, which must be accounted for when analyzing the overall velocity shear. This will be addressed in Sec. 3.7 where the mapping of local $v_\perp$ measurements to the OMP is tested.

3.4 Overview of main TCV diagnostics and quantities used

Besides to the DBS system described above, the analysis of TCV experiments conducted in this work relies on the following additional diagnostics, with their respective measurement locations indicated in Fig. 3.13.

TS. The Thomson scattering (TS) diagnostic [178] was already mentioned in Sec. 3.2.3, as

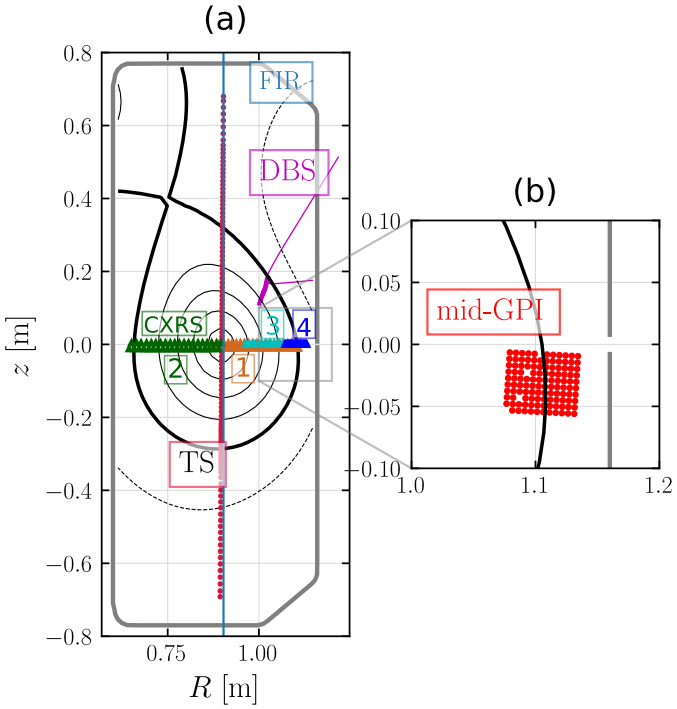

Figure 3.13: *Overview of TCV diagnostics locations used in this work. Data points represent measurement locations. The numbers 1–4 correspond to the different CXRS systems (SYS1, SYS2, ...). A representative DBS beam trajectory is represented by a magenty ray. The vertical blue line going through the plasma center corresponds to the central FIR chord. The inset (b) zooms into the edge OMP to visualize the field of view of the midplane-GPI system.*

it provides the density used as input to the beamtracing. In addition to electron density ($n_e \equiv n$), it also provides the electron temperature (T_e), along 117 observation points (red dots in Fig. 3.13 a) along a vertical chord ($R \approx 0.9\,\mathrm{m}$), at mid-radius of the vessel. The data cover the core and edge regions and typically include points in the near-SOL region. The n_e and T_e are the main data complementing the analysis and interpretation of the $v_\perp$ profiles. These electron kinetic profiles are nearly always available—TS being a standard diagnostic in TCV—and of good quality.

CXRS. Kinetic profiles of the ion impurtiy are obtained by charge exchange recombination spectroscopy (CXRS [43]), in combination with a diagnostic neutral beam (DNBI [39], previously mentioned in Sec. 1.2.4). Owing to its graphite-tiled wall, the main impurity species in TCV is carbon. Accordingly, the CXRS systems in TCV [141, 181] use the CX reaction between fully-stripped carbon ions (C^{6+}) and the hydrogen neutrals from the DNBI. The DNBI pulses typically cover a 1 s period of the discharge with ON/OFF times set to 8/16 ms (33% duty cycle). The CXRS acquisition, synchronized with the DNBI blips, consists of four systems (SYS1–4) [141, 181]. Their measurement locations, shown in Fig. 3.13, cover the inboard (SYS2) and outboard (SYS1 and SYS3) midplanes, and SYS4 covers the LFS edge.

The four systems independently measure the C^{6+} temperature and density. Following previous studies at TCV [141, 182], the C^{6+} temperature serves here as a proxy for the main ion (deuterium) temperature T_i, neglecting possible deviations noted e.g. on DIII-D [60]. Moreover, the CXRS systems provide C^{6+} poloidal[9] and toroidal rotation profiles, which, combined with the density and temperature, are used for a complementary estimation of E_r through the radial force balance. The details of this procedure are described in Sec. 3.6.

Midplane GPI. TCV is equipped with gas puff imaging (GPI) systems [183] that can provide 2D data on the size and propagation of turbulent structures at different poloidal locations, from the SOL to just inside the separatrix. GPI relies on the injection of a small amount of neutral gas—Helium in the discharges considered here—into the plasma edge. The gas cloud interacts locally with the plasma, emitting visible light that is collected by a detector array or camera[10]. Fluctuations in the measured brightness of a given spectral line—associated with both electron density and temperature fluctuations [183]—are used to detect and track individual filamentary structures with high temporal resolution. In particular, this enables the determination of their poloidal velocity—nearly aligned with $v_\perp$, which will be compared to DBS measurements in Sec. 3.5.

Here, only the *midplane* GPI system is used, which has a field of view located around the outboard midplane (inset in Fig. 3.13). It is spanned by a 12×10 Avalanche Photodiode (APD) detector array covering a $5\,\mathrm{cm} \times 4\,\mathrm{cm}$ area in the radial and poloidal directions, respectively [183]. The optical chords have a spot size of $\Delta \approx 4\,\mathrm{mm}$ in the focal plane (roughly equal to their radial or poloidal spacing), limiting the sensitivity to perpendicular

[9] As will be explained in Sec. 3.6, poloidal rotation measurements are not used in this work, and instead replaced by a neoclassical estimation.

[10] At TCV, both detection methods are available; The camera has a higher spatial but lower temporal resolution and detection efficiency than the Avalanche Photodiode (APD) detector array. Only the latter was used in this work.

structures equal or larger than Δ, that is, the midplane GPI signals are not sensitive to perturbations with wavenumbers $k_r, k_\theta \gtrsim \pi/4\,\mathrm{mm} \approx 8\,\mathrm{cm}^{-1}$. The turbulence $k_\theta \simeq k_\perp$ ranges accessed by the GPI and DBS close to the separatrix therefore typically overlap to some extent, although the GPI tends to be more sensitive to larger scales (lower $k_\perp$).

Conditional average sampling (CAS) [184], combined with a tracking algorithm, allows the average turbulence structure size and velocity to be estimated. The detector sampling frequency ($f_\mathrm{s} = 2\,\mathrm{MHz}$) is sufficient to resolve the dynamics of fluctuations if their velocity does not exceed $\Delta \times f_s \approx 8\,\mathrm{km/s}$, whereas typical $v_\perp$ magnitudes in TCV L-mode discharges around the LCFS rarely exceed a $4\,\mathrm{km/s}$ according to the DBS measurements presented subsequently (Sec. 3.8).

FIR. In TCV, a Mach-Zehnder interferometer [185] is used in particular for real-time density feedback control. This diagnostic detects the phase shift between a reference and several probing FarInfraRed (FIR) laser beams [186]. It provides routine measurements of the line-integrated electron density, $\int n_e \mathrm{d}l$, along the 14 vertical beam chords. A conventional metric for measuring and comparing integrated density measurements across different scenarios and machines is the line-*averaged* density. It is obtained from the line-integrated measurement from the central chord, divided by that chord length in the plasma.

PD. The D_α line radiation, measured from a vertically-viewing photodiode (PD#1), is used to monitor changes in confinement regimes; Macroscopic perturbations associated in particular with edge-localized modes (ELMs) in H-mode, or higher-frequency I-phase LCOs are clearly visible in the D_α signal. The latter can therefore be used to identify the L-H transition time, or ELM-free phases during H-mode.

Confinement metrics. In the subsequent chapters, confinement is quantified using conventional 0D metrics. They consist of the steady-state ($\mathrm{d}W/\mathrm{d}t = 0$) energy confinement time,

$$\tau_E = W/P_\mathrm{in}\,,$$

the H-mode enhancement factor (H-factor),

$$H_{98\mathrm{y}2} = \tau_E/\tau_E^{\mathrm{IPB98(y,2)}}$$

and the normalized beta,

$$\beta_N = \beta[\%]a[\mathrm{m}]B_0[\mathrm{T}]/I_p[\mathrm{MA}]\,.$$

In these expressions, W is the total stored energy content, P_in is the injected power, $\tau_E^{\mathrm{IPB98(y,2)}}$ the IPB98(y,2) scaling law [10] and $\beta = 2\langle p\rangle\mu_0/B_0^2$ the thermal to magnetic pressure ratio.

The energy content, $W = \frac{3}{2}\int p\mathrm{d}V$ in the confined plasma volume V, is computed using a standard routine (`anaprofs`) available for post-processing at TCV. It uses the pressure profile $p = n_eT_e + n_iT_i$ inferred from TS and CXRS data. The routine also accounts for main ion dilution by C^{6+} impurities; n_i is obtained from n_e using a global estimate of the effective charge state, $Z_\mathrm{eff} = \sum_a n_a Z_a^2/n_e$, where the sum is over the main ion and the dominant impurity species (deuterium and carbon, respectively).

Additionally, in particular if the case of missing or incomplete CXRS (T_i) data coverage, the electron energy content, $W_e = \frac{3}{2}\int n_e T_e \mathrm{d}V$, is considered. The latter provides a robust—albeit simplified—proxy for confinement level. An alternative estimate of W_{tot} based on diamagnetic loop measurements (often denoted as W_{MHD}) is not used in this work, as it has been found to be sometimes unreliable in TCV.

3.5 Comparison of DBS and GPI measurements

TCV's midplane GPI (introduced in Sec. 3.4) and the DBS diagnostics rely on fundamentally different measurement techniques, but should provide comparable information on the perpendicular velocity of turbulent structures. This redundancy provides an opportunity for cross-comparison of the independent estimates of $v_\perp$. Below, we present a few representative examples of such comparisons between the two diagnostics.

The distinction between perpendicular and poloidal projections of the turbulence velocity is considered small compared to the measurement uncertainties and therefore neglected here. The helium gas is injected over 100 ms during a stationary discharge phase. The DBS data are analyzed for the same phase, but outside the puff injection period. Fig. 3.14 shows a comparison for three different L-mode plasma scenarios. Here, the average size of the structures detected by the aforementioned CAS analysis varies depending on the plasma scenario and radial location, ranging from $\Delta_\theta \approx 0.5\,\mathrm{cm}$ to 5 cm in the poloidal direction, or $k_\perp \sim \pi/\Delta_\theta \approx 0.6$ to $6\,\mathrm{cm}^{-1}$.

In all cases, good agreement is found in the overlapping radial range, which lends confidence to both measurement techniques. Furthermore, it highlights the complementarity of the two diagnostics when it comes to measuring the full structure of the velocity across the separatrix, including the E_r "hill" outside the separatrix.

3.6 Comparison of DBS and C^{6+} radial force balance

As a further test, we compare the DBS measurements to the E_r inferred from the ion radial force balance equation (see Sec. 2.2), repeated here for clarity:

$$E_r = V_{a,\varphi} B_\theta - V_{a,\theta} B_\varphi + \frac{\nabla_r p_a}{Z n_a e}\,. \tag{3.8}$$

In this section, we only consider the carbon (C^{6+}, $Z = 6$) impurity profiles, measured by CXRS, and drop the species index.

The toroidal velocity V_φ can be obtained from the horizontal SYS1 and SYS2 systems at the low (LFS) and high field sides (HFS), respectively (seerefer Fig. 3.13). Because of stronger attenuation of the neutral beam, the HFS system suffers from lower active signal compared to the LFS, and is therefore not considered here. V_φ is thus obtained from SYS1. The poloidal velocity V_θ can be measured at the LFS with the vertical systems SYS3 and SYS4. The latter was designed to provide highly resolved edge profiles [141], but currently does not deliver reliable measurements of V_θ. This leaves SYS3 as the sole

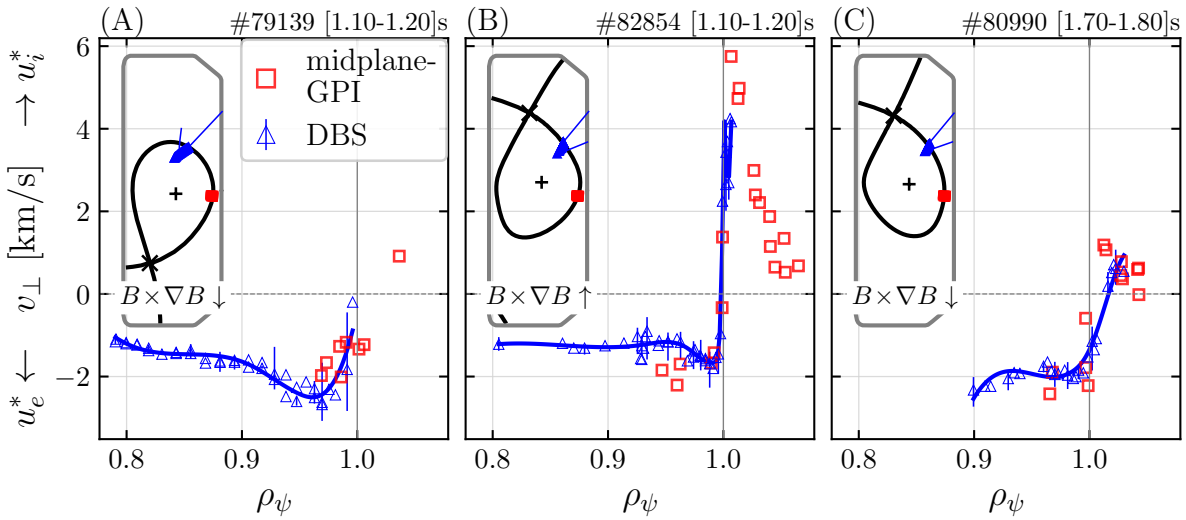

(a)

	Heating	I_p [kA]	$\bar{n}_l^{19}$ [m^{-3}]
(A)	Ohmic	−210	4.0
(B)	ECRH (560 kW)	180	4.5
(C)	Ohmic	−180	6.1

(b)

Figure 3.14: *(a) Comparison of the velocity profiles measured by the DBS and the midplane GPI diagnostics, respectively, in various plasma conditions (b) and shapes at fixed $B_0 = -1.44$ T. The DBS and GPI probing regions are highlighted in blue and red, respectively, in the plasma shape insets. In (B), the GPI profiles have been shifted by $\Delta\rho_\psi = +0.04$ to account for a clear radial mismatch with respect to the expected velocity reversal around the separatrix.*

system available for measuring V_θ. However, the data from SYS3 exhibits significant scatter, and the resulting profiles are often questionable, especially towards the edge[11].

For a meaningful comparison with the DBS, we therefore resort to a neoclassical estimation as a proxy for V_θ instead. Though potentially inaccurate in certain plasma conditions or regions [100, 101, 187], past studies have found neoclassical estimates of the carbon poloidal flow to be in reasonable agreement with the measured one in L-mode TCV discharges [188][141, Fig. 6.20]. Here, the first order neoclassical poloidal flow of the carbon impurity is computed using the NEO code [189, 190]. NEO is an established and publically available[12], multi-species, neoclassical transport code.

The remaining terms on the right-hand side of Eq. (3.8) are estimated from weighted smoothing spline fits to the CXRS data. The weights are taken as $1/\sigma^2$, where σ is the y-uncertainty of the data points. The diamagnetic term, $(\nabla p/Zne)$, is obtained from a weighted spline fit through the combined data from SYS(1,3,4). All terms are divided by B, so that their sum, $v_{E_r\times B} = E_r/B$, is compared to the velocity $v_\perp$ measured by DBS.

Fig. 3.15 shows the results of such a comparison for an example Ohmic L-mode discharge phase (#80190 around 1.8 s, USN, favorable $B\times\nabla B$, $B_0 = 1.44\,\mathrm{T}$, $I_p = 200\,\mathrm{kA}$, $\bar{n}_l = 3\times10^{19}\,\mathrm{m}^{-3}$). In this particular scenario, a reasonable agreement is found regarding the general $E_r\times B$ velocity level derived from DBS and via Eq. (2.2). However, the quantitative agreement is not generally satisfactory in other cases considered; Appendix A provides other representative examples in L-mode, analogous to Fig. 3.15, with various levels of agreement between the DBS and the force balance. Moreover, the fine structure of E_r—in particular the well—does not appear to be captured by the radial force balance result.

On one hand, inaccuracies in the NEO-derived V_θ may stem from a deviation of the impurity flow from neoclassical predictions (as mentioned above), or uncertainties in the input data—especially towards the very edge. On the other hand, the significant scatter in CXRS data, evident in Fig. 3.15b suggests large statistical uncertainties. Moreover, the spatial resolution of the CXRS systems may limit their ability to resolve small-scale corrugations in the impurity kinetic profiles.

We conclude that a fine-scale analysis of the E_r radial structure at the very edge is challenging to complement with the impurity force balance in TCV, based on the current CXRS diagnostics capabilities. Nevertheless, when restricting the analysis to the (coarse) E_r level from the outer core to $\rho_\psi \approx 0.95$, no systematic or unreasonable disagreement is found between the DBS measurements and the force balance. This approach will be used to complement the analyses in Chapters 4 and 5.

3.7 Mapping $v_\perp$ to the OMP

The steerable launcher allows various regions of the plasma to be probed, from the top to the outboard midplane (OMP), with positive and negative poloidal tilt angles relative to

[11] For illustration, Appendix A, Fig. A.3, shows the results of using V_θ from SYS3 rather than the neoclassical estimate, as outlined here.

[12] https://gacode.io/neo.html

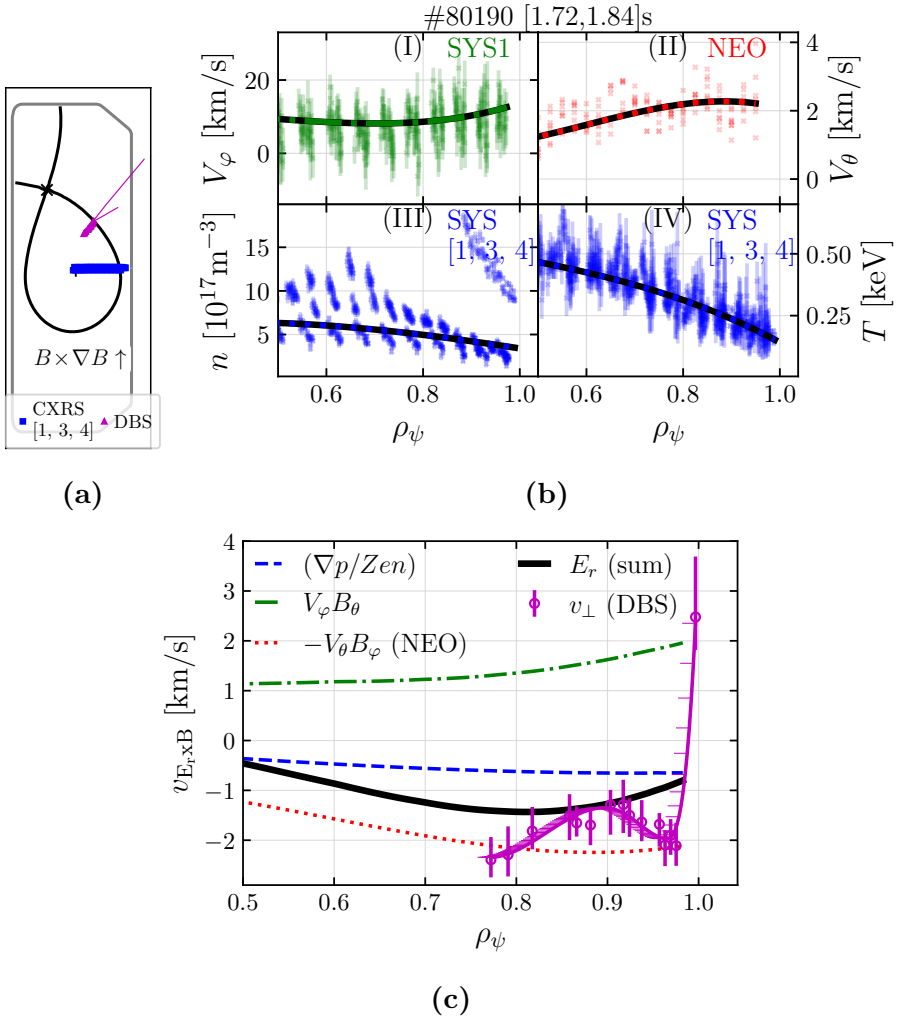

Figure 3.15: *Comparison between DBS and radial force balance for C^{6+}, using CXRS measurements combined with a neoclassical prediction of V_θ. (a) Equilibrium reconstruction of the considered scenario, showing the DBS and CXRS probing regions. (b) Spline fits to the CXRS data (I,III,IV) and to the V_θ results from NEO (II). The scatter in V_θ is due to repeated NEO runs for each of the 12 CXRS acquisitions within the considered time window. (c) Radial force balance terms overplotted with the DBS $v_\perp$ profile.*

normal incidence. Making use of this flexibility, we aim to investigate how the measured $v_\perp$ data is influenced by the beam poloidal tilt angle and/or by the poloidal probing location. This investigation is partly motivated by the geometrical constraints of the DBS launcher pointed out in Sec. 3.3.

To begin with, we point out that the $E_r \times B$ flow not only varies poloidally with the magnetic field strength as $1/B$, but may also depend on the local flux expansion since the radial gradient of the electrostatic potential ϕ is weaker where flux surfaces lie further apart. In vertically elongated plasmas (or in case of strong Shafranov shift), E_r and the associated drift velocity should thus be weaker at the top than at the OMP, if the electrostatic potential ϕ is constant on a flux surface.

Following the example on AUG [191], we proceed to map the $v_\perp$ data measured by DBS from different poloidal locations to the OMP, assuming that it reflects the local $E_r \times B$ velocity, and that ϕ is a flux function. Then, since $v_\perp = E_r/B = -\phi'(\psi)\nabla\psi/B$, the local velocity measurement ($v_\perp$) should map to the OMP according to:

$$v_{\perp,\mathrm{OMP}} = v_\perp \frac{|\nabla\psi|_{\mathrm{OMP}}}{|\nabla\psi|} \frac{B}{B_{\mathrm{OMP}}} \,, \tag{3.9}$$

where the flux expansion ratio $f_x/f_{x,\mathrm{OMP}} = |\nabla\psi|_{\mathrm{OMP}}/|\nabla\psi|$ can be significant when probing outside the OMP region in shaped TCV plasmas. Here, B varies moderately over the accessible probing range (typically $\lesssim 25\%$), but since $B/B_{\mathrm{OMP}} \geq 1$ (on a given flux surface), both the flux expansion and B-field variation tend to increase the magnitude of the velocity profiles when mapped to the OMP.

The mapping procedure is applied to $v_\perp$ profiles obtained at various beam poloidal angles within a fixed plasma scenario. First, we focus on the situation illustrated in Fig. 3.16 (a), where the beam is reflected towards the top (*upward* probing), and the poloidal angle is swept from -28 to $-22°$ over 1.2 s.

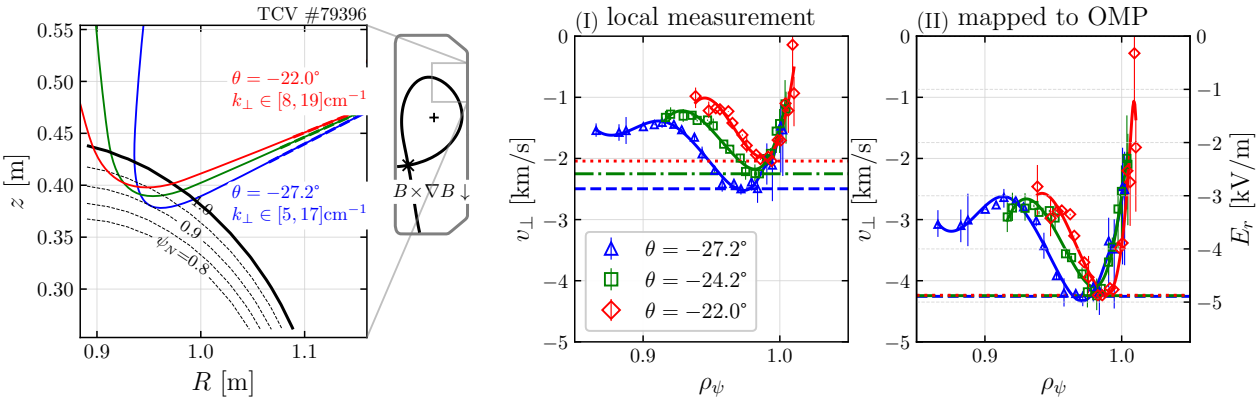

(a) **(b)**

Figure 3.16: *(a) Zoom onto the poloidal plane, showing the surfaces of constant normalized poloidal flux ψ_N, along with the computed ray trajectories at different tilt angles (for a given probing frequency). (b) Velocity profiles before (I) and after (II) mapping to the outboard midplane (OMP). The scale on the right-hand side represents the $E_r = v_\perp B$ values at the OMP, neglecting the radial variation of B of a few % over the probing range.*

The DBS profiles corresponding to three acquisition time windows along the sweep are displayed in Fig. 3.16 (b), confronting the velocities obtained (I) locally at the beam turning point with (II) the ones mapped to the OMP as per Eq. (3.9). The mapping almost accounts for a factor 2 increase in the magnitude of the velocity (or E_r) well. Moreover, the initially differing well depths (dashed horizontal lines in Fig. 3.16 (b)) are brought together by the projection. The shape of the profiles, on the other hand, including the radial location of the well, differs between the three cases, and the difference persists after the mapping. The observed discrepancy ($\Delta\rho_\psi \sim 0.03$) could stem from radial localization uncertainties associated with the input magnetic equilibrium or density profile used in the beamtracing. Indeed, sensitivity studies revealed that slight differences in these input data could explain differences of the order of the observed radial shift. Additionally, systematic errors inherent to the beamtracing modelling are conceivable: At larger tilt angles relative to normal incidence (e.g., red trajectory in Fig. 3.16,a), both the spatial resolution and accuracy of the beamtracing tend to degrade [192]. We conclude that in this particular case, the projection to the OMP according to Eq. (3.9) yields similar profiles—except for small radial shifts.

By contrast, the behavior is different when comparing the previous scattering geometry, that is, using *upward* probing, with the *downward* probing counterpart, see Fig. 3.17 (a). A separate, well-matched discharge phase is used for this comparison. Now, the *local* $v_\perp$

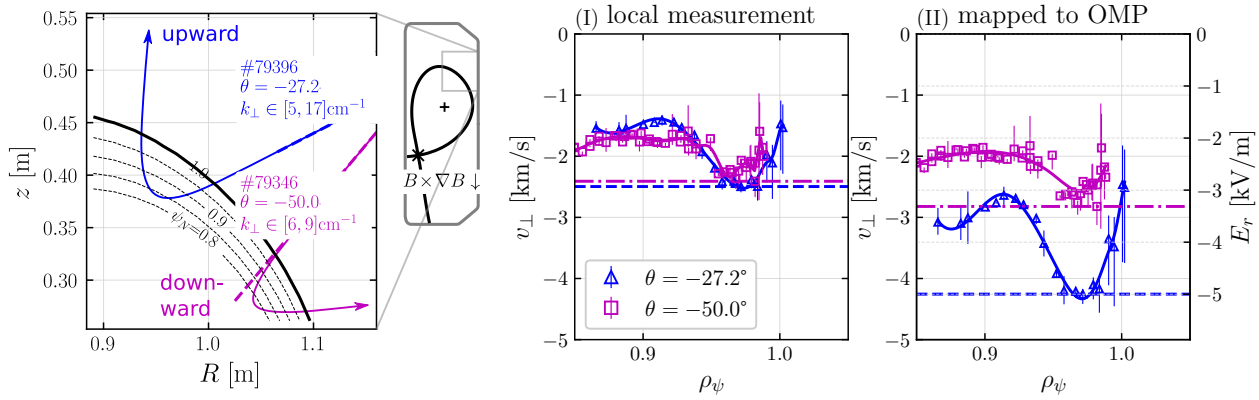

Figure 3.17: *Same representation as in Fig. 3.16, but with the comparison of up- and downward probing geometry. Here, the profiles agree well before (I), and disagree after mapping to the OMP (II).*

profiles are similar, resulting in a large discrepancy once projected to the OMP, due to the combined effects—as mentioned previously—of higher flux expansion and lower $|B|$ in the top compared to the OMP region. A qualitatively similar behavior is observed in other scenarios (including in upper single-null discharges where the effect is enhanced due to the presence of the X-point), or in the same scenario but with reversed B-field and same helicity. Any hypothetical explanation for the discrepancy in terms of an effect that should reverse with the sign of B, therefore appears unlikely. Moreover, the $k_\perp$ ranges probed in either beam direction partly overlap, as annotated in Fig. 3.17 (a), ruling out any dominating influence of the selected structure sizes on the results.

A straightforward explanation for the results shown in Fig. 3.17 is therefore not immedi-

ately apparent. Possible causes that could be investigated in future work include: poloidal asymmetries in the electrostatic potential linked to neoclassical effects and/or ballooned turbulence, or diagnostic effects associated e.g. with eddy tilting.[13] Poloidal asymmetries in $v_\perp$ beyond what is implied by Eq. (3.9) have been reported in other devices [193–195]. Such a poloidal asymmetry was not observed in a study performed at AUG under conditions that are somewhat closer in terms of probing geometry and magnetic configuration, yet not entirely comparable, to the present TCV scenarios [191].

To conclude, when probing upward, the local $v_\perp$ measurements are scaled significantly if mapped to the OMP according to Eq. (3.9), leading to a possible inconsistency with the downward probing case. Hence, the DBS measurements obtained in the upward and downward probing case in TCV can presently not be considered equivalent.

Consequently, the choice was made to renounce entirely on upward probing for the remainder of this work. Presented measurements henceforth correspond exclusively to the *downward* probing configuration, which are, at present, considered sufficiently trustworthy based on the previously shown GPI and radial force balance results. Moreover, unless stated otherwise, $v_\perp$ represents measurements of the *local* turbulence velocity, whereas values of $v_\perp$ or E_r that are mapped to the OMP according to Eq. (3.9) are explicitly labeled as such. For most cases considered in this work, the flux expansion in the probed region does not differ substantially from that at the OMP ($f_x/f_{x,\mathrm{OMP}} \approx 1$), such that local and OMP-mapped values of $v_\perp$ (or E_r) are similar. This holds in particular for the scenarios shown in Fig. 3.15, or in Appendix A, for the radial force balance comparison to the DBS. In most of the remaining cases, the interpretation is unaffected by using local rather than OMP-mapped measurements, as the analysis isolates the influence of a single parameter while keeping the magnetic geometry between the probing location and the OMP fixed. However, in specific situations (Sec. 5.4), taking into account flux expansion has notable implications on the results and their interpretation.

3.8 Survey of the edge E_r in TCV

We conclude the present chapter with a brief phenomenological survey of the edge E_r profile in TCV, by investigating its sensitivities to density, auxiliary heating and helicity.

3.8.1 Density scan

We consider the evolution of $v_\perp$ across a density ramp performed in a pair of Ohmic discharges with comparable main parameters ($I_p \approx -170\,\mathrm{kA}$, $B_0 = -1.44\,\mathrm{T}$, $q_{95} \approx 3.8$–4.0, $B{\times}\nabla B$ pointing down), but different shapes: one limited, the other in diverted, upper single-null (USN) configuration.

In the limited case, Fig. 3.18a, the initially pronounced velocity well ($v_\perp \approx -4\,\mathrm{km/s}$) becomes shallower with increasing density, until it vanishes entirely at the highest density. At the same time, an opposite trend is observed with respect to the inner (core) region of

[13] In the presence of a non-zero mean tilt angle of the turbulent structures, the diagnostic response could be modified by 2D wave scattering effects depending on the probing direction relative to the structures tilt angle.

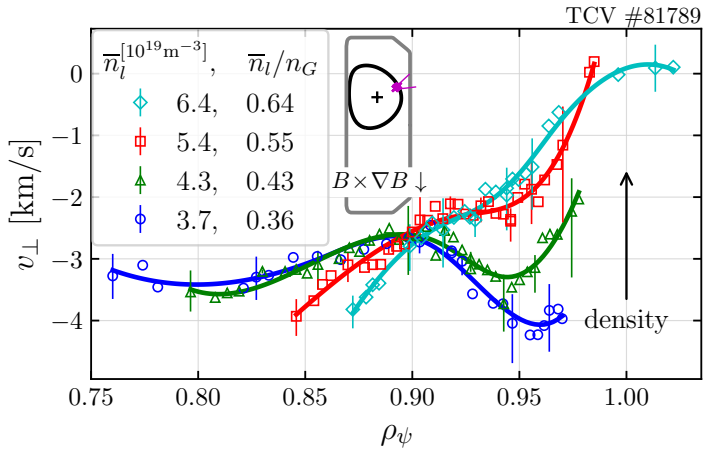

(a)

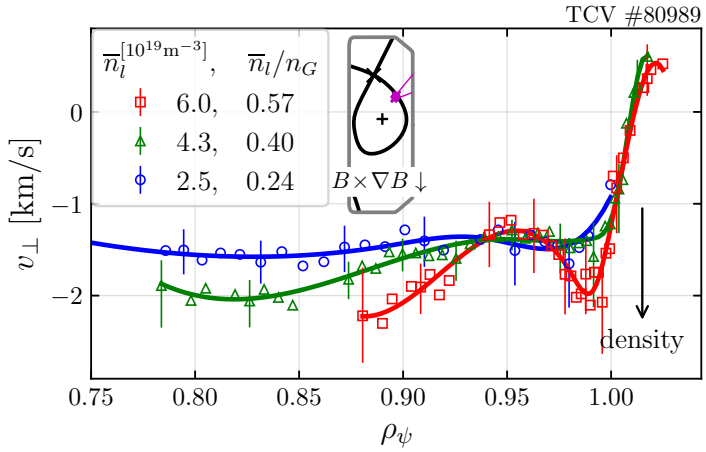

(b)

Figure 3.18: *(a) Density ramp in limited configuration: The well disappears with increasing density. (b) Density ramp in diverted configuration: The $v_\perp$ well becomes slightly more pronounced with increasing density. The line-averaged density $\overline{n}_l$ is indicated in the legend along with the Greenwald fraction $\overline{n}_l/n_G$.*

the profile: The velocity becomes more negative, which could be linked to a shift of the intrinsic toroidal velocity in the counter-current direction. Due to the lack of CXRS data for the limited discharge, this cannot be confirmed experimentally here, but it would be consistent with the reported trend of increasing counter-current rotation of the carbon impurity with density in limited Ohmic TCV discharges [196, 197].[14] By contrast, in the diverted case, Fig. 3.18b, the well only becomes clearly pronounced at the highest density[15], as emphasized also by the appearance of a velocity "hill" to the inner side of the well, around $\rho_\psi = 0.95$. This recurring *inner* hill feature, which appears also in other TCV L-mode scenarios, is particularly visible here at high density. It is reminiscent of a similar observation made on WEST for a comparable magnetic configuration (USN, unfavorable $B \times \nabla B$) [198]. The density is thus found to affect the E_r well structure in a qualitatively different way depending on the magnetic boundary condition and/or shape. In the core, however, the trend appears consistent between the limited and diverted case. A deepening of the E_r well with density has been documented in JET [199] and in AUG [122]. General conclusions on the density (or collisionality) dependence of E_r in TCV, however, require systematic investigations over a larger set of plasma conditions, including favorable $B \times \nabla B$ drift. This will be addressed in Sec. 4.4, within the study of the $B \times \nabla B$ drift effect.

3.8.2 Auxiliary heating scan

We proceed to investigate the impact of auxiliary heating on the E_r profile, starting with electron cyclotron resonance heating (ECRH), followed by neutral beam injection (NBI).

ECRH. We consider an USN, favorable $B \times \nabla B$ discharge with $I_p \approx 170\,\mathrm{kA}$, $B_0 = 1.44\,\mathrm{T}$, $q_{95} \approx 4.2$ and $\overline{n}_l = 2.2\text{–}2.9 \times 10^{19}\,\mathrm{m}^{-3}$. Stepped power increments are applied, using second-harmonic (X2) ECRH at 84 GHz, delivered by one gyrotron. According to linear raytracing performed with the TORAY-GA code [200], the power is deposited in the plasma center and completely absorbed within $\rho_\psi \lesssim 0.4$. Note that this requires relatively low plasma densities to prevent a reflection by the X2 cutoff.

The initial Ohmic phase and two subsequent steps of increasing ECRH power are examined over stationary time windows. The evolution of the $v_\perp$ profile is shown in Fig. 3.19, along with the kinetic profiles in Fig. 3.20.

The direct electron heating is evident from the increase in electron temperature (T_e) shown in Fig. 3.20 (b). Also the edge density increases with the ECRH power, Fig. 3.20 (a). This is accompanied by the formation of a pronounced L-mode pedestal and an increase of the line-averaged density by $< 30\,\%$ across the scan. By contrast, the $v_\perp$ profiles, Fig. 3.19, show little variation with P_{ECRH} inside the LCFS, neither in the well region nor deeper in the core. The ion impurity temperature measured by CXRS (c) does not display

[14] Note that the plasma current is well below the threshold ($I_p \approx 290\,\mathrm{kA}$) above which intrinsic rotation reversals (from counter- to co-current) are expected to occur when exceeding a certain density in this configuration [197].

[15] Although not entirely ruled out, a detachment under these discharge conditions seems unlikely, based on its absence during a comparable density ramp in LSN (#74400) with better diagnostics coverage. This interpretation aligns with the observed non-vanishing E_r peak in the SOL, indicative of attached divertor conditions [116].

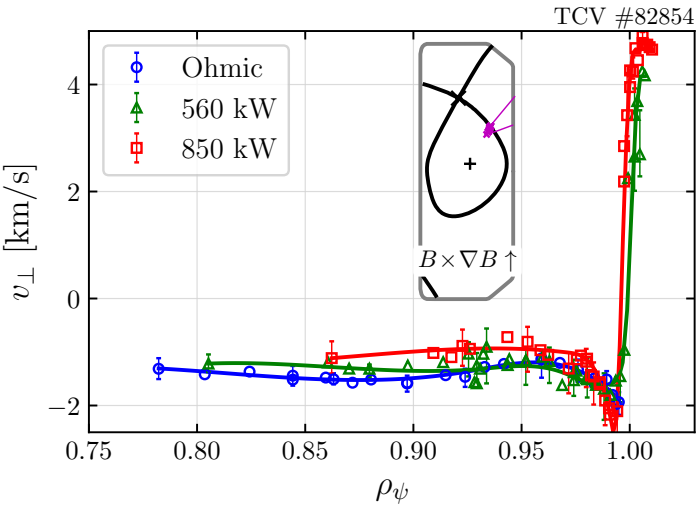

Figure 3.19: *ECRH power scan: The velocity profile shows little variation with increasing ECRH heating.*

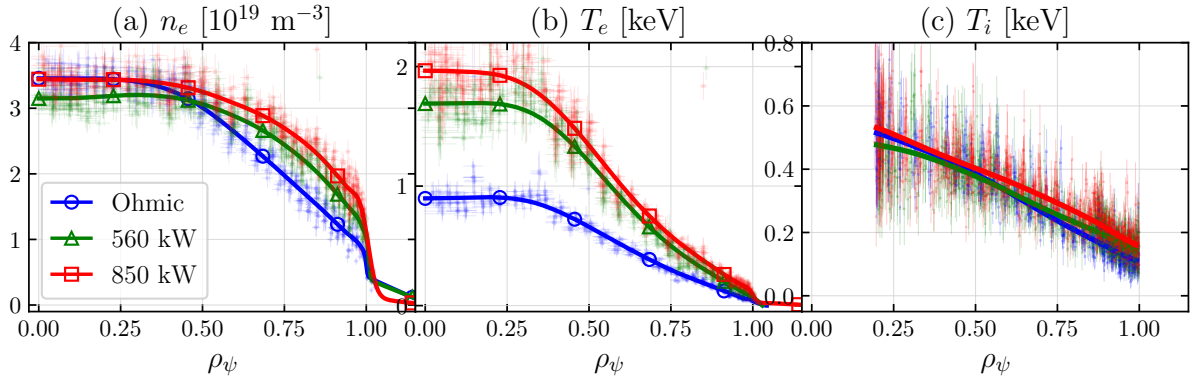

Figure 3.20: *(a) Electron density, (b) electron temperature and (c) carbon temperature profiles across the ECRH power scan. Curves represent fits to Thomson scattering (a,b) and CXRS (c) data, respectively.*

significant changes across the power scan. Only a mild increase by 30% or $\Delta T_{C^{6+}} \approx 50\,\text{eV}$ is found in the outer core region ($\rho_\psi \in [0.7, 0.9]$).

Finally, note that *outside* the LCFS, the velocity "hill" in the presence of ECRH is notably higher ($v_\perp > 4\,\text{km/s}$) than for instance in the green and red profiles shown in Fig. 3.18b ($v_\perp \lesssim 1\,\text{km/s}$), which correspond to a comparable equilibrium at higher density and without ECRH (hence cooler edge).[16] This is consistent with an increased T_e—and associated gradient—across the LCFS in the ECRH case, leading to higher E_r values in the near SOL according to the expected $E_r^{\text{SOL}} \sim -\nabla_r T_{e,\text{OMP}}/e$ scaling (see Sec. 2.7).

Next, the impact of NBI heating is investigated in both limited and diverted plasmas. The NBI-1 system is used (see Sec. 1.2.4) with beam injection in the co-current direction. In addition to the preferential ion heating, the toroidal torque associated with the NBI is expected to drive changes in E_r, since according to the ion radial force balance, Eq. (2.2), a co-I_p (counter-I_p) toroidal momentum increment tends to increase (reduce) E_r. Fig. 3.21 shows the evolution with stepped power increments, for (a) limited and (b) diverted L-mode discharges, respectively. Apart from the different magnetic configuration and shape, and a higher initial density ($\overline{n}_l = 3.3 \times 10^{19}\,\text{m}^{-3}$) in the limited compared to the diverted case ($2.5 \times 10^{19}\,\text{m}^{-3}$), the macroscopic plasma parameters are otherwise similar ($I_p = -170\,\text{kA}$, $B_0 = -1.44\,\text{T}$, $q_{95} \approx 4$).
In both cases, the core $v_\perp$ profile shifts upwards with increasing NBI power, and reverses the sign increasingly closer to the edge. This is qualitatively consistent with the expected E_r increment in response to the co-I_p torque, as discussed above. The first power step leads to a notable reduction in the magnitude of the E_r well compared to the Ohmic phase. The subsequent power increments do not lead to any further significant evolution of the well. The velocity *shear*, on the other hand, keeps increasing as the inner branch of the profile shifts upwards.
The overall density and that of the pedestal increase with the NBI power—especially in the diverted case, Fig. 3.21 (d). This could be due to a neutral beam fueling effect and/or increased particle confinement. Thus, there is inevitably some level of mixing between the effect of increased density and NBI power on the rotation and E_r. Systematic DBS measurements in dedicated *counter-I_p* NBI scans have not been performed yet. While the expected opposite trend ($v_\perp$ becomes more *negative* towards the core) has been observed for increasing counter-I_p torque, this is yet to be confirmed and documented over a broader range of discharge conditions and NBI powers.

3.8.3 Magnetic field helicity

The helicity sign, given by the relative sign between the plasma current (I_p) and toroidal magnetic field (B_0), determines the winding direction of the field lines around the torus. As will be explained, the interpretation of certain NBI experiments in this work relies on the assumption that both signs of the helicity are equivalent, as might be expected from a symmetry argument. However, possible symmetry-breaking effects, including those that might arise from diagnostic biases or plasma-wall interactions, cannot be excluded. Hence,

[16] The reduction in SOL E_r peak with reduced electron heating and/or increasing density is also evident from comparing the GPI data in Fig. 3.14a (B) and (C).

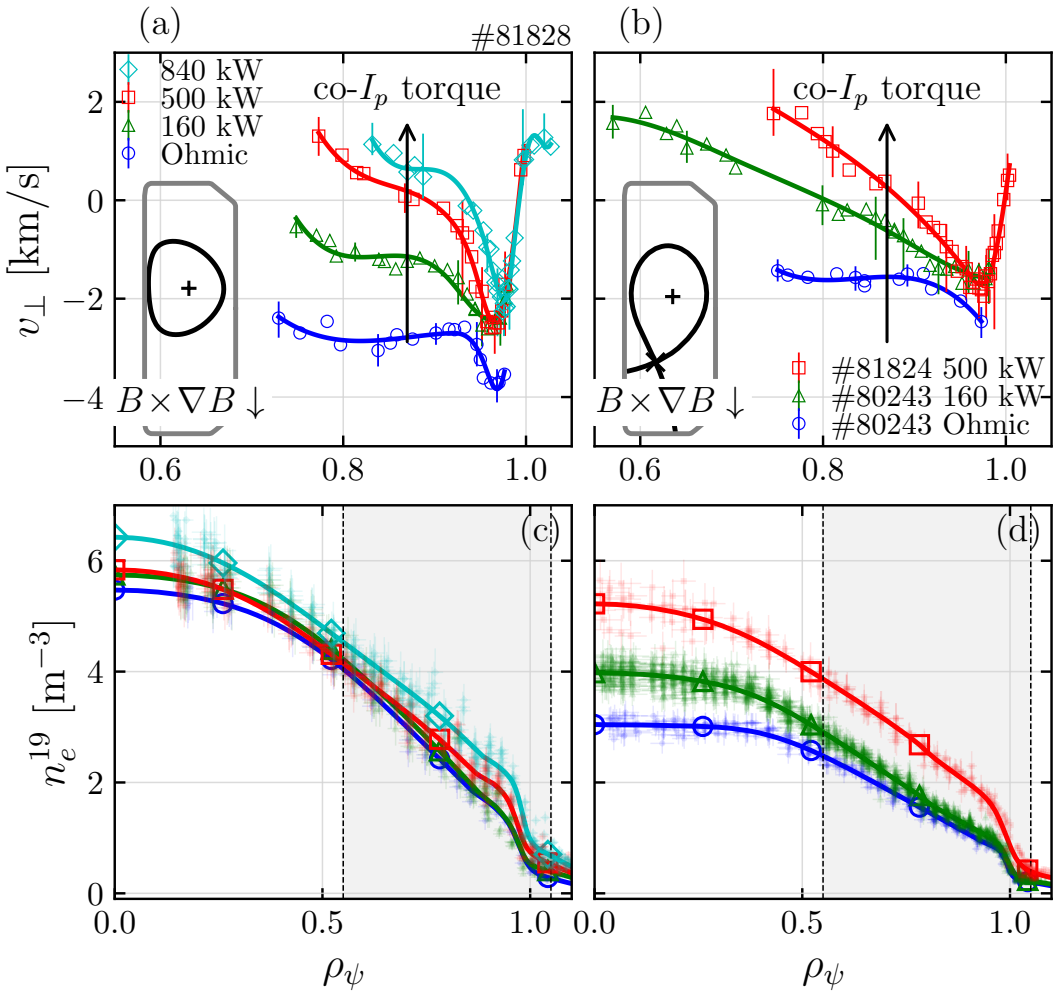

Figure 3.21: *Co-current injected NBI power steps in (a) inner wall limited and (b) diverted configuration, for otherwise comparable plasma conditions. (c) and (d) show the corresponding density profile fits, respectively. Note the different radial ranges displayed in the upper and lower graphs.*

we proceed with a verification of this assumption. We denote the case where $I_p B_0 > 0$ as the "right-handed" (R) helicity, and $I_p B_0 < 0$ as the "left-handed" (L) one.

We consider the four possible sign permutations of I_p and B_0 in an Ohmic scenario with fixed LSN shape. Fig. 3.22 shows the corresponding E_r measurements obtained from a quartet of matched discharges with $I_p = \pm 210\,\mathrm{kA}$ and $B_0 = \pm 1.44\,\mathrm{T}$.

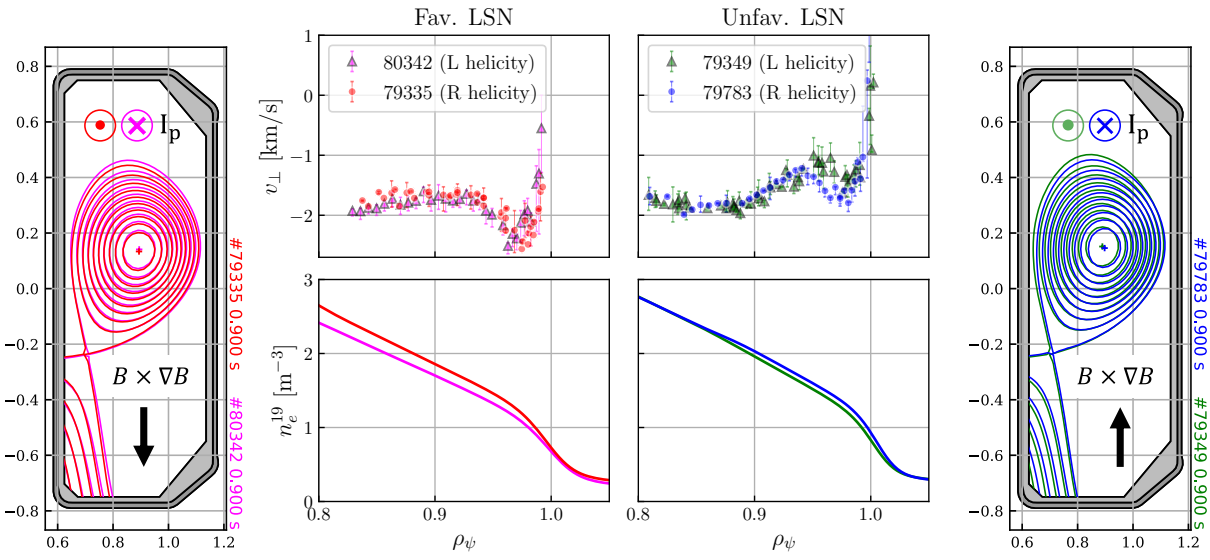

Figure 3.22: *B-field direction and helicity scan at $I_p = \pm 210\,\mathrm{kA}$ and $B_0 = \pm 1.44\,\mathrm{T}$: (a) and (c) Equilibrium reconstructions for the pairs with favorable (left) and unfavorable (right) $B\times\nabla B$ drifts, respectively. (b) Measured velocity profiles from DBS, showing good agreement between R and L helicities in a given $B\times\nabla B$ configuration.*

The difference between the favorable (left) and the unfavorable (right) $B\times\nabla B$ drift case will be investigated systematically in Chapter 4. Here, focusing only on the effect of flipping the helicity for a given drift configuration—whether favorable or unfavorable—no significant difference is observed in the $v_\perp$ profiles. The slight differences outside the errorbars in the reversed (unfavorable) $B\times\nabla B$ case could be due to an imperfect match in plasma conditions[17], or an actual effect related to the helicity reversal—albeit small. The relative insensitivity of the DBS profiles to the helicity sign were also confirmed in a similar comparison at $I_p = 150\,\mathrm{kA}$ and otherwise same conditions.

Although the equivalence of the two helicity signs may not be guaranteed in other plasma conditions, we conclude that for this particular scenario, the sign may be chosen freely. A practical implication for this work is that the favorable/unfavorable $B\times\nabla B$ configurations may thus be meaningfully compared under NBI heating (as will be done in Sec. 4.5), keeping the direction of I_p fixed to use the *same* neutral beam source—an important consideration given that the two neutral beams in TCV are not strictly comparable.

[17] The shapes do not exactly overlap between L and R helicity, and the core T_e in 79783 is lower by 10-15% compared to the remaining discharges. The core density, on the other hand, is well-matched between 79783 and 79349, while it differs by 10-15% in the favorable pair.

3.9 Chapter summary

Doppler backscattering, the principal diagnostic employed in this study, yields radial profiles of the turbulence $v_\perp$ velocity, which serves as a proxy for the mean $E_r \times B$ drift. We have presented the commissioning and features of a dual channel V-band DBS system on TCV. This enabled the first detailed edge E_r investigations on this device. It also forms the foundation for the systematic studies in chapters 4 and 5.

To probe the edge in TCV L-mode discharges, X-mode polarization is used, typically covering the region between the LCFS and $\rho_\psi \approx 0.7$–0.9. In standard operation, a 40-point profile of $v_\perp \approx E_r \times B$ is acquired every 100 ms. Digital demodulation—a distinguishing feature of this DBS system—allows for high accuracy measurements even in the case of small Doppler shifts. Cross-comparison between the DBS and GPI diagnostics shows good agreement, and the DBS-inferred level of E_r is found compatible with the one obtained from the impurity radial force balance. Yet, attempts to map local $v_\perp$ measurements from different poloidal beam orientations (upward versus downward probing) onto the outboard midplane remain partly inconclusive. Consequently, the probing beam is maintained in a downward tilt configuration throughout the subsequent studies.

The E_r profile in TCV L-mode plasmas was analyzed over scans in density, auxiliary heating, and magnetic field helicity. In diverted configuration, the velocity well just inside the LCFS typically attains $v_\perp \approx -2\,\mathrm{km/s}$ (corresponding to $E_r \approx -2.5\,\mathrm{kV/m}$), exhibiting moderate variation across these parameters. In a limited configuration, the velocity well is pronounced ($v_\perp \approx -4\,\mathrm{km/s}$) at low density and becomes notably shallower with increasing density. NBI consistently modifies the outer core E_r profile in both limited and diverted scenarios, in qualitative agreement with the expected positive E_r shift resulting from co-I_p toroidal torque. By contrast, electron cyclotron resonance heating (ECRH) induces only minimal changes in E_r inside the separatrix. Finally, the E_r well exhibits no substantial sensitivity to the sign of magnetic field helicity.

The influence of the $B \times \nabla B$ drift configuration and shaping was not addressed by this E_r survey, as they are the focus of the next two chapters, respectively.

Chapter 4

Sensitivity of E_r to Magnetic Drift Configuration

Contents

4.1 Review of FAV/UNFAV studies and proposed mechanisms **87**
4.2 FAV/UNFAV comparison in L-mode TCV discharges **92**
4.3 Influence of plasma current in WEST, TCV and AUG **100**
4.4 Density scans in TCV **113**
4.5 Power scans in TCV **117**
4.6 `GENE-X` simulations of TCV experiments **125**
4.7 Chapter summary and discussion **131**

Tokamak plasmas are known to respond sensitively to the configuration of the confining magnetic field. A particularly striking manifestation of this sensitivity (already introduced in Sec. 1.2) is the dependence of the L-H transition power threshold ($P_{\mathrm{L}\to\mathrm{H}}$) on the ion magnetic (or $B\times\nabla B$) drift direction: $P_{\mathrm{L}\to\mathrm{H}}$ is markedly lower when the $B\times\nabla B$ drift is directed towards the active X-point rather than away from it. The magnetic drift configurations[1] are therefore referred to as *favorable* (FAV) and *unfavorable* (UNFAV), respectively, reflecting how conducive each is to H-mode access.

To clarify the terminology, consider a diverted tokamak equilibrium with a lower (LSN) or upper single-null (USN) X-point divertor as illustrated in Fig. 4.1. The respective FAV

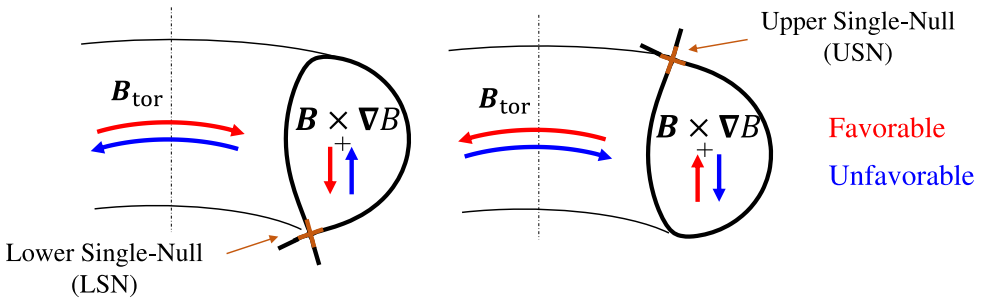

Figure 4.1: *Illustration of the favorable (FAV) and unfavorable (UNFAV) magnetic configurations in diverted (lower or uppper single-null) plasma shapes.*

[1] They are sometimes also called magnetic topologies, or X-point topologies as in [201]. Here, the term "configuration" is preferred over "topology" for clarity.

(UNFAV) drift cases are indicated in red (blue). The same color-code is used throughout this chapter. Switching the drift configuration may be achieved either by reversing the toroidal magnetic field (B_{tor}) direction or by flipping the X-point geometry between a LSN or USN. For a limiter configuration without magnetic X-point, the distinction between FAV and UNFAV drift does not apply (conventionally). However, as will be highlighted subsequently, some analogies exist between diverted and limited configurations with respect to their sensitivity to the $B\times\nabla B$ drift.

As mentioned earlier (Sec. 1.2), and elaborated in more detail in the next section, the FAV and UNFAV drift configurations differ not only in $P_{\mathrm{L}\to\mathrm{H}}$, but also in their respective E_r profile—with the FAV configuration exhibiting a deeper E_r well [46, 122, 137]. This discrepancy in E_r constitutes the main focus of this chapter.

Before turning to the results of this work, we summarize relevant past observations and corresponding interpretations of the FAV/UNFAV phenomenon. As will be elaborated, diverse candidate mechanisms for the sensitivity of $P_{\mathrm{L}\to\mathrm{H}}$ and/or E_r to the drift configuration have been suggested in the literature. They can be grouped into the following categories: edge or scrape-off layer (SOL) flows driven by cross-field transport [201–203], Reynolds stress associated with eddy tilting by magnetic shear [112, 113, 204], or collisional edge effects, specifically ion-orbit losses (IOL) [82, 90, 91]. Note that the concepts of IOL and magnetic-shear-induced Reynolds stress were introduced already in Chapter 2.

4.1 Review of FAV/UNFAV studies and proposed mechanisms

The dependence of $P_{\mathrm{L}\to\mathrm{H}}$ on the magnetic drift configuration was recognized soon after the discovery of the H-mode on ASDEX [205]. The observation was then confirmed on various other tokamaks, as documented in particular for DIII-D [206], Alcator C-Mod [207], ASDEX Upgrade [208] and EAST [209], highlighting the universal character of the phenomenon. Typically, $P_{\mathrm{L}\to\mathrm{H}}$ increases by a factor of 2–3 when $B\times\nabla B$ points away from the active X-point (UNFAV) rather than toward it (FAV).

In the Alcator C-Mod tokamak (C-Mod, for short), parallel flows in the SOL were observed to depend strongly on the drift configuration [201, 202, 210]. A poloidally asymmetric flow pattern was found; At the inner side of the SOL, the flow is directed towards the inner divertor, in both LSN and USN configurations (as sketched in Fig. 4.2). This implies an inboard SOL flow in the co- (counter-) direction in the case of a FAV (UNFAV) drift configuration. The origin of this flow pattern was attributed to ballooning-like cross-field transport—that is, enhanced turbulent transport from the outboard midplane (OMP) into the SOL—driving the flow along field lines toward the inboard side. These "transport-driven" SOL flows were interpreted as setting a boundary condition on the toroidal rotation of the confined plasma, acting in favor or against the L-H transition. Indeed, the direction of the inboard SOL flow correlated with a co- or counter-current offset in the core and edge ion toroidal velocity profiles [210], suggesting a coupling of the flows across the separatrix.

Further evidence for ballooning-like transport and the associated transport-driven SOL

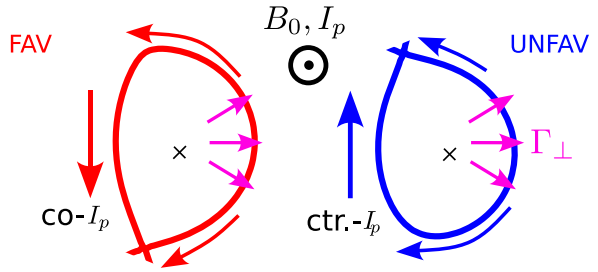

Figure 4.2: *Sketch of the transport-driven SOL flow mechanism proposed by LaBombard et al. [201, 202], inspired by [201, Fig. 3]; Ballooning-like transport (symbolized by $\Gamma_\perp$) from the OMP into the SOL drives a SOL flow along field lines towards the inner divertor leg. This flow is co-(counter-) current in the FAV (UNFAV) drift case.*

flows came from Tore Supra [211, 212] and other tokamaks [213]. Regarding the *coupling* of the SOL parallel dynamics with the toroidal edge rotation, indications from Tore Supra [212] were consistent with the hypothesis by LaBombard *et al.* [202], but no definitive confirmation followed. Likewise, a recent study on AUG found no clear dependence of the edge impurity toroidal rotation on drift configuration [122].

Sec. 2.8.2 already anticipated some historic observations of magnetic configuration influences on the edge E_r or turbulence velocity—they are briefly recalled here. In DIII-D, asymmetries in the edge turbulence flow characteristics were detected by BES [134, 135], pointing to a stronger turbulence velocity shear in matched FAV compared to UNFAV discharges. The DIII-D results also indicated a sensitivity of the E_r profile to the drift configuration [134]. This was subsequently confirmed in AUG [137] and MAST [125] (Fig. 2.13); In MAST, the L-mode E_r shear was found to be strongest in double-null (DN) shape, which on this spherical tokamak comes with facilitated H-mode access compared to FAV or UNFAV (single-null) configurations [125, 214]. In AUG [137], the E_r well was found to be weaker—if not absent—in the UNFAV configuration, which sets it apart from the FAV and DN case.

These early findings were underpinned by more recent and systematic edge E_r measurements in WEST [46] and AUG [115, 122]. The detailed studies established that the two conventional tokamaks share a clear and common dependence of the L-mode E_r well with respect to magnetic drift configuration. As exemplified by Fig. 4.3 (a-b), in both WEST and AUG L-mode discharge pairs, the E_r well is substantially shallower (or even absent) in the UNFAV case. The stronger edge $E_r \times B$ shear associated with the FAV E_r well strengthened the idea of a link with the faciliated H-mode access compared to the UNFAV drift case.

Another notable finding that emerged from the investigations on WEST is that the E_r well deepens sharply with increasing plasma current (I_p) in the UNFAV configuration, while in FAV the effect of I_p is less pronounced [46]. A similar trend was observed previously also on WEST's predecessor Tore Supra [212]. A detailed account of these results (see Fig. 4.12) will be given in Sec. 4.3.1. The remarkable response of E_r to I_p, and the fact that this sensitivity varies with the magnetic configuration, called for an experimental cross-device comparison with TCV and AUG that constitutes a main block of the present chapter (Sec. 4.3).

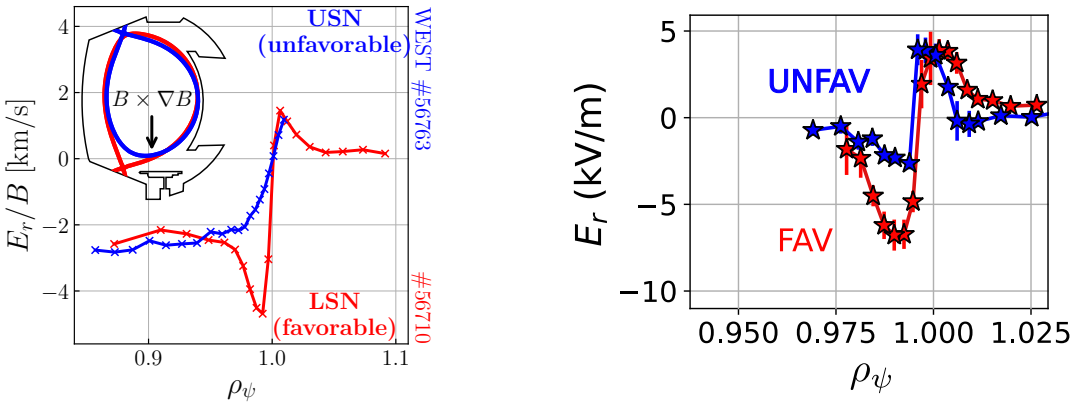

(a) **(b)**

Figure 4.3: *Comparison of the edge E_r profile between FAV and UNFAV, acquired via DBS in L-mode discharges in (a) WEST and (b) AUG—figure adapted from [115, Fig. 7.8].*

Further, the strong E_r sensitivity to I_p in Tore Supra/WEST gave rise to a comprehensive numerical study using the gyrokinetic `GYSELA` code [50, 215, 216]. The simulations self-consistently describe E_r with ITG turbulence and neoclassical effects in a limited, circular geometry with fixed $B \times \nabla B$ drift. This study provided an interpretation that relates the influence of I_p on E_r (through the edge safety factor) to the competition between neoclassical flow damping and turbulent flow drive. However, it does not offer an explanation for the E_r difference observed experimentally between the FAV and UNFAV configurations, or why they respond differently to I_p.

It is worth highlighting the analogy between WEST and Tore Supra observations concerning the edge E_r dependence on magnetic configuration. In the circular-shaped, *limited* Tore Supra plasmas, switching the limiter contact point from the bottom to the top of the device (Fig. 4.4) results in a shallower E_r well in the latter (with $B \times \nabla B$ pointing

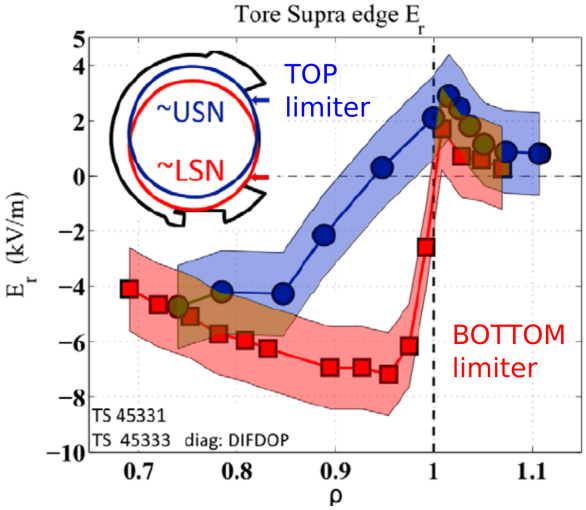

Figure 4.4: *E_r profiles measured by DBS on Tore Supra for bottom versus top limiter configuration, showing an analogous effect as the FAV/UNFAV difference in the diverted case of WEST or AUG. Figure adapted from [112].*

down) [112, 212]. This behavior is strikingly similar to the trend observed in diverted—and

therefore shaped—WEST discharges when changing between an USN and LSN geometry. As will be elaborated in Sec. 4.3.1, this suggests a certain universality of the underlying mechanism, which reaches beyond the conventional definition—that applies to single-null geometries—of "favorable" and "unfavorable" configurations.

In this context, a turbulence-driven (Reynolds stress) asymmetry was put forward by Fedorczak *et al.* [112, 113] to explain the E_r sensitivity to the drift configuration. The mechanism is based on the effect of eddy tilting by magnetic shear—previously introduced in Sec. 2.6, giving rise to a residual stress in an up-down asymmetric magnetic geometry. This "magnetic-shear-induced" Reynolds stress tends to reinforce or weaken mean $E_r \times B$ flow shear in the case of a FAV or UNFAV drift configuration, respectively.

A simplified model based on this theory found good quantitative agreement with experimental E_r profiles from Tore Supra [112], as well as an extended version—based on a fluid description of interchange turbulence—that was applied to WEST [217]. A self-consistent numerical study [218] based on a gyrofluid electromagnetic code recovered an effect on the Reynolds stress and E_r minimum in qualitative agreement with Tore Supra experiments and the model by Ref. [112][2]. The idea of Refs. [112, 113] was further pursued and incorporated in a heuristic model that recovers the $P_{\mathrm{L}\to\mathrm{H}}$ dependence with magnetic configuration in AUG [204]. The work by Grover *et al.* [204] recognized the importance of accounting for the poloidally dependent contribution from local magnetic shear to the average Reynolds stress[3].

The potential relevance of turbulent flow drive was reinforced by evidence from C-Mod: Ref. [220] reported stronger nonlinear energy transfer from turbulence to zonal flows in the FAV configuration.

A recent study [221] based on gyrokinetic edge turbulence simulations using the `GENE-X` code [222] offers a first-principles interpretation of the FAV/UNFAV asymmetry in a diverted AUG geometry. It strengthens the initial idea of Refs. [112, 113] of a predominantly turbulence-driven mechanism as the cause for the different E_r wells in FAV and UNFAV. Likewise, the key ingredient is a difference in the Reynolds stress drive, associated with the interplay between $E_r \times B$ flow and magnetic shear in an up-down asymmetric equilibrium. An analogous `GENE-X` study to the one in [221] has been carried out very recently for TCV instead of AUG plasmas, with preliminary results that will be presented in Sec. 4.6.

Other efforts to model the FAV/UNFAV asymmetry from first-principles were made using different codes. They include global electromagnetic gyro-fluid simulations with the

[2] The study in Ref. [218] models the impact of the poloidal limiter position for circular, Tore Supra-like plasmas. Although the simulations qualitatively capture its impact on the Reynolds stress and E_r, the magnitude of the effect appears weak except for limiter positions that are close to (but not exactly at) the OMP.

[3] In the initial formulation of Refs. [112, 113], a ballooning-like turbulence envelope centered around the OMP was assumed. The truncation of this poloidal envelope by the X-point provided the up-down symmetry breaking responsible for the residual magnetic shear stress. In contrast, a generalization of the effective tilt by magnetic shear was proposed in Ref. [204, Eq. 13]. This proxy was validated against fluid edge turbulence simulations using the GRILLIX code [219]. The generalized magnetic shear captures the Reynolds stress asymmetry in the simulations at the separatrix. The asymmetry is mainly attributed to a weaker local magnetic shear between the OMP and the active X-point, whereas the poloidal envelope of the fluctutations intensity—or its truncation around the X-point—is not found to be a key ingredient.

FELTOR code [223], which qualitatively recovered the E_r well asymmetry at the OMP [224]. Through analysis of a current conservation equation, the difference in E_r was attributed to a different parallel current balance at the edge, possibly affected by inward parallel transport from the SOL. However, the study also points out that the details of how SOL parallel dynamics influence the confined plasma edge remain unclear.

More recently, electromagnetic fluid simulations were performed also using the GBS code [225], as part of a numerical L-H transition study in simplified X-point geometry and for half the TCV plasma size [226]. The simulations point to a stronger resistive ballooning mode drive in UNFAV compared to FAV, owing to an $E_r \times B$ symmetry breaking effect [226]. This stronger turbulence drive is interpreted as hampering the steepening of the pressure profile observed in the UNFAV simulations as the heat source is increased; a higher power is therefore required in UNFAV to bring the heat diffusivity down to the FAV level.

Finally, ion-orbit losses (IOL) (see Sec. 2.4) are an alternative mechanism for the FAV/UNFAF asymmetry that is also discussed in the literature [82, 83, 91, 92]. The thermal IOL rate has been predicted to be stronger in favorable $B\times\nabla B$ configuration, as a result of shorter loss orbit path lengths [82, 83, 91, 227]. The path length differences translate into different effective collisionalities, and ion scattering rates out of their loss cones. A higher non-ambipolar IOL flux in FAV tends to reduce E_r, which could qualitatively explain the deeper E_r well. Yet, it remains unclear whether the magnitude of the IOL current and its sensitivity to $B\times\nabla B$ can quantitatively account for the experimental differences in E_r [227]. A preliminary application of the IOL model from [82, 83] on experimental conditions in Ohmic WEST discharges points to a weak IOL-driven current [50].

In summary, despite substantial experimental and theoretical investigations, a conclusive answer to the origin of the FAV/UNFAV asymmetry is still outstanding. The phenomenon remains an active research topic. There are timely efforts addressing the edge E_r discrepancy through advanced first-principles simulations. Expanding the experimental characterization of E_r in the two drift configurations is, therefore, of high interest. This work substantiates the available database for comparison with these simulations, particularly for TCV plasmas, which, so far, lack such a characterization.

The remainder of this chapter investigates the FAV/UNFAV asymmetry based on recent experiments performed primarily in TCV, and partly also in WEST and AUG; Sec. 4.2 compares E_r and other plasma quantities in representative FAV versus UNFAV discharges in TCV. The I_p sensitivity of E_r in both drift configurations is examined in Sec. 4.3. Here, we first revisit past results from Tore Supra and WEST and extend them with more recent WEST discharges. We then present the outcomes of similar studies on TCV and AUG. Subsequent sections focus again on TCV, where the FAV/UNFAV asymmetry is further characterized over density (Sec. 4.4) and auxiliary heating scans (Sec. 4.5). The comparison of TCV experiments to GENE-X simulations is presented in Sec. 4.6. A chapter summary is provided in Sec. 4.7.

4.2 FAV/UNFAV comparison in L-mode TCV discharges

As an introduction, this section provides an in-depth comparison of E_r and other edge properties for an example pair of L-mode FAV/UNFAV discharges in TCV—for the first time on this device. Along the way, observations from TCV are contrasted to AUG and WEST.

4.2.1 Discharge parameters and edge profiles

We consider a representative pair of lower single-null (LSN) Ohmic deuterium discharges with opposite $B\times\nabla B$ and I_p directions, but otherwise largely matched macroscopic parameters. The equilibria are shown in Fig. 4.5a. The main plasma parameters (listed in Tab. 4.1) fall within intermediate L-mode Ohmic operating conditions on TCV. The

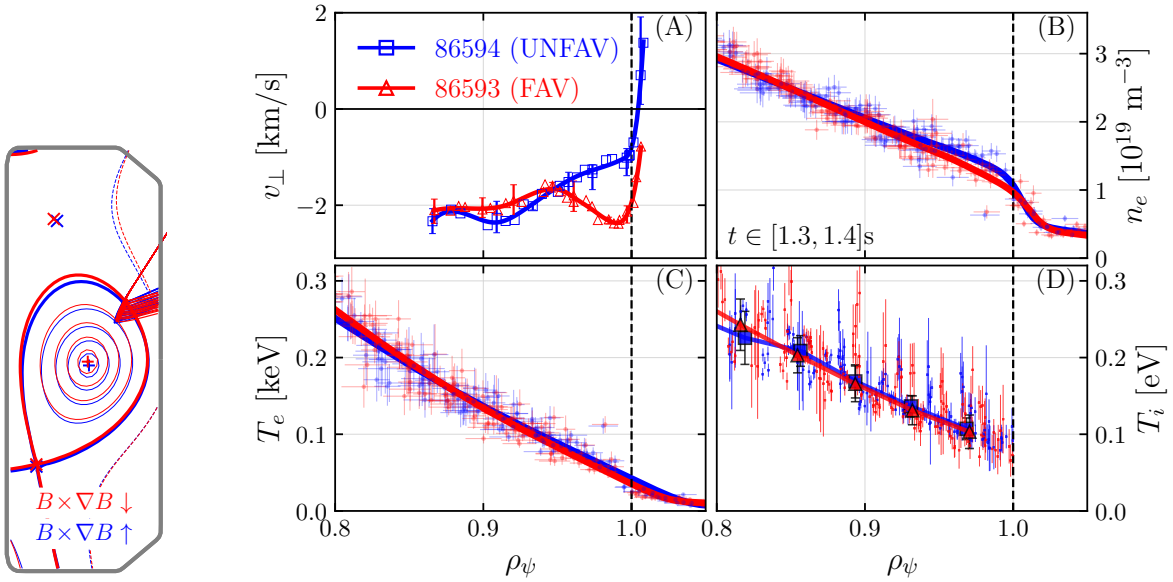

(a) **(b)**

Figure 4.5: *(a) Contours of ρ_ψ for a representative pair of matched LSN TCV discharges with opposite $B\times\nabla B$ drift. (b) Edge profiles acquired over a* 100 ms *time window: (A) Turbulence perpendicular velocity from DBS, (B) electron density and (C) electron temperature from TS, and (D) carbon temperature measured on the LFS by the CXRS (SYS 1,3 and 4). Fits are overlaid to guide the eye; for T_i, markers show the binned weighted average and standard deviation.*

edge $v_\perp$ profiles are displayed in Fig. 4.5b(A), along with the main kinetic profiles (B-D). Consistent with the trends reported on WEST [46] and AUG [122, 137], the E_r well (Fig. 4.5b-A) is clearly more pronounced in the FAV case. Meanwhile, the kinetic profiles are nearly identical, from the edge (B-D) up to the core (not shown). This is reflected by similar confinement levels; the (ion + electron) energy content W_{tot}, and the normalized beta β_N are matched to within 8% and 2%, respectively (Tab. 4.1). Note that the injected gas rate is higher by a factor of 1.6 in FAV, and the plasma volume (not listed in Tab. 4.1) by 2–3%. The turbulence wavenumbers probed by the DBS within the E_r well region,

drift	B_0 [T]	I_p [kA]	q_{95}	$\bar{n}_{l,19}$ [m^{-3}]	$\bar{n}_l/n_G$	W_{tot} [kJ]	β_N	gas [10^{21} p./s]
FAV	−+1.44	−+210	3.6	3.6	0.29	7.0	1.06	0.27
UNFAV						6.5	1.04	0.17

Table 4.1: *Main discharge parameters of the matched FAV/UNFAV Ohmic L-mode TCV discharges (Fig. 4.5b) compared in this section (Sec. 4.2).*

between $\rho_\psi = 1.0$–0.95, lie within $k_\perp \approx 6$–$8\,\mathrm{cm}^{-1}$, or $k_\perp \rho_s \approx 0.5$–$0.8$ (decreasing towards the separatrix). They are about 15% lower in UNFAV, owing to imperfectly matched flux surfaces (Fig. 4.5a).

An estimate of the deuterium diamagnetic contribution to the radial force balance Eq. (2.2), $(\nabla_r p_i)/(n_i e)$, is displayed as dashed lines in Fig. 4.5b alongside the DBS data ($v_\perp B$), both mapped the OMP. $(\nabla_r p_i)/(n_i e)$ is approximated using $n_e \approx n_i \equiv n$ and using the carbon

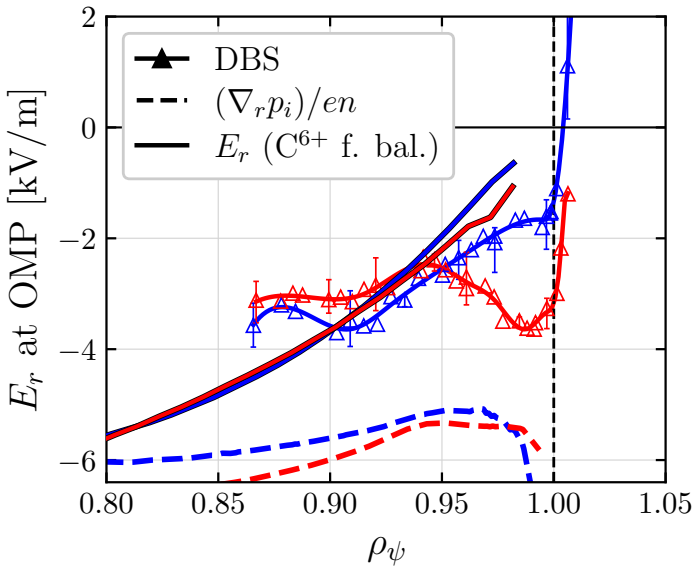

Figure 4.6: *Comparison of DBS measurements of $E_r = v_\perp B$ mapped to the OMP with the main ion diamagnetic contribution $(\nabla_r p_i)/(n_i e)$, and with the E_r profile derived from the C^{6+} radial force balance.*

temperature as a proxy for the deuterium temperature.

The $(\nabla_r p_i)/(ne)$ levels are similar for FAV and UNFAV—consistent with the matched edge kinetic profiles, and in line with AUG results [122]. Thus, the TCV results reinforce the findings from AUG [122], indicating that the E_r well asymmetry between FAV and UNFAV cannot be accounted for solely by differences in $(\nabla_r p_i)/(ne)$. That said, near the separatrix, the estimation of kinetic profile gradients is subject to large uncertainties, preventing a firm conclusion on the precise magnitude of $(\nabla_r p_i)/(ne)$, or how it compares between FAV and UNFAV.

In addition, the magnitude of $(\nabla_r p_i)/(ne)$ is significantly higher than the E_r level derived from the DBS measurements. The fact that the diamagnetic contribution to E_r alone cannot generally account for the L-mode E_r profile has been reported on AUG as well [122],

indicating non-negligible contributions from poloidal and/or toroidal rotation to the radial force balance, thereby questioning the neoclassical "approximation" $E_r \approx (\nabla_r p_i)/(n_i e)$.

For completeness, Fig. 4.6 also includes the E_r profile estimated from the impurity radial force balance, following the procedure described in Sec. 3.6. Up to $\rho_\psi \approx 0.95$, it shows good quantitative agreement with the DBS data and is nearly identical between FAV and UNFAV profiles. As established in Sec. 3.6, the C^{6+} force balance result is not considered reliable towards the very edge. In the following, we therefore restrict the analysis of radial force balance results mainly to the outer core region, and up to $\rho_\psi \approx 0.95$.

4.2.2 Toroidal rotation

We proceed to a comparison of the impurity toroidal rotation measured by CXRS. The poloidal rotation is not analyzed in this study due to a lack of reliable measurements (see Sec. 3.6). Since direct measurements of the main ion (deuterium) rotation are unavailable, only the C^{6+} toroidal velocity (V_φ) is considered here, and the carbon species index is dropped as there is no risk of confusion with deuterium.

The profiles of V_φ acquired during same time window as the edge profiles in Fig. 4.5b, are displayed in Fig. 4.7 (a,b) along the IMP and OMP, respectively. Towards the core,

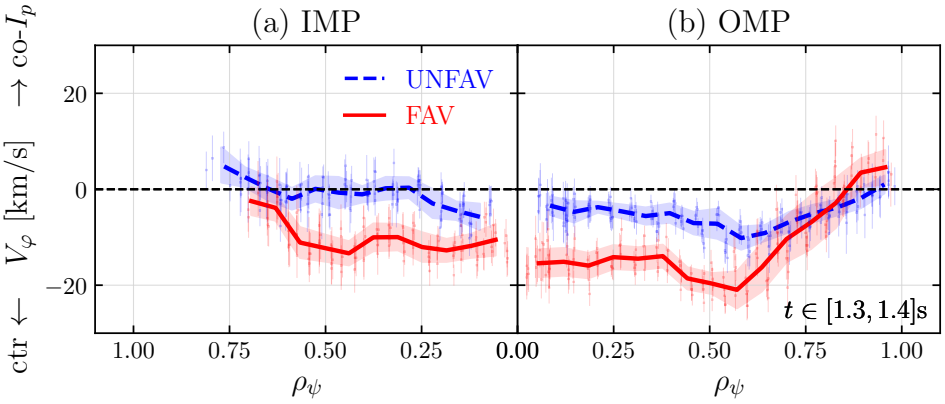

Figure 4.7: *Carbon toroidal rotation along the (a) inboard and (b) outboard midplanes. Positive values correspond to co-current rotation. Lines and errorbands represent the mean and standard deviation, respectively, from a binned weighted average through the data points.*

V_φ tends to be counter-current, with a stronger magnitude in FAV. At the IMP, the edge region is not covered by the CXRS data, probably due to stronger DNBI attenuation. On the other hand, at the OMP, the outer core and edge V_φ is close to zero in both discharges.

It should be noted, however, that the presented CXRS measurements have high relative uncertainties towards the edge. Together with limited spatial resolution, a possible, fine-scale corrugation of V_φ near the separatrix may currently not be detectable.

It is instructive to inspect V_φ during an earlier, lower density phase ($\overline{n}_l \approx 2.7 \times 10^{19}\,\mathrm{m}^{-3}$) of the same discharges (still nearly matched), as shown in Fig. 4.8. In this case, the FAV and UNFAV toroidal rotations are nearly aligned within error bars across the entire accessible region, both in the core and the edge. At the same time, the difference in the

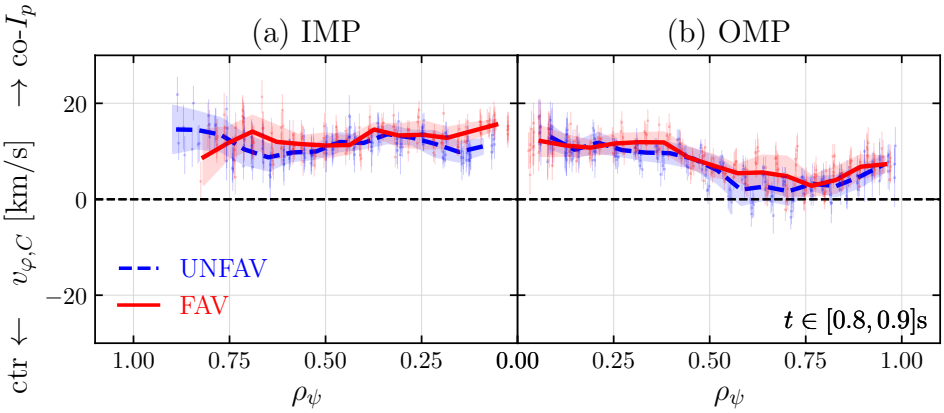

Figure 4.8: *Same represantation as in Fig. 4.7, showing the data collected during a lower density phase of the same (matched) discharges. In this case, the toroidal rotation profiles are nearly matched.*

E_r profiles—not shown here, but in Fig. 4.16 b from a later section—remains similar to what is presented in Fig. 4.5.

More broadly, beyond the present scenario no systematic offset in V_φ is observed (outside of statistical uncertainties) between Ohmic FAV and UNFAV discharges at the edge. Meanwhile, depending on plasma conditions such as density and current, the *core* toroidal rotation may show significant discrepancies—even opposite signs—between FAV and UNFAV. This behavior might be linked to intrinsic rotation reversal [196], but it does not seem to affect the E_r well asymmetry. Combined with the weak correlation—already noted in Ref. [197]—between core and edge toroidal impurity rotation in TCV, this appears to indicate different momentum driving mechanisms in the core and at the edge.

4.2.3 Density fluctuation properties

As noted in Sec. 3.1.4, besides $v_\perp$, the DBS data can also provide complementary information on other turbulence properties, such as the density fluctuations intensity ($\tilde{n}$).

As a qualitative proxy for $\tilde{n}(k_\perp)$, the power spectral density (PSD) of the complex DBS signals is compared between the FAV and UNFAV discharges of Fig. 4.5b. Note that this proxy, computed as the integral over the Doppler peak, can only provide a relative measure (between discharges) around a common radial location ρ_ψ, scattering wavenumber $k_\perp$ and probing frequency. It cannot be used to compare $\tilde{n}(k_\perp)$ across different radial locations of a given discharge. The latter would require a relative calibration across different probing frequencies, not attempted in this work. Furthermore, the discharges must have nearly identical edge density profiles, and—to ensure a comparable diagnostic response—the DBS probing geometry must be identical (launcher settings, plasma shapes, and magnetic helicities).

An example PSD corresponding to $\rho_\psi \approx 0.98$—around the minimum of the E_r well—is shown in Fig. 4.9(a). Besides the stronger Doppler shift in FAV (reflecting the stronger $E_r \times B$ velocity in the well), the peak is also higher and broader compared to UNFAV. The integral over the Doppler peak, which reflects the backscattered power (as the proxy

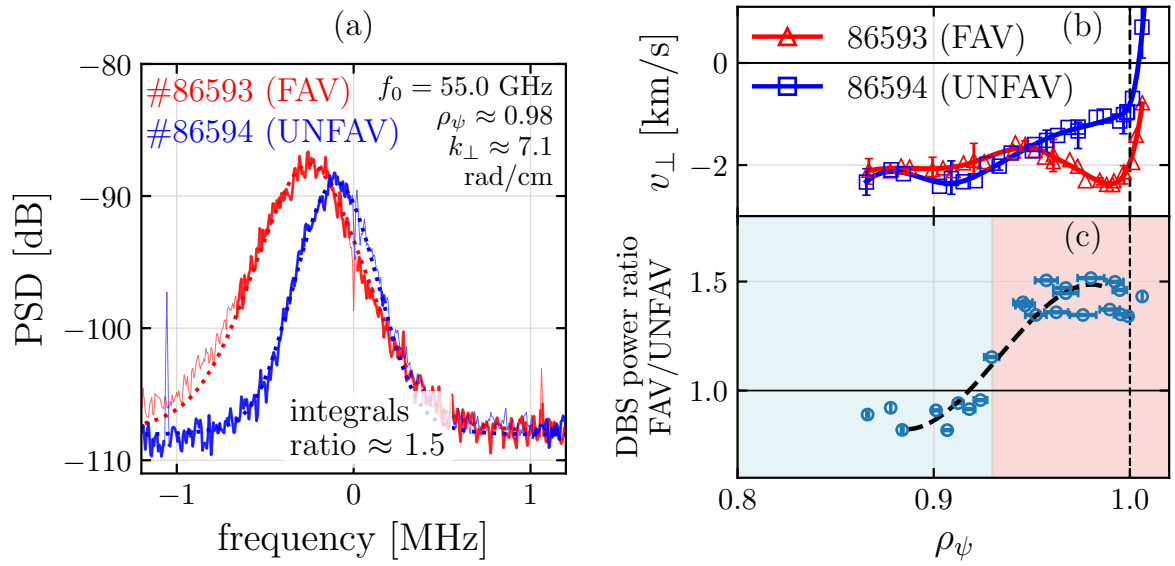

Figure 4.9: *(a) DBS power spectral density (PSD) compared between FAV and UNFAV in the minimum of the E_r well. The higher integrated power in FAV suggests a stronger density fluctuation level $|\tilde{n}(k_\perp)|$.*

for $\sim |\tilde{n}(k_\perp)|^2$), is higher by a factor of about 1.5 in the FAV case. The ratio of these integrals is computed for each common probing frequency, and shown in Fig. 4.9(c). The trend persists across the region of the E_r well, and appears to reverse further inward. This seems to suggest higher density fluctuation levels in FAV near the separatrix and within a range of $k_\perp \rho_s \sim 0.5$–0.8. At the same time, the edge $E_r \times B$ shear is stronger by the deeper well in FAV.

As noted before, due to imperfectly matched shapes, $k_\perp$ is slightly lower (15 %) in UNFAV. As the turbulence power—within this $k_\perp$ range—is known to decrease with $k_\perp$[146], the offset in $k_\perp$ cannot qualitatively explain the DBS power difference between FAV and UNFAV. This reasoning is supported by another comparison (USN, 250 kA, not shown) where $k_\perp$ is instead higher in UNFAV than FAV. There, the difference in DBS power persists qualitatively as in Fig. 4.9, and is even enhanced. This is consistent with the dependence of turbulence level on $k_\perp$, adding to the effect of the drift configuration.

Parallel with Tore Supra observations.

Tore Supra experiments also found that the DBS signal power depends on magnetic configuration. This is illustrated in Fig. 4.10 for a pair of matched Ohmic discharges ($B_0 = -3.53$ T, $I_p = -1.0$ MA, $q_{95} \approx 3.3$, from Ref. [212]) with different limiter contact points (bottom versus top). As previously mentioned in Sec. 4.1, the limiter position in Tore Supra has a similar effect on the E_r well as the X-point location in diverted plasmas. This difference is also observed in the pair of Tore Supra discharges considered here, where the E_r well is more pronounced in the bottom limiter case—in analogy to a LSN, with $B \times \nabla B$ pointing down.

Fig. 4.10b compares the PSD of DBS signals acquired with X-mode polarization, originating from the well minimum at a fixed radius $r/a \approx 0.96$, wavenumber $k_\perp \approx 10\,\mathrm{cm}^{-1}$ and

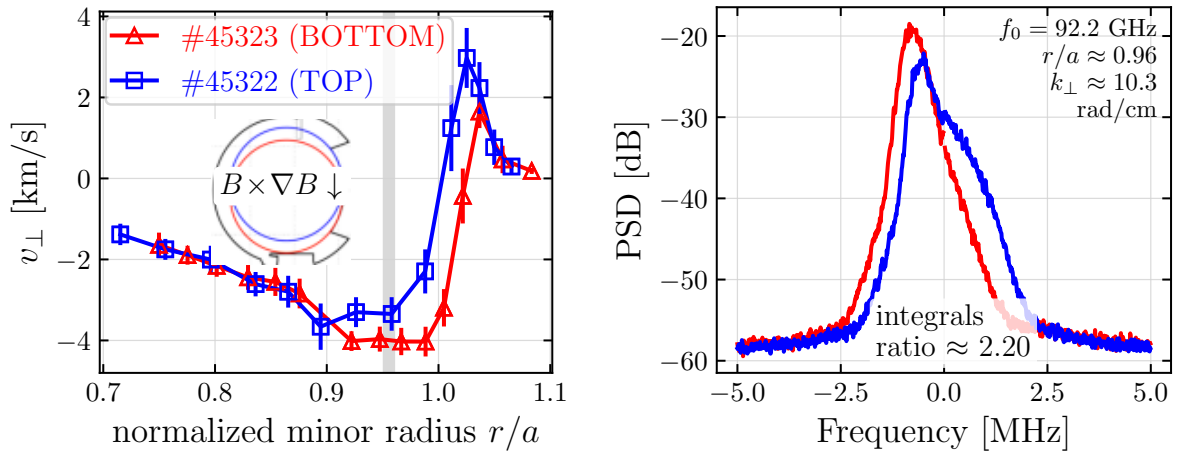

Figure 4.10: *Similar comparison of the DBS signal amplitude as in Fig. 4.9, for a pair of Ohmic Tore Supra discharges; (a) $v_\perp$ profiles (a) PSDs of the DBS signals collected around the E_r well minimum—indicated the grey vertical line in (a).*

probing frequency f_0. In line with TCV, the Tore Supra configuration with the deeper well (bottom limiter, similar to a FAV drift topology) exhibits a higher DBS power. The difference—over a factor of two—is relatively pronounced[4].

Whether this trend also persists in WEST or AUG discharges is a question left for future work.

4.2.4 Oscillations of the $E_r \times B$ flow

As outlined in Sec. 3.2.2, the MUSIC algorithm provides pseudo-spectra from which the *instantaneous* Doppler shift can be obtained from the DBS signal. This approach enables quantitative analysis of the dynamical behavior of $\tilde{v}_\perp(t)$. Fluctuations of the $E_r \times B$ flow, particularly those associated with GAMs, are thus accessible. The latter may yield further insights into the interplay between mean and oscillatory flow shear and turbulence.

The DBS signals of the considered TCV discharges display a coherent mode feature around 20–25 kHz. This is presumably a signature of the GAM, as it matches the typical frequency expected in TCV. Confirmation of the mode's nature is left for future work. Here, we will refer to it as the "GAM-like" mode and compare its behavior between the FAV and UNFAV configurations.

A different pair of discharges is used here than in Fig. 4.5. These discharges are identical to the reference scenarios of Fig. 4.5b, except for being stationary and with a slightly lower density ($\overline{n}_l \approx 3.2 \times 10^{19}$ instead of $3.6 \times 10^{19}\,\mathrm{m}^{-3}$). These stationary conditions,

[4] Note that these discharges have a relatively high plasma current. As will be seen in Sec. 4.3.1, this tends to reduce the $v_\perp$ asymmetry between bottom and top limiter. Unfortunately, a similar comparison at matched $k_\perp$ is not available in Tore Supra discharges with lower I_p—where $v_\perp$ differs more strongly between the two configurations. It therefore remains unclear how the difference in DBS power would extend to Tore Supra discharges in which the E_r wells differ more notably.

combined with longer DBS frequency patterns, provide more data points and therefore better statistics. The observations, however, remain qualitatively consistent in both cases.

Fig. 4.11 (a) shows the PSD of the MUSIC-derived $v_\perp(t)$ for an example common probing frequency and radial location ($\rho_\psi \approx 0.96$)[5]. The peak in the PSD around 22 kHz,

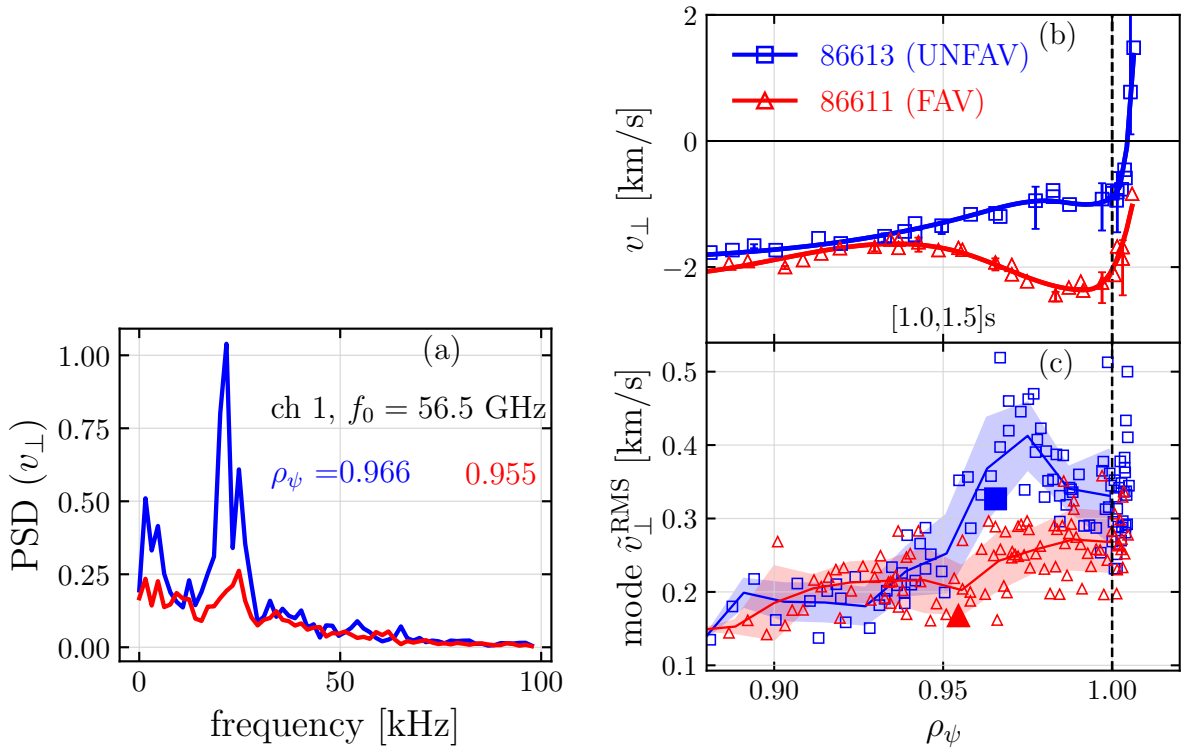

Figure 4.11: *(a) Power spectral density (PSD) of the instantaneous $v_\perp(t)$ at radial locations close to the well minimum, (b) mean $v_\perp$ profiles, and (c) amplitude of the GAM-like mode around* 20–25 kHz*. Large filled symbols indicate the measurement locations corresponding to the PSDs in (a).*

attributed to the aforementioned coherent mode, is more prominent in the UNFAV case.

Integrating the PSD around the peak—within the frequency interval 22–25 kHz—and taking the square root provides a proxy for its amplitude, $\tilde{v}_\perp^{\mathrm{RMS}}$, associated with the $E_r \times B$ oscillations. The radial profile of $\tilde{v}_\perp^{\mathrm{RMS}}$ is displayed in Fig. 4.11 c. It is shown alongside the mean flow profile (Fig. 4.11 b). In the region of the inner-side E_r shear layer, between $\rho_\psi \approx 0.95$ and 0.98, the mode amplitude is higher in UNFAV than in FAV—by an offset of 100–200 m/s that is significant compared to the statistical spread[6]. This region also corresponds to reduced DBS power in UNFAV, as observed for the reference discharges (Fig. 4.9 (a)) and confirmed in the present ones.

[5] The MUSIC algorithm is applied on windows of $n_{\mathrm{ws}} = 128$ points with 50% overlap, using an autocorrelation matrix of size 4 and an expected number of frequencies to detect $n_f = 1$, see Ref. [168] for a discussion of the choice of these parameters.

[6] While the oscillation amplitude in Fig. 4.11 (c) is given in km/s, the absolute value should be used with caution, as it may vary depending on the details of the data analysis. However, the relative comparison using the same analysis parameters is robust.

It should be noted that the DBS probing frequency pattern used in these discharges (5 ms steps) is not optimized for dynamical analysis. Such analysis typically benefits from longer steps for higher statistics. A systematic characterization of the GAM-like mode is beyond the present scope. However, ongoing studies [228] indicate that the mode amplitude correlates to some degree with the E_r well depth. When the mean $E_r \times B$ flow is weaker in the well region, its GAM-like oscillations appear to be enhanced—a trend that seems to hold beyond the present comparison of FAV and UNFAV discharges.

4.2.5 Discussion

This concludes the in-depth comparison of FAV versus UNFAV in a fixed TCV scenario. We summarize the main observations so far and provide some discussion points before proceeding to other characterizations.

The presented TCV data show that the E_r well is deeper in FAV than UNFAV—in line with WEST [46] and AUG [122, 137]. The simultaneous observation of similar edge kinetic profiles at different edge $E_r \times B$ shear is noteworthy (Fig. 4.5b); This behavior seems at odds with a neoclassical description of E_r in TCV, according to either Eq. (2.7) or Eq. (2.9). This is consistent with the observations and interpretations of comparable L-mode AUG experiments [122]. It might also appear surprising; If stronger $E_r \times B$ shear reduces turbulent transport, why are edge kinetic profiles and global confinement so similar for FAV and UNFAV? A higher fueling rate in UNFAV cannot explain this, since fueling is actually higher in the FAV case of Fig. 4.5, which might instead indicate *lower* particle confinement in FAV. One possible explanation is that in these Ohmic L-mode conditions—far from any critical $E_r \times B$ shearing rate associated with the L-H transition—the E_r shear difference between FAV and UNFAV may simply not be sufficient to affect edge transport in a notable way.

The TCV data show no systematic influence of the drift configuration on the carbon edge or core toroidal rotation (Fig. 4.8). This contrasts with the Alcator C-Mod results [201, 202, 210] mentioned earlier (see Sec. 4.1), but agrees with the findings from AUG [122]. Although direct measurements of SOL parallel flows are presently not available in TCV, a previous study [229] reported co-current flows at the LFS of comparable magnitude in both drift configurations, indicative of a dominant field-dependent drive consistent with the neoclassical Pfirsch-Schlüter (PS) return flow. An indirect assessment on AUG [122], based on the edge V_φ behavior, points to the same conclusion. Taken together, the results from TCV and AUG therefore do not support the interpretation of the FAV/UNFAV asymmetry proposed by LaBombard *et al.* [202] in terms different edge toroidal rotation boundary conditions caused by parallel SOL flows (see Sec. 4.1).

The higher DBS power level observed in FAV (Fig. 4.9) might indicate that the enhanced edge flow shear is partly compensated by a stronger turbulence intensity. At the same time, higher fluctuation levels may also reflect a higher turbulent Reynolds stress drive, but in the absence of measurements of this stress, this remains highly speculative. Moreover, a possible reduction in turbulence levels in UNFAV remains to be confirmed by complementary edge fluctuation diagnostics. A preliminary analysis of midplane-GPI fluctuation levels (not shown) did not reveal notable differences in relative fluctuation levels between FAV and UNFAV in the well. Note also that the DBS data provide poloidally

localized measurements, which may not reflect the turbulence level at the OMP, nor its average on a given flux surface, or the associated cross-field transport. In fact, the FELTOR simulations [224] mentioned in Sec. 4.1 predict a complex and drift-dependent poloidal distribution of edge density fluctuations, with the intensity being more poloidally concentrated in FAV and locally exceeding that in UNFAV. Furthermore, the DBS signals correspond to a selected (ion-scale) $k_\perp$ range, while the full $k_\perp$ spectrum determines the overall turbulent intensity and transport.

Finally, the interpretation of the stronger GAM-like mode activity observed in the UNFAV drift configuration (Fig. 4.11) is not straightforward. The role of GAMs in turbulence regulation can be (at least) twofold: their oscillating flow shear may either contribute to turbulence reduction, or, conversely, GAMs may hinder it by competing with mean or low-frequency zonal flows for turbulence energy. As pointed out in [215, § 5.4.2], stationary $E_r \times B$ shear is likely more efficient at decorrelating eddies. It is worth noting that the experimental trend shares analogies with the observations in C-Mod [220]; There, GAMs are detected only in the so-called "I-mode", a regime that is almost exclusively associated with the UNFAV drift configuration.

Subsequently, we further examine the FAV/UNFAV asymmetry as a function of different parameters (plasma current, density and auxiliary heating). The next section focuses on the influence of I_p, drawing also on WEST and AUG experiments to complement and compare with the TCV data.

4.3 Influence of plasma current in WEST, TCV and AUG

As mentioned at the beginning of the chapter (Sec. 4.1), past studies on WEST [46] and Tore Supra [212] have shown that plasma current (I_p) can strongly influence the E_r well in Ohmic L-mode discharges, with a sensitivity depending on the magnetic configuration. The findings are reviewed below (Sec. 4.3.1) and complemented with more recent WEST experiments (Sec. 4.3.2 and 4.3.3). They have motivated analogous experiments on TCV and AUG, presented in Sec. 4.3.4 and 4.3.5.

4.3.1 Review of I_p scans in WEST and Tore Supra

An overview of the aforementioned findings from WEST [46] and Tore Supra [212] is compiled in Fig. 4.12 (a) and (b), respectively. The $v_\perp$ data were obtained with an older version of WEST's current DBS setup. This version supported only a limited number of profile acquisitions during discharges. The profiles in Fig. 4.12 are from selected trigger times during linear I_p ramps in Ohmic L-mode discharges.

As indicated by the insets in Fig. 4.12, the left and right columns compare the different magnetic configurations: (a) LSN/USN diverted shapes in WEST and (b) bottom/top limited in Tore Supra. In both devices, $B \times \nabla B$ is fixed and pointing down, so that a LSN (USN) shape always corresponds to a FAV (UNFAV) drift direction. As previously noted (see Figs. 4.4 and 4.10a), the E_r well displays an analogous response in WEST and Tore

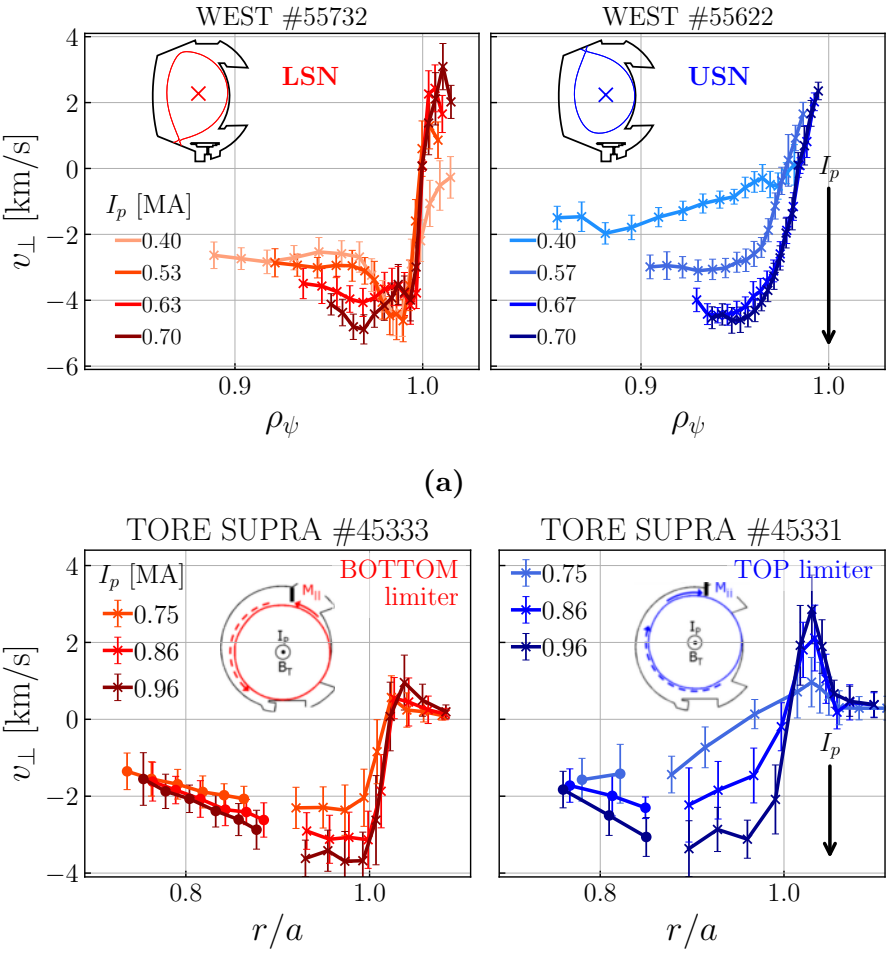

Figure 4.12: *Summary of the results of I_p scans in Ohmic L-mode discharges in (a) WEST [46] and (b) Tore Supra [212]. Left and right columns compare different magnetic configurations, with $B\times\nabla B$ pointing down. The $v_\perp$ well depth varies sharply with I_p in USN (UNFAV) configuration for WEST (a), or analogously in the top limited case for Tore Supra (b).*

Supra with respect to the poloidal location of, respectively, the X-point or the limiter contact point.

Fig. 4.12 highlights the analogy between the two devices, now also with respect to the impact of I_p. $v_\perp$ shows a pronounced sensitivity to I_p. The effect is clear and systematic in USN (UNFAV) configuration in WEST[46], or in the top limited configuration in case of Tore Supra [212]; The depth of the well increases sharply with I_p, evolving from a relatively flat well at low I_p to a deeper one at high I_p that is comparable to their LSN (FAV) or bottom limited counterparts.

The consistent trends between circular, limited Tore Supra, and diverted, shaped WEST discharges suggest some generality in the effect of magnetic configuration on E_r; It does not seem tied only to a diverted or shaped geometry. In other terms, the X-point does not appear essential to cause the FAV/UNFAV difference in E_r. Instead, it seems replaceable, to some extent, by the up-down symmetry breaking of the magnetic geometry associated

with the presence of a limiter.

This remarkable response of E_r to I_p, enhanced in UNFAV (or top limited) magnetic configuration, motivated a more careful investigation through further experiments in WEST, to which we now turn.

4.3.2 Confirmation of WEST trend in stationary conditions

A caveat of the Tore Supra and WEST results just presented (Fig. 4.12) is that the E_r data was collected over non-stationary I_p ramps. Despite density feedback control, the overall density increased along these I_p ramps, complicating the interpretation of the results since the effects of increased density and I_p could potentially mix. Follow-up experiments were therefore performed in WEST under stationary conditions to better isolate the influence of I_p and assess the robustness of the trend observed in E_r.

Fig. 4.13 assembles the DBS measurements in a shot-to-shot scan of I_p, again comparing LSN (FAV) and USN (UNFAV) configurations in the left and right columns, respectively. In these discharges, the on-axis magnetic field is $B_0 \approx -3.7\,\mathrm{T}$ (slightly lower magnitude

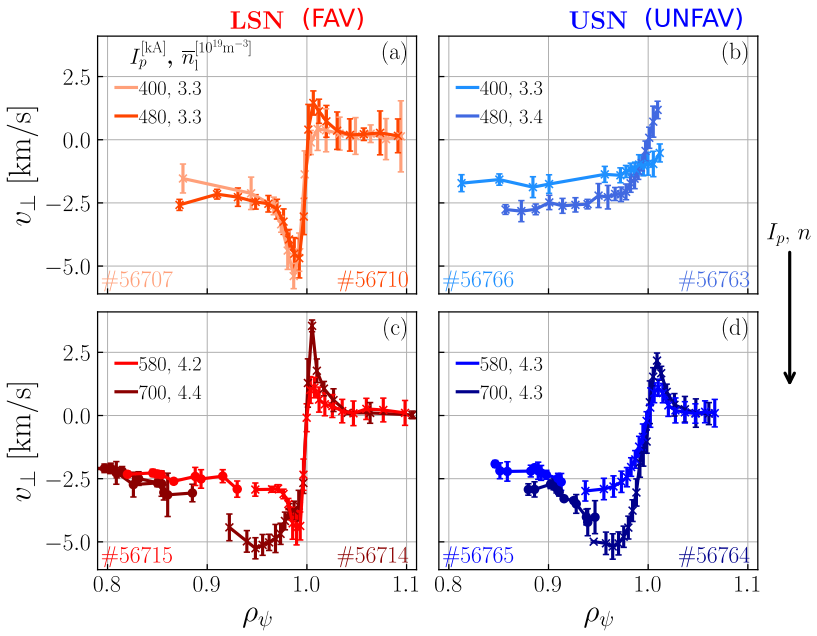

Figure 4.13: *Ohmic I_p scan in WEST, similar to the one in Fig. 4.12a, but now with a stationary I_p, varied from shot to shot. The I_p and line-averaged density values are annotated; the first (second) row corresponds to the lower (upper) pairs of I_p values, with a higher density in the latter.*

in USN). The I_p range covered by the scan is similar to the previous I_p ramps, comprising four values, $I_p = 400, 480, 580$ and $700\,\mathrm{kA}$. Instead of keeping the density fixed over the entire I_p range—likely not feasible in practice, a good pairwise match was achieved separately between the lower two (Fig. 4.13 a,b) and the upper two I_p values (Fig. 4.13 c,d). In the latter, the line averaged density—annotated in Fig. 4.13—is 20-30% higher.

The qualitative response of $v_\perp$ to I_p in the two drift cases agrees with the previous find-

ings; From 400 to 480 kA, no substantial change is seen in LSN (Fig. 4.13 a), whereas in USN the initially flat $v_\perp$ profile steepens notably near separatrix, reducing the edge $v_\perp$ level (Fig. 4.13 b). The observation holds also for the higher I_p and higher density pair, Fig. 4.13 (c-d): The well depth remains roughly at $v_\perp^{\min} \approx -5$ km/s in LSN, although a notable change occurs in the E_r structure, akin to a broadening of the well. By contrast, in USN the E_r well continues to deepen, marking a jump from 580 to 700 kA that almost doubles its depth, reaching a minimum value $v_\perp^{\min} \approx -5$ km/s and an overall shape comparable to the LSN.

We conclude that the trend previously found in I_p ramps in WEST is recovered now also under stationary conditions and at fixed density. That is, E_r shows a pronounced deepening with increasing I_p in the USN (UNFAV) configuration, while in the LSN (FAV) counterpart, the response of E_r is weaker and appears more as a change in structure than in the depth of the well. The reproducible findings suggest a robust mechanism genuinely controlled by I_p and not by hidden dependencies, such as density.

4.3.3 I_p sensitivity under auxiliary heating in WEST

The observations from WEST and Tore Supra just presented in Sec. 4.3.1 and 4.3.2, were for Ohmically discharges only. To examine how the I_p effect on E_r extends to more relevant plasma conditions, we consider a set of auxiliary heated discharges performed during the early 2023 WEST campaign. Complications in coupling the external heating to the plasma prevented the dataset from being fully completed, especially in LSN configuration. The available data therefore does not enable a proper comparison between the FAV and UNFAV configurations. Subsequent attempts in late 2024 to complete the missing data were unsuccessful, too. However, in the USN (UNFAV $B \times \nabla B$) case, where for Ohmic heating the E_r well displays the strongest sensitivity to I_p, sufficient levels of heating power (2.5–4 MW) were achieved to study the I_p influence on E_r when the plasma is exposed to additional heating.

The considered set of discharges consists of a fixed USN shape, repeated at $I_p = 500$ and 700 kA and applying either ion cyclotron resonance (ICRH) or lower-hybrid (LH) heating. Here, the DBS measurements do not cover the inner side of the E_r well at $I_p = 700$ kA, but this is not critical for the present discussion. Fig. 4.14 compares E_r for the two I_p values at various LH heating power levels, including the case without auxiliary heating for reference.

Similarly to the Ohmic cases discussed earlier, the edge $v_\perp$ levels at $I_p = 700$ kA are clearly distinguishable from the ones at 500 kA with a magnitude about twice higher in the former. This holds regardless of the applied heating power, implying relatively little sensitivity of E_r to heating, in spite of the density and core temperature increase (as annotated in Fig. 4.14). Interestingly, in the 700 kA case, with increasing heating power the edge density profile clearly steepens near the separatrix as indicated by the reflectometry data (Fig. 4.14, lower right panel), whereas the E_r profile remains largely unaffected.

For the case of ICRH heating, the results are displayed in Fig. 4.15. They are qualitatively similar to the case of LH heating, except that, with the ICRH, a change is observed in

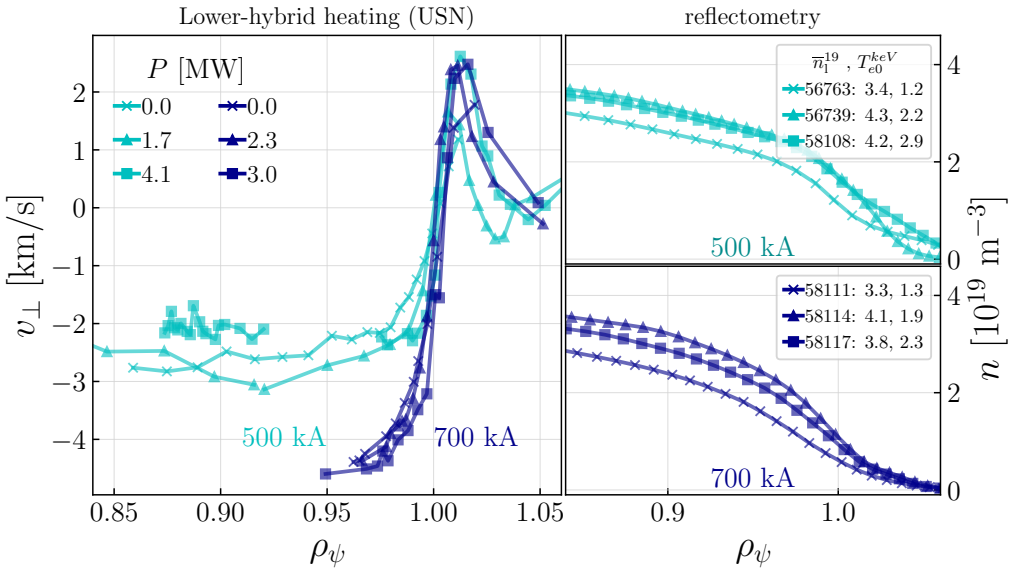

Figure 4.14: *Lower hybrid (LH) heating scan for two different I_p values in USN (UNFAV $B\times\nabla B$) discharges in WEST. Color brightness is used to distinguish between different I_p, while symbols correspond to varying levels of LH power (P). E_r (left) varies notably with I_p while P has little impact on it, despite notable changes in the density profile (right), average density ($\langle n\rangle_{\text{vol}}$) and core electron temperature (T_{e_0}).*

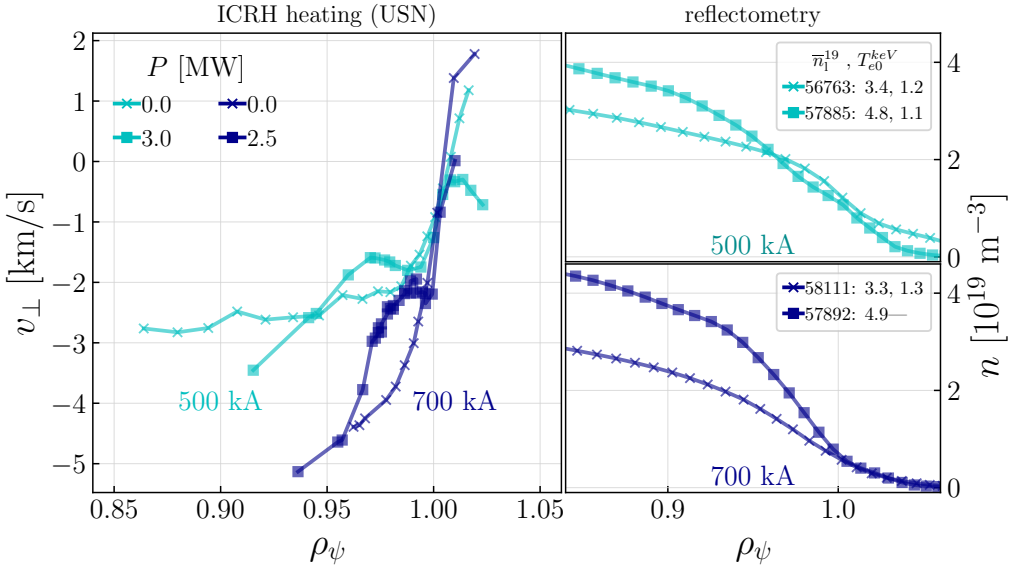

Figure 4.15: *Same representation as Fig. 4.14, using ICRH instead of LH heating.*

the fine-scale radial structure of E_r just inside the separatrix. This modification of the E_r profile is observed both at $I_p = 500\,\mathrm{kA}$ and $700\,\mathrm{kA}$. However, the overall, larger-scale level of E_r appears to be still determined mainly by I_p rather than the heating power.

We conclude from these subsidiary I_p scans in WEST that the particularly pronounced sensitivity of the edge E_r profile to I_p in USN (UNFAV) configuration extends across different heating regimes (Ohmic, LH, or ICRH), strengthening the previous indications of a genuine effect of I_p rather than a hidden dependence on other plasma parameters such as density or heating power. This provides strong motivation for further investigations into the role of I_p in setting the edge flow structure. In particular, it calls for extending the study to other tokamaks beyond WEST/Tore Supra. This is the aim of the I_p scans in TCV (Sec. 4.3.4) and in AUG (Sec. 4.3.5), presented hereafter.

4.3.4 Comparison with I_p scans in TCV

A bulk part of the this work's experiments conducted in TCV between 2023 and 2025 were dedicated to the characterization of the E_r well response to plasma current (I_p) variations in FAV and UNFAV $B \times \nabla B$ configurations. As explained above (Sec. 4.3.1–4.3.3), the motivation for such study stems from the I_p sensitivity of E_r observed in WEST—especially pronounced in UNFAV topology. A first series of shot-by-shot scans of I_p was performed in late 2023, as part of the very first dedicated TCV experiments using the newly installed DBS system. E_r was compared in matched FAV and UNFAV discharges by keeping a fixed LSN shape and flipping the toroidal field (B_0) direction, along with I_p to keep the same helicity. These preliminary I_p scans [230] indicated little variation of E_r with I_p, in both configurations—in clear contrast to WEST.

Yet, several possible caveats of that initial study were identified, namely:

(I) The equilibria were shifted upward (for better access with the DBS diagnostic), which resulted in poor coverage or absence of other diagnostics (in particular CXRS).

(II) A fixed LSN geometry was used, while in WEST the comparison is made between LSN and USN shapes.

(III) The density was not sufficiently constant throughout the I_p scan, nor was it always well-matched between FAV and UNFAV at a fixed I_p.

For a more careful analysis, new I_p scans were performed in TCV with the following improvements. Measurements are conducted in both LSN and USN shapes (with their respective FAV and UNFAV $B \times \nabla B$ drift configurations). Moreover, the equilibria are vertically centered in the chamber ($z_{\mathrm{axis}} = 0$). Aspect (III) is partly inevitable because of the density profile modification by I_p. Nevertheless, the possible influence of overall (line-integrated) density changes can be assessed, and whether it might bias the comparison at different I_p. A linear density ramp is thus programmed in every discharge, while I_p is varied from shot to shot, scanning three different values. The combined I_p and density scans help to disentangle the effects of I_p and density. The influence of density alone (at fixed I_p) is examined in a dedicated section (Sec. 4.4). Here, we merely select appropriate time windows along the density ramps to optimize the match between FAV and UNFAV and keep the line-averaged density roughly fixed throughout the I_p scan.

The $v_\perp$ profiles are compiled in Fig. 4.16 and Fig. 4.17 for the LSN and USN shapes, respectively. The line-averaged density $\overline{n}_l^{19}$ in $[10^{19}\,\mathrm{m}^{-3}]$ and the greenwald fraction

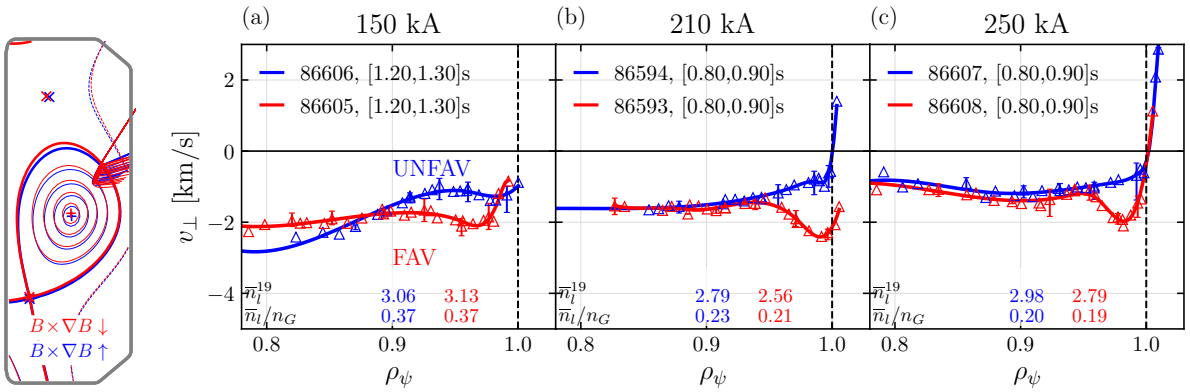

Figure 4.16: *Edge perpendicular velocity at different values of I_p in FAV versus UNFAV drift configuration, for a LSN shape (left) and fixed line-averaged density ($\overline{n}_l^{19}$, annotated at the bottom). In contrast to WEST, $v_\perp$ shows no clear sensitivity to I_p.*

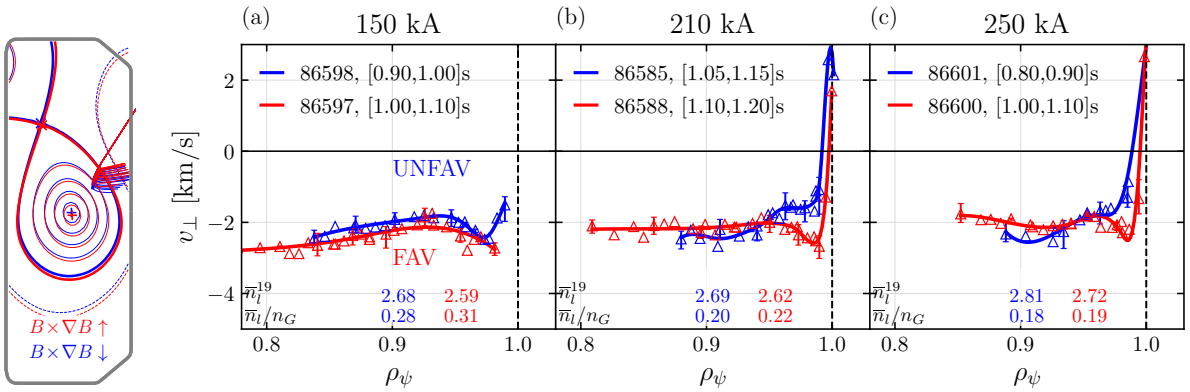

Figure 4.17: *Same representation as Fig. 4.16 for an analogous I_p scan using an USN shape instead.*

$\overline{n}_l/n_G$ are annotated at the bottom of the graphs.

Focussing on the LSN case (Fig. 4.16), there is no pronounced trend with I_p, whether in FAV or UNFAV configuration. However, subtle variations of the E_r profiles can be discerned; with increasing I_p, the well appears to become narrower in FAV, without significant change of the well depth. In UNFAV, the increased I_p tends to flatten the shallow E_r well even further, until it disappears completely at the highest current.

These results are largely consistent with the aforementioned initial I_p scan (that was performed with a comparable LSN shape) in that they do not display a striking sensitivity of the E_r well to I_p. This is now confirmed at nearly constant, low-to-intermediate, line-averaged density. A similar analysis at higher density ($\overline{n}_l \approx 4\times10^{19}\,\mathrm{m}^{-3}$) does not reveal a qualitative change in how E_r responds to the different plasma currents (not shown).

In USN (Fig. 4.16), the narrowing of the E_r well with increasing I_p is less apparent in FAV. Moreover, in UNFAV, the E_r well depth is reduced more drastically from 150 kA to

210 kA. Otherwise, the results of the scans in LSN and USN are qualitatively consistent; there is no evident, systematic trend of the E_r well with I_p comparable to that observed in WEST. If anything, focusing on the UNFAV drift case in TCV, the flattening of the E_r well with increasing I_p appears qualitatively opposite to the deepening observed in WEST. This remains true, in particular, when considering the LSN-FAV (Fig. 4.16) and the USN-UNFAV (Fig. 4.17) cases, which correspond more directly to the WEST magnetic configurations. Note, however, that the LSN and USN shapes considered here are not up-down antisymmetric, nor is the DBS poloidal probing location—with respect to the X-point location—the same, preventing the effect of $B \times \nabla B$ from being isolated when comparing these LSN and USN shapes.

To better resolve the subtle E_r profile changes with I_p, Fig. 4.18 a-b combines all I_p cases into a single graph, presented separately (in left and right columns) for the FAV and UNFAV LSN discharges. An equivalent is provided in Fig. 4.18 c-d for the USN case. This alternative representation further confirms the absence of a consistent variation of E_r with I_p near the separatrix, with the exception of the aforementioned narrowing of the FAV E_r well with increasing I_p. Moving further inwards ($\rho_\psi \lesssim 0.9$), however, E_r displays a gradual increase with I_p, which occurs consistently in all but the USN UNFAV configuration (Fig. 4.18 d).

Concomitantly with this E_r behavior, the carbon toroidal velocity becomes more co-current as I_p increases. This is shown in Fig. 4.19. The variation is most pronounced in the core, yet it appears to extend partly up to the edge. Taken together, these observations suggest a link between the E_r increase in the outer core and the co-I_p shift of the intrinsic toroidal rotation, which would be qualitatively consistent with the ion radial force. However, caution is required in this interpretation since it assumes that the impurity toroidal flow reflects—to some degree at least—also the behavior of the main ion (deuterium). This hypothesis is not addressed here. However, experiments on DIII-D found that the deuterium toroidal rotation can deviate from the carbon one, even in L-mode [60]. This is also expected based on a neoclassical estimation, as performed for TCV in Ref. [231].

In summary, the I_p scans performed in TCV show little variation of the edge E_r profile, whereas the core E_r level increases with increasing I_p, in a similar way for both drift configurations. Thus, unlike in WEST, increasing I_p does not reduce the magnitude of the E_r well asymmetry between FAV and UNFAV in TCV, at least not within the parameter range scanned.

4.3.5 Comparison with a restricted I_p scan in AUG

The results presented in Sec. 4.3.1–4.3.3 and Sec. 4.3.4 for WEST and TCV, respectively, point to a clear discrepancy concerning the sensitivity of the E_r well to the plasma current (I_p). It is instructive to extend this cross-device comparison to a third tokamak, AUG, which, as a tungsten-wall device and in terms of plasma size ($\sim a$) and magnetic field, is closer to WEST than the carbon-walled TCV tokamak. Thus, AUG might be expected to exhibit plasma behavior more similar to that of WEST.

In AUG, the dependence of the E_r well on I_p has not yet been investigated systematically

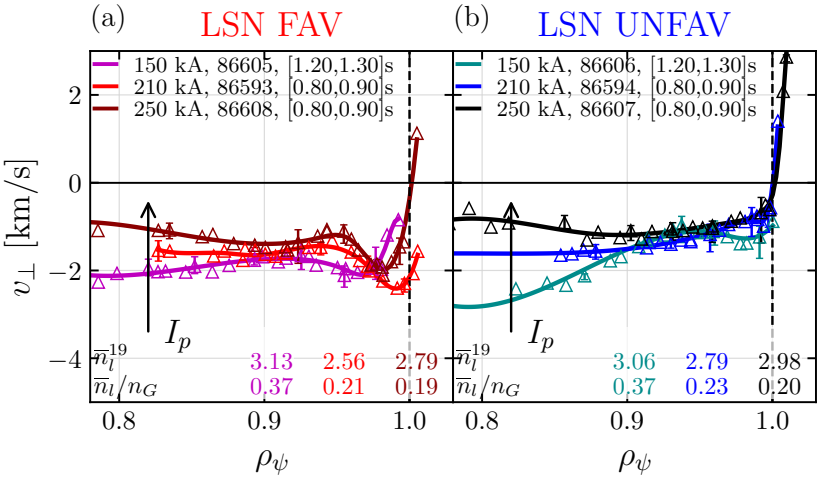

(a)

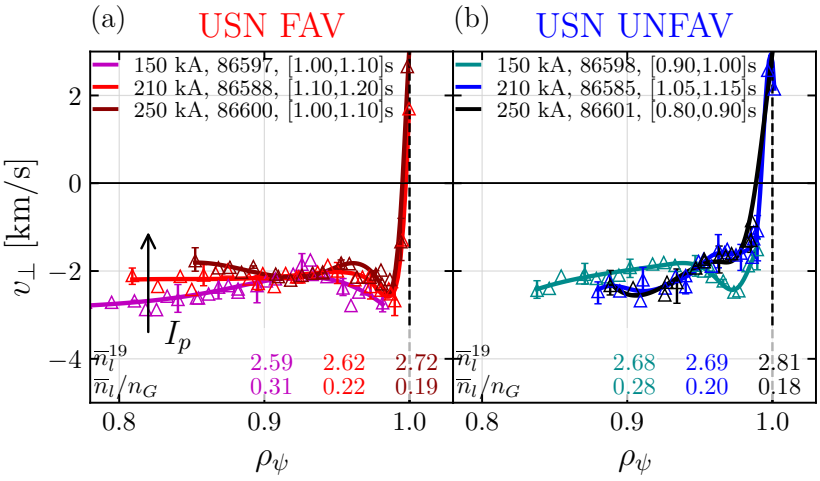

(b)

Figure 4.18: *Alternative visualization of the data in Figs. 4.16–4.17; The $v_\perp$ profiles for different I_p are combined into separate graphs for the FAV and UNFAV configurations (left and right panels), while (a) and (b) correspond to the LSN and USN cases, respectively.*

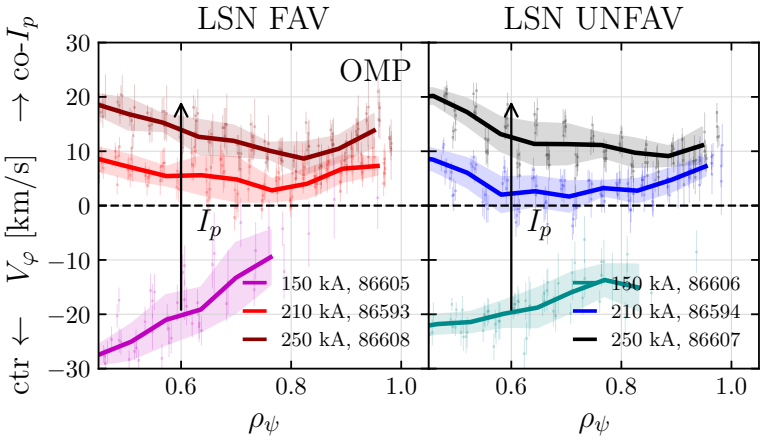

(a)

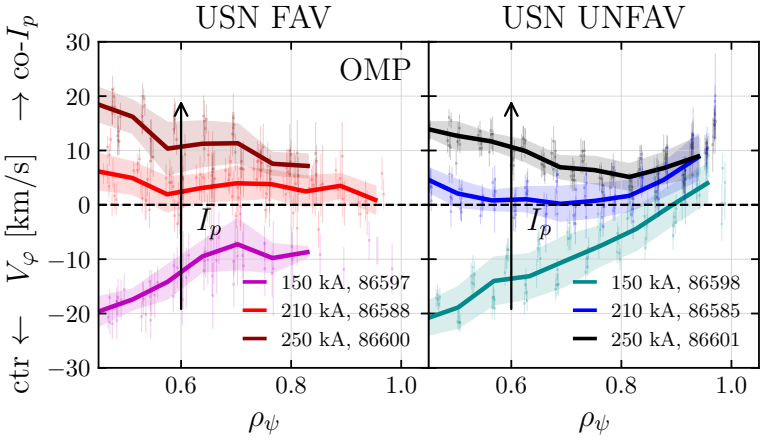

(b)

Figure 4.19: *Carbon toroidal rotation along the outer core and edge OMP regions. The curves are organized in the same way as in Fig. 4.18.*

in the two drift configurations. Accordingly, a corresponding study was undertaken on AUG, with dedicated discharges conducted in early 2025.

Owing to the limited number of available discharges, the investigation was restricted to a single shape and drift direction—USN with UNFAV $B\times\nabla B$ drift—corresponding to the configuration in WEST exhibiting a strong E_r well dependence on I_p.

Method and discharge design

As the methodology presented in Chapter 3 was, to a large part, specific to TCV, we briefly outline here the methodology used for the analysis of the AUG experiments, together with the discharge design.

The $v_\perp$ profiles are measured via X-mode DBS using two systems installed in AUG (section 11): a dual channel V-band and a W-band system [165]. The W-band is now a comb DBS system [232], injecting 7 equidistant probing frequencies simultaneously around a central hopping frequency. A sequence of 10 $\times$10 ms probing frequency steps was programmed for both the V-bands and the comb system's central frequency. The poloidally steerable launcher was kept at a fixed angle of $\theta = -18\,^\circ$. Another V-band DBS system (section 13) [144] was not available at the time of the experiments. Beamtracing is performed using `beam3d` (see Sec. 3.2.3), which has been interfaced to the AUG equilibrium reconstruction and the density profile fit from integrated data analysis (IDA) [233].

Neutral beam blips were programmed for CXRS measurements, except for one discharge (#42591, 800 kA). The DBS profiles are analyzed within time windows immediately preceding the beam blips to minimize interference from beam torque. However, owing to an unreasonable scatter in the impurity poloidal velocity, the edge radial force balance estimate of E_r from direct measurements of impurity profiles is not available for these discharges. Another independent estimation of the edge E_r profile was attempted using He II spectroscopy (HES) [115]. However, the resulting edge $|E_r|$ level (5–10 kV/m) disagrees quantitatively with that from the DBS ($\lesssim$ 2 kV/m). The reason for this discrepancy is presently not understood. However, the DBS measurements are quantitatively consistent with those reported, e.g., in [122, Fig. 10-11] for the same UNFAV $B\times\nabla B$ configuration.

In these L-mode deuterium discharges, the magnetic field is fixed at $B_0 = -2.5$ T, while I_p is varied from shot to shot, ranging from $I_p = +400$ to $+1$ MA. However, in the 1 MA case, the target density of $\overline{n}_l \approx 3\times10^{19}\,\mathrm{m}^{-3}$ was largely exceeded. Moreover, only a restricted (outer) part of the E_r well is covered due to a failure of the W-band DBS system during that discharge. As a result, that discharge was excluded in the following. Additionally, the 400 kA discharge exhibits a MARFE[7] up to $t \approx 3.5$ s, compromising the initial phase of the shot. A repeat discharge showed no improvement.

As commonly done in AUG experiments, a small amount of background ECRH heating power ($P_{\mathrm{ECRH}} \approx 400$ kW) is injected from the start of the discharge. P_{ECRH} is then increased in steps to cover different plasma conditions—farther and closer to the L-H transition threshold. However, in spite of up to $P_{\mathrm{ECRH}} = 4$ MW at 400 kA and 3 MW at 600 kA and 800 kA, no confinement transition was observed, so that the proximity to $P_{\mathrm{L}\to\mathrm{H}}$ cannot be assessed here.

[7] MARFE [234] is an acronym for "multifaceted asymmetric radiation from the edge".

Results of the I_p scan in AUG (UNFAV drift only)

Fig. 4.20b compares the $v_\perp$ profiles at a fixed auxiliary heating of $P_{\mathrm{ECRH}} = 1.8\,\mathrm{MW}$ and for three different values of I_p. The USN shapes (Fig. 4.20a) are well-matched and the edge density profiles (Fig. 4.20c) show reasonable agreement, although the line-averaged density is higher at 400 kA by roughly 25 %.

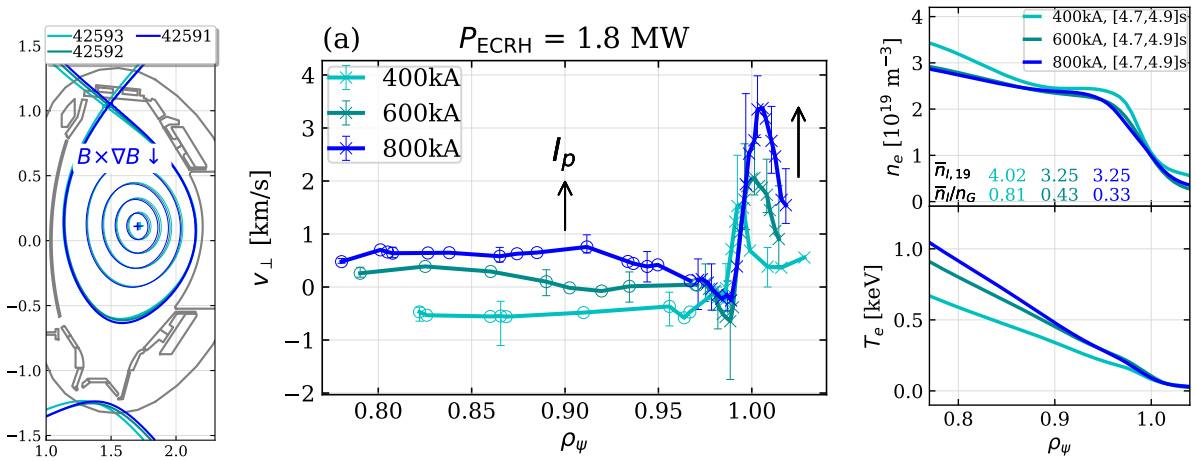

(a) **(b)** **(c)**

Figure 4.20: *(a) Contours of magnetic flux for USN discharges at different values of I_p, with unfavorable $B\times\nabla B$ drift. (b) $v_\perp$ profiles from DBS and (c) electron kinetic profiles from integrated data analysis (IDA),*

Consistent with expectations for UNFAV discharges, the edge E_r profile is nearly flat, and a well-like shape is only faintly visible close to the separatrix, with no clear variation in its depth observed as I_p increases. Further inward ($\rho_\psi \lesssim 0.9$), the E_r level increases systematically with I_p, similar to the trend observed in TCV (Sec. 4.3.4). Moreover, the E_r "hill" outside the separatrix, although not the focus of this study, also shows an increase with I_p. This is consistent with Ref. [116] that reports an inverse dependency between the maximum of E_r in the SOL and the edge Greenwald fraction (as previously noted in Sec. 2.7). Taken together, these results suggest that the edge $E_r \times B$ shear increases to some extent with I_p, not owing to the deepening of the E_r well as seen in WEST, but rather from an increase of E_r on both sides of the well.

These observations hold qualitatively for various levels of ECRH power, as illustrated in Fig. 4.21. At the lowest power of $P_{\mathrm{ECRH}} = 0.3\,\mathrm{MW}$, the low-current (400 kA) discharge is omitted as the phase is perturbed by a MARFE. Although the MARFE has dissipated at 1.2 MW (Fig. 4.21 b), the E_r SOL profile appears suspiciously flat, possibly indicating a residual effect associated with the MARFE. Nevertheless, the dataset confirms the qualitative effect of I_p seen in Fig. 4.20b across the various levels of ECRH heating: E_r increases in the core and SOL with rising I_p, while the well depth remains nearly unchanged.

To conclude, the reduced I_p scan conducted on AUG for an UNFAV drift configuration does not reveal a pronounced sensitivity of the E_r well depth to I_p. In this respect, and in the increase of E_r in the outer core region, TCV and AUG results are consistent. WEST, on the other hand, stands out with a sharp deepening of the E_r well with I_p.

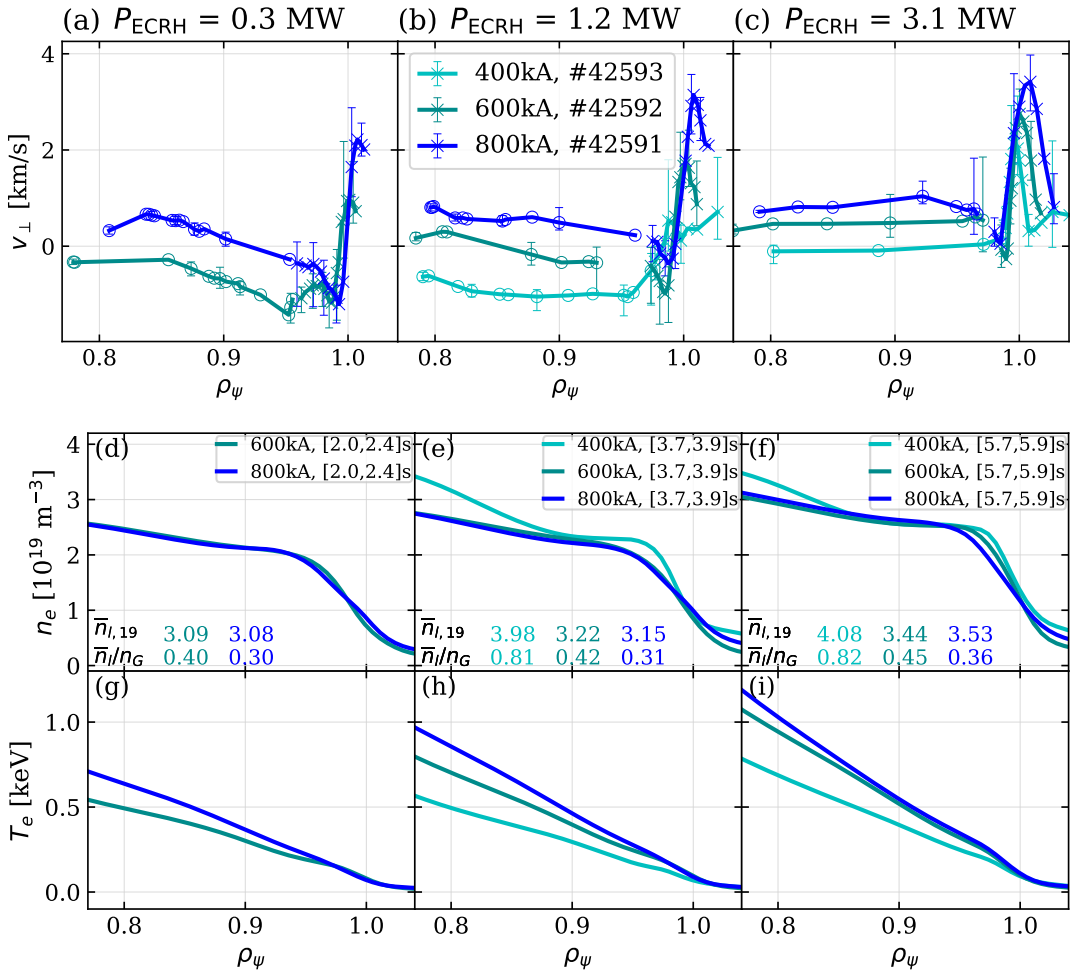

Figure 4.21: *Extension of the I_p scan of Fig. 4.20 to various levels of ECRH power. For a given P_{ECRH}, the qualitative increase of E_r in the outer core and SOL with rising I_p persists, while the well depth remains nearly constant.*

4.4 Density scans in TCV

After examining plasma current effects in WEST, TCV, and AUG earlier, we now—and for the remainder of this chapter—return to TCV experiments. This section proceeds with comparing FAV and UNFAV discharges, now as a function of density.

Earlier, in Sec. 3.8 of Chapter 3, we saw that density affects the edge E_r structure in TCV, notably in limited plasmas and to some degree in diverted ones. Drawing on more recent and better diagnosed discharges, we now study the role of density more systematically in diverted discharges, focusing on the difference between FAV and UNFAV drift cases.

Fig. 4.22 compares the E_r profiles between matched FAV and UNFAV discharges at different line-averaged densities ($\overline{n}_l$) between 3 and $5 \times 10^{19}\,\mathrm{m}^{-3}$. These Ohmic discharges correspond to a subset at $I_p = -/+250\,\mathrm{kA}$ ($q_{95} \approx 3$) from the I_p scan of Sec. 4.3.4, starting with the LSN shape. The line-averaged density ($\overline{n}_l^{19}$) in $[10^{19}\mathrm{m}^{-3}]$ is annotated at the

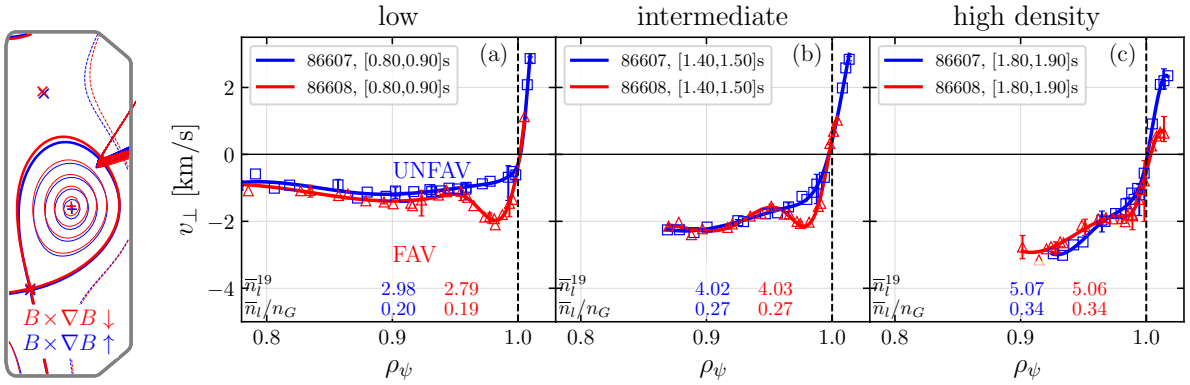

Figure 4.22: *FAV/UNFAV comparison at three different densities, for an example LSN scenario in TCV at* 250 kA*. As density is increased, the pronounced difference in the $v_\perp$ well fades out.*

bottom of the graphs, together with the Greenwald fraction $\overline{n}_l/n_G$.

As density increases, the E_r well becomes less pronounced in the FAV discharge. The UNFAV case, on the other hand, which lacks well at all densities, shows a marked decrease in the edge E_r with increasing density, thereby approaching the level of the FAV case. Thus, at high density, the clear distinction between FAV and UNFAV edge E_r profiles disappears.

For a closer look at this trend, Fig. 4.23(a,b) shows the variation of $v_\perp$ with density separately for the FAV and UNFAV cases, along with the corresponding edge kinetic profiles in (c–h). Regardless of drift configuration, $v_\perp$ decreases with increasing density. This effect is most pronounced towards the core ($\rho_\psi \lesssim 0.95$). In the UNFAV case, this decrease extends nearly to the separatrix. In the FAV case, $v_\perp$ remains almost unchanged near the well minimum. As a result, the inner-side slope of the E_r well weakens or even reverses, making the well less distinct at higher density. Outside the separatrix, the E_r hill appears higher in UNFAV. This observation is also confirmed by midplane GPI measurements (not shown). It is indicative of different SOL conditions (see Eq. (2.16)). For completeness, we note that, inside the separatrix, the edge T_e and T_i profiles show

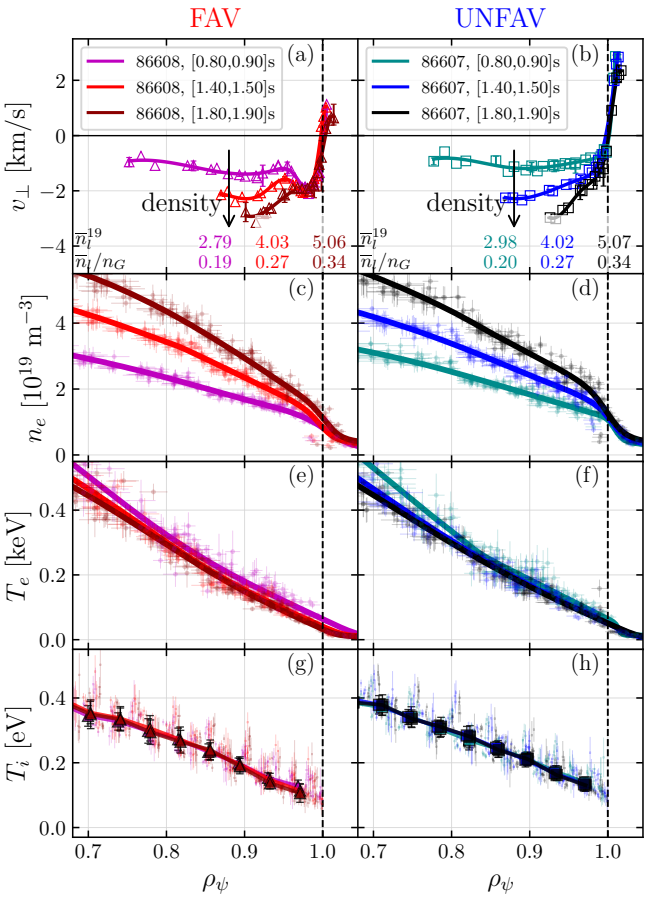

Figure 4.23: *Alternative representation of the $v_\perp$ profiles of Fig. 4.22, combining the $v_\perp$ measurements at various densities, for FAV and UNFAV (left and right panels), separately. (c-h) show the corresponding kinetic profiles.*

only minor or no variations across the density scans (Fig. 4.23 e-h). This underpins that the observed changes in E_r and carbon rotation are attributed to density variations alone.

Qualitatively consistent results are obtained in the USN counterparts (the same discharges as in Sec. 4.3.4, Fig. 4.17 c). Again, as shown in Fig. 4.24, the core $v_\perp$ level decreases with rising density while the FAV $v_\perp$ well flattens. At intermediate density (b), the edge $v_\perp$

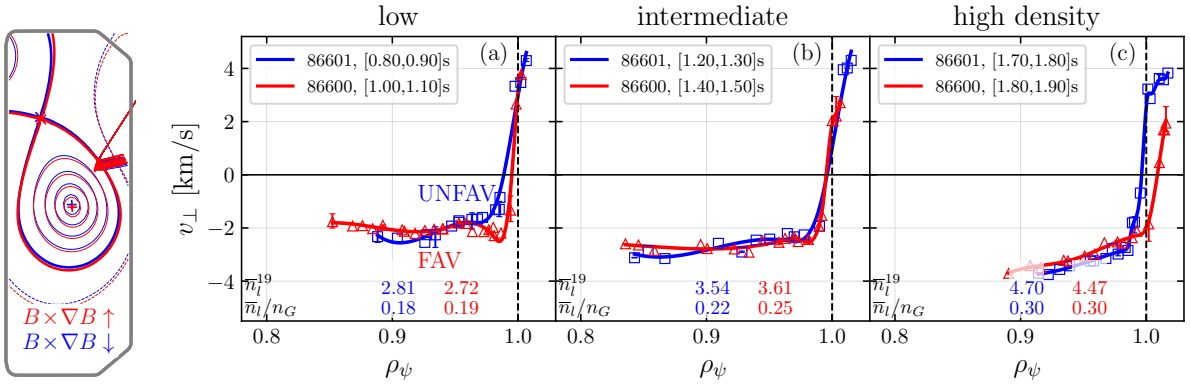

Figure 4.24: *Results of an anlogous density scan to Fig. 4.22 in USN (instead of LSN) geometry.*

profiles of FAV and UNFAV become nearly indistinguishable. A further density increase (c) appears to even reverse to some degree the usual difference between FAV and UNFAV; the edge $v_\perp$ now being slightly lower in UNFAV than in FAV.

The gradual decrease in $v_\perp$ for $\rho_\psi \lesssim 0.95$ as density increases is consistent with the earlier results presented in Sec. 3.8 (Fig. 3.18b) for a different scenario (with unfavorable $B\times\nabla B$). In the present density scans, CXRS data are available to confirm that the trend correlates with a systematic counter-current shift of the carbon toroidal velocity (V_φ) at the outboard midplane (OMP), extending from the core to the edge. This is exemplified in Fig. 4.25 for the LSN scenario of Fig. 4.22.

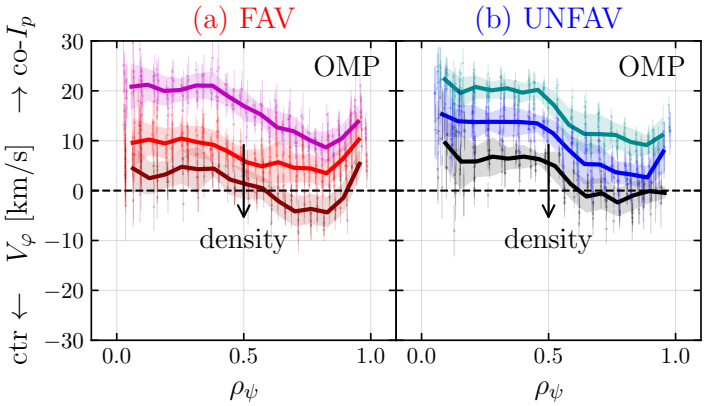

Figure 4.25: *Carbon toroidal rotation (V_φ) along the outboard midplane (OMP), for the LSN (a) FAV and (b) UNFAV drift configurations of Fig. 4.22. In both cases, increasing the density shifts V_φ in the counter-current direction.*

The corresponding $V_\varphi B_\theta$ contribution to the impurity radial force balance is shown along-

side the DBS measurements in Fig. 4.26a. The magnitude of the $V_\varphi B_\theta$ variation with

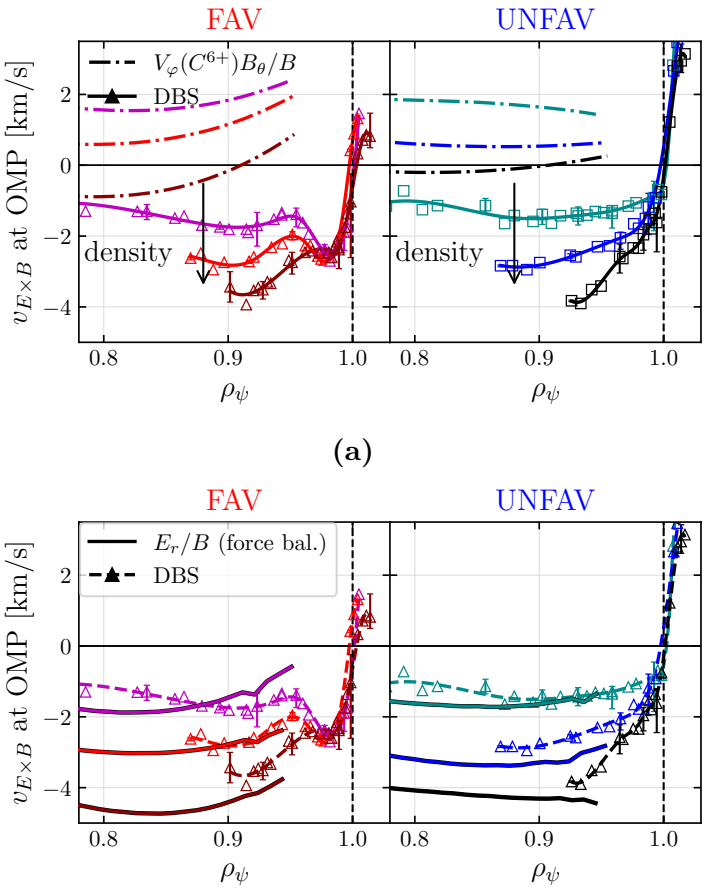

(a)

(b) *DBS*

Figure 4.26: *(a) Toroidal rotation contribution and (b) E_r in the C^{6+} radial force balance, together with the DBS data, for the LSN scenarios of Fig. 4.22.*

density can account for the one observed in $v_\perp$. This might indicate that the density dependence of $v_\perp$ is partly—or mainly—driven by intrinsic rotation changes in the core. Yet, as pointed out previously in Sec. 4.3.4, the deuterium rotation might differ from the carbon one. Therefore, a firm conclusion on the role of ion toroidal rotation in these E_r changes cannot be drawn at this point.

For completeness, the $v_{E_r\times B} = E_r/B$ level inferred from the carbon radial force balance is provided in Fig. 4.26b. It shows a reasonable qualitative and quantitative agreement with the OMP-mapped DBS measurements up to $\rho_\psi \approx 0.95$. At the very edge, the force balance estimation of E_r is omitted. As mentioned previously (Sec. 4.2.1), it is considered unreliable in this region.

The counter-current shift in impurity toroidal rotation with increasing density is in line with previous findings in TCV [197, Fig. 15] and AUG [122, Fig. 19]. In AUG, the change in V_φ was also found to correlate with a decrease in E_r on both sides of the separatrix. However, in this respect, Ref. [122] does not report any qualitative difference between the two drift configurations. In a recent study based on JET density scans [199] (FAV configuration only), the correlation with toroidal rotation is not reported; however, E_r

qualitatively follows the behavior of AUG—the overall edge and SOL E_r level are reduced with increasing density. In WEST, on the other hand, a systematic comparison of FAV and UNFAV over density scans has not yet been carried out; several recent attempts with matched density ramps in LSN (FAV) versus USN (UNFAV) were only partially successful due to missing diagnostics or MHD perturbations.

Finally, the variation of confinement is examined across the presented density scans in TCV. Fig. 4.27(a,b) displays the stored thermal energy W (total and electron) as a function of density, respectively for LSN and USN. In both cases, W increases almost linearly

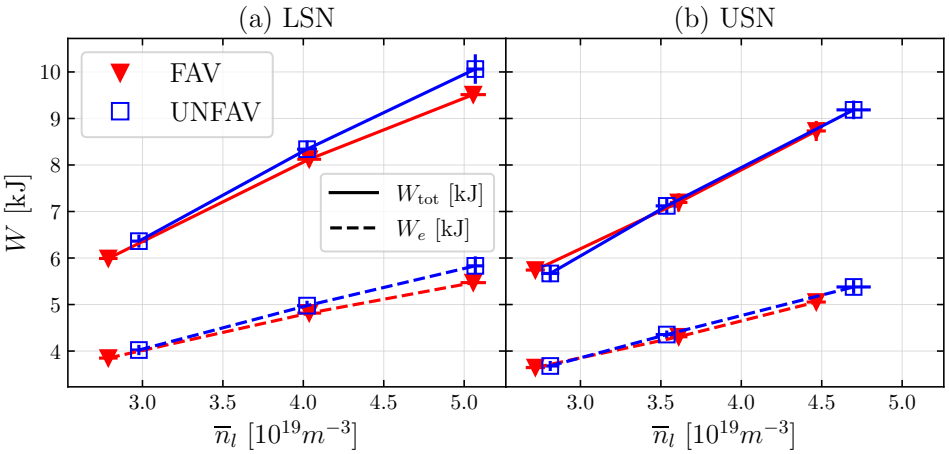

Figure 4.27: *Total (W) and electron thermal energy (W_e) as a function of density for (a) the LSN and (b) the USN shapes. The energy increases similarly for FAV and UNFAV.*

with density, and behaves similarly for the FAV and UNFAV cases. In the LSN case, W rises slightly faster in the UNFAV than in the FAV configuration. This might be related to the observation that the edge $E_r \times B$ shear appears to grow stronger with density in the UNFAV, and not in the FAV case. However, this connection remains speculative, given the small difference in slopes and other possible contributing factors and/or experimental uncertainties.

4.5 Power scans in TCV

As established in this chapter and previous studies, the L-mode E_r well in WEST, AUG, and TCV is more pronounced in FAV than UNFAV, up to certain exceptions (high I_p in WEST or high density in TCV). The discrepancy in mean $E_r \times B$ shear can be very pronounced even in the absence of auxiliary heating, that is, far from any L- to H-mode transition power threshold ($P_{\mathrm{L}\to\mathrm{H}}$). To further investigate the presumed connection between mean $E_r \times B$ shear and the $P_{\mathrm{L}\to\mathrm{H}}$ dependence on magnetic drift direction, we conducted auxiliary-heated TCV discharges to probe the E_r well near the L-H transition in FAV and UNFAV configurations.

4.5.1 NBI

First, we consider a pair of equilibria similar to the $|I_p| = 150\,\mathrm{kA}$ LSN scenarios from the Ohmic I_p scans (Sec. 4.3.4, Fig. 4.16 a), but with an upward shift of $z_{\mathrm{axis}} \approx 13\,\mathrm{cm}$. The

heating power is delivered by a co-current neutral beam (NBI-1) and ramped up as shown in Fig. 4.28. The same NBI-1 ramp is repeated for the two drift cases by keeping the sign of I_p fixed and reversing only the B-field. This results in an opposite helicity between the two cases. Yet, in Sec. 3.8.3, it was shown that the helicity sign has not sizeable effect on E_r in the present LSN references (without NBI).

Three L-mode phases are examined along the ramp: an initial Ohmic phase (I), an intermediate power step (II) and a third phase (III) which, in the FAV discharge, is followed by an L-H transition around 1.6 s at an injected power of $P_{\mathrm{NBI}} = 700$–750 kW. The UNFAV discharge remains in L-mode throughout the ramp.

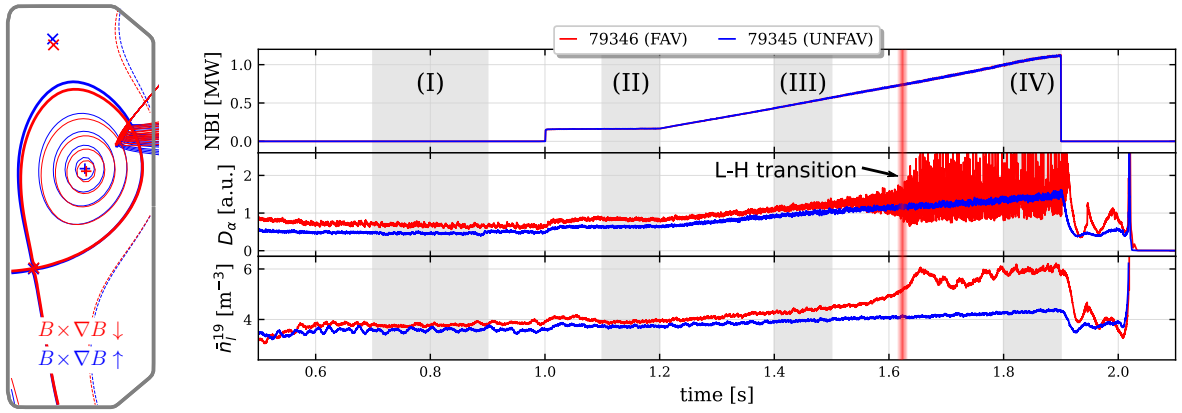

Figure 4.28: *From top to bottom: Time traces of NBI power, vertically detected D_α line signal and line-averaged density along the heating ramp. The shaded areas indicate the three time windows investigated, where phase (III) is close to the L-H transition triggered around* 1.63 s *for the FAV case.*

The $v_\perp$ measurements are displayed in Fig. 4.29 for the different phases. In both drift

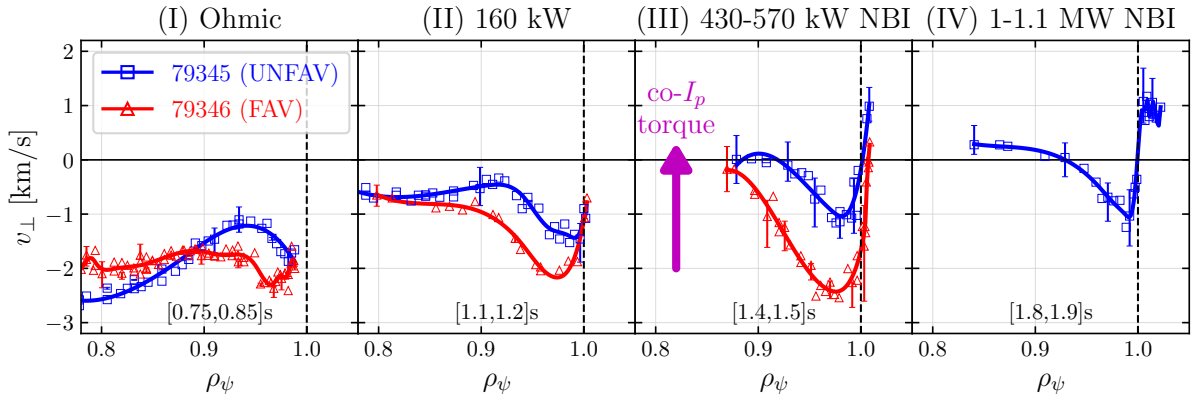

Figure 4.29: *Perpendicular velocity inferred from DBS for the phases displayed in Fig. 4.28.*

configurations, the outer core E_r level ($\rho_\psi \lesssim 0.9$) increases with the NBI power, as consistently observed in response to NBI heating (and noted already in Sec. 3.8.2); This can be attributed to the neutral beam torque, shifting the toroidal rotation in the co-I_p direction. Meanwhile, the response of the E_r well minimum ($0.95 \lesssim \rho_\psi \lesssim 0.99$) to the NBI reveals a qualitative difference between FAV and UNFAV (Fig. 4.29): In FAV, the initial

well depth is maintained along the ramp, whereas it becomes shallower in the UNFAV case. Even around the highest delivered beam power, $P_{\mathrm{NBI}} = 1$–$1.1\,\mathrm{MW}$ (Fig. 4.29–phase IV), the E_r well remains shallow in UNFAV. Note that $P_{\mathrm{L}\to\mathrm{H}}$ is not known in the present UNFAV discharge due to the missing transition. It is not excluded that the UNFAV E_r well could become deeper just prior to its L-H transition. However, other experiments (not shown here) indicate that the mean E_r well remains shallow even then.

Thus, increasing the NBI power and approaching $P_{\mathrm{L}\to\mathrm{H}}$ leads to a steepening of E_r in the inner-side shear layer of the well (negative E_r slope), while enhancing the FAV/UNFAV asymmetry in E_r. These observations are compatible with the inner flow shear being important in triggering the L-H transition, as suggested by recent observations on AUG [235].

An analogous NBI ramp is performed, replacing LSN shapes by their USN counterparts (Fig. 4.30). Although the programmed NBI-1 ramp is identical to the LSN case, and the

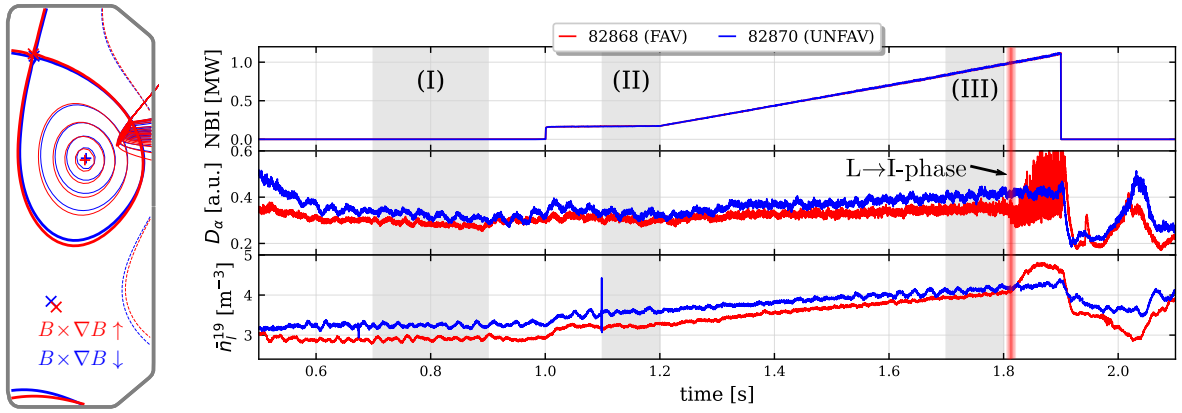

Figure 4.30: *Same representation as Fig. 4.28, for an analogous NBI ramp with the USN counterparts.*

USN shapes are close to up-down symmetric counterparts to the LSN ones, the results of these two NBI experiments are not directly comparable. Indeed, both shapes are offset from the neutral beam (centred at $z = 0$), which might result in different heat and/or momentum deposition efficiencies in LSN compared to USN. This could explain the apparently different $P_{\mathrm{L}\to\mathrm{H}}$; A transition in FAV is observed shortly after 1.8 s, corresponding to a higher power ($\approx 1\,\mathrm{MW}$) than in the LSN case. Moreover, the regime after that transition is more likely to be an I-phase (rather than an established H-mode), judging by the high-frequncy bursts in the D_α signal.

Fig. 4.31 shows the results of this second NBI ramp applied to the USN discharges. Despite the differences in H-mode access noted aboved, the $v_\perp$ behavior is qualitatively consistent with the LSN case. Likewise, increasing the NBI power tends to enhance the E_r well difference between FAV and UNFAV; The well becomes shallower in UNFAV, whereas in FAV, the well is maintained, and the inner E_r shear is enhanced by the increased E_r in the outer core.

It is also instructive to examine how the edge kinetic (n_e and T_e profiles) evolve during the NBI ramps. Fig. 4.32 compares the Ohmic (I) and the high NBI power (III) phases.

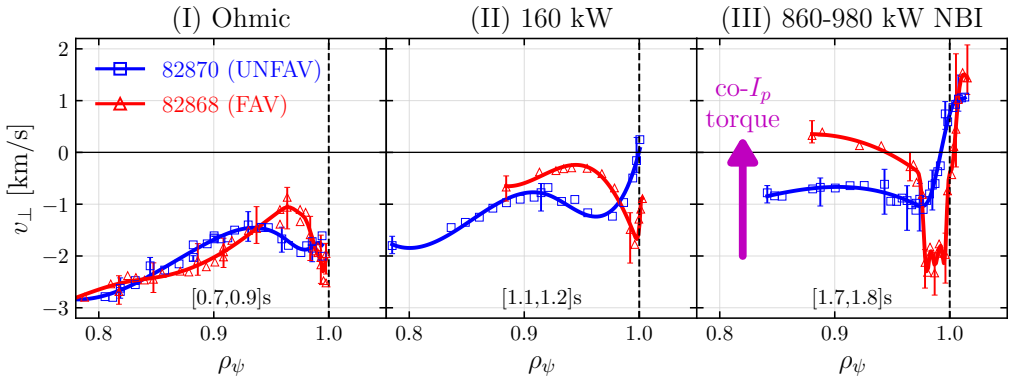

Figure 4.31: *Perpendicular velocity inferred from DBS for the phases displayed in Fig. 4.31.*

The upper panel (a) shows the LSN case, and the lower panel (b) corresponds to the USN case.

Again, the LSN and the USN discharges show consistent trends. Initially, in phase (I), the edge n_e and T_e profiles are closely matched between FAV and UNFAV, consistent with the previous Ohmic comparison of Fig. 4.5b. With the additional NBI heating, however, stronger gradients form at the edge and around the separatrix, resulting in higher edge electron pressure in the FAV than in the UNFAV configuration. Owing to the high vertical position of the plasma shapes, the CXRS diagnostic coverage is suboptimal, and so the impurity profiles are omitted[8].

4.5.2 ECRH

Another heating scan was conducted replacing NBI with second-harmonic (X2) ECRH-heating. Compared to NBI, the discharge conditions are quite different (and therefore complementary): lower density (to avoid the X2 cutoff), direct electron heating, and absence of external torque.

The ECRH scan is carried out using pair of matched USN shapes—different from the equilibria used in the previous NBI ramps. Their main parameters are: $B_0 = +/-1.43\,\mathrm{T}$, $I_p = +/-170\,\mathrm{kA}$, $q_{95} \approx 4$, $\overline{n}_l = 2.3\text{–}3.3 \times 10^{19}\,\mathrm{m}^{-3}$. The power of one gyrotron is increased in steps as shown in Fig. 4.33, with full power absorption in the plasma center according to raytracing using the TORAY-GA code [200].

Following the approach in Sec. 4.5.1, three successive L-mode phases are examined: (I) the initial Ohmic phase, (II) the first ECRH step at $P_{\mathrm{ECRH}} = 580$, and (III) the second ECRH step at $P_{\mathrm{ECRH}} = 860\,\mathrm{kW}$. The UNFAV discharge remains in L-mode during all these phases. In contrast, for the FAV case, when $P_{\mathrm{ECRH}} = 1\,\mathrm{MW}$ (immediately after phase III), there is a transition from L-mode to the I-phase regime—this is indicated by the onset of characteristic I-phase bursts in the DBS signal amplitude. This observation implies that during phase (III), the FAV discharge is near the L–I-phase transition threshold, and therefore, not far from H-mode access.

[8] In particular, in the absence of edge (SYS4) CXRS measurements, the estimation of T_i (or $\nabla p_i/ne$) from SYS1 and SYS3 alone are considered unreliable and are therefore not analyzed here.

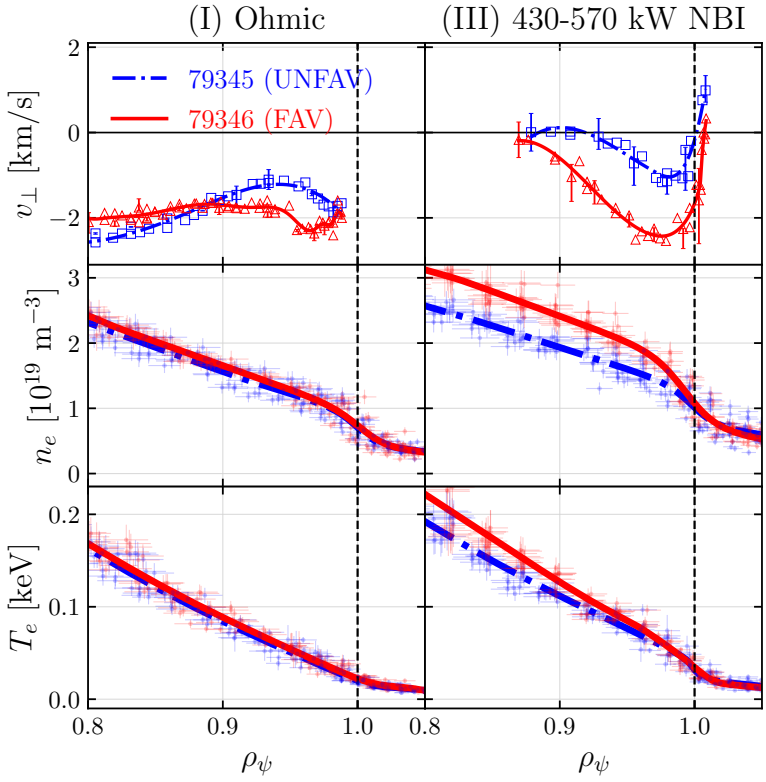

(a)

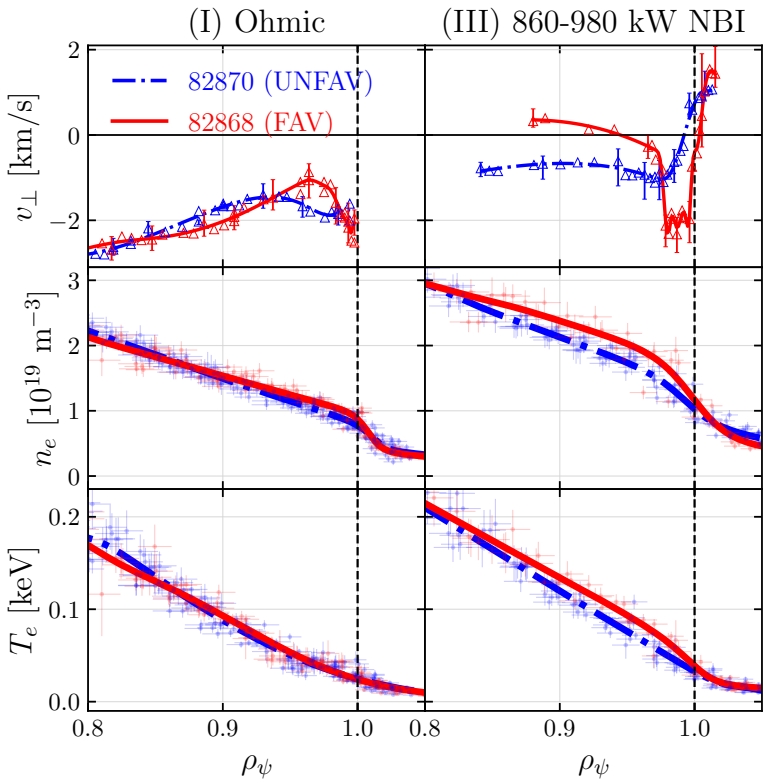

(b)

Figure 4.32: *Comparison of the electron kinetic profiles (together with $v_\perp$ for convenience) during the Ohmic phase (left column) and the high power NBI phase (right column). Panels (a) and (b) correspond to the LSN and USN discharges. With the NBI power, the initially matched n_e and T_e profiles diverge, with n_e and T_e increasing more notably in the FAV case.*

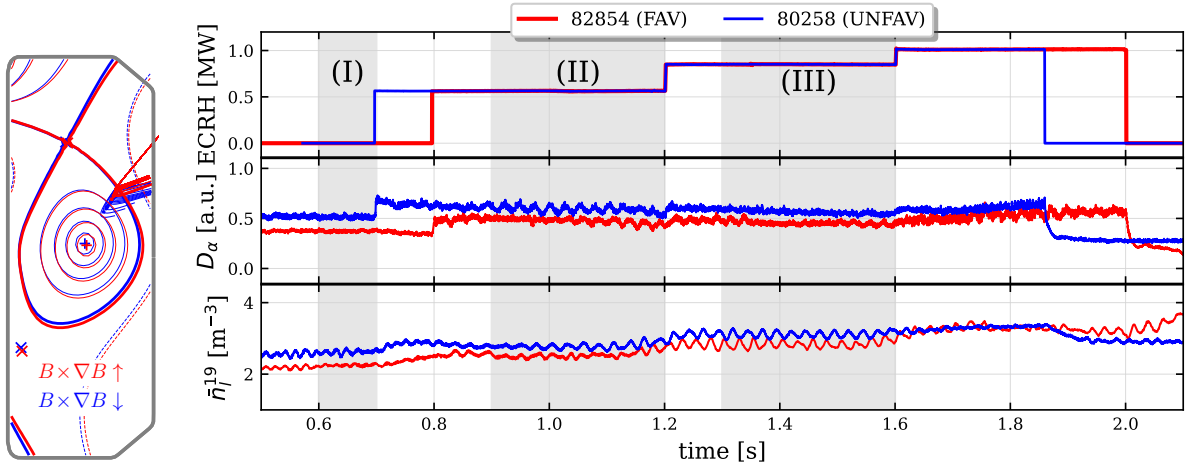

Figure 4.33: *From top to bottom: Time traces of ECRH power, vertical D_α signal and line-averaged density during a stepped ECRH scan.*

Focussing on the L-mode phases only, the $v_\perp$ profiles are displayed in Fig. 4.34. Close

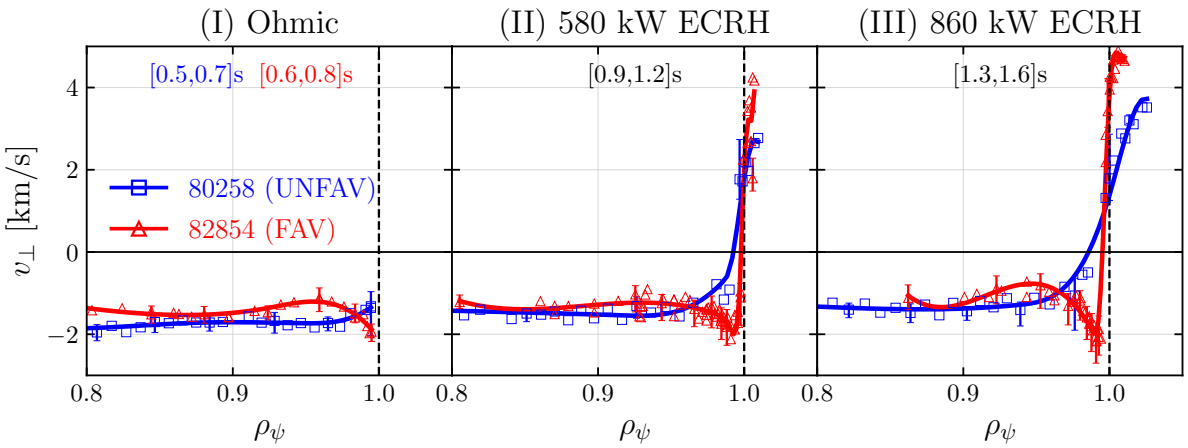

Figure 4.34: *Perpendicular velocity inferred from DBS for the phases displayed in Fig. 4.31.*

to the separatrix, the behavior of $v_\perp$ is qualitatively consistent with the NBI cases. As the power increases, the FAV well depth is maintained or slightly enhanced. In UNFAV, however, the well becomes shallower. Here, the stronger edge $E_r \times B$ shear in FAV appears to be further enhanced compared to UNFAV by a sharper jump of E_r across the separatrix. Thus, taken together with the previous NBI scans, there is evidence that both the inner and the outer shear E_r layer can be enhanced by auxiliary heating in FAV compared to UNFAV. It remains unclear which of the two (if any) is more relevant for edge confinement and H-mode access.

Similarly to the NBI scans, increasing the ECRH power also amplifies the difference between FAV and UNFAV in the edge kinetic profiles. Fig. 4.35 compares the phases (I) and (III). (Fig. 4.35). Again, the steepening of the n_e and T_e profiles as P_{ECRH} increases is enhanced in the FAV case. Note that Fig. 4.35 also includes the edge T_i data where available; within statistical uncertainties, T_i display a notable difference between FAV and UNFAV in phase (III), neither in the edge nor in the core.

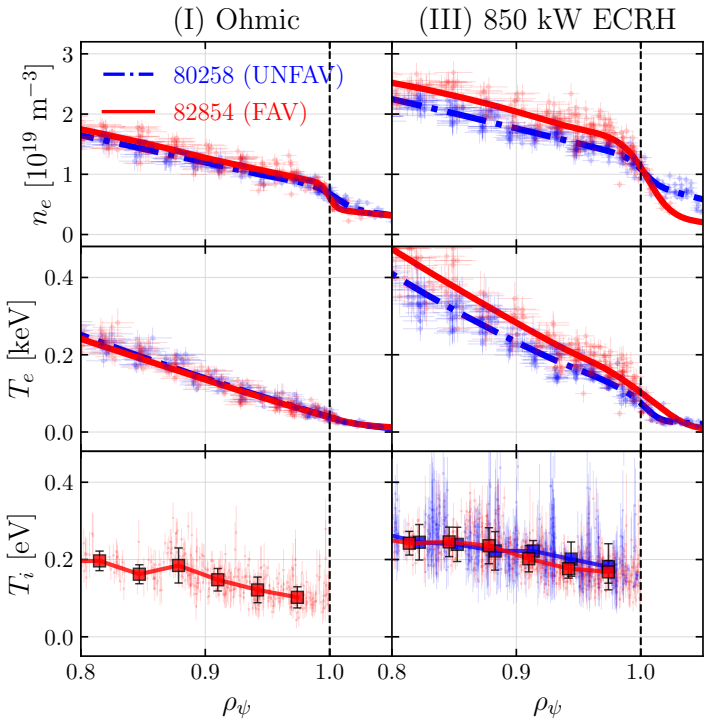

Figure 4.35: *Comparison of the edge kinetic profiles in the Ohmic phase (left column) and the high power ECRH phase (right column). Edge T_i data (bottom panel) is also displayed where available.*

4.5.3 Confinement analysis

Having analyzed the behavior of the edge E_r and kinetic profiles, we now proceed to examine the global confinement over the power scans. The expectation is that the trend of growing FAV/UNFAV asymmetry in edge $E_r \times B$ flow shear and kinetic profiles with increasing auxiliary power should also be correlated to a certain degree with the global confinement.

Since the CXRS (T_i) data coverage is incomplete here, we resort to the electron thermal energy (W_e)—as explained Sec. 3.4—in order to assess the confinement behavior in a consistent way across the different heating scans. Fig. 4.36 displays the evolution of W_e for the NBI and ECRH power scans just presented. The phases in which the FAV discharge has entered either I-phase or H-mode are also included for reference. The non-L-mode discharge phases are marked as such. Expectedly, W_e consistently increases with P_{NBI} or P_{ECRH}, and more steeply in FAV than in UNFAV, except for the NBI ramp in USN (Fig. 4.36b) where there is no apparent difference in the slopes.

For reference, the phases in which the FAV discharge enters the I-phase or H-mode are included, with non-L-mode phases marked. As expected, W_e consistently increases with P_{NBI} or P_{ECRH}. Notably, as the transition is approached, W_e rises more steeply in FAV than UNFAV, mirroring the qualitative behavior of the edge kinetic profiles previously highlighted in Fig. 4.32b.

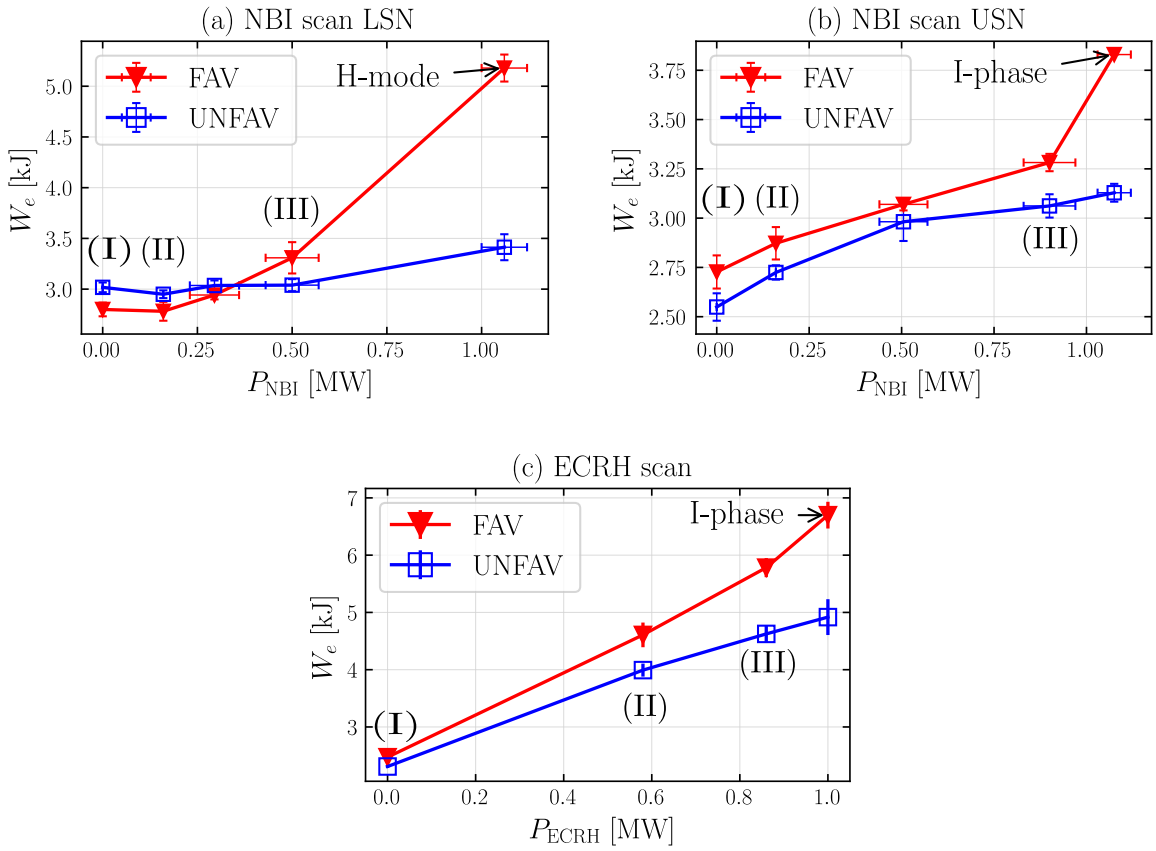

Figure 4.36: *Scaling of electron energy content as a proxy for the confinement over the various heating scans. Unless specified otherwise, markers indicate L-mode confinement phases. In (a) and (c), the L-mode W_e rises more steeply with auxiliary power in FAV than in UNFAV.*

4.5.4 Discussion

We conclude that, as the plasma approaches H-mode or the I-phase—whether by NBI or ECRH, the L-mode edge E_r shear difference between FAV and UNFAV is enhanced. This coincides with steeper edge n_e and T_e gradients across the separatrix in FAV, as reflected also by the global confinement (W_e) behavior. Taken together, these observations support the idea that the impact of drift configuration on $P_{\mathrm{L}\to\mathrm{H}}$ is connected to the mean E_r shear difference.

Yet, the presented TCV data do not provide a clear indication of causality; It may be speculated that the enhancement of the FAV $E_r \times B$ shear close to L-H transition threshold merely mirrors the steepening of ion kinetic profiles, and therefore a stronger $(\nabla p_i)/n_i e$ contribution to the shear—this remains to be tested[9]. In that case, that is, if $\Delta(E_r) \approx \Delta((\nabla p_i)/n_i e)$ in both FAV and UNFAV, where $\Delta(\cdot)$ denotes the incremental change along the power scan, then the root cause for the differing $E_r \times B$ flow behavior would remain hidden—reflecting the "hen-or-egg" problem of experimentally distinguishing the origin and consequence of pressure profile steepening. Indeed, this would allow for an interpretation in which the FAV/UNFAV asymmetry could be primarily caused by a higher turbulent transport in UNFAV (rather than a different E_r or momentum drive), as indicated for instance by the `GBS` simulations [226] mentioned in Sec. 4.1. If, on the other hand, just prior to the L-H transition, the magnitude of the E_r change was found incompatible with the diamagnetic one, this could indicate that different momentum drives—and their enhancement with auxiliary power—are the primary cause for the differing $E_r \times B$ shear and, therefore, $P_{\mathrm{L}\to\mathrm{H}}$.

Thus, although the auxiliary heating scans support a role for mean $E_r \times B$ shear in explaining the $P_{\mathrm{L}\to\mathrm{H}}$ difference between FAV and UNFAV, they do not by themselves establish causality. Nor do they explain why the E_r shear difference becomes amplified with increasing heating power. From a practical standpoint, however, the study identified the auxiliary heating power as an experimental knob capable of enhancing the FAV/UNFAV asymmetry to a level detectable not only in the edge E_r structure, but also in the kinetic profiles. Such conditions (closer to the $P_{\mathrm{L}\to\mathrm{H}}$ threshold) may facilitate the experimental identification or quantification of the key ingredients breaking the symmetry between the two drift configurations. This warrants more detailed investigations in heated FAV/UNFAV discharges close to their respective $P_{\mathrm{L}\to\mathrm{H}}$, combining high-quality edge T_i, E_r and edge turbulence measurements.

4.6 `GENE-X` simulations of TCV experiments

Having presented the experimental results of this work regarding the FAV/UNFAV asymmetry, we now turn to the interpretation of the E_r well disparities based on recent modeling using the gyrokinetic `GENE-X` code.

`GENE-X` [222, 236] solves the electromagnetic and collisional gyrokinetic Vlasov equation for

[9] To investigate whether changes in $(\nabla p_i)/n_i e$ can account for the evolution of E_r approaching the L-H transition, high-quality edge T_i data are necessary. Yet, most of the auxiliary-heated discharges used a vertically elevated shape, not suited for high-quality edge CXRS measurements of T_i.

the full distribution function f of both electrons and ions. Contrary to the local approach, the equilibrium and fluctuation parts of f are evolved self-consistently. Consequently, the profiles are free to evolve self-consistently within the simulation boundaries. This is essential for a meaningful description of the intricate coupling between turbulence, flows, and kinetic profiles. `GENE-X` stands out as one of the few gyrokinetic codes for turbulence modeling in the edge and SOL regions, supporting flexible magnetic geometries with X-points.

Here, the spectrally accelerated version of the code [236] is used. It relies on a spectral expansion of f onto Hermite and Laguerre polynomials in velocity space, thereby reducing the resolution compared to the conventional grid-based version of the code.

The following `GENE-X` simulations compare the FAV and UNFAV drift configurations in TCV, using the same approach as the analogous study performed recently for AUG [221]. The simulations model a single ion species (deuterium) and kinetic electrons, with a spectral expansion that uses $N_{v_\parallel} = 6$ and $N_\mu = 4$ coefficients in the parallel and transverse velocity phase spaces, respectively for both species. The equilibria and plasma conditions are based on the representative pair of Ohmic TCV discharges presented in Sec. 4.2.1. Specifically, the simulations use the magnetic equilibrium of the FAV discharge (TCV #86593), and its experimental profiles to set the boundary conditions at $\rho_\psi = 0.85$ and 1.03. To ensure a perfect match that facilitates interpretations, the numerical UNFAV counterpart is obtained by reversing the direction of B and keeping all other inputs fixed. Note that this comparison differs from the experimental one of Fig. 4.5b in that the sign of helicity changes in the former. However, it was verified experimentally in Sec. 3.8.3 that the helicity sign has little impact on the edge E_r in this scenario in particular. An ad hoc density source is used near the separatrix to mimic the effects of neutral ionization[10].

Their analysis, although still preliminary at the time of completing this manuscript, yields results that seem to align well with the AUG case [221], presented hereafter. The results, which are outlined hereafter, will be submitted for publication in a forthcoming paper [237].

Fig. 4.37 compares the simulated mean[11] E_r radial profiles at the OMP with the DBS measurements. Both FAV and UNFAV E_r profiles from `GENE-X` display a well-like structure just inside $\rho_\psi \approx 1.0$. The simulations qualitatively reproduce the experimental trend, with a well depth roughly twice as deep in FAV as in UNFAV. Moreover, there is reasonable quantitative agreement in E_r around the well's minimum, which, by itself, is a remarkable finding that lends confidence to the simulation results.

Further inwards, for $\rho_\psi \lesssim 0.97$, E_r sharply rises to $\approx 0\,\mathrm{kV/m}$ in the simulations. This feature is absent in the experimental data. The possible reason for this discrepancy has not yet been investigated. Nevertheless, both `GENE-X` and experiments agree in that the FAV and UNFAV mean E_r profiles are similar except near the very edge.

Another notable observation is the higher statistical E_r spread in the UNFAV case (shown as error bands in Fig. 4.37). The difference is particularly pronounced at the E_r well,

[10] The density source is poloidally and toroidally homogeneous, and has a Gaussian distribution radially centered around $\rho_\psi = 0.99$, with a width of 0.005 and an amplitude of 3×10^{21} parts /s

[11] Here, "mean" refers to toroidal and time-average over 0.1 ms.

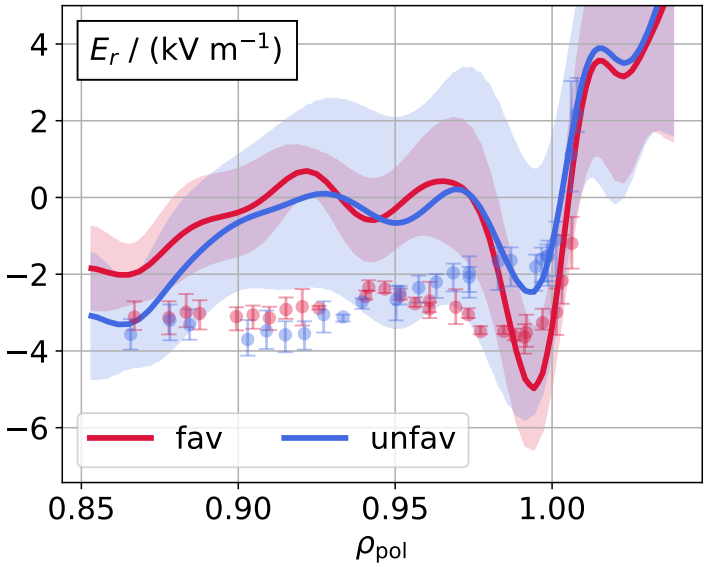

Figure 4.37: *Mean E_r profiles from* `GENE-X` *at the OMP, alongside the experimental DBS data. Errorbands represent the standard deviation from time and toroidal averaging. Courtesy of B. J. Frei.*

reflecting stronger perturbations to the mean flow in UNFAV. An example frequency spectrum of E_r at $\rho_\psi = 0.98$ is displayed in Fig. 4.38. It reveals that the stronger flow perturbations in UNFAV are attributed to a spectral feature peaking between 20–30 kHz. This indicates a pronounced coherent mode activity—possibly associated with the GAM, consistent with the experimental data (see Sec. 4.2.4). Whether the intensity of this GAM-like mode correlates more systematically with the magnitude or the shear of the mean E_r profile is an interesting question to be addressed in future experimental and numerical studies.

In the following, we restrict our attention to the origin of the different E_r well depths in the simulations. Consider the ion radial force balance, shown in Fig. 4.39 for the FAV (top) and UNFAV case (bottom panel). In both configurations, the diamagnetic and toroidal contributions nearly cancel around the location of the E_r well, $\rho_\psi \approx 0.99$, and are similar between FAV and UNFAV. Consequently, the depth of the well corresponds roughly to that of the poloidal velocity contribution ($-u_{\theta i} B_\phi$), which accounts for the difference in the E_r well depths. A neoclassical estimate of the ion poloidal rotation has not yet been computed for these simulations. However, in the similar AUG runs [221], the discrepancy in the FAV and UNFAV poloidal rotations near the edge was found incompatible with the neoclassical predictions from the NEO code. As argued in [221] and elaborated below, this points to a nonlinear turbulence-driven acceleration of the poloidal flow.

As explained in Sec. 2.5, turbulent fluctuations accelerate the perpendicular ($E_r \times B$) flow $V_\perp$ if there is a finite radial gradient of the Reynolds stress component $\mathcal{R}_{r\perp} = \langle \tilde{V}_r \tilde{V}_\perp \rangle$, or, when considering the *poloidal* momentum projection:

$$\frac{\partial}{\partial t} \langle V_\theta \rangle \, |_{\text{fluct.}} = -\frac{\mathrm{d}\mathcal{R}_{r\theta}}{\mathrm{d}r} \,, \quad \text{with } \mathcal{R}_{r\theta} = \langle \tilde{V}_r \tilde{V}_\theta \rangle \,. \tag{4.1}$$

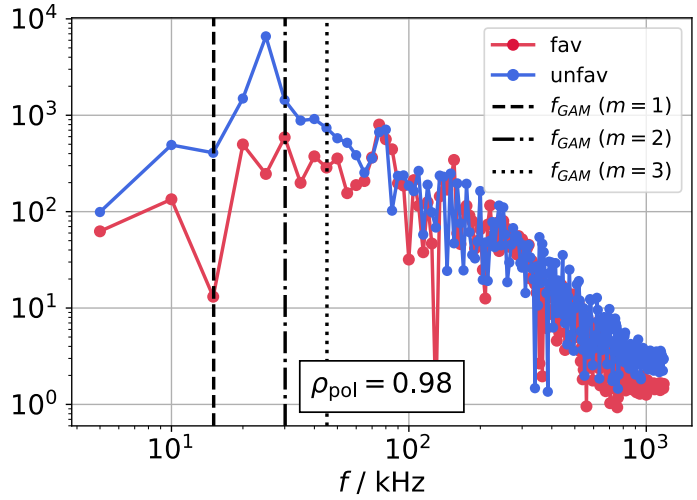

Figure 4.38: *Frequency spectrum of the OMP E_r at $\rho_\psi = 0.98$, showing a prominent peak around 20–30 kHz in UNFAV, probably associated with stronger GAM activity. $m = 1, 2, 3$ are the harmonics of the theoretical GAM frequency. Courtesy of B. J. Frei.*

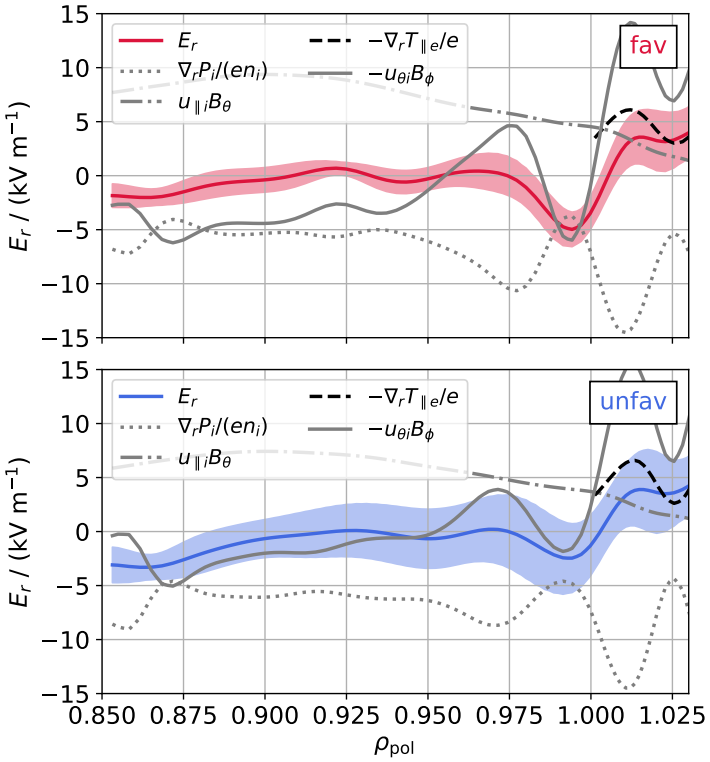

Figure 4.39: *Main ion radial force balance in the FAV and UNFAV* `GENE-X` *simulations. The toroidal rotation is approximated by the parallel ion velocity, $u_{\phi i} \approx u_{\parallel i}$.*

In simple terms, Eq. (4.1) states that net poloidal acceleration from turbulence requires a radial variation in the average tilt of eddies on a flux surface.

Figure Fig. 4.40 shows 2D snapshots of potential fluctuations in GENE-X near the bottom of the simulation domain (including the X-point). In both drift configurations, the eddies

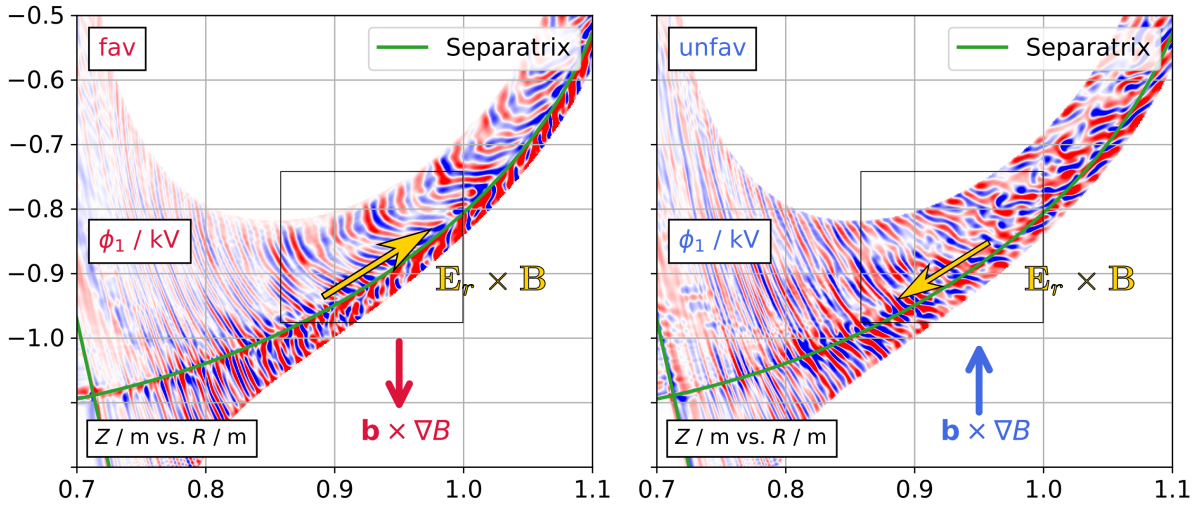

Figure 4.40: *Snapshots of the poloidal cross-section of potential fluctuations (ϕ_1) in GENE-X for the FAV (left) and UNFAV (right) configuration.*

are radially stretched and tilted poloidally. This generates a $(\tilde{V}_r\tilde{V}_\theta)$ contribution to the total stress $(\Pi_{r\theta})$. The latter is defined in Ref. [221] and represents a full-f generalization of the velocity stress, which includes the conventional Reynolds stress $\mathcal{R}_{r\theta} = \langle\tilde{V}_r\tilde{V}_\theta\rangle$. As emphasized in Ref. [221], the radial gradient of $\Pi_{r\theta}$ may contain additional contributions from poloidal density asymmetries and/or radial tubulent transport of poloidal momentum density. Here, to simplify the qualitative discussions, we approximate $\Pi \simeq M\mathcal{R}$ (with M the total mass density), that is, no distinction is made between the Reynolds and the total velocity stress. Within this approximation, $\Pi_{r\theta}$ remains a measure of the eddy tilting, like the Reynolds stress. The 2D map of the *local* stress contributions to $\Pi_{r\theta}$ is displayed in Fig. 4.41 for the upper and lower regions of the plasma. The sign of $\Pi_{r\theta}$ tends to reverse between the top and bottom regions, which tends to cancel its average on a flux surface[12]. However, poloidal regions of high flux expansion—such as the X-point region—weigh strongly in the flux surface average [204]. Combined with the higher turbulence intensity in the LFS, this implies that the LFS region between the X-point and the OMP accounts for the bulk of the overall stress.

We therefore limit the discussion to this region (lower panels in Fig. 4.41). A closer look at the radial structure of $\Pi_{r\theta}$ reveals a qualitative difference: In FAV, $\Pi_{r\theta}$ displays a notable radial variation, whereas it is radially more homogeneous in UNFAV. This translates into a $\mathrm{d}\Pi_{r\theta}/\mathrm{d}r$ term that is larger near the separatrix in FAV than in UNFAV, driving the poloidal rotation more strongly away from its neoclassical value.

The underlying mechanism for this difference relates to the concept of magnetic-shear-induced Reynolds stress, originally put forward in Refs. [112, 113] and introduced in

[12] This relates to the up-down antisymmetric pattern of magnetic-shear-induced tilting, peviously mentioned in Sec. 2.6.

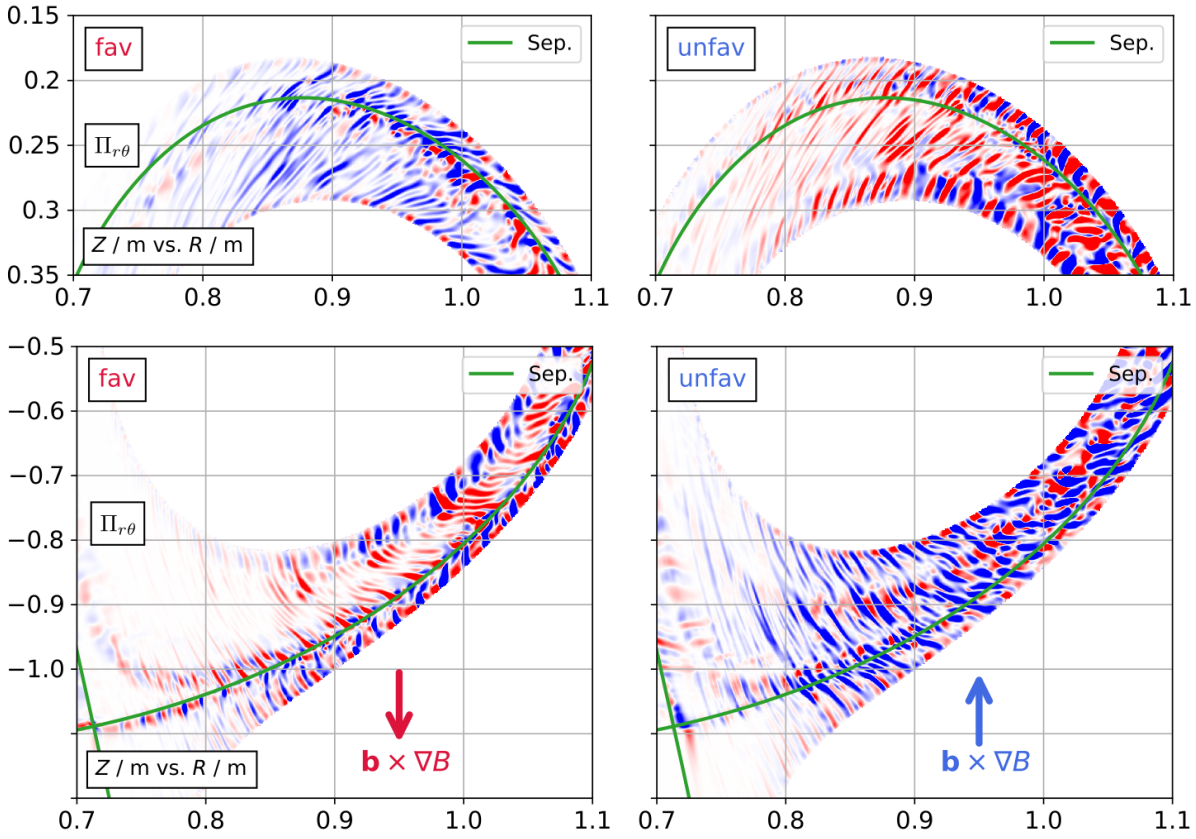

Figure 4.41: *2D map of the local velocity stress ($\Pi_{r\theta}$) in the upper and lower plasma regions (top and bottom panels, respectively). $\Pi_{r\theta}$ displays a stronger radial variation near the X-point in FAV than in UNFAV, reflecting a higher turbulence-driven poloidal flow acceleration. Courtesy of B. J. Frei.*

Sec. 2.6. This stress synergizes or competes with the $E_r \times B$ shear depending on the drift configuration, creating an asymmetry that promotes the enhancement of flow shear in the FAV case.

The nonlinear energy transfer from turbulence to the mean poloidal flow was investigated in the AUG simulations from Ref. [221]. The transfer was found to be substantially higher in FAV. The authors concluded that this difference causes the FAV/UNFAV asymmetry, as local neoclassical effects do not explain the edge E_r profile difference.

To conclude, `GENE-X` simulations of both AUG [221] and TCV experiments reveal an E_r well enhancement in FAV compared to UNFAV, consistent with experiments. This enhancement is due to a more efficient nonlinear energy transfer from the turbulence (primarily between the X-point and OMP) to the mean poloidal flow, promoted by the $E_r \times B$ flow shear direction. These comparisons between experiments and simulations provide strong support for an explanation of the FAV/UNFAV E_r well difference along the lines of previous work [112, 113, 204, 217, 218]: They confirm that a Reynolds stress asymmetry can qualitatively and quantitatively account for the experimental trend, within a *self-consistent* description of edge turbulence-flow interaction in a realistic X-point geometry.

4.7 Chapter summary and discussion

The FAV/UNFAV asymmetry of the L-H transition power threshold ($P_{\mathrm{L}\to\mathrm{H}}$) in tokamaks with regard to the magnetic ($B \times \nabla B$) drift configuration lacks a generally accepted explanation. This chapter investigated the influence of drift configuration on the L-mode E_r profile at the edge. The study was based primarily on new experiments on TCV, complemented by comparisons with WEST and AUG results. The FAV/UNFAV comparisons in TCV covered a wide range of plasma conditions, with variations in the shape (LSN or USN), plasma current, density and heating.

Overall, the FAV $B\times\nabla B$ configuration exhibits a deeper L-mode E_r well than the UNFAV case, consistent with earlier studies on AUG [122, 137] and WEST [46]. It underpins the robustness of the E_r well asymmetry across different machines and plasma conditions. The TCV results also confirm the existence—in Ohmic heating—of pronounced edge $E_r \times B$ shear differences between FAV and UNFAV even under well-matched edge kinetic profiles (Sec. 4.2.1). This behavior does not appear compatible with a neoclassical description of E_r in TCV, as given by Eq. (2.7) or Eq. (2.9). This conclusion aligns with the AUG study [122], and points to other edge E_r drives not captured by neoclassical theory, such as IOL or Reynolds stress.

Another notable finding of the TCV analysis is that the edge impurity toroidal rotation appears largely uncorrelated to the $B \times \nabla B$ drift (Sec. 4.2.2). This observation is in contrast with Alcator C-Mod [201, 202, 210] and in agreement with AUG results [122]. Together, these results from TCV and AUG do not support the interpretation proposed by LaBombard *et al.* [202], which attributes the FAV/UNFAV asymmetry to differences in toroidal rotation boundary conditions imposed by transport-driven parallel SOL flows.

Near the E_r well minimum, a more pronounced oscillating flow component is identified in

the UNFAV drift case—indicative of a stronger GAM activity (Sec. 4.2.4). A consistent trend is also seen in GENE-X simulations (Sec. 4.6). Further combined E_r and GAM characterizations in TCV are necessary to assess how they correlate more generally, beyond the considered Ohmic scenarios. A corresponding effort is ongoing [228].

Particular attention in this FAV/UNFAV study was devoted to the E_r dependence on plasma current (I_p), motivated by previous observations on Tore Supra [212] and WEST [46], see Sec. 4.3. The previously reported deepening of the E_r well with increasing I_p in the UNFAV configuration [46] is now unambiguously confirmed in WEST, both in well-matched, stationary Ohmic and in auxiliary-heated discharges (Sec. 4.3.2 f). In contrast, on TCV, detailed I_p scans show only a weak sensitivity of the E_r well to I_p (Sec. 4.3.4). Instead, both FAV and UNFAV configurations exhibit an increase in the core E_r level, accompanied by a co-current shift in the toroidal impurity rotation. Consequently, unlike in WEST, no clear, drift configuration dependent response of E_r to changes in I_p is observed. Likewise, a restricted I_p scan in AUG in the UNFAV configuration (Sec. 4.3.5) displays little variation in the E_r well depth, while E_r increases in the core (in agreement with TCV) and in the SOL. The differing behavior between WEST and TCV/AUG, albeit puzzling, may offer an opportunity: Forthcoming detailed comparisons of plasma conditions between the devices may help pinpoint the key ingredients responsible for this discrepancy, and, thereby, for the E_r well formation in general.

Density scans in TCV reveal that increasing density reduces the E_r well disparity between FAV and UNFAV (Sec. 4.4)—a trend which has not been reported yet on WEST or AUG. Meanwhile, both drift cases exhibit a decrease of E_r in the core with rising density, accompanied by a counter-current shift in toroidal rotation. Practically, this implies that density variations must be carefully controlled or accounted for when assessing the influence of other parameters on E_r, thereby justifying the effort to maintain constant density during the I_p scans presented in Sec. 4.3. An effect of density on the edge E_r (or intrinsic rotation) may be expected in particular from charge-exchange interaction with neutrals [51–55]. As pointed out in [122], the latter may depend on the precise magnetic configuration [55]. Whether neutral effects can explain the reduced E_r well FAV/UNFAV difference at higher density is an open question left for future studies.

As TCV plasmas approach the L-H transition, the difference in the E_r well between FAV and UNFAV becomes increasingly pronounced, in parallel with a growing asymmetry in edge gradients and confinement. This is consistent with a tight connection between the mean $E_r \times B$ shear and $P_{\mathrm{L}\to\mathrm{H}}$ in TCV, although it does not, by itself, establish causality. In general, this observation aligns with the L-H transition studies on DIII-D and AUG reviewed in Sec. 2.8, while contrasting with JET and MAST results.

The comprehensive set of matched FAV/UNFAV TCV experiments—both Ohmically and auxiliary heated—provides a solid foundation for detailed comparisons with simulations. Such joint analysis appears essential for disentangling the E_r drives, and to identify the key ingredient underlying the FAV/UNFAV asymmetry: parallel SOL flows, ion orbit losses, or turbulence-driven Reynolds stress. Recent GENE-X simulations of AUG [221] and TCV discharges (Sec. 4.6) provide strong support for the latter. They self-consistently recover differences in the E_r well depth similar to the experiments. This is attributed to a nonlinear energy transfer at the very edge from the turbulence to the mean poloidal

flow, that is enhanced in FAV compared to UNFAV by the direction of $E_r \times B$ shear—akin to the interplay between magnetic and $E_r \times B$ shear underlying the idea of previous models [112, 113, 204, 217, 218].

In summary, the TCV experiments broadly confirm the $B \times \nabla B$ drift effect on E_r previously documented in WEST and AUG. The cross-device comparison, however, highlighted also a discrepancy in the I_p dependence, with WEST exhibiting a markedly stronger sensitivity to I_p than the other two devices. In addition, in TCV, density and auxiliary heating were found to modulate the FAV/UNFAV difference in E_r. The experiments served as the basis for modeling of the FAV/UNFAV asymmetry in TCV using `GENE-X`, with results corroborating the existence of a turbulence-driven edge $E_r \times B$ asymmetry that can account for the experimental observations.

Chapter 5

Influence of Shaping: E_r in Positive versus Negative Triangularity TCV Plasmas



Contents

5.1 Review of NT (edge) studies **136**
5.2 NT/PT comparison in USN **138**
5.3 NT/PT comparison in LSN **150**
5.4 Limited configuration **153**
5.5 Towards higher performance in fully NT shape **156**
5.6 Chapter summary and discussion **161**

This chapter investigates the impact of triangularity on the edge E_r profile in TCV plasmas. As previously explained, triangularity gives the plasma its typical "D"-shape. While conventional tokamak plasmas usually have positive triangularity, Fig. 5.2 (b), negative triangularity (c) corresponds to a flipped "D"-shape. The average edge triangularity is

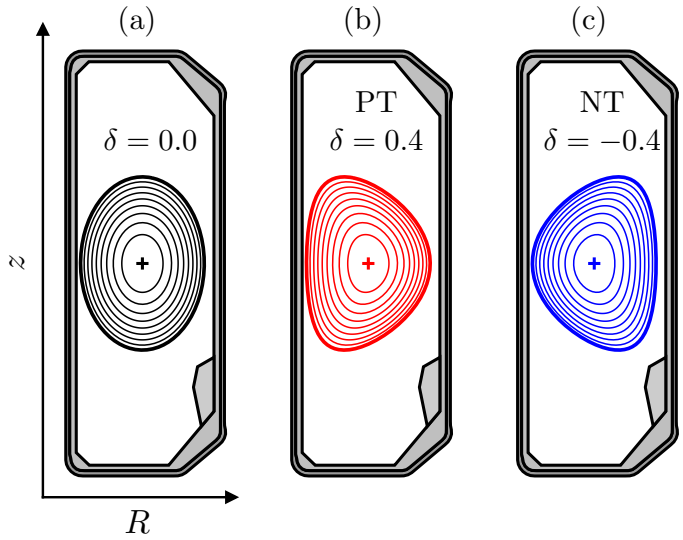

Figure 5.1: *Triangularity (δ) measures the "D-ness" of the plasma shape. Flux surfaces are sketched for the cases of (a) zero, (b) positive and (c) negative δ, respectively.*

denoted δ. For up/down asymmetric equilibria, the top and bottom triangularities (δ_{top}

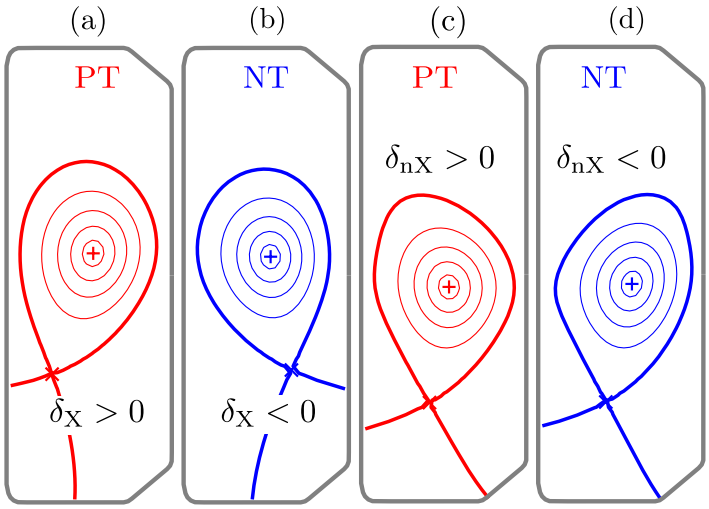

Figure 5.2: *Illustration of the distinction between X-point and non-X-point triangularities (δ_{X} and δ_{nX}) in case of diverted configurations. Shapes (a) and (b) have neutral δ_{nX}, and postive/negative δ_{X}. Conversely, (c) and (d) have neutral δ_{X}, and postive/negative δ_{nX}. The sign of the overall δ is indicated by the color-code and the NT/PT labels.*

and δ_{bot}) may be distinguished. The definitions of δ_{top}, δ_{top} and δ are provided in Appendix B. Further, we adopt the following terminology in case of diverted configurations (Fig. 5.2); the *X-point* triangularity, δ_{X}, refers to δ_{bot} (δ_{top}) in case of a lower (upper) single-null, and vice-versa for the *non-X-point* triangularity, δ_{nX}. The distinction δ_{X} and δ_{nX} will be relevant in the following.

Negative triangularity (NT) has emerged in recent years as a promising candidate reactor configuration (see [238] for a review), aligned with a "power-handling-first" reactor design strategy [239]; By preventing the transition from L- to H-mode, NT passively suppresses so-called "edge-localized modes" (ELMs). These harmful instabilities associated with typical H-modes must be avoided or mitigated in future reactors [240], as they might cause prohibitively large heat fluxes to plasma-facing components. At the same time, NT-shaped plasmas exhibit particularly good L-mode confinement [18, 20–23, 241–243], comparable with H-mode in positive triangularity (PT).

These favorable NT properties, which will be elaborated in the review section below, strongly motivate further investigation of their underlying mechanisms. Such an understanding is essential for assessing how NT scenarios extrapolate to reactor-relevant conditions.

Moreover, owing to their exotic shape—accessible only to few tokamaks and often with significant constraints, NT plasmas have been studied and diagnosed less than their PT counterparts. Characterizing the edge E_r profile in NT is therefore especially relevant, as it is scarcely documented so far. In particular, comparing E_r in NT and PT discharges could clarify whether improved L-mode confinement in NT is linked to enhanced edge $E_r \times B$ shear. This motivates the present study, whose results are presented after reviewing the relevant context below.

5.1 Review of NT (edge) studies

A key feature of NT—albeit not the main focus here—is the avoidance of H-mode in sufficiently strong NT shapes. This was convincingly demonstrated in TCV [20] and DIII-D [23–25]. In particular, the DIII-D database [24] provides a critical threshold, $\delta_{\text{crit}} \sim -0.15$, below which ELMy H-modes are robustly suppressed, and intermediate (presumably I-phase) regimes are absent for $\delta \lesssim -0.3$. On AUG, on the other hand, plasmas with negative top triangularity readily enter ELMy H-modes [241, 244]. Nevertheless, even in H-mode, NT has a beneficial impact on the ELM behavior; It tends to increase their frequency, thereby reducing their intensity compared to typical type-I ELMs [20, 241, 244]. A prominent hypothesis for the H-mode suppression invokes the destabilization of infinite-n MHD ballooning modes, closing access to second stability [245–247]. Consequently, the growth of the pressure pedestal is limited to levels below H-mode, preventing the triggering of large edge localized modes (ELMs)—which are possible showstoppers for the operation of future reactors.

Concerning the outstanding L-mode confinement observed in NT—on which the study focuses, a generally conclusive picture has not emerged yet. However, several relevant hints have been obtained: The empiric reduction of fluctuation levels in NT compared to PT [21, 22, 248–253], as well as modeling results [254–260], point to a beneficial effect of NT on ion-scale turbulence. In particular, modeling results suggest a stabilization of trapped electron modes (TEM) [254, 259, 260], while recent studies find a similar impact also on ion temperature gradient (ITG) driven modes [256, 258]. Past numerical studies focused mainly on the core, with NT edge modelling in realistic diverted geometry emerging more recently [84, 86, 87, 260].

Further, experimental findings from DIII-D [24, 25] and TCV [243, 261] highlight the importance of the plasma edge, attributing the performance gain in NT partly to increased values of pressure and of its gradient near the separatrix. Yet, the fundamental reason for this distinct edge behavior remains unclear.

A possible enhancement of the $E_r \times B$ shear in NT has been alluded to in Ref. [253] to explain differences in turbulence level, notably around the separatrix. However, clear supporting evidence from detailed edge E_r measurements are not presented. The geometric sensitivity of $E_r \times B$ shear to triangularity has been examined theoretically [262]. It was found that the NT configuration benefits from an overall increase in shear compared to PT—for a fixed radial profile of the electrostatic potential—due to a stronger Shafranov shift gradient. Moreover, the poloidal distribution of the shearing rate changes going from PT to NT, resulting in a weaker shearing efficiency in NT at the OMP. Whether the magnitude of this direct geometrical effect is relevant compared to typical experimental shearing rates associated with the edge E_r well is a question left for future work.

Intrinsic toroidal rotation is discussed as another possible factor in explaining the good edge confinement in NT. Strongly NT shapes in DIII-D exhibit a pronounced counter-current rotation in NT just inside the separatrix [263], contrasting with a usually co-current rotation in PT. In addition, a scan of the X-point triangularity (δ_X) in diverted TCV shapes [89] revealed a counter-current shift with decreasing δ_X. This observation was found consistent with predictions based on a model of enhanced turbulent loss of co-

passing ions in NT compared to PT [89]. This turbulent-IOL effect is invoked in a recent contribution [264] to explain the enhancement of the edge E_r well and confinement in DIII-D for strong NT shaping. However, the details of this study are not available at the time of writing this manuscript. In contrast to the above results, a different study on TCV [265, Fig. 23] finds no clear correlation between edge toroidal rotation and δ in a limited shape—despite the notable confinement improvement observed with decreasing δ. We will return to these various observations linked to toroidal rotation and discuss them in the light of new results presented in this chapter.

Recently, numerical investigations compared NT and PT shapes with respect to collisional edge effects associated with ion orbit losses (IOL) [84, 87] and/or finite orbit widths (FOWs) [86]. Ref. [84] finds that with an outward-shifted X-point, trapped ions are lost more easily, enhancing the overall loss rate of edge ions compared to PT. A test particle study [86] in DIII-D-like geometries examines IOL and FOWs effects in NT versus PT and how they connect to E_r. It is argued that the aforementioned higher IOL in NT prevents the buildup of the strong, highly-localized E_r well observed in PT H-mode, the latter being attributed—as advanced in [266]—to charge separation by FOWs. At the same time, [86] points out that the non-ambipolar IOL also drive a negative E_r inside the LCFS (broader than the PT one). In the absence of an imposed negative E_r, the simulations find a co-current edge flow in both NT and PT, while including a negative E_r at the edge leads to counter-current flow in NT, suggesting closer agreement with DIII-D experiments.

On the other hand, neoclassical edge simulations using the gyrokinetic `XGC` code find little difference in the self-consistent toroidal or $E_r \times B$ edge flow between NT and PT [87]. The simulations include the effects of neutrals and IOL, questioning the relevance of IOL effects alone in accounting for the difference between the NT and the PT edge.

Finally, nonlinear (edge) turbulence simulations comparing NT and PT along the lines of Ref. [260] (using the `GENE-X` code) are scarce, the resulting $E_r \times B$ flow behavior not documented yet. However, corresponding efforts are underway using various gyrokinetic codes [267–269]. The experimental characterization of the NT and PT edge E_r presented next is well-suited to guide and validate these timely numerical developments.

In this context, the present chapter examines the edge E_r profile in NT versus PT shaped plasmas in TCV. Thanks to the exceptional shaping flexibility of this device, careful NT/PT comparisons under otherwise matched conditions are performed across different L-mode plasma scenarios and geometries, thereby isolating the impact of triangularity. This study extends the scarce database on the E_r well in NT [241, 244, 253, 264] and provides—to the author's knowledge, the first systematic comparison of E_r in matched NT/PT discharges.

The remainder of this chapter is organized as follows. Sec. 5.2.1 compares the E_r well and other edge quantities in USN shapes with opposite bottom δ. This geometry is suitable for isolating the effect of non-X-point triangularity while minimizing potential measurement biases. The sensitivity to slight variations of these reference shapes is investigated in Sec. 5.2.2, and the case of auxiliary heating in Sec. 5.2.3. The DBS signal intensity, used as an indicator of the density fluctuation level in NT versus PT, is analyzed in Sec. 5.2.4. Then, we test how the findings extend to other geometries, in a comparable

LSN geometry—this time isolating the X-point triangularity (Sec. 5.3)—as well as in a limited NT/PT configuration (Sec. 5.4). Finally, Sec. 5.5 examines a higher-performance, strongly-shaped NT scenario in view of more reactor-relevant conditions. A summary and discussion are provided in Sec. 5.6. A selection of this chapter's key findings can be found in [270].

5.2 NT/PT comparison in USN

5.2.1 Ohmic case

Fig. 5.3 shows the equilibria of the Ohmic USN discharges, with favorable $B\times\nabla B$ drift, examined here. The shapes have opposite $\delta_{\text{bot}} \approx \pm 0.3$, but the equilibria are largely matched otherwise. Keeping the upper half of the shapes fixed ensures nearly identical DBS probing geometries. This minimizes possible biases e.g. due to differences in local flux expansion (see Sec. 3.7) or probed turbulence wave numbers ($k_\perp$). The latter varies radially in the range of $k_\perp \in [5, 6]$ rad/cm ($k_\perp \rho_s \sim 0.5$)[1], but differs only slightly ($\lesssim 10\%$) between NT and PT.

	PT / NT
P_{Ohm} [kW]	195
I_p [kA]	170
B_0 [T]	1.44
κ	1.5
δ_{top}	0.22/0.25
δ_{bot}	0.32/-0.34
q_{95}	4.2 /3.9
τ_E [ms]	22 /28
H_{98y2}	0.87 /1.0
β_N	0.83 /1.0
Z_{eff}	2.0 /2.4

Table 5.1: *Discharge parameters of the matched NT/PT pair.*

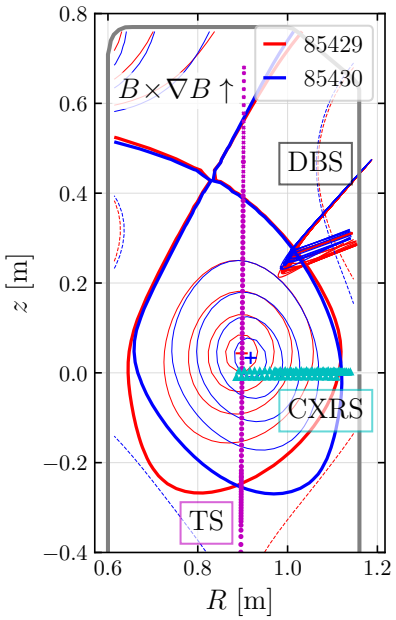

Figure 5.3: *Contours of ρ_ψ for the two shapes, with DBS beam paths and TS/CXRS diagnostic locations indicated.*

The main discharge parameters are summarized in Tab. 5.1. At fixed I_p and B_0, the NT geometry results in an edge safety factor (q_{95}) about 7% lower than in PT. This small difference is unlikely to affect the comparison, especially since the TCV experiments of Sec. 4.3 indicate only a minor influence of plasma current—and therefore q_{95}—on the E_r well.

[1] The ion Larmor radius at soundspeed, $\rho_s = \sqrt{T_e m_i}/eB$, is evaluated using $T_e(\rho_\psi = 0.95) \approx 0.1$ keV.

The $v_\perp$ profiles corresponding to a stationary phase of the discharges are displayed in Fig. 5.4 (a), T_i in (b), and n_e and T_e in (c) and (d), respectively. A remarkable difference

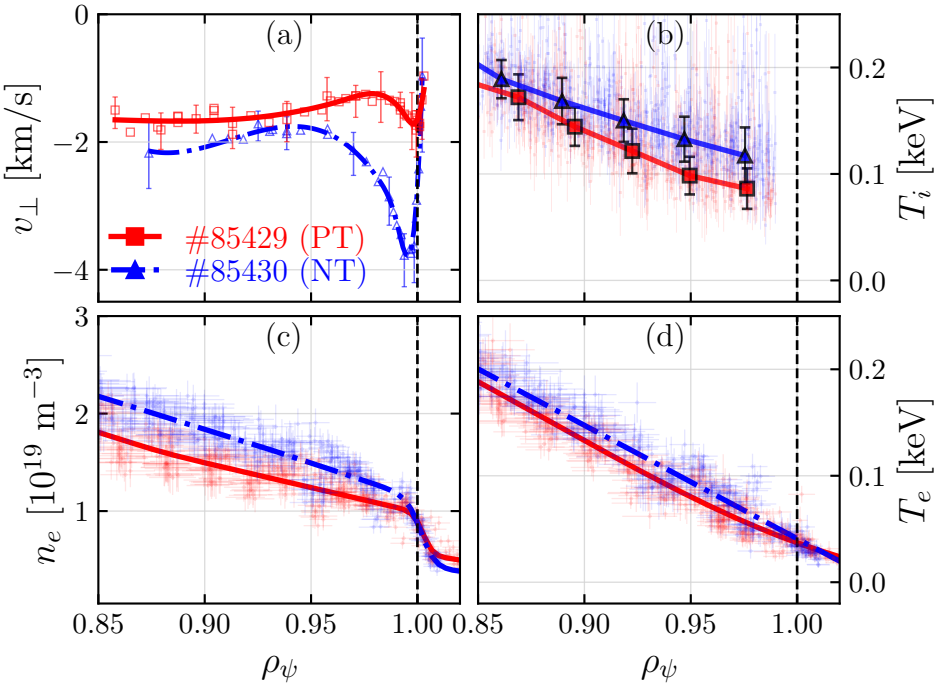

Figure 5.4: *Edge profiles acquired over a stationary phase $t \in [1.0, 1.5]$s: (a) Perpendicular ($E_r \times B$) velocity from DBS, (b) impurity (C^6+) ion temperature from CXRS, (c) density and (d) electron temperature from TS. Fits are overlaid to guide the eye; for T_i, markers also show the binned weighted average and standard deviation.*

is observed: The NT case exhibits a sharp well with a minimum of $v_\perp^{\min} \approx -4\,\mathrm{km/s}$. In contrast, that of the PT case has a depth of $v_\perp^{\min} \approx -2\,\mathrm{km/s}$, typical of comparable L-mode PT discharges in TCV, as seen in previous chapters (e.g. Chapter 3).

The kinetic profiles reveal a higher L-mode density pedestal in NT, radially coinciding with the velocity well, where $v_\perp$ differs most between NT and PT. At same levels of Ohmic heating, τ_E is increased by roughly 30 % in the NT case (see Tab. 5.1), as reflected by higher density—despite $\approx 35\,\%$ lower fueling rate—and slightly higher ion and electron temperatures, up to the core (not shown). The carbon impurity content is higher by roughly 30% in the NT case, translating into $Z_{\mathrm{eff}} \approx 2.4$ versus 2 in the PT case.

The C^{6+} toroidal velocity (V_φ), shown in Fig. 5.5, does not differ significantly between NT and PT. In particular in the outer core and edge regions, there is no notable difference in V_φ outside of the statistical spread. In the core, the intrinsic rotation is counter-current with a magnitude of $V_\varphi \approx 15 \pm 5\,\mathrm{km/s}$ (slightly weaker in PT), decaying toward near-zero at the edge. We will return to this observation at the end of this chapter, where it is discussed together with V_φ comparisons performed subsequently in other scenarios.

The impurity radial force balance results are displayed in Fig. 5.6a, alongside the OMP-mapped DBS data. The reconstructed E_r profile shows a reasonable agreement with the DBS mesurements; It qualitatively recovers the offset in E_r levels—with NT exhibiting a more negative E_r between the outer-core and edge ($0.85 \lesssim \rho_\psi \lesssim 0.95$). From the C^{6+} force

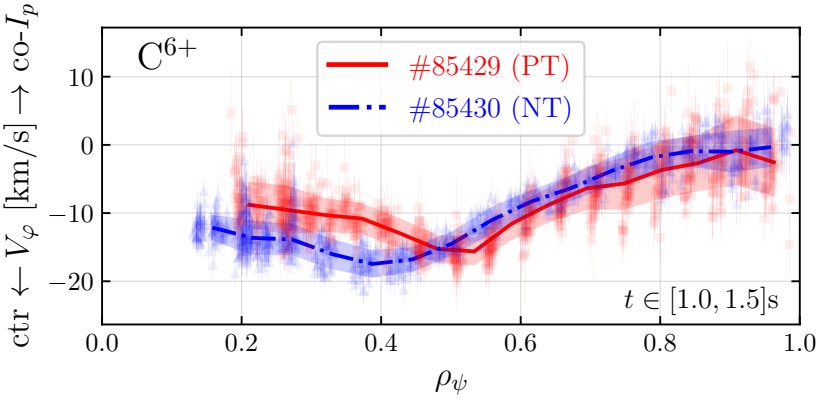

Figure 5.5: *Carbon toroidal rotation profiles measured by CXRS along the OMP. Curves representing the binned weighted average and standard deviation are overlaid on the CXRS data.*

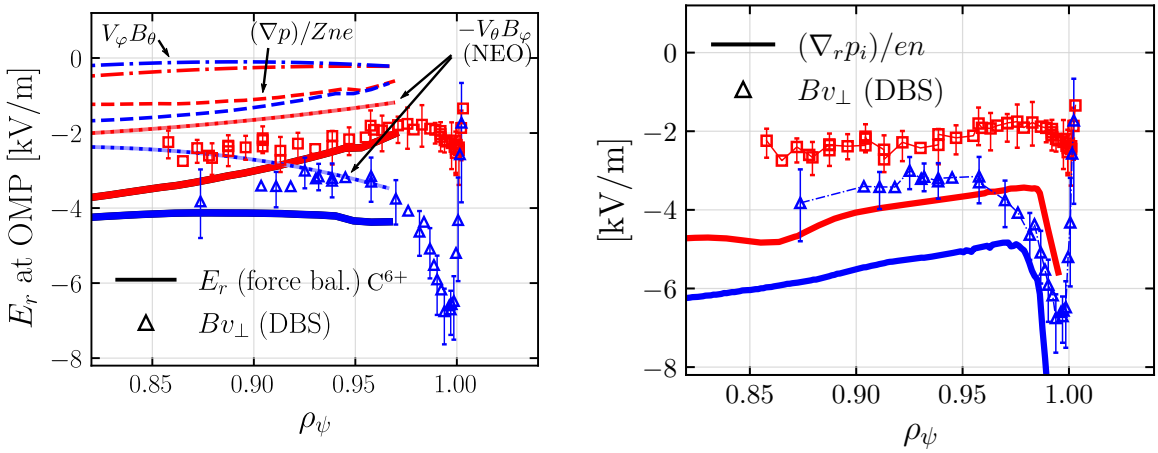

(a) **(b)**

Figure 5.6: *E_r data from DBS (mapped to the OMP) for the NT/PT pair of Fig. 5.4 compared to (a) the constituents of the C^{6+} force balance and to (b) the deuterium diamagnetic contribution to E_r.*

balance contributions (Fig. 5.6a), it is observed that the difference in E_r levels towards edge is mainly associated with the neoclassical V_θ contribution (derived from NEO, see Sec. 3.6). The impurity toroidal rotation and diamagnetic contributions, on the other hand, are very similar between NT and PT towards the edge. Yet, as was repeatedly pointed out earlier, the C^{6+} contributions provide limited intuition about the main ion force balance. These results should therefore be considered a consistency check rather than providing elements for interpreting the E_r drives.

Next, the deuterium diamagnetic contribution, $(\nabla_r p_i)/en$, is shown together with the DBS data in Fig. 5.6b. As before, it is estimated using the carbon T_i and with the approximation $n_e \approx n_i \equiv n$. It is observed that $(\nabla_r p_i)/en$, too, displays a clear, almost rigid offset between NT and PT over the entire outer core and edge region. This offset can account for the difference in the DBS-derived E_r level (at least up to $\rho_\psi \approx 0.97$). It appears challenging, however, to draw a conclusion as to the contribution of $(\nabla_r p_i)/en$ at the minimum of the E_r well, as the term tends to diverge towards the very edge (owing to the $T_i(\nabla_r n)/n$ contribution). This highlights the difficulty of precisely determining the relevant kinetic profiles and their gradients across the LCFS, even under the present stationary Ohmic conditions and despite the relatively good statistics.

5.2.2 Shape variations

The previous section compared two fixed USN geometries with opposite bottom triangularities $\delta_{\text{bot}} \approx \pm 0.3$, with the NT case exhibiting a notably deeper E_r well and improved confinement. Next, the sensitivity of this finding to slight variations in the plasma shapes is investigated.

Based on the reference USN scenarios of the previous section, a similar NT/PT pair is programmed. It starts from the same equilibria as previously displayed in Fig. 5.3. Two shape modifications are programmed during the flat-top, applied respectively to the δ_{bot} and δ_{top}. Each shape is maintained for a stationary time window of at least 200 ms.

The various shapes are shown in Fig. 5.7a and Fig. 5.7b for the PT and NT case, respectively; From the reference shape (I) to the second shape (II), the magnitude of δ_{bot} is increased symmetrically for both the PT and NT shapes. Then, in the transition from (II) to (III), the X-point location is shifted towards the HFS. This increases δ_{top} and the overall δ (not their magnitude) for both shapes.

Fig. 5.8 compares the edge $v_\perp$ and electron kinetic profiles for NT and PT acquired during the phases of (I–III). $v_\perp$ shows little variation with the different PT shapes. In contrast, the NT E_r well becomes increasingly deeper from (I) to (III), exceeding a well depth of -4 km/s. As noted earlier, we stress that for typical diverted discharges in TCV, $v_\perp^{\text{min}} \simeq -4$ km/s is already an exceptional value.

From (I) to (II), this deepening is accompanied by an increase in the edge n_e and T_e in NT. These changes occur despite gradually less fueling, which results from the density feedback-control. From (II) to (III), while the depth of the well clearly deepens further, the edge electron pressure increase is more subtle.

Next, we consider the thermal energy as a measure of confinement. Note that from Fig. 5.7,

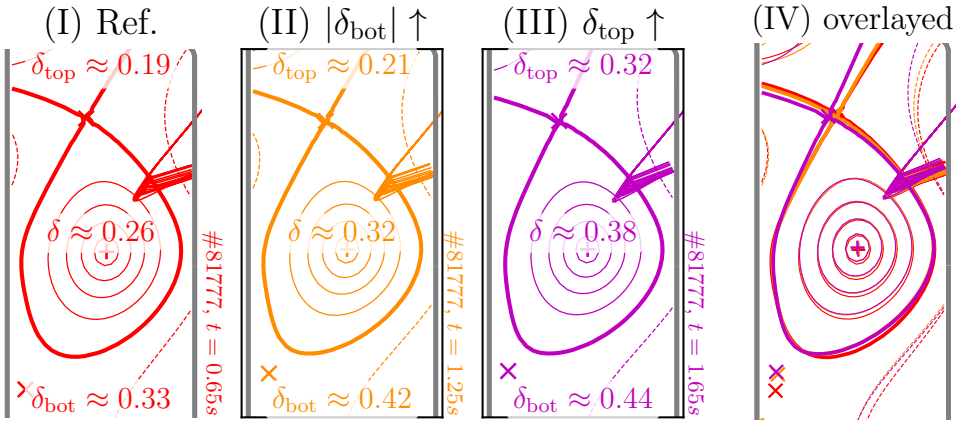

(a)

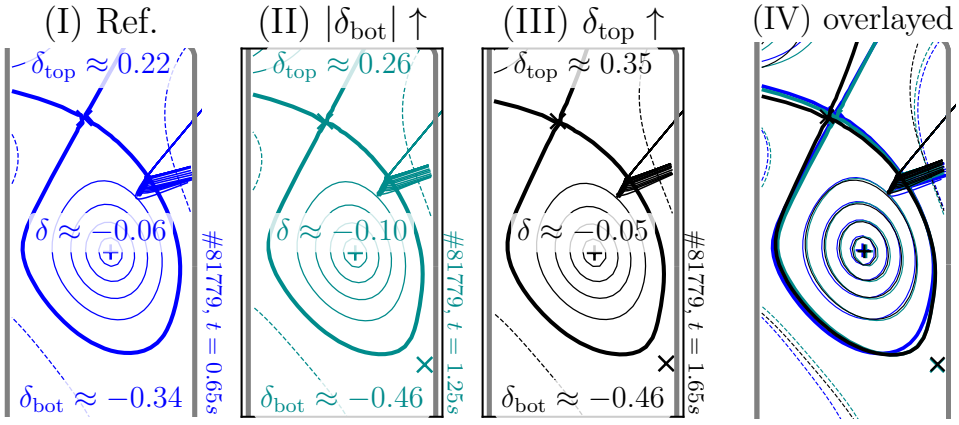

(b)

Figure 5.7: *Shaping variations applied symmetrically to the (a) PT and (b) NT case: Starting from the reference shapes of Sec. 5.2.1 (I), the magnitude of the bottom triangularity is increased (II), and subsequently the top triangularity is increased (III).*

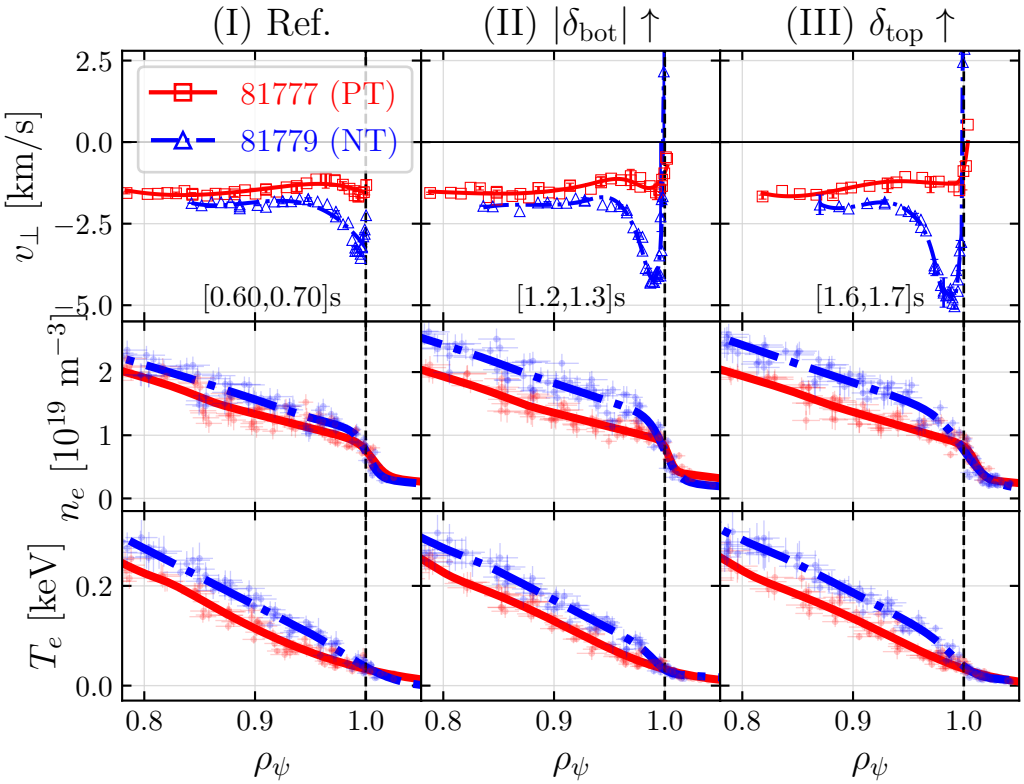

Figure 5.8: *From top to bottom: perpendicular velocity, electron density and temperature profiles. The columns (I–III) correspond to the shapes shown in Fig. 5.7.*

panels (IV), variations in the plasma volume are small and therefore neglected in the following. The total and electron energies (W_{tot} and W_e) are displayed in Fig. 5.9. In PT, both W_{tot} and W_e stagnate or slightly decrease from (I) to (II). In NT, on the other hand, they exhibit a notable increase from shape (I) to (II), indicating a gain in confinement. From (II) to (III), the total energy appears to stagnate—within uncertainties—in both NT and PT, despite the further E_r well deepening observed in NT. This observation might indicate that the depth of the E_r well may not always be a good proxy for its shear in general. Alternatively, the shear might not be relevant enough here to impact global confinement. In any case, due to the considerable statistical uncertainties in W_{tot} during phase (II), repeating these experiments seems appropriate to assess the robustness of this observation. Further, it would be interesting to monitor global confinement changes as a function of edge $E_r \times B$ *shear*—quantified using an appropriate proxy. This is left for future work. Here, we focus on a qualitative discussion of their correlation.

We conclude that the growing NT/PT differences observed between (I) and (II)—in terms of E_r well, kinetic profiles, and confinement—are consistent with an amplification of the shaping-related effects as δ_{bot} decreases from -0.33 to -0.46. This supports a robust and genuine effect associated with negative δ_{nX}. Interestingly, *increasing* top (δ_{X}) triangularity in the NT shape—thereby *reducing* the magnitude of the overall δ—further enhances the E_r well depth, albeit with a lesser impact (if any) on the overall confinement.

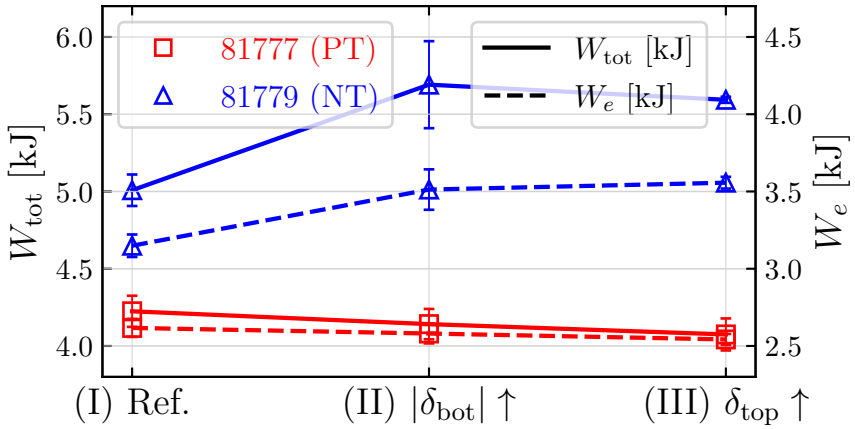

Figure 5.9: *Total and electron thermal energy (W_{tot} and W_e) for the different shapes of Fig. 5.7. The NT/PT confinement difference is notably enhanced from (a) to (b). Note the different scales used for W_{tot} and W_e (left and right axis), which maintain an equal spacing.*

5.2.3 Auxiliary Heating

Having examined how the NT/PT scenarios of Sec. 5.2.1–5.2.2 compare under Ohmic heating, we now investigate whether the higher L-mode confinement and deeper E_r well observed in NT persist under moderate auxiliary heating.

To begin this analysis, the NT/PT USN shapes of Sec. 5.2.1 are compared at the same heating power, delivered either by a co-current neutral beam (NBI-2) or by second-harmonic electron cyclotron resonance heating (ECRH). Following this, we perform a similar comparison at different heating powers—higher in PT—to match the kinetic profiles.

Fig. 5.10 displays the edge $v_\perp$ and kinetic profiles for the comparison at equal heating powers, with $P_{\text{NBI}} = 420\,\text{kW}$ (left column) and $P_{\text{ECRH}} = 580\,\text{kW}$ (right column). It shows that the E_r well difference noted previously in the Ohmic cases, persists clearly under both NBI or ECRH. Similarly, the edge n_e, T_e and T_i remain higher in NT. The difference is particularly visible when considering T_e and n_e in the ECRH case; Compared to the Ohmic counterpart (Fig. 5.4), the E_r well depth, as well as the n_e and T_e L-mode pedestal heights, are further enhanced in NT.

Next, the heating power is adjusted between NT and PT to achieve a closer match in the kinetic profiles. Not only does it offer a more direct comparison at fixed turbulent drives associated with the kinetic profile gradients. From a practical perspective, the matched density profiles also enable a meaningful comparison of DBS signal amplitudes, performed subsequently in Sec. 5.2.4.

Fig. 5.11 shows the results of this comparison. Compared to Fig. 5.10, the PT data are replaced by that obtained in a different time window of the same discharges—corresponding to a higher heating power. As intended, a notable difference to the previous "equal heating" comparison (Fig. 5.10) is that the edge n_e and T_e profiles are now reasonably matched between NT and PT. In the ECRH case, this is true also for T_i (Fig. 5.11 f), whereas in the NBI case (Fig. 5.11 c), no T_i data is availale in PT within the precise time window

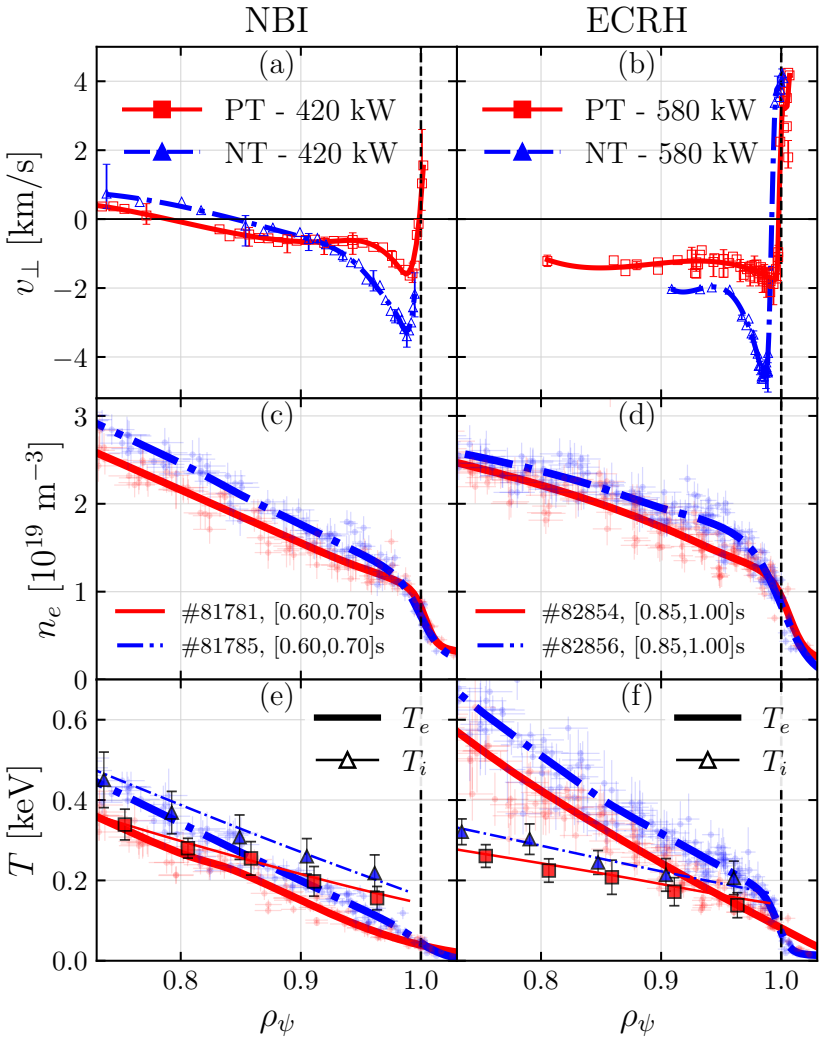

Figure 5.10: *(a-b) Perpendicular velocity and (c-f) edge kinetic profiles for a NT/PT comparison under auxiliary heating via NBI (left) or ECRH (right columns), using the same power in NT and PT. The USN equilibria are close to those in Fig. 5.3. .*

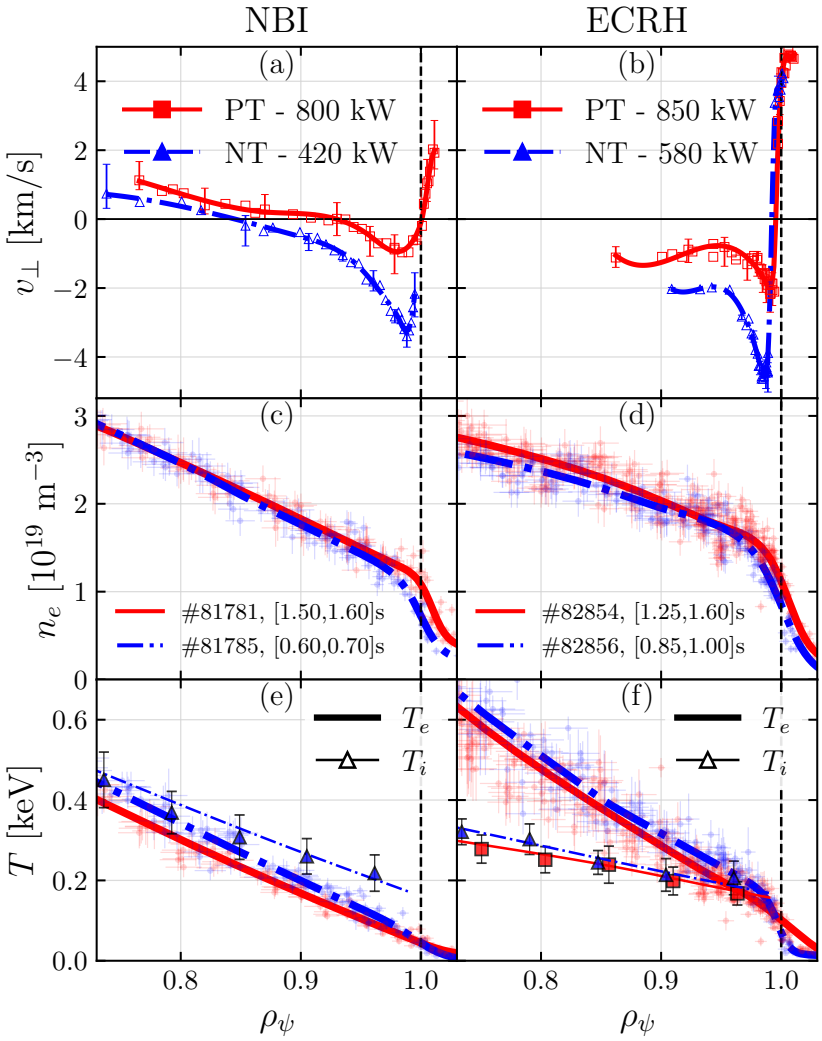

Figure 5.11: *Same representation as in Fig. 5.10, except for the PT data which corresponds to a higher heating power, chosen for a better NT/PT match of the kinetic profiles. Due to missing CXRS data in this interval, T_i profiles are omitted for #81781.*

considered. However, the preceding CXRS data indicates that T_i remains similar to the lower heating phase of Fig. 5.10 (e) and, therefore, still lower than in NT.[2] It should be emphasized that, in spite of the closer match in edge kinetic profiles, the E_r well depth in NT, and the associated inner $E_r \times B$ shear layer, remain considerably more pronounced than in PT.

Next, Fig. 5.12 provides an overview of the stored (total and electron) energy in the various heated NT/PT scenarios. For reference, the Ohmic case from Sec. 5.2.1 is included as well. Superior L-mode confinement was already found in Ohmic conditions, and it is also

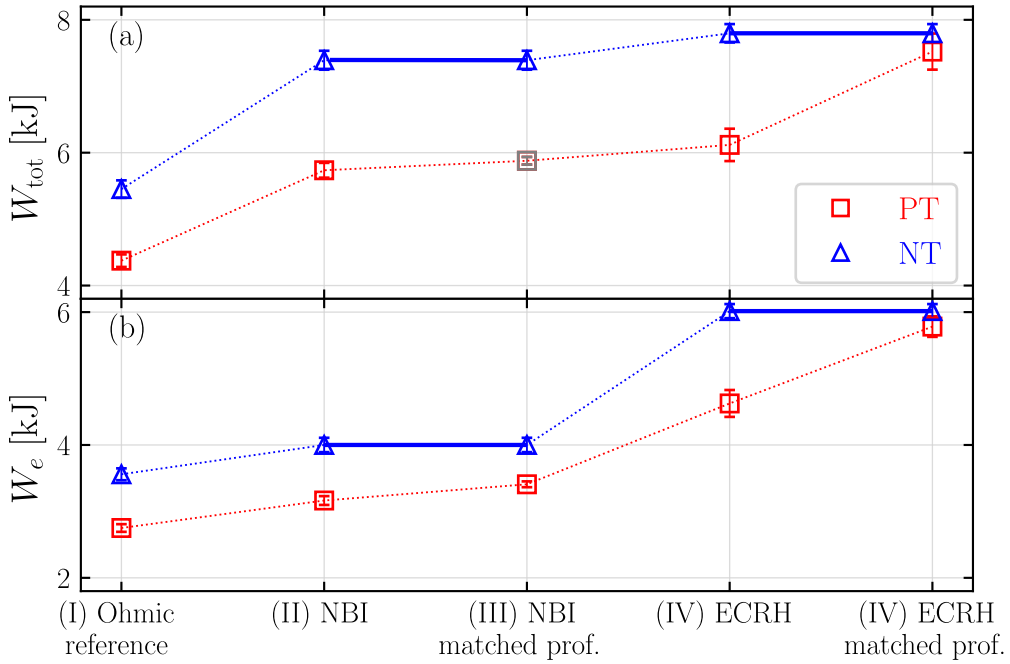

Figure 5.12: *(a) Total and (b) electron thermal energies for the various NT/PT comparisons discussed above. Dotted lines are included for visual reference, and identical data points are connected by solid lines. The greyed data point in (a) corresponds to the closest available PT time window with T_i data (see note [2]). The ECRH comparison with matched kinetic profiles (V), corresponding to the right column of Fig. 5.11, shows good agreement in terms of global energy, too.*

evident from (I) in Fig. 5.12. Next, we focus on the "equal heating" scenarios (II and IV in Fig. 5.12). The relative NT/PT difference in terms of W_{tot} and W_e persists, or is even slightly enhanced, with auxiliary heating, whether by NBI (II) or ECRH (IV).

Next, we consider the cases with higher heating in PT than NT (Fig. 5.12, II and V). In the ECRH "matched profiles" comparison (V), the agreement between the stored energies in NT and PT is evident. This reflects the close match in kinetic profiles mentioned

[2] In the 100 ms preceding the considered time window in PT, the average NBI power is only slightly lower (770 kW instead of 800 kW), and CXRS data indicates little difference in the (core and edge) T_i compared to 420 kW (Fig. 5.10 e). As a consequence, it is reasonable to assume that T_i remains higher in NT here, despite the good match in electron kinetic profiles.

previously (Fig. 5.11, right column)[3]. In contrast, the match in W_{tot} is not good in the NBI counterpart (III). This is likely attributed to the lower T_i in PT, as noted earlier.

In conclusion, given the consistently sharper well in NT compared to PT, these results suggest that the previous findings of Sec. 5.2.1 hold robustly also for auxiliary heated discharges. In particular, the NT/PT difference in edge $E_r \times B$ shear and L-mode confinement appear resilient, whether external momentum is applied or the dominant heating species is changed (which causes $T_i \sim T_e$ or $T_i \ll T_e$ in the core for NBI and ECRH, respectively).

Moreover, a higher auxiliary power is needed in PT to sustain edge kinetic profiles and stored energies similar to NT. This suggests that NT tends to reduce turbulent heat diffusivity, in line with the general expectation based on past experiments and simulations mentioned earlier in Sec. 5.1, and further discussed below. It is worth noting that such a reduction in turbulent transport might not necessarily be associated with $E_r \times B$ flow shear. It might be caused also by lower turbulence drive and/or higher stabilization through other, non-trivial effects related to the different geometries. However, the fact that the E_r well remains sharper in NT *even though the kinetic profiles are matched*—as is clearly the case in Fig. 5.11 (b)—supports the possibility of a turbulent transport reduction caused by enhanced $E_r \times B$ shear.

5.2.4 Comparison of DBS power

For a qualitative assessment of the density flucutation levels based on the DBS data, we compare the PSDs as previously performed in Chapter 4, Sec. 4.2.3. Here, the method is applied to the NT/PT pair with ECRH heating and matched edge kinetic profiles (Fig. 5.11) discussed earlier.

Fig. 5.13 compares the PSDs for a few representative probing frequencies (f_0). The measurements correspond to radial locations in the E_r well region. Thanks to the matched

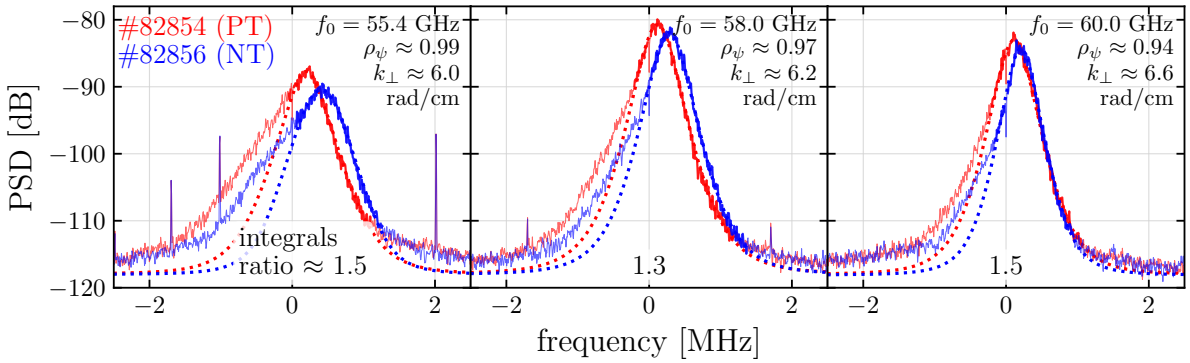

Figure 5.13: *DBS power spectral density (PSD) comparison between NT and PT at matched density (ECRH scenarios from Fig. 5.11). Dashed lines indicate fits to the main peak, whose integral reflects the turbulence intensity $|\tilde{n}(k_\perp)|^2$. The PT to NT ratio of this integral is annotated at the bottom.*

probing geometry and density profiles, for given f_0, ρ_ψ and $k_\perp$ are nearly the same, to

[3] Note that the L-mode confinement level, measured e.g. in terms of τ_E (not shown), remains clearly higher in NT than PT (12 ms and 8 ms, respectively), since the ECRH power is higher in the latter.

within 1 % and 2 %, respectively. As noted previously, this allows for a meaningful comparison of the integral over the Doppler peak, used as a proxy for $|\tilde{n}(k_\perp)|^2$.

Looking at the Doppler peaks in Fig. 5.13, the stronger Doppler shift merely reflects the deeper E_r well in NT. Notably, the maximum of the peak is somehwhat higher in PT. This results in an integrated PSD that is higher in PT. The ratio between PT and NT of these integrals is annotated at the bottom of Fig. 5.13.

This trend persists, except for few outliers, across the available data points. They are displayed in Fig. 5.14 (b) together with the $v_\perp$ profiles (a) as a reference. Owing to the

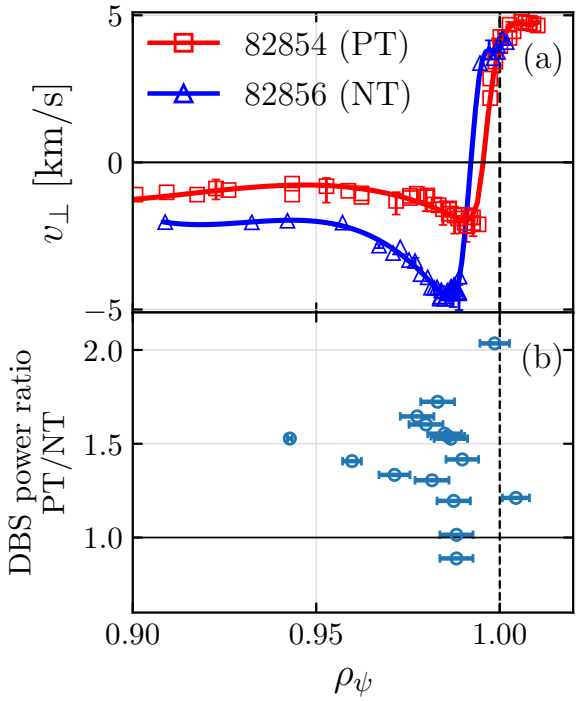

Figure 5.14: *Edge (a) $v_\perp$ profiles (same as in Fig. 5.11) compared between NT and PT and (b) the corresponding PT-to-NT ratio of DBS power computed from the Doppler peak. The higher power in PT suggests a stronger intensity of density fluctuations $|\tilde{n}(k_\perp)|$.*

different time intervals corresponding to the considered NT and PT scenarios, the DBS probing frequencies only partly match; Therefore, only a subset of the data in (a) is represented in (b).

This indicates a reduction in density fluctuations in the NT discharge, within the region of the E_r well, for the wavenumber $k_\perp \rho_s$ delected by the DBS. The latter assumes values within $k_\perp \rho_s \sim 0.4$–0.8 between $\rho_\psi = 1.0$ and 0.95, which corresponds to the ion-scale turbulence range. At the edge of TCV plasmas, linear gyrokinetic simulations often find the TEM to be the dominant type of instability at these $k_\perp \rho_s$ scales. This was also confirmed to be the case in the present discharges, using linear flux-tube simulations with the gyrokinetic `GENE` [155] code, as shown in Appendix C.

The suggested reduction of ion-scale (probably TEM) edge turbulence in NT appears consistent with previous experimental findings for matched NT/PT profiles [250, 271] and the modeling results [254–260] mentioned earlier. Further analyses are foreseen to assess

how systematic the trend is and how it correlates to differences in the E_r profile, drawing also on other edge turbulence diagnostics, such as the GPI, or the thermal helium beam (THB [180]).

5.3 NT/PT comparison in LSN

We now proceed to investigate a different, lower single-null (LSN) scenario. By analogy with the USN case (Sec. 5.2.1), the upper geometry remains fixed while the bottom (X-point) triangularity (δ_{bot}) is varied. The shapes are represented in Fig. 5.15a. This NT/PT comparison is complementary (not symmetric) to the one of Sec. 5.2.1; This time it, isolates the effect of the *X-point* triangularity (δ_{X}), for a fixed *non-X-point* triangularity (δ_{nX}). Note that B_0 and I_p are flipped with respect to the USN case, to keep the same helicity and a favorable $B\times\nabla B$ drift. Also, the requested density and the magnitudes of I_p and B_0 are identical to the USN discharges of Sec. 5.2.1.

We consider an Ohmic discharge in which δ_{bot} is reduced in steps. Fig. 5.15b compiles the relevant edge profiles acquired during the time windows corresponding to the extremal values, $\delta_{\text{bot}} = 0.53$ and -0.42, respectively. In Fig. 5.15b (I), NT displays a negative

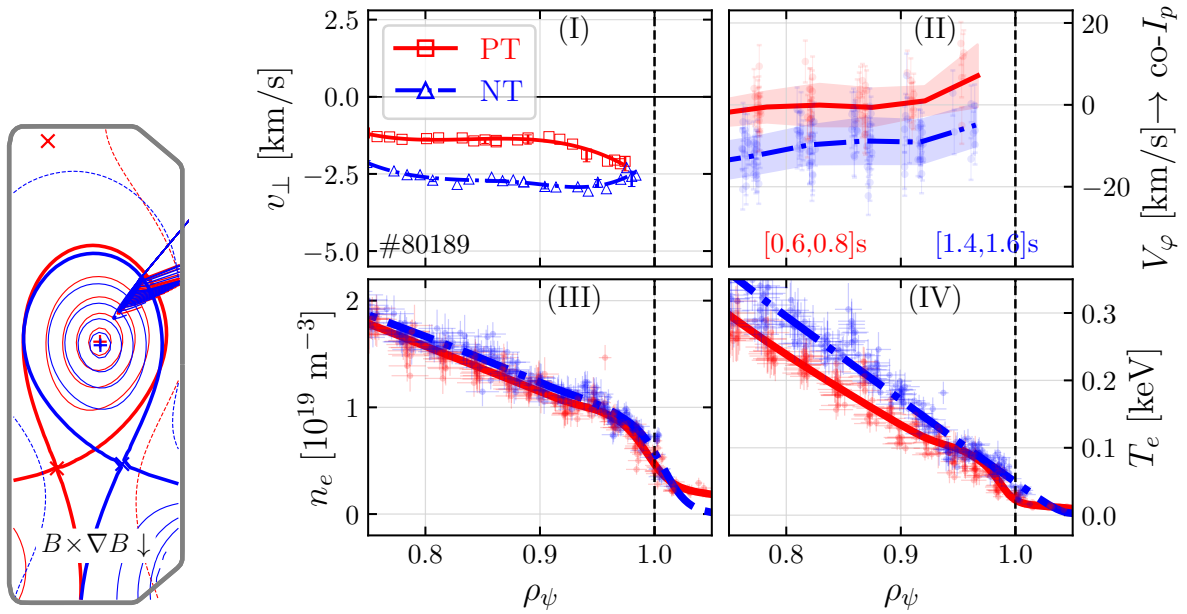

(a) **(b)**

Figure 5.15: *(a) Matched NT/PT comparison analogous to Fig. 5.4, but in LSN geometries, this time comparing positive versus negative X-point triangularities. (b) Edge profiles of (I) the perpendicular velocity, (II) carbon toroidal velocity, (III) electron density and (IV) electron temperature. The ion temperature is omitted due to the lack of high-quality edge CXRS (SYS4) data.*

offset in $v_\perp$ with respect to PT, by roughly 1 km/s, across the probed region ($\rho_\psi \lesssim 0.98$). However, when examining the profiles, there is no clear enhancement in the edge flow shear. Specifically, the well-like shape of E_r is not evident here, neither in PT nor NT. This absence can be partly attributed to the DBS radial probing range, which does not

extend up to the separatrix—where E_r is expected to rise again. Furthermore, a genuine difference in the E_r structure, compared to the previously examined USN shapes, is especially apparent for the NT case; The narrow E_r well seen in case of negative δ_{nX} (Fig. 5.4 or Fig. 5.8), is absent in the present scenario.

It is instructive to consider the edge C^{6}+ toroidal rotation, V_φ, displayed in Fig. 5.15b (II); In NT, V_φ is shifted in the counter-current direction with respect to PT, by roughly 10 km/s, which is slightly outside of the statistical spread. Inspection of the full radial profile (Fig. 5.16) shows that the V_φ offset extends almost rigidly to the core, on both the

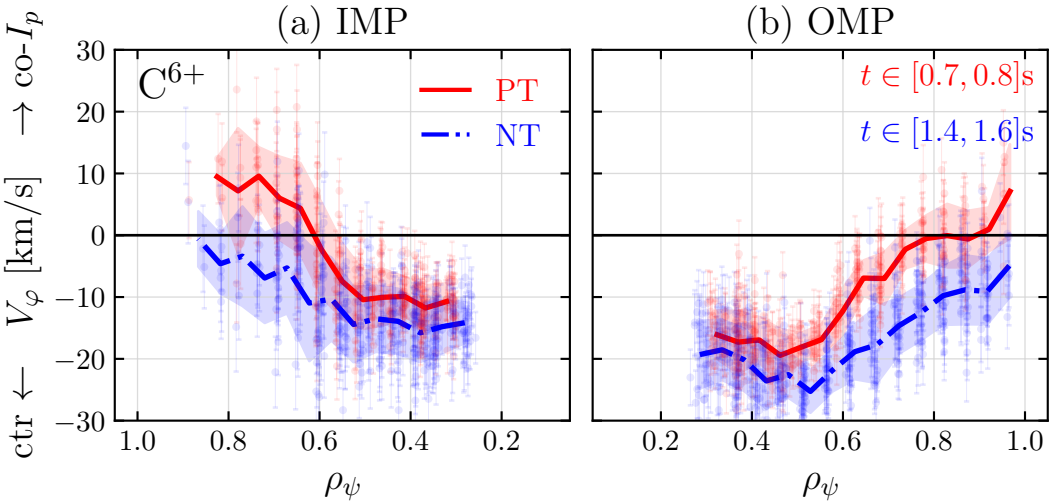

Figure 5.16: *Inboard and outboard (IMP and OMP) midplane profiles of the carbon toroidal rotation. The counter-current offset in NT extends almost rigidly across the entire radial range.*

low and high-field sides. It also persists in the inner core, but appears more pronounced in the outer core.

The greater counter-current rotation in NT can largely account for the more negative E_r level compared to PT. Indeed, the radial impurity force balance recovers a similar offset in E_r (Fig. 5.17 b). The latter stems predominantly from the $V_\varphi B_\theta$ contribution (dash-dotted line in Fig. 5.17 a), although both $(\nabla p/Zen)$ and $-V_\theta B_\varphi$ terms increasingly enhance the NT/PT difference in E_r closer to the edge.

Meanwhile, the density profiles are closely matched at the edge (Fig. 5.15b (III)), and remain similar in the core (with a 10% higher central density in PT). This observation ensures that the V_φ difference is genuinely linked to the geometry, and not to the density, which also affects V_φ—as was established in Sec. 4.4[4]. The edge T_e is higher in NT (Fig. 5.15b (IV)), but this difference fades towards the core. Although high-quality edge T_i data are not available here, there is no evident difference in the core T_i data, either. Consequently, the total and electron energy contents are similar—if not slightly reduced in NT. This stands in contrast to the Ohmic USN scenario discussed previously (Sec. 5.2.1),

[4] The weaker NT/PT difference in V_φ in the inner compared to the outer regions (Fig. 5.16), noted above, appears consistent with the slightly higher core density in PT. As higher density tends to increase counter-current rotation (Sec. 4.4), it might be expected to somewhat compensate the shaping-related V_φ discrepancy.

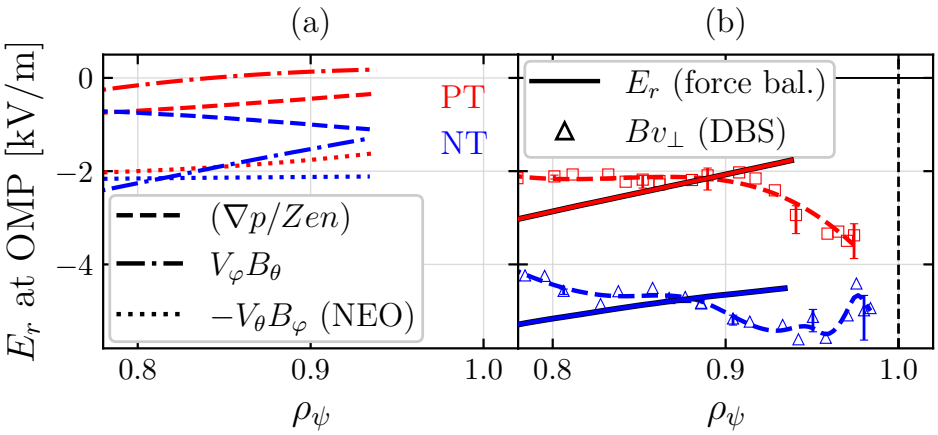

Figure 5.17: *(a) Contributions to the carbon force balance and (b) their sum (E_r), alongside the DBS data which is mapped to the OMP. The NT/PT offset in E_r (b) is reflected notably by a more negative $V_\varphi B_\theta$ contribution to the C^{6+} force balance—the dashdotted line in (a).*

where NT shows better confinement and in particular higher edge n_e. It should be noted, however, that the gas fueling rate decreases here along the discharge to keep the density constant and ends up roughly 40% lower in the NT phase than in the PT phase. This could, to some extent, hide a certain improvement in the NT particle confinement.

We now turn to the case of auxiliary heating, using the same NT geometry as in Fig. 5.15a, and a similar PT shape with less pronounced triangularity ($\delta_X \approx 0.36$ instead of 0.53). Fig. 5.18 shows the edge profiles acquired in auxiliary-heated pairs of discharges, using co-current NBI (II) or X2-ECRH (III). For reference, the Ohmic case is also shown in (I). We find that the negative $v_\perp$ offset in NT compared to PT persists, in both NBI (330 kW) and ECRH (850 kW) The NT electron energy content is about 20% higher in the NBI case (II), whereas it is 10% lower in the ECRH case (III). Owing to incomplete CXRS data, the ion (or total) energy cannot be compared, nor can V_φ. It remains, therefore, to be confirmed how systematic the V_φ variation with δ_X is under auxiliary heating, and beyond the present scenarios.

Overall, the confinement and $E_r \times B$ shear enhancement in NT appear small—or even absent—compared to the analogous USN case of Sec. 5.2.1. This suggests that negative δ_X and δ_{nX} do not play symmetrical roles. In particular, they have different impacts on L-mode confinement—a finding that aligns well with a previous study on TCV [272]. The latter indicated that confinement in NT improves when reducing δ_{nX}, whereas δ_X has the opposite effect. Moreover, the differing sensitivity of the edge toroidal rotation to δ_X or δ_{nX} provides a useful clue to which we will return later.

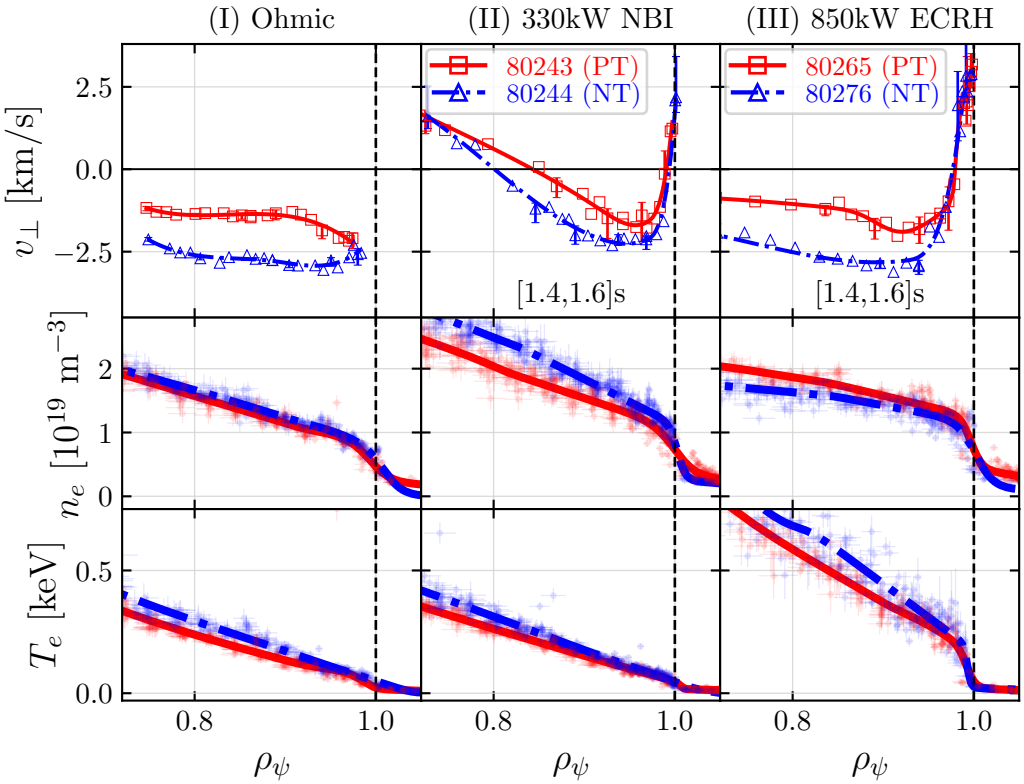

Figure 5.18: *Extension of the NT/PT comparison of Fig. 5.15b, reproduced in (I) for reference, to the cases with auxiliary (II) co-current NBI or (III) ECRH heating.*

5.4 Limited configuration

Next, we consider a pair of inner-wall limited PT/NT shapes (Fig. 5.19a), with $\delta \approx 0.23$ and -0.28, respectively. The considered phase has 540 kW of auxiliary ECRH (X2) heating, deposited and fully absorbed in the plasma center. The edge $v_\perp$ and kinetic profiles are shown in Fig. 5.19b. In examining the edge profiles, we note that the higher n_e, T_e and T_i in NT (II–IV) are qualitatively similar to the diverted USN case (Fig. 5.4) even though the plasma conditions differ notably[5]. The overall higher confinement in NT is recovered, too; both ion and electron thermal energies (W_i and W_e) are higher in NT by roughly 20 and 30%, respectively (or close to 30% in terms of W_{tot}, which is dominated by W_e).

However, unlike the previous comparisons in diverted (LSN or USN) shapes, the present limited shapes are up-down symmetric. Thus, the upper geometry (where the DBS measurements are performed) differs between NT and PT. Notably, the local flux expansion (f_x) and the probed turbulence wavenumbers ($k_\perp$) differ; at the edge, f_x and $k_\perp$ are higher in NT by factors of 1.6 and 1.8, respectively.

This yields a $v_\perp$ well depth, which—in terms of local DBS measurements—appears shallower in NT than in PT (solid lines in Fig. 5.19b (I)). Yet, as highlighted by the blue arrow,

[5] In addition to the geometrical differences and the ECRH, the present limited discharges have higher I_p values (250 kA instead of 170 kA) compared to the USN Ohmic case of Fig. 5.4.

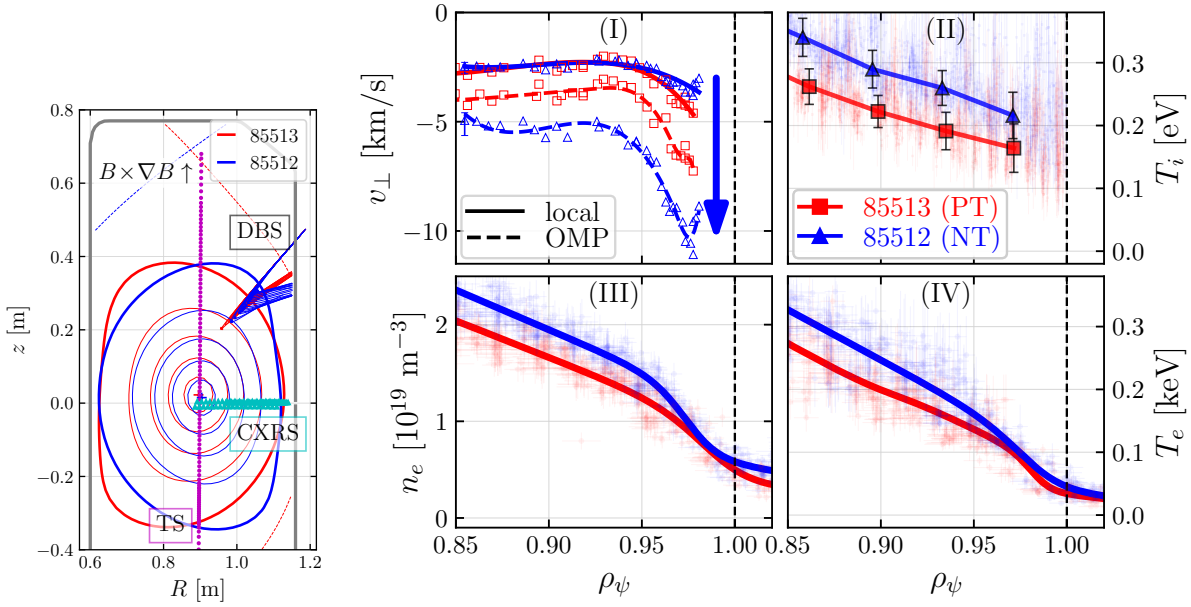

(a) **(b)**

Figure 5.19: *NT/PT comparison in (a) inner-wall-limited, up-down symmetric configurations. (b) Edge profiles of the (I) local and OMP-mapped $v_\perp$ from DBS, (II) carbon temperature, (III) electron density and (IV) electron temperature.*

the relatively high f_x in NT translates into a much deeper well when mapped to the OMP (dashed line), largely exceeding the PT well depth. Thus, despite the seemingly weaker local $v_\perp$ shear in the DBS probing region for NT, the data are actually consistent with a stronger edge $E_r \times B$ shear at the OMP, in line with the previous NT/PT comparisons in USN shapes.

To increase confidence in the OMP mapping and the drastic rescaling of E_r associated with it, Fig. 5.20 (a,b) compares OMP-mapped DBS data with the carbon radial force balance at the OMP, for PT and NT. In the NT case (b), at $\rho_\psi \approx 0.9$, the two are in good quantitative agreement. By contrast, the local $v_\perp B$ values from DBS (dotted lines in Fig. 5.20) are smaller by a factor of 2. The OMP mapping also improves agreement for the PT case, but does not capture the small "hill" in $v_\perp$ between $\rho_\psi = 0.9$–0.95. We conclude that the OMP-mapped DBS measurements are more consistent with the radial force balance, supporting a deeper E_r well (at the OMP) in NT compared to PT.

At the same time, the carbon V_φ profiles (Fig. 5.21) do not reveal any significant difference between NT and PT, in particular at the OMP edge (b). Consequently, V_φ does not account for the NT/PT difference in E_r derived from the C^{6+} force balance. Instead, the lower E_r in NT is reflected by a stronger neoclassical poloidal velocity and diamagnetic contribution (not shown). The absence of any notable impact of (negative) triangularity on the edge V_φ in these limited shapes is in line with Ref. [265, Fig. 23]. As previously mentioned in Sec. 5.1, that study reported no clear trend in the edge V_φ when varying δ in limited TCV plasmas.

Finally, we compare the deuterium diamagnetic contribution, $(\nabla_r p_i)/en$ in Fig. 5.22. As observed previously in different TCV L-mode scenarios (Fig. 4.6 and Fig. 5.6b), the over-

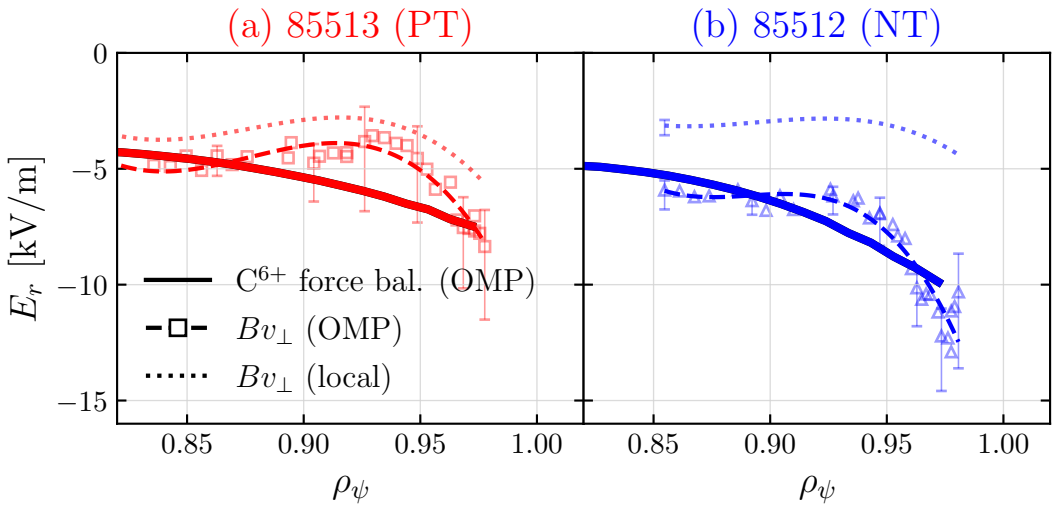

Figure 5.20: *E_r at the OMP as reconstructed from the carbon radial force balance (solid line), and from the DBS data (dashed line). For reference, the local DBS measurements are shown as a dotted line. The local $Bv_\perp$ values are clearly incompatible with the force balance results in NT, whereas the OMP-mapped values show good agreement.*

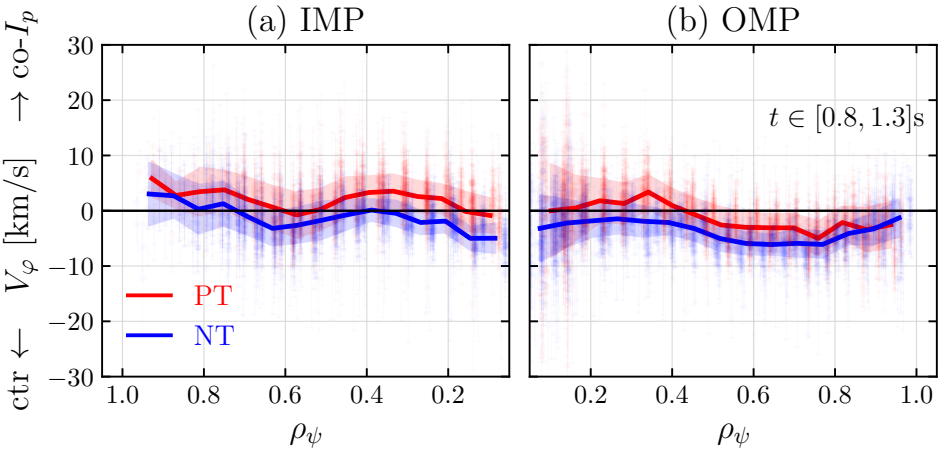

Figure 5.21: *Carbon toroidal rotation profiles, with negligible differences between NT and PT.*

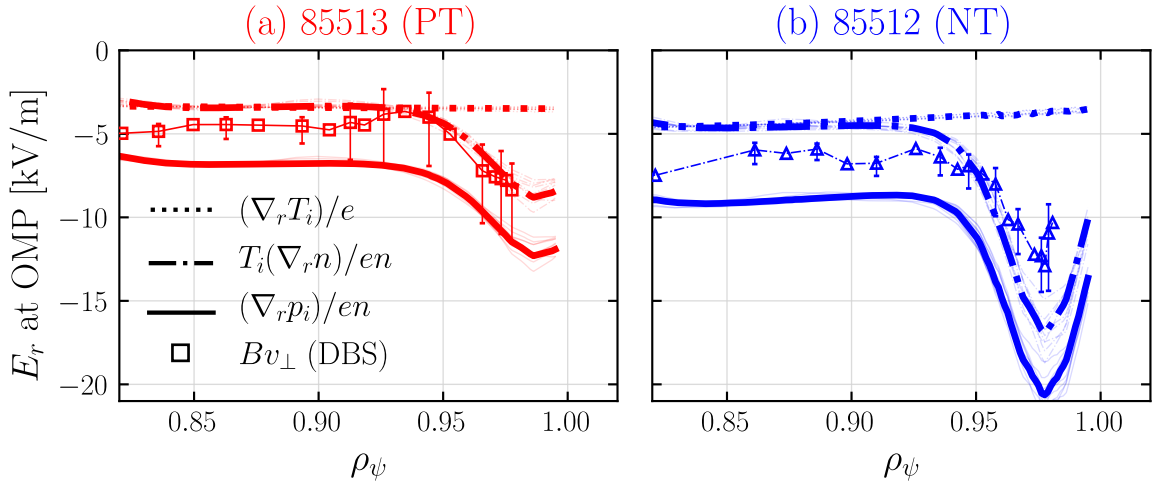

Figure 5.22: *Comparison of the DBS-derived E_r profile at the OMP (squares and triangles) to the deuterium diamagnetic contribution (dashed lined) and its two components (solid and dashdotted lines). The $T_i(\nabla_r n)/en$ term can account for the difference in E_r well depths.*

all edge $(\nabla_r p_i)/en$ level exceeds that of the E_r inferred via DBS. Importantly, however, it displays a pronounced difference between PT and NT, that aligns well with the DBS measurements. Interestingly, the two components of the diamagnetic term—proportional to $\nabla_r T_i$ and $T_i(\nabla_r n)/n$—have precisely equal weights from the outer core to $\rho_\psi \approx 0.92$. Yet, towards the very edge, $T_i(\nabla_r n)/n$ follows the E_r well shape, while $\nabla_r T_i$ remains flat and merely offsets the overall $(\nabla_r p_i)/en$ level. Hence, it appears that, in this limited pair, $T_i(\nabla_r n)/en$—and, therefore, the diamagnetic contribution—primarily accounts for the different edge E_r profiles in NT and PT. This finding warrants additional experiments aimed at matching their kinetic profiles. This could be attempted by adjusting the auxiliary heating, as done for the USN scenarios discussed earlier (Sec. 5.2.3). It may be speculated that, consistent with the USN case (Fig. 5.11), a difference in E_r and its shear would persist even if $(\nabla_r p_i)/en$ can be matched. This would permit further testing of the reasoning expressed at the end of Sec. 5.2.3—which points towards a causal role of edge $E_r \times B$ shear in the NT/PT confinement differences[6].

5.5 Towards higher performance in fully NT shape

Lastly, we investigate E_r in NT versus PT scenarios at higher performance, which is more representative of conditions in future reactors. The NT equilibrium is shown in Fig. 5.23-I. The shape is DIII-D-like; Unlike the previous diverted NT geometries, this one has a fully developed (X-point and non-X-point) negative triangularity, $\delta \approx -0.5$.

At fixed auxiliary heating power ($P_{\mathrm{NBI}} = 850\,\mathrm{kW}$) delivered by a co-current NBI beam[7], the NT scenario is confronted both to its mirrored PT L-mode counterpart (Fig. 5.23-II),

[6] That said, it is not guaranteed that the kinetic profiles can, in fact, be matched in this particular scenario.

[7] Note that since $I_p < 0$ in the PT H-mode and $I_p > 0$ in the NT and PT L-mode discharges, different neutral beam sources are used (NBI-1 and NBI-2, respectively), possibly biasing the comparison.

and to a PT H-mode discharge (Fig. 5.23-III).

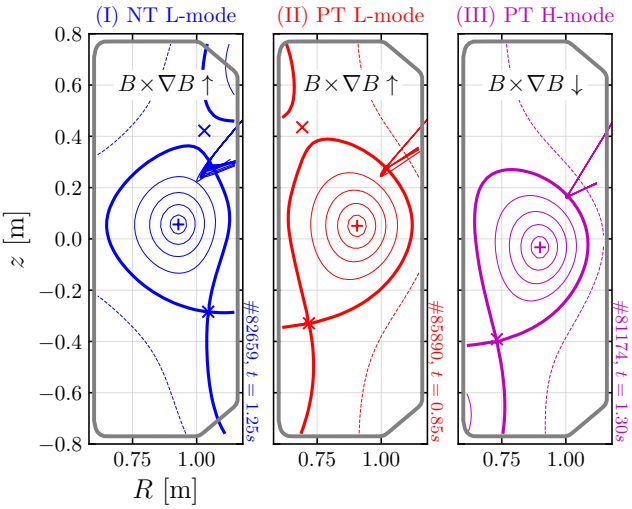

Figure 5.23: *Plasma shapes of the higher performance scenarios.*

	NT L	PT L	PT H
#	82659	85890	81174
t window [s]	[1.2,1.3]	[0.8,0.9]	[1.2,1.4]
P_{NBI} [kW]	850	850	850
I_p [kA]	+150	+150	−150
B_0 [T]	+1.44	+1.44	−1.44
κ	1.35	1.48	1.51
δ	−0.49	0.52	0.48
q_{95}	4.0	5.7	5.1
τ_E [ms]	8.5	6.6	14
$H_{98\mathrm{y2}}$	0.98	0.64	1.2
β_N	1.5	1.1	2.4
Z_{eff}	2.2	1.3	2–2.3

Table 5.2: *Overview of main discharge parameters.*[8]

The PT L-mode scenario enables a clean comparison with the NT case. Both have an unfavorable $B\times\nabla B$ drift. This keeps the PT discharge in L-mode at this level of NBI heating, which might otherwise exceed $P_{\mathrm{L}\to\mathrm{H}}$. The PT H-mode, on the other hand, has a favorable $B\times\nabla B$ drift. Here, it serves only as a representative, reactor-relevant reference to situate the NT L-mode. It is not intended as a direct PT counterpart for isolating the effect of triangularity. The externally controlled parameters of the PT H-mode are not exactly identical: Its geometry and the signs of both I_p and B_0 differ from the NT/PT L-mode cases, but the magnitudes of δ, I_p and B_0 are consistent. The discharge parameters are summarized in Tab. 5.2.

The time traces of neutral beam injection (NBI) power, vertical photodiode (D_α) signal and line-averaged density ($\overline{n}_l$) are shown in Fig. 5.24, where the considered discharge phases are highlighted. The corresponding kinetic profiles are displayed in Fig. 5.25 [8].

The PT H-mode exhibits quasi-regular type-I ELMs, evident from the D_α signal (Fig. 5.24), while the other two discharges are entirely ELM-free, consistent with L-mode. Moreover, the PT H-mode features a pronounced pedestal in n_e and T_e (Fig. 5.25b–c) which sets it apart from the L-mode cases. The NT discharge displays an L-mode-like edge density profile, but with respect to the PT L-mode, the NT edge temperature is notably higher, both in terms of T_e—in line with the tendency reported on DIII-D [25], as well as T_i.

Judging by its kinetic profiles, and by the confinement metrics listed in Tab. 5.2, the NT scenario shows an intermediate performance between the PT L- and H-mode. Yet, due to markedly different edge conditions—notably in density—any comparison of E_r or confinement level between L- and H-mode remains inherently limited. Furthermore, the

[8] Owing to the lack of CXRS data in #85890 (PT L-mode), the T_i profile (Fig. 5.25) and confinement metrics τ_E, $H_{98\mathrm{y2}}$ and β_N (Tab. 5.2) are taken from an equivalent discharge phase in #84932 ($t \in [0.65, 0.8]$ s), which lacks usable DBS data.

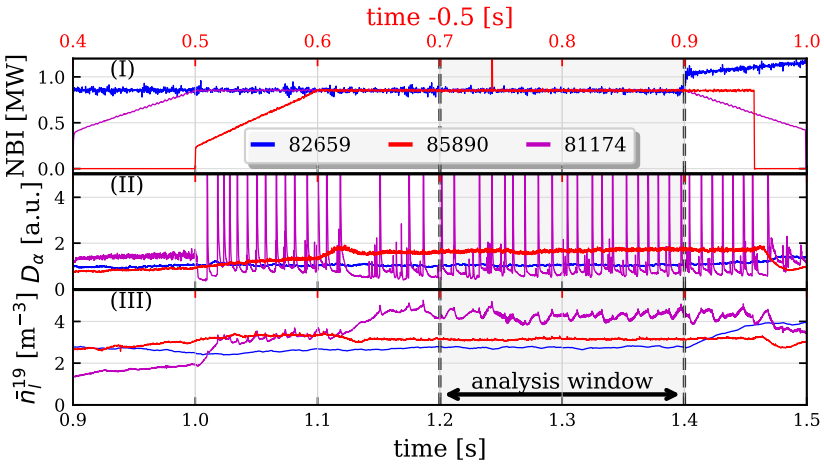

Figure 5.24: *Time traces of (I) co-I_p injected NBI power (after accounting for losses in the beam duct), (II) top-down photodiode D_α signal and (III) line-averaged density. The time axis of #85890 has been shifted for visual convenience.*

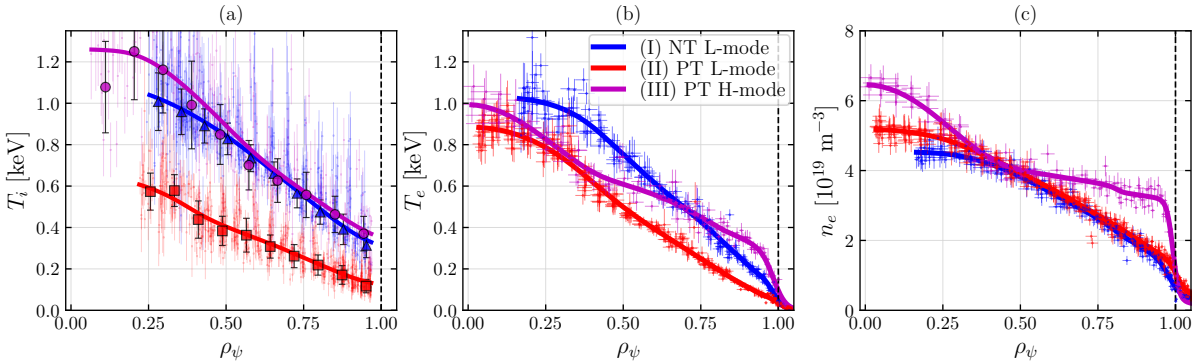

Figure 5.25: *Kinetic profiles for the cases shown in Fig. 5.23, using inter-ELM data in H-mode: (a) impurity ion temperature from CXRS, (b) electron temperature and (c) density from TS.*

higher overall density in the present H-mode tends to overstate its performance relative to the L-modes.

The edge $v_\perp$ profiles are shown in Fig. 5.26 (a). Consistent with preceding findings of

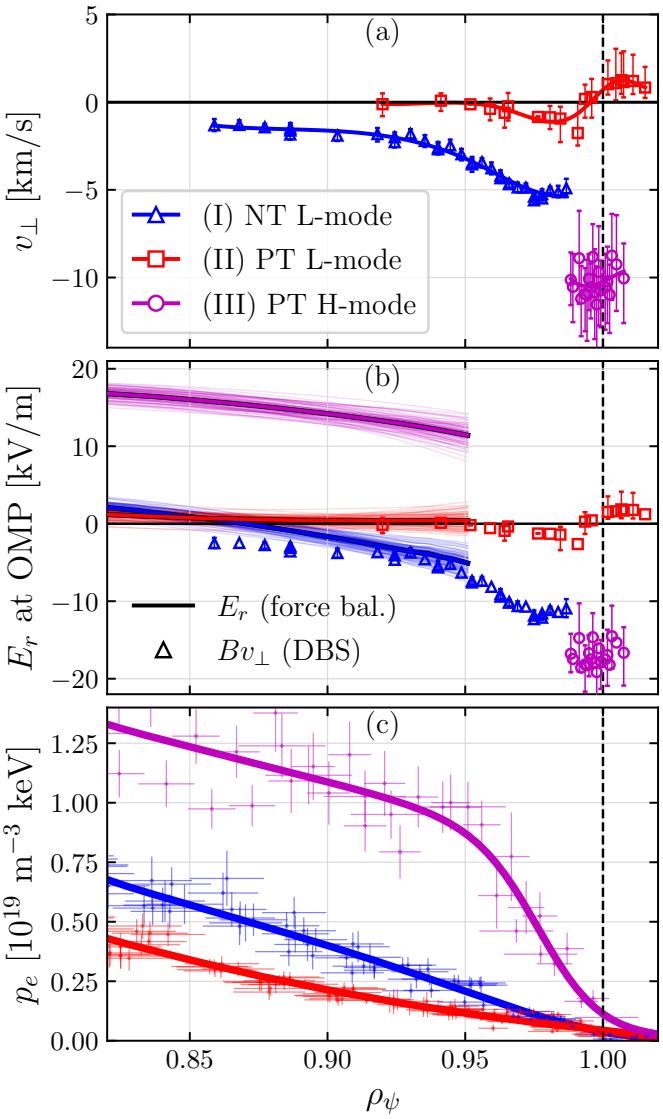

Figure 5.26: *Edge profile comparison for the scenarios in Fig. 5.23: (a) local DBS velocity, (b) DBS data expressed in terms of E_r and mapped to the OMP with the force balance result, and (c) electron pressure. The shaded set of curves in (b) represents the spread in E_r obtained from a simplified Monte Carlo sampling approach.*

this chapter (e.g. Sec. 5.2.1), the NT discharge exhibits a deeper well compared to its L-mode PT counterpart ($v_\perp^{\min} \approx -5\,\mathrm{km/s}$ and $-2\,\mathrm{km/s}$, respectively), and the associated inner-side $E_r \times B$ shear around $\rho_\psi \approx 0.95$–0.98 is visibly stronger in NT.

In the PT H-mode, $v_\perp$ is extracted during ELM-free intervals as outlined in Sec. 3.2.2. However, the low turbulence level and steep density pedestal limit the usable DBS data to a narrow radial range near the well minimum, preventing an assessment of the edge velocity shear from DBS alone. We therefore resort to a complementary estimation of E_r

through the C^{6+} radial force balance. Its profile is displayed in Fig. 5.26 (b), along with the DBS data which is expressed in terms of $E_r = v_\perp B$ and mapped to the OMP. Good consistency is found for the NT and PT L-modes between the DBS and the force balance E_r estimations in the outer core, lending confidence to the analysis procedure. Note also that the E_r well difference is enhanced in (b) compared to (a) due to the stronger local flux expansion in NT, as discussed earlier for the limited NT/PT comparison (Sec. 5.4). In the PT H-mode, the jump in E_r between $\rho_\psi \approx 0.95$ and 1 (Fig. 5.26b) indicates a strong shear layer—as expected for H-mode—coinciding with the steep region of the p_e pedestal (Fig. 5.26 c).

The positive offset of E_r in the core by $\approx$ 10–15 kV/m in the H-mode compared to the PT L-mode discharge, is reflected by a stronger co-current carbon toroidal rotation in the former. This evident from the profiles shown in Fig. 5.27. The difference in V_φ might be related to the known discrepancies in the neutral beam properties, and/or to substantial intrinsic rotation changes going from L- to H-mode. It is worth noting that the difference

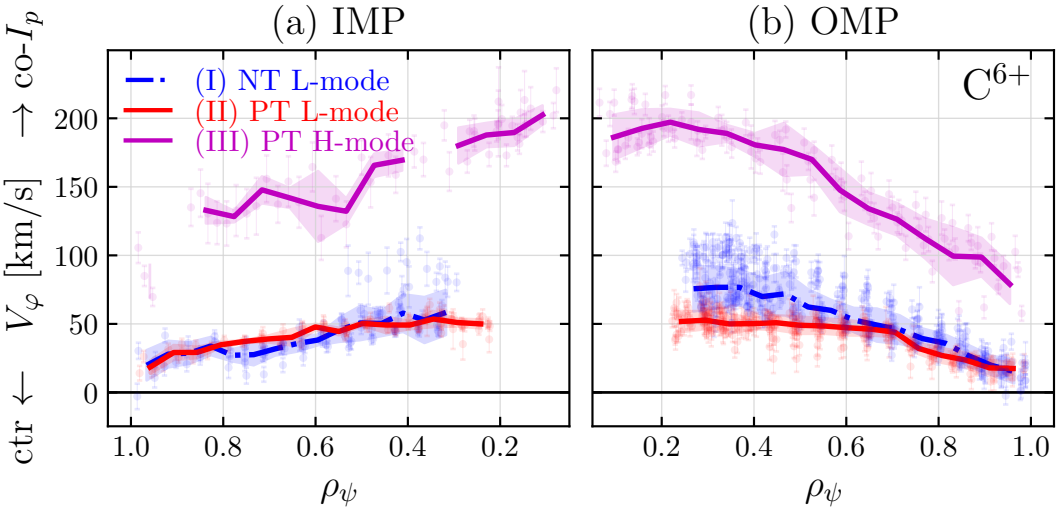

Figure 5.27: *Carbon toroidal rotation profiles at (a) the inboard and (b) outboard midplanes, corresponding to the scenarios analyzed in Fig. 5.26. Discontinuous lines for the PT H-mode on the IMP result from the poor statistics, sometimes preventing a meaningful binned average.*

in V_φ between the NT and PT L-mode plasma is small, particularly towards the edge. This aligns with the insensitivity of V_φ to triangularity observed in the USN (δ_{nX}, Fig. 5.5) and the limited NT/PT comparisons (Fig. 5.21). Meanwhile, the LSN (δ_{X}, Fig. 5.16) case suggests that negative δ_{X} shifts V_φ in the counter-I_p direction. Since both δ_{nX} and δ_{X} are negative in the present NT scenario, one might expect V_φ to display a similar counter-current offset. However, the absence of this effect could be linked to the intrinsic rotation difference being insignificant compared to the beam-driven rotation.

In summary, in a higher performance scenario with full NT shaping, the E_r well remains remarkably pronounced for an L-mode discharge with an unfavorable $B\times\nabla B$ direction—a configuration usually associated with a shallow L-mode edge E_r (see Chapter 4), as verified in the PT L-mode counterpart. Thus, the NT edge $E_r \times B$ shear appears to lie between the PT L- and H-mode levels. However, at the very edge, the absence of a pronounced

pressure pedestal suggests that the E_r well and its shear remain well below that of the H-mode pedestal region, where E_r measurements are not fully accessible. With a favorable $B\times\nabla B$ drift, the L-mode E_r well is expected to deepen further, possibly bringing the NT performance and edge $E_r \times B$ shear closer to H-mode; this could be explored in future work.

5.6 Chapter summary and discussion

This chapter explored the influence of triangularity on the E_r well and confinement in TCV, thereby comparing, for the first time, the edge E_r profile in matched negative (NT) versus positive (PT) triangularity discharges.

The NT/PT pairs included the following L-mode plasma scenarios and geometries:

(1) USN with fixed upper but opposite bottom, *non-X-point* triangularities (δ_{nX})

(2) LSN with fixed upper but opposite bottom, *X-point* triangularities (δ_{X})

(3) inner-wall limited, up/down symmetric shapes

(4) LSN with fully developed (δ_{X} and δ_{nX}) triangularity

Comparisons were performed both under Ohmic and auxiliary heating. They uncovered the following observations.

The NT case nearly systematically displays a stronger L-mode E_r well, except for the specific situation (2) where $\delta_{\mathrm{nX}} \approx 0$ and only δ_{X} is negative. USN discharges (1) with negative δ_{nX}, on the other hand, exhibit an E_r well that is clearly and robustly deeper than their PT counterparts, along with a higher edge pressure and global confinement. This NT/PT difference is sensitive to small variations in shaping (Sec. 5.2.2); It can be enhanced by further decreasing δ_{nX}, or via auxiliary ECRH or NBI heating (Sec. 5.2.3). When injecting more heating power in PT to better match the NT kinetic profiles, the E_r well remains deeper in NT.

In contrast, reducing δ_{X} in the corresponding LSN scenario (2) does not show a significant impact on either the edge E_r shear or confinement (Sec. 5.3). Instead, it shifts the toroidal impurity rotation rigidly in the counter-current direction, consistently with past δ_{X}-scans in TCV [89]. This effect is not observed in the other scenarios. Thus, δ_{X} and δ_{nX} appear to play distinct roles, strengthening previous findings from TCV [272]. It is worth noting that compared to the USN scenario (1), the analogous comparisons in LSN (2) were less systematic, and often lacked impurity data from CXRS. This warrants further experiments to confirm the robustness of the toroidal rotation and confinement observations in this scenario (2) with the same rigor as for scenario (1). Moreover, the findings generally motivate further investigations into the separate roles of δ_{X} and δ_{nX} beyond the present scenarios.

In the limited NT/PT scenario (3), NT again displays a deeper E_r well and stronger shear at the OMP than PT. It is reflected by a larger $(\nabla p_i/en_e)$ contribution to E_r, while no significant difference is found in the impurity toroidal rotation, in line with [265, Fig. 23].

Finally, a higher performance, fully NT-shaped scenario reveals a remarkable L-mode E_r well—despite unfavorable $B\times\nabla B$ drift (Sec. 5.5). Its confinement and edge $E_r \times B$ shear clearly exceed that of the PT L-mode counterpart, while remaining below the level of a reference PT H-mode.

Thus, overall, the study revealed a consistently sharper E_r well in NT, except for the specific case where only δ_X is negative. The higher $E_r \times B$ shear in NT is accompanied by a substantial increase in edge density and temperature, as well as global confinement. This suggests a causal link consistent with the expected stabilization of turbulence by sheared flows, as further discussed below.

Here, the comparison at matched kinetic profiles (Fig. 5.11 b) is particularly insightful. The backscattered power in the DBS signals is higher for PT, supporting a reduction of ion-scale edge density fluctuations in NT at the probed $k_\perp$ scale. This observation remains to be substantiated by a more extensive edge turbulence characterization, including by other diagnostics. That said, the suggested reduction of turbulence intensity in NT would be consistent with the general picture of a stabilizing effect of NT on turbulence, which is backed by experiments [21, 22, 248–253, 273], in particular for the case of matched NT/PT kinetic profiles in TCV [271, § 3.3.2][250], and the modeling results [254–260] mentioned earlier. Note, however, that, so far, documented NT/PT characterizations of fluctuation levels in L-mode focused either on the outer core [21, 22, 248–250] or on the SOL regions [251, 273, 274]. Similar studies comparing fluctuations just inside the separatrix—where the E_r well is located—are scarce [252]. This gap could be addressed in future work by exploiting the full suite of edge fluctuation diagnostics available on TCV (SPR, DBS, THB, and GPI), enabling a more comprehensive analysis of how differences in mean $E_r \times B$ shear correlate with turbulence in NT and PT discharges.

Whether density fluctuation levels are reduced in NT or not, the improved L-mode confinement very likely reflects a reduced turbulent heat diffusivity. It is possible that the latter results from mechanisms other than $E_r \times B$ shear; Several theoretical studies have shown an effect of triangularity—independently from considerations of mean $E_r \times B$ flow shear—on linear stability and/or nonlinear transport,[254–259, 275]. However, in Fig. 5.11 (b) the E_r well remains more pronounced in NT despite the matched edge kinetic profiles with PT. This observation supports an interpretation of a turbulent transport reduction caused by enhanced $E_r \times B$ shear (and not vice-versa), although it does not demonstrate such causality, either.

We now turn to the question of what might underlie the observed E_r well differences between NT and PT.

The effect of triangularity on edge toroidal rotation [89, 263] has been proposed as a primary ingredient for the NT edge E_r enhancement on DIII-D,[264]. By contrast, the present study establishes that, in TCV, the impurity toroidal velocity (V_φ) does not generally differ between NT and PT. Instead, a counter-current shift in V_φ appears to originate from negative *X-point* triangularity in TCV. This is compatible with the counter-current edge V_φ observed in DIII-D for fully NT shapes [263], which have a pronounced negative δ_X. Yet, the TCV results suggest that intrinsic V_φ differences are not a necessary ingredient—although they might contribute—to observing a confinement improvement, or a deeper E_r well in NT.

As was mentioned in Sec. 5.1, the neoclassical `XGC` simulations of Ref. [87] suggest that collision-driven effects—including ion orbit losses—are, by themselves, insufficient to explain experimentally relevant differences in edge E_r or rotation between NT and PT [87]. Such collisional effects might, however, still be relevant in a self-consistent description *including* the turbulence.

The lack of experimental or numerical indications that edge toroidal rotation and/or collisional mechanisms alone dominate the E_r well sensitivity to triangularity, points instead to the role of turbulence-driven ion poloidal rotation. This conclusion is reminiscent of the discussions of Chapter 4 based on the `GENE-X` simulations in FAV and UNFAV drift configuration; It is plausible that the origin of the NT/PT difference in the E_r well shares similarities with the Reynolds stress asymmetry between FAV and UNFAV.

This perspective motivates dedicated nonlinear turbulence simulations, with emphasis on the contribution of turbulence-driven flows at the edge. Ongoing efforts are investigating the turbulence and $E_r \times B$ flow behavior in NT versus PT geometries with the help of various gyrokinetic codes; `JOREK-GK` [267], `GYSELA` [268] and `GENE-X` [269]. In particular, an analysis of `GENE-X` simulations based on the NT/PT scenarios of Sec. 5.2.3 is underway. As these studies are either preliminary or not yet publicly available at the time of writing this manuscript, a discussion and comparison with the present experimental results are left for future work. Together with the robust experimental trends identified here, such experiment-simulation comparisons are well positioned to elucidate the underlying cause for the NT/PT differences in E_r.

In summary, in matched TCV discharge pairs, higher confinement in NT coincides with a deeper E_r well than in PT. This suggests a causal link consistent with the turbulence stabilization paradigm by sheared flows [11, 12], strengthening the picture of reduced turbulent transport in NT. Our study confirms the distinct behavior of the NT edge now also in terms of the $E_r \times B$ flow—a key element for advancing our understanding of edge transport and overall confinement in tokamaks.

Chapter 6

Conclusion and Outlook

This PhD thesis investigated the mean E_r well at the edge of tokamak plasmas, with the overarching goal of clarifying its drives and connection to confinement properties.

The experimental study systematically isolated the effects of two magnetic geometry parameters—(A) drift configuration and (B) triangularity—on the L-mode E_r well. Both parameters are empirically known to substantially influence L-mode confinement and/or access to higher confinement regimes, such as H-mode. Yet, the origin of their effects, or their possible link to differences in the mean $E_r \times B$ shear at the edge, are not conclusively understood.

The experiments were conducted primarily on the TCV tokamak, which offers the required flexibility to access the various drift configurations and plasma shapes explored in this work. The measurements were performed using a Doppler backscattering (DBS) diagnostic, successfully installed and tested over the course of this PhD thesis. This DBS system provided the basis for the subsequent E_r studies in TCV, whose main findings are described below.

Summary of findings

In both research aspects (A and B), TCV experiments reveal a clear influence of magnetic geometry on the structure of the edge E_r profile:

(A) In matched discharges with favorable (FAV) and unfavorable (UNFAV) $B{\times}\nabla B$ drift, the L-mode E_r well is shallower in the UNFAV configuration. This is consistent with previous observations from WEST and AUG and underlines the universality of the phenomenon across various tokamaks. However, WEST stands out with a high E_r sensitivity to plasma current that is not observed in TCV nor AUG. No evident correlation is found in TCV between the differences in the E_r well, and the edge kinetic profiles or global confinement. Only when approaching the L-H transition with auxiliary heating does FAV show a measurable confinement gain, coinciding with a growing $E_r \times B$ shear enhancement over UNFAV. The E_r and confinement behaviors preceding the L-H transition in TCV are consistent with a key role of mean $E_r \times B$ shear: It may reduce $P_{\mathrm{L}\to\mathrm{H}}$ in the FAV $B \times \nabla B$ compared to the UNFAV case, although the data do not permit a conclusion regarding the causality (see Sec. 4.7).

(B) This work documents, for the first time, the comparison of the edge E_r between matched negative (NT) and positive (PT) triangularity discharges. The comparisons

reveal nearly systematically a deeper E_r well in NT, except for the case of diverted shapes where only δ_{X} is negative (and $\delta_{\mathrm{nX}} \approx 0$). The stronger edge E_r shear in NT is accompanied by a notable improvement in the L-mode global confinement, even under Ohmic heating, along with steeper edge density and temperature profiles. The findings are compatible with a reduction in turbulent transport in NT genuinely caused by enhanced edge $E_r \times B$ shear (see Sec. 5.6). Alternative mechanisms for turbulence stabilization in NT are also possible. However, since the deeper E_r well in NT persists even in the case of matched kinetic profiles, this supports the hypothesis that $E_r \times B$ shear stabilization is involved to some degree in the NT edge confinement improvement.

Discussion and parallels between FAV/UNFAV and NT/PT

A conclusion emerging from the combined investigations is that the neoclassical approximation (Sec. 2.3.3)—in which E_r mainly balances ($\nabla p_i / n_i e$) and a neoclassical (small) poloidal velocity, does not seem to account for the pronounced L-mode sensitivities observed here, whether related to drift configuration or triangularity. In both studies, discharge pairs were found with well-matched edge kinetic profiles, yet differing E_r well profiles (see Fig. 4.5b and Fig. 5.11 b). This corroborates the conclusion from a previous study on AUG [122] that emphasized the importance of the Lorentz ($-v \times B$) contribution to the L-mode edge E_r.

A further similarity between the drift configuration and the triangularity studies concerns the role of the ion toroidal rotation. The impurity edge toroidal velocity did not systematically mirror the differences observed in E_r. Assuming the *main* ion toroidal rotation behaves similarly—a point that remains to be verified—the results from TCV do not support interpretations in which toroidal rotation differences are the primary driver of either the FAV/UNFAV [201, 202] or the NT/PT E_r disparities [264]. This conclusion aligns with Ref. [122] concerning the FAV/UNFAV asymmetry in AUG. Toroidal rotation may nevertheless act as a secondary contributor; for instance, it could further enhance the edge E_r shear in NT—as suggested by DIII-D experiments [263, 264]—under certain plasma conditions or geometries.

Taken together, the experimental data point to the relevance of the main ion poloidal rotation ($V_{i\theta}$) in explaining the L-mode E_r well sensitivities investigated here. A deviation of $V_{i\theta}$ from its standard neoclassical value appears likely given the substantial variations in the E_r well with largely similar kinetic and impurity toroidal rotation profiles.

A sensitivity of the edge $V_{i\theta}$ (or E_r) to magnetic geometry may arise in particular from collision-driven mechanisms such as IOL or from turbulence through Reynolds stress acceleration. The presented E_r measurements do not, on their own, allow one to disentangle these contributions. However, recent simulations provide valuable insights into this discussion.

While IOL are predicted to depend on both magnetic drift configuration and triangularity, recent `XGC` simulations [87] indicate that neoclassical and IOL effects alone cannot account for a substantial edge flow difference between NT and PT.
Regarding the turbulence-driven mean $E_r \times B$ flow, while published work on its role in NT versus PT is scarce [276], it is the subject of ongoing simulation efforts [267–269].

As for explaining the FAV/UNFAV asymmetry in E_r, shear induced Reynolds stress [112, 113, 204, 218] remains a promising turbulence-driven candidate mechanism, as underpinned by very recent edge turbulence simulations using `GENE-X` [221]. Analogous `GENE-X` simulations based on this work's TCV data—although still preliminary at the time of writing this manuscript—show qualitatively consistent trends to the analogous study for AUG [221]. Likewise, the E_r well discrepancy between FAV and UNFAV is recovered in these simulations. It is attributed to differences in the nonlinear energy transfer from the turbulence to the edge mean poloidal flow. The latter is increased in FAV by a mechanism that is closely linked to the original idea of Fedorczak *et al.* [112, 113]; The residual stress associated with magnetic shear in an up-down asymmetric equilibrium promotes the enhancement of the edge $E_r \times B$ shear in the FAV drift case. Corresponding efforts using `GENE-X` are underway to address also the E_r well disparities between NT and PT. In addition, a PhD project has just begun with the aim of comparing experimental E_r well sensitivities to fluid edge simulations using the `SOLEDGE` code.

These experiment/simulation comparisons might help to further clarify the role of Reynolds stress in shaping the mean $E_r \times B$ flow, and how it responds to magnetic geometry. In addition, when combined with forthcoming analyses of the E_r dynamics (e.g., associated with GAM oscillations) and with more detailed edge turbulence characterizations, they may further illuminate the interplay between turbulent transport, equilibrium $E_r \times B$ shear, and mean or fluctuating zonal flow shear.

Outlook and suggestions for future work

This work has focused on the *mean* E_r profile and the associated mean flow shear. The dynamical properties of flow shear, on the other hand, were not addressed. In principle, they are accessible from the DBS data using time-frequency techniques—such as the pseudo-spectral MUSIC method (see Sec. 3.2.2)—to estimate the intantaneous Doppler shift, combined with multi-point DBS measurements (using two or more coupled channels)—to access the instantaneous $v_\perp$ *shear*. Such a dynamical analysis appears necessary to better understand flow shear behavior near confinement regime transitions. Indeed, the usual analysis of mean $v_\perp(\rho_\psi)$ flow profiles does not capture phenomena on shorter time scales than the typical DBS profile repetition rate ($\sim 100\,\mathrm{ms}$)—the latter being also limited by the time resolution of other diagnostics (for density profile reconstruction). Yet, faster changes before the transition, including intermittencies in $v_\perp$, could be just as relevant to clarify the access conditions to higher confinement regimes, and in particular the difference between FAV and UNFAV $P_{\mathrm{L}\to\mathrm{H}}$ thresholds. Future studies could therefore revisit or extend the auxiliary heating experiments of Sec. 4.5 with particular attention to the dynamic behavior of $v_\perp$ and its shear.

Another, related aspect that merits further investigation, as it was only marginally addressed in this study, is the role of GAMs. By extracting the instantaneous $v_\perp(t)$ signal from the DBS, the intensity of GAM-like oscillations in $v_\perp$ could be documented more systematically to assess their correlation with the shape of the mean E_r profile. This could shed light on the interplay among turbulence, the mean, and oscillatory flow shear, while providing additional information for turbulence code validation. A corresponding experimental effort is ongoing based on TCV and WEST experiments [228].

In general, complementary information on edge turbulence (across different k-scales and/or

poloidal locations of measurements) is important for obtaining a clearer picture of how $E_r \times B$ shear, turbulent transport, and confinement properties are connected. This could be obtained using other fluctuation diagnostics than the DBS; for TCV, these include thermal helium beam (THB [180]), short-pulse reflectometry (SPR [176]), and gas puff imaging (GPI [183], used in Chapter 3). In addition to fluctuation levels, the turbulence radial correlation length could be estimated, using SPR [252] and—owing to its two channels—also the DBS system [8, 149][1]. Such a comprehensive cross-diagnostic characterization of edge turbulence would complement, in particular, the trends documented here in E_r and in the DBS signal amplitude when comparing FAV and UNFAV, as well as NT and PT plasmas.

Furthermore, the study of magnetic geometry influences on the E_r profile could be extended to other parameters not addressed in this work. These include, for instance, the elongation, or—partly inspired by the JET experiments mentioned in Sec. 2.8—the divertor geometry.

Moreover, we recall that the tiltable DBS launcher in TCV, combined with the flexibility in vertical plasma positioning, allows access to different poloidal measurement locations from the top to the OMP. This enables addressing possible poloidal asymmetries in the electrostatic potential (see Sec. 3.7)—as previously observed in other devices [193–195]. It also allows investigation of possible diagnostic-related effects. More specifically, as discussed in Sec. 3.7, the interpretation of differences between upward versus downward DBS probing configurations remains inconclusive. The upward configuration, not used here except marginally in Chapter 3, is particularly relevant for accessing E_r and turbulence properties near the X-point in TCV. A corresponding study—focused on H-mode and other high confinement regimes—is in progress. In addition, an ongoing PhD project [160] investigates the influence of the probed $k_\perp$ on the DBS-inferred $v_\perp$, using existing and forthcoming measurements in TCV and WEST.

[1] The DBS radial correlation technique has been used extensively within past TCV experiments [8, 149] aimed at studying short-range and long-range radial correlations in different turbulent regimes. A corresponding paper is in preparation.

Bibliography

[1] J. Wesson. *Tokamaks*. 3rd edition. Oxford university press, 2004 (cit. on pp. 9, 10, 12, 32, 33).

[2] Francis F Chen. *Introduction to plasma physics and controlled fusion*. Vol. 1. Springer, 1984 (cit. on p. 10).

[3] O. Sauter and S. Yu Medvedev. "Tokamak coordinate conventions: COCOS". In: *Computer Physics Communications* 184.2 (2013), pp. 293–302 (cit. on p. 12).

[4] VD Shafranov. "Plasma equilibrium in a magnetic field". In: *Reviews of plasma physics* 2 (1966), p. 103 (cit. on p. 12).

[5] Per Helander and Dieter J. Sigmar. *Collisional transport in magnetized plasmas*. Vol. 4. Cambridge university press, 2005 (cit. on pp. 12, 31–33).

[6] Gabriele Merlo. "Flux-tube and global grid-based gyrokinetic simulations of plasma microturbulence and comparisons with experimental TCV measurements". en. PhD thesis. Lausanne: EPFL, 2016. DOI: 10.5075/epfl-thesis-7065. URL: https://infoscience.epfl.ch/handle/20.500.14299/126949 (cit. on p. 13).

[7] Virginie Grandgirard et al. "A 5D gyrokinetic full-f global semi-Lagrangian code for flux-driven ion turbulence simulations". In: *Computer physics communications* 207 (2016), pp. 35–68 (cit. on pp. 15, 18).

[8] Olivier Panico. "Edge turbulence self-organization in fusion plasmas". PhD thesis. Ecole Polytechnique (Palaiseau, France), 2024 (cit. on pp. 15, 55, 167).

[9] J. D. Lawson. "Some Criteria for a Power Producing Thermonuclear Reactor". In: *Proceedings of the Physical Society. Section B* 70.1 (Jan. 1957), p. 6. ISSN: 0370-1301. DOI: 10.1088/0370-1301/70/1/303. URL: https://dx.doi.org/10.1088/0370-1301/70/1/303 (cit. on p. 16).

[10] ITER Physics Expert Group on Confinement and Transport, ITER Physics Expert Group on Confinement Modelling and Database, and ITER Physics Basis Editors. In: *Nucl. Fusion* 39.12 (1999), pp. 2175–249. DOI: 10.1088/0029-5515/39/12/302 (cit. on pp. 16, 71).

[11] H. Biglari, P. H. Diamond, and P. W. Terry. "Influence of sheared poloidal rotation on edge turbulence". In: *Physics of Fluids B: Plasma Physics* 2.1 (Jan. 1990), pp. 1–4. DOI: 10.1063/1.859529 (cit. on pp. 17, 163).

[12] K. H. Burrell. "Effects of E×B velocity shear and magnetic shear on turbulence and transport in magnetic confinement devices". In: *Physics of Plasmas* 4.5 (May 1997), pp. 1499–1518. ISSN: 1070-664X. DOI: 10.1063/1.872367 (cit. on pp. 17, 163).

[13] Zhihong Lin et al. "Turbulent transport reduction by zonal flows: Massively parallel simulations". In: *Science* 281.5384 (1998), pp. 1835–1837 (cit. on pp. 18, 38).

[14] G. D. Conway et al. "Plasma flows and turbulence interaction in ASDEX Upgrade". In: *Workshop on Electric Fields, Turbulence and Self-Organisation in Magnetised Plasmas (EFTSOMP)*. Oral contribution. July 2011 (cit. on p. 19).

[15] M. Shimada et al. "Chapter 1: Overview and summary". In: *Nuclear Fusion* 47.6 (June 2007), S1. DOI: 10.1088/0029-5515/47/6/S01 (cit. on p. 19).

[16] F. Wagner et al. "Regime of Improved Confinement and High Beta in Neutral-Beam-Heated Divertor Discharges of the ASDEX Tokamak". In: *Physical Review Letters* 49.19 (Nov. 1982), pp. 1408–1412. DOI: 10.1103/PhysRevLett.49.1408 (cit. on pp. 19, 26).

[17] A Pochelon et al. "Energy confinement and MHD activity in shaped TCV plasmas with localized electron cyclotron heating". In: *Nuclear Fusion* 39.11Y (1999), p. 1807 (cit. on p. 23).

[18] Y. Camenen et al. "Impact of plasma triangularity and collisionality on electron heat transport in TCV L-mode plasmas". In: *Nuclear fusion* 47.7 (2007), p. 510 (cit. on pp. 23, 135).

[19] Antoine Pochelon et al. "Recent TCV results-innovative plasma shaping to improve plasma properties and insight". In: *Plasma and Fusion Research* 7 (2012), pp. 2502148–2502148 (cit. on p. 23).

[20] S. Coda et al. “Enhanced confinement in diverted negative-triangularity L-mode plasmas in TCV”. In: *Plasma Physics and Controlled Fusion* 64.1 (Dec. 13, 2021), p. 014004. DOI: 10.1088/1361-6587/ac3fec (cit. on pp. 23, 135, 136).

[21] Max E. Austin et al. “Achievement of reactor-relevant performance in negative triangularity shape in the DIII-D tokamak”. In: *Physical review letters* 122.11 (2019), p. 115001 (cit. on pp. 23, 135, 136, 162).

[22] A. Marinoni et al. “H-mode grade confinement in L-mode edge plasmas at negative triangularity on DIII-D”. In: *Physics of Plasmas* 26.4 (2019) (cit. on pp. 23, 135, 136, 162).

[23] Kathreen E. Thome et al. “Overview of results from the 2023 DIII-D negative triangularity campaign”. In: *Plasma Physics and Controlled Fusion* 66.10 (2024), p. 105018 (cit. on pp. 23, 135, 136).

[24] Andrew O. Nelson et al. “Robust avoidance of edge-localized modes alongside gradient formation in the negative triangularity tokamak edge”. In: *Physical Review Letters* 131.19 (2023), p. 195101 (cit. on pp. 23, 136).

[25] A. O. Nelson et al. “Characterization of the ELM-free negative triangularity edge on DIII-D”. In: *Plasma Physics and Controlled Fusion* 66.10 (Sept. 2024), p. 105014. DOI: 10.1088/1361-6587/ad6a83 (cit. on pp. 23, 136, 157).

[26] International Atomic Energy Agency (iaea). *World Survey of Fusion Devices 2022*. Text. IAEA, 2022, pp. 1–180. URL: https://www.iaea.org/publications/15253/world-survey-of-fusion-devices-2022 (cit. on p. 24).

[27] J. Bucalossi et al. “Operating a full tungsten actively cooled tokamak: overview of WEST first phase of operation”. In: *Nuclear Fusion* 62.4 (Feb. 2022), p. 042007. ISSN: 0029-5515. DOI: 10.1088/1741-4326/ac2525 (cit. on p. 24).

[28] U. Stroth et al. “Progress from ASDEX Upgrade experiments in preparing the physics basis of ITER operation and DEMO scenario development”. In: *Nuclear Fusion* 62.4 (Mar. 2022), p. 042006. ISSN: 0029-5515. DOI: 10.1088/1741-4326/ac207f (cit. on pp. 24, 26).

[29] H. Reimerdes et al. “Overview of the TCV tokamak experimental programme”. In: *Nuclear Fusion* 62.4 (Mar. 2022), p. 042018. ISSN: 0029-5515. DOI: 10.1088/1741-4326/ac369b (cit. on pp. 24, 26).

[30] J. Jacquinot. “Steady-state operation of tokamaks: key experiments, integrated modelling and technology developments on Tore Supra”. In: *Nuclear Fusion* 45.10 (Oct. 2005), S118. DOI: 10.1088/0029-5515/45/10/S10 (cit. on p. 24).

[31] J. Bucalossi et al. “The WEST project: Testing ITER divertor high heat flux component technology in a steady state tokamak environment”. In: *Fusion Engineering and Design*. Proceedings of the 11th International Symposium on Fusion Nuclear Technology-11 (ISFNT-11) Barcelona, Spain, 15-20 September, 2013 89.7 (Oct. 2014), pp. 907–912. ISSN: 0920-3796. DOI: 10.1016/j.fusengdes.2014.01.062. URL: https://www.sciencedirect.com/science/article/pii/S0920379614000635 (cit. on p. 24).

[32] P. Moreau et al. “The Commissioning of the WEST Tokamak: Experience and Lessons Learned”. In: *IEEE Transactions on Plasma Science* 48.6 (June 2020), pp. 1376–1381. ISSN: 1939-9375. DOI: 10.1109/TPS.2020.2987160 (cit. on p. 24).

[33] H. Zohm et al. “Overview of ASDEX upgrade results in view of ITER and DEMO”. In: *Nuclear Fusion* 64.11 (2024), p. 112001 (cit. on p. 24).

[34] Albrecht Herrmann and Otto Gruber. “Chapter 1: ASDEX Upgrade - Introduction and Overview”. In: *Fusion Science and Technology* 44.3 (2003), pp. 569–577. DOI: 10.13182/FST03-A399. eprint: https://doi.org/10.13182/FST03-A399 (cit. on p. 26).

[35] F. Hofmann et al. “Creation and control of variably shaped plasmas in TCV”. In: *Plasma Physics and Controlled Fusion* 36.12 (Dec. 1994), B277. ISSN: 0741-3335. DOI: 10.1088/0741-3335/36/12B/023 (cit. on p. 26).

[36] S. Coda et al. “Overview of the TCV tokamak program: scientific progress and facility upgrades”. In: *Nuclear Fusion* 57.10 (June 2017), p. 102011. DOI: 10.1088/1741-4326/aa6412 (cit. on p. 26).

[37] B. P. Duval et al. “Experimental research on the TCV tokamak”. In: *Nuclear Fusion* 64.11 (2024), p. 112023 (cit. on pp. 26, 27).

[38] Jonas Degrave et al. “Magnetic control of tokamak plasmas through deep reinforcement learning”. In: *Nature* 602.7897 (2022), pp. 414–419 (cit. on p. 26).

[39] Alexander N. Karpushov et al. “Upgrade of the neutral beam heating system on the TCV tokamak–second high energy neutral beam”. In: *Fusion Engineering and Design* 187 (2023), p. 113384 (cit. on pp. 27, 70).

[40] Antti Salmi et al. “TCV intrinsic torque in balanced NBI experiment”. In: *50th EPS Conference on Plasma Physics*. European Physical Society. 2024 (cit. on p. 27).

[41] A Salmi et al. “Measurements of the intrinsic torque driven by up-down asymmetric L-mode plasmas in TCV”. In: *51st EPS Conference on Plasma Physics*. European Physical Society. 2025 (cit. on p. 27).

[42] Alexander N. Karpushov et al. “The diagnostic neutral beam injector with arc-discharge plasma source on the TCV Tokamak”. In: *Fusion Engineering and Design*. Proceeding of the 25th Symposium on Fusion Technology 84.2 (June 2009), pp. 993–997. ISSN: 0920-3796. DOI: 10.1016/j.fusengdes.2008.12.006. URL: https://www.sciencedirect.com/science/article/pii/S0920379608004626 (cit. on p. 27).

[43] RJ Fonck, DS Darrow, and KP Jaehnig. “Determination of plasma-ion velocity distribution via charge-exchange recombination spectroscopy”. In: *Physical Review A* 29.6 (1984), p. 3288 (cit. on pp. 27, 31, 70).

[44] Kimitaka Itoh and Sanae-I. Itoh. “The role of the electric field in confinement”. In: *Plasma physics and controlled fusion* 38.1 (1996), p. 1 (cit. on p. 30).

[45] Ulrich Stroth, P. Manz, and M. Ramisch. “On the interaction of turbulence and flows in toroidal plasmas”. In: *Plasma Physics and Controlled Fusion* 53.2 (2011), p. 024006 (cit. on pp. 30, 34).

[46] L. Vermare et al. “Formation of the radial electric field profile in the WEST tokamak”. In: *Nuclear Fusion* 62.2 (Dec. 2022), p. 026002. DOI: 10.1088/1741-4326/ac3c85 (cit. on pp. 30, 87, 88, 92, 99–101, 131, 132).

[47] E. Trier et al. “Radial electric field measurement in a tokamak with magnetic field ripple”. In: *Nuclear Fusion* 48.9 (Aug. 2008), p. 092001. ISSN: 0029-5515. DOI: 10.1088/0029-5515/48/9/092001 (cit. on pp. 30, 35, 36, 57).

[48] X. Garbet et al. “Entropy production rate in tokamaks with nonaxisymmetric magnetic fields”. In: *Physics of Plasmas* 17.7 (2010) (cit. on pp. 30, 35, 36).

[49] R. Varennes et al. “Synergy of Turbulent Momentum Drive and Magnetic Braking”. In: *Physical Review Letters* 128.25 (June 2022), p. 255002. DOI: 10.1103/PhysRevLett.128.255002 (cit. on pp. 30, 35).

[50] L. Vermare. “Confinement, turbulence and flow sensitivity to plasma current in tokamak plasmas (To be presented EPS Plasma)”. In: *49th EPS Conference on Plasma Physics*. Invited talk, July 2023. 2023 (cit. on pp. 30, 89, 91).

[51] S.-I. Itoh and K. Itoh. “Model of the H-mode in tokamaks”. In: *Nuclear Fusion* 29.6 (June 1989), p. 1031. DOI: 10.1088/0029-5515/29/6/013 (cit. on pp. 30, 132).

[52] P. Monier-Garbet et al. “Effects of neutrals on plasma rotation in DIII-D”. In: *Nuclear Fusion* 37.3 (Mar. 1997), p. 403. DOI: 10.1088/0029-5515/37/3/I09 (cit. on pp. 30, 132).

[53] D. A. D’ippolito and J. R. Myra. “Effect of ion-neutral charge exchange on radial electric fields in the edge plasma”. In: *Physics of Plasmas* 9.3 (Mar. 2002), pp. 853–860. ISSN: 1070-664X. DOI: 10.1063/1.1447919. eprint: https://pubs.aip.org/aip/pop/article-pdf/9/3/853/19278659/853_1_online.pdf (cit. on pp. 30, 132).

[54] T. W. Versloot et al. “Momentum losses by charge exchange with neutral particles in H-mode discharges at JET”. In: *Plasma Physics and Controlled Fusion* 53.6 (2011), p. 065017 (cit. on pp. 30, 132).

[55] John Omotani et al. “Plasma rotation from momentum transport by neutrals in tokamaks”. In: *Nuclear Fusion* 56.12 (2016), p. 124002 (cit. on pp. 30, 132).

[56] R. J. Taylor et al. “H-mode behavior induced by cross-field currents in a tokamak”. In: *Phys. Rev. Lett.* 63 (21 Nov. 1989), pp. 2365–2368. DOI: 10.1103/PhysRevLett.63.2365 (cit. on p. 30).

[57] R. R. Weynants, S. Jachmich, and G. Van Oost. “Demonstration of the role of flow shear in improved confinement”. In: *Plasma Physics and Controlled Fusion* 40.5 (May 1998), p. 635. DOI: 10.1088/0741-3335/40/5/013 (cit. on p. 30).

[58] G. D. Conway et al. “Impact of magnetic perturbation coils on the edge radial electric field and turbulence in ASDEX Upgrade”. In: *Plasma Physics and Controlled Fusion* 57.1 (2014), p. 014035 (cit. on p. 30).

[59] M. Willensdorfer et al. "Dependence of the L–H power threshold on the alignment of external non-axisymmetric magnetic perturbations in ASDEX Upgrade". In: *Physics of Plasmas* 29.3 (Mar. 2022), p. 032506. ISSN: 1070-664X. DOI: 10.1063/5.0073841 (cit. on p. 30).

[60] S. R. Haskey et al. "Main ion and impurity edge profile evolution across the L-to H-mode transition on DIII-D". In: *Plasma Physics and Controlled Fusion* 60.10 (2018), p. 105001 (cit. on pp. 31, 70, 107).

[61] Y. B. Kim, P. H. Diamond, and R. J. Groebner. "Neoclassical poloidal and toroidal rotation in tokamaks". In: *Physics of Fluids B: Plasma Physics* 3.8 (Aug. 1991), pp. 2050–2060. ISSN: 0899-8221. DOI: 10.1063/1.859671. URL: https://doi.org/10.1063/1.859671 (cit. on pp. 31, 33, 34).

[62] J. Kim et al. "Rotation characteristics of main ions and impurity ions in H-mode tokamak plasma". In: *Physical review letters* 72.14 (1994), p. 2199 (cit. on pp. 31, 34).

[63] Benjamin A. Carreras. "Progress in anomalous transport research in toroidal magnetic confinement devices". In: *IEEE Transactions on plasma science* 25.6 (1997), pp. 1281–1321 (cit. on p. 32).

[64] F. L. Hinton and Richard D. Hazeltine. "Theory of plasma transport in toroidal confinement systems". In: *Reviews of Modern Physics* 48.2 (1976), p. 239 (cit. on p. 32).

[65] Alexander Lebschy. "Experimental characterization of the core plasma flow at the ASDEX Upgrade tokamak". Available from INIS: http://inis.iaea.org/search/search.aspx?orig_q=RN:49081666 INIS Reference Number: 49081666. PhD thesis. Technische Universität München, Apr. 2018 (cit. on p. 33).

[66] Thomas H. Stix. "Decay of poloidal rotation in a tokamak plasma". In: *The Physics of Fluids* 16.8 (1973), pp. 1260–1267 (cit. on p. 33).

[67] P. Helander. "Classical and Neoclassical Transport in Tokamaks". In: *Fusion Science and Technology* 61.2T (2012), pp. 133–141. DOI: 10.13182/FST12-A13500 (cit. on pp. 33, 34).

[68] Philippe Ghendrih et al. *Rotation and momentum transport in magnetized plasmas*. Vol. 2. World Scientific, 2014 (cit. on p. 34).

[69] U Plank et al. "Overview of L- to H-mode transition experiments at ASDEX Upgrade". In: *Plasma Physics and Controlled Fusion* 65.1 (Dec. 6, 2022), p. 014001. DOI: 10.1088/1361-6587/aca35b (cit. on pp. 34, 43–45, 49).

[70] E. Viezzer et al. "High-accuracy characterization of the edge radial electric field at ASDEX Upgrade". In: *Nuclear Fusion* 53.5 (Apr. 2013), p. 053005. ISSN: 0029-5515. DOI: 10.1088/0029-5515/53/5/053005 (cit. on pp. 35, 37, 44).

[71] E. Viezzer et al. "Evidence for the neoclassical nature of the radial electric field in the edge transport barrier of ASDEX Upgrade". In: *Nuclear Fusion* 54.1 (Dec. 2013), p. 012003. ISSN: 0029-5515. DOI: 10.1088/0029-5515/54/1/012003 (cit. on pp. 35, 44, 45).

[72] P. C. De Vries et al. "Effect of toroidal field ripple on plasma rotation in JET". In: *Nuclear Fusion* 48.3 (2008), p. 035007 (cit. on p. 35).

[73] C. Fenzi et al. "On plasma rotation with toroidal magnetic field ripple and no external momentum input". In: *Nuclear Fusion* 51.10 (Sept. 2011), p. 103038. ISSN: 0029-5515. DOI: 10.1088/0029-5515/51/10/103038 (cit. on pp. 35, 36).

[74] J. W. Connor and R. J. Hastie. "Neoclassical diffusion arising from magnetic-field ripples in Tokamaks". en. In: *Nuclear Fusion* 13.2 (Mar. 1973), p. 221. ISSN: 0029-5515. DOI: 10.1088/0029-5515/13/2/011 (cit. on pp. 35, 36).

[75] H. Zhu et al. "Effects of collisional ion orbit loss on tokamak radial electric field and toroidal rotation in an L-mode plasma". In: *Nuclear Fusion* 63.6 (Apr. 2023), p. 066009. ISSN: 0029-5515. DOI: 10.1088/1741-4326/acc815 (cit. on pp. 36, 37).

[76] J. A. Boedo et al. "Experimental evidence of edge intrinsic momentum source driven by kinetic ion loss and edge radial electric fields in tokamaks". In: *Physics of Plasmas* 23.9 (Sept. 2016), p. 092506. ISSN: 1070-664X. DOI: 10.1063/1.4962683 (cit. on p. 37).

[77] F. L. Hinton and M. S. Chu. "Neoclassical ion transport through the separatrix in divertor tokamaks". In: *Nuclear fusion* 25.3 (1985), p. 345 (cit. on p. 37).

[78] F. L. Hinton. "Neoclassical transport effects and the H-mode transition". In: *Nuclear fusion* 25.10 (1985), p. 1457 (cit. on p. 37).

[79] Sanae-I. Itoh and Kimitaka Itoh. "Model of L to H-mode transition in tokamak". In: *Physical review letters* 60.22 (1988), p. 2276 (cit. on p. 37).

[80] K. C. Shaing and E. C. Crume. "Bifurcation theory of poloidal rotation in tokamaks: A model for L-H transition". In: *Physical Review Letters* 63.21 (Nov. 1989), pp. 2369–2372. DOI: 10.1103/PhysRevLett.63.2369 (cit. on p. 37).

[81] J. W. Connor and H. R. Wilson. "A review of theories of the L-H transition". In: *Plasma Physics and Controlled Fusion* 42.1 (Jan. 2000), R1. ISSN: 0741-3335. DOI: 10.1088/0741-3335/42/1/201 (cit. on pp. 37, 44).

[82] Robert W. Brzozowski Iii et al. "A geometric model of ion orbit loss under the influence of a radial electric field". In: *Physics of Plasmas* 26.4 (Apr. 2019), p. 042511. ISSN: 1070-664X. DOI: 10.1063/1.5075613 (cit. on pp. 37, 87, 91).

[83] Robert William Brzozowski. "Thermal Ion Orbit Loss in Diverted Tokamaks and its Role Approaching the LH Transition". PhD thesis. University of California, Los Angeles, 2021 (cit. on pp. 37, 91).

[84] Y. Nishimura, F. L. Waelbroeck, and L. J. Zheng. "Computational analysis of ion orbital loss in diverted positive- and negative-triangularity tokamaks". In: *Physics of Plasmas* 27.1 (Jan. 2020), p. 012505. ISSN: 1070-664X. DOI: 10.1063/1.5131157 (cit. on pp. 37, 136, 137).

[85] H. Zhu et al. "Effects of collisional ion orbit loss on neoclassical tokamak radial electric fields". In: *Nuclear Fusion* 62.6 (Apr. 2022), p. 066012. ISSN: 0029-5515. DOI: 10.1088/1741-4326/ac5b8a (cit. on p. 37).

[86] Gerrit J. Kramer, Andrew Oakleigh Nelson, and Kathreen E. Thome. "On the formation of edge electric fields in negative triangularity plasmas". In: *Plasma Physics and Controlled Fusion* (2025) (cit. on pp. 37, 136, 137).

[87] S. Ku et al. "Difference in Neoclassical Edge Flows Between Strongly Negative and Positive Triangularities in the XGC Gyrokinetic Simulation". In: *arXiv preprint arXiv:2510.05287* (2025) (cit. on pp. 37, 136, 137, 163, 165).

[88] D. J. Battaglia et al. "Dependence of the L–H transition on X-point geometry and divertor recycling on NSTX". In: *Nuclear Fusion* 53.11 (Oct. 2013), p. 113032. DOI: 10.1088/0029-5515/53/11/113032 (cit. on p. 37).

[89] T. Stoltzfus-Dueck et al. "X-Point-Position-Dependent Intrinsic Toroidal Rotation in the Edge of the TCV Tokamak". In: *Physical Review Letters* 114.24 (June 2015), p. 245001. DOI: 10.1103/PhysRevLett.114.245001 (cit. on pp. 37, 136, 137, 161, 162).

[90] A. V. Chankin and G. M. Mccracken. "Loss ion orbits at the tokamak edge". In: *Nuclear Fusion* 33.10 (Oct. 1993), p. 1459. ISSN: 0029-5515. DOI: 10.1088/0029-5515/33/10/I05 (cit. on pp. 37, 87).

[91] K. C. Shaing. "Direction of ion∇ B drift and power threshold in high confinement mode in diverted tokamaks". In: *Physics of Plasmas* 9.1 (2002), pp. 1–3 (cit. on pp. 37, 87, 91).

[92] Seunghoe Ku, Hoyul Baek, and C. S. Chang. "Property of an X-point generated velocity-space hole in a diverted tokamak plasma edge". In: *Physics of Plasmas* 11.12 (Dec. 2004), pp. 5626–5633. ISSN: 1070-664X. DOI: 10.1063/1.1812273. eprint: https://pubs.aip.org/aip/pop/article-pdf/11/12/5626/19060319/5626_1_online.pdf (cit. on pp. 37, 91).

[93] P. H. Diamond and Y.-B. Kim. "Theory of mean poloidal flow generation by turbulence". In: *Physics of Fluids B: Plasma Physics* 3.7 (1991), pp. 1626–1633. ISSN: 0899-8221. DOI: 10.1063/1.859681. eprint: https://pubs.aip.org/aip/pfb/article-pdf/3/7/1626/12661511/1626_1_online.pdf (cit. on p. 38).

[94] B. A. Carreras, V. E. Lynch, and L. Garcia. "Electron diamagnetic effects on the resistive pressure-gradient-driven turbulence and poloidal flow generation". In: *Physics of Fluids B: Plasma Physics* 3.6 (1991), pp. 1438–1444 (cit. on p. 38).

[95] P. H. Diamond et al. "Zonal flows in plasma—a review". In: *Plasma Physics and Controlled Fusion* 47.5 (Apr. 1, 2005), R35–R161. DOI: 10.1088/0741-3335/47/5/r01 (cit. on pp. 38, 49).

[96] C. Hidalgo et al. "Generation of sheared poloidal flows via Reynolds stress and transport barrier physics". In: *Plasma Physics and Controlled Fusion* 42.5A (2000), A153 (cit. on p. 38).

[97] Y. Sarazin et al. "Key impact of phase dynamics and diamagnetic drive on Reynolds stress in magnetic fusion plasmas". In: *Plasma Physics and Controlled Fusion* 63.6 (May 2021), p. 064007. DOI: 10.1088/1361-6587/abf673 (cit. on p. 38).

[98] Akihide Fujisawa. "A review of zonal flow experiments". In: *Nuclear Fusion* 49.1 (Dec. 9, 2008), p. 013001. DOI: 10.1088/0029-5515/49/1/013001 (cit. on p. 38).

[99] Guilhem Dif-Pradalier et al. “Interplay between Gyrokinetic Turbulence, Flows, and Collisions:<? format?> Perspectives on Transport and Poloidal Rotation”. In: *Physical Review Letters* 103.6 (2009), p. 065002 (cit. on p. 38).

[100] Tuomas Tala et al. “Toroidal and poloidal momentum transport studies in JET”. In: *Nuclear fusion* 47.8 (2007), p. 1012 (cit. on pp. 38, 74).

[101] W. M. Solomon et al. “Experimental test of the neoclassical theory of impurity poloidal rotation in tokamaks”. In: *Physics of Plasmas* 13.5 (2006) (cit. on pp. 38, 74).

[102] B. A. Grierson et al. “Collisionality scaling of main-ion toroidal and poloidal rotation in low torque DIII-D plasmas”. In: *Nuclear Fusion* 53.6 (2013), p. 063010 (cit. on p. 38).

[103] P. H. Diamond et al. “Self-Regulating Shear Flow Turbulence: A Paradigm for the L to H Transition”. In: *Physical Review Letters* 72.16 (Apr. 1994), pp. 2565–2568. DOI: 10.1103/PhysRevLett.72.2565 (cit. on pp. 38, 49).

[104] Eun-Jin Kim and P. H. Diamond. “Zonal flows and transient dynamics of the l-h transition”. In: *Physical review letters* 90.18 (2003), p. 185006 (cit. on pp. 38, 49).

[105] G. R. Tynan et al. “Recent progress towards a physics-based understanding of the H-mode transition”. In: *Plasma Physics and Controlled Fusion* 58.4 (2016), p. 044003 (cit. on p. 38).

[106] L. Schmitz. “The role of turbulence–flow interactions in L- to H-mode transition dynamics: recent progress”. In: *Nuclear Fusion* 57.2 (Jan. 9, 2017), p. 025003. DOI: 10.1088/1741-4326/57/2/025003 (cit. on pp. 38, 49).

[107] Ö. D. Gürcan et al. “Intrinsic rotation and electric field shear”. In: *Physics of Plasmas* 14.4 (Apr. 26, 2007), p. 042306. DOI: 10.1063/1.2717891 (cit. on p. 38).

[108] J. E. Rice et al. “Inter-machine comparison of intrinsic toroidal rotation in tokamaks”. en. In: *Nuclear Fusion* 47.11 (Oct. 2007), p. 1618. ISSN: 0029-5515. DOI: 10.1088/0029-5515/47/11/025 (cit. on p. 38).

[109] Niels Winsor, John L. Johnson, and John M. Dawson. “Geodesic Acoustic Waves in Hydromagnetic Systems”. In: *The Physics of Fluids* 11.11 (Nov. 1968), pp. 2448–2450. ISSN: 0031-9171. DOI: 10.1063/1.1691835 (cit. on pp. 38, 62).

[110] G. D. Conway, A. I. Smolyakov, and T. Ido. “Geodesic acoustic modes in magnetic confinement devices”. In: *Nuclear Fusion* 62.1 (Dec. 2021), p. 013001. ISSN: 0029-5515. DOI: 10.1088/1741-4326/ac0dd1 (cit. on pp. 38, 62).

[111] T. M. Antonsen Jr et al. “Physical mechanism of enhanced stability from negative shear in tokamaks: Implications for edge transport and the L-H transition”. In: *Physics of Plasmas* 3.6 (1996), pp. 2221–2223 (cit. on p. 39).

[112] N. Fedorczak et al. “Dynamics of tilted eddies in a transversal flow at the edge of tokamak plasmas and the consequences for L–H transition”. In: *Plasma Physics and Controlled Fusion* 55.12 (Nov. 2013), p. 124024. ISSN: 0741-3335. DOI: 10.1088/0741-3335/55/12/124024 (cit. on pp. 39, 40, 87, 89, 90, 129, 131, 133, 166).

[113] N. Fedorczak et al. “Shear-induced Reynolds stress at the edge of L-mode tokamak plasmas”. In: *Nuclear Fusion* 52.10 (Sept. 2012), p. 103013. ISSN: 0029-5515. DOI: 10.1088/0029-5515/52/10/103013 (cit. on pp. 39, 40, 87, 90, 129, 131, 133, 166).

[114] P Stangeby. In: *The plasma boundary of magnetic fusion devices*. Vol. 224. Philadelphia, Pennsylvania: Institute of Physics Pub, 2000, pp. 296–323 (cit. on p. 40).

[115] U. Plank. “The Effect of the Radial Electric Field around the Separatrix on the Access to the High Confinement Mode at ASDEX Upgrade”. PhD thesis. Ludwig-Maximilians-Universität München München, 2022. URL: https://pure.mpg.de/pubman/faces/ViewItemOverviewPage.jsp?itemId=item_3373610 (cit. on pp. 40, 44, 88, 89, 110).

[116] D. Brida et al. “Physics of the electric field in the scrape-off layer in ASDEX Upgrade L-mode discharges and comparison to experiments”. In: *Nuclear Materials and Energy* 33 (Sept. 27, 2022), p. 101262. DOI: 10.1016/j.nme.2022.101262 (cit. on pp. 40–42, 80, 111).

[117] Martin Greenwald. “Density limits in toroidal plasmas”. In: *Plasma Physics and Controlled Fusion* 44.8 (July 2002), R27. DOI: 10.1088/0741-3335/44/8/201 (cit. on p. 42).

[118] K. H. Burrell et al. “Role of the radial electric field in the transition from L (low) mode to H (high) mode to VH (very high) mode in the DIII-D tokamak”. In: *Physics of plasmas* 1.5 (1994), pp. 1536–1544 (cit. on pp. 42, 43).

[119] R. A. Moyer et al. “Beyond paradigm: Turbulence, transport, and the origin of the radial electric field in low to high confinement mode transitions in the DIII-D tokamak”. In: *Physics of Plasmas*

2.6 (June 1995), pp. 2397–2407. ISSN: 1070-664X. DOI: 10.1063/1.871263. eprint: https://pubs.aip.org/aip/pop/article-pdf/2/6/2397/19319980/2397_1_online.pdf (cit. on pp. 42, 43).

[120] K. H. Burrell et al. "Edge radial electric field structure in quiescent H-mode plasmas in the DIII-D tokamak". In: *Plasma Physics and Controlled Fusion* 46.5 (Apr. 2004), A165. ISSN: 0741-3335. DOI: 10.1088/0741-3335/46/5A/018 (cit. on p. 43).

[121] M. Cavedon et al. "Connecting the global H-mode power threshold to the local radial electric field at ASDEX Upgrade". In: *Nuclear Fusion* 60.6 (May 12, 2020), p. 066026. DOI: 10.1088/1741-4326/ab8777 (cit. on p. 44).

[122] U. Plank et al. "Experimental study of the edge radial electric field in different drift configurations and its role in the access to H-mode at ASDEX Upgrade". In: *Physics of Plasmas* 30.4 (Apr. 2023), p. 042513. ISSN: 1070-664X. DOI: 10.1063/5.0102763 (cit. on pp. 45, 46, 80, 87, 88, 92, 93, 99, 110, 116, 131, 132, 165).

[123] C. Silva et al. "Structure of the JET edge radial electric field in He and D plasmas". In: *Nuclear Fusion* 61.12 (Oct. 22, 2021), p. 126006. DOI: 10.1088/1741-4326/ac2abb (cit. on pp. 46, 47).

[124] C. Silva et al. "Effect of the divertor configuration on the JET edge radial electric field". In: *Nuclear Fusion* 62.12 (Nov. 2022), p. 126057. ISSN: 0029-5515. DOI: 10.1088/1741-4326/ac97f4 (cit. on pp. 46, 47).

[125] H Meyer et al. "The structure, evolution and role of the radial edge electric field in H-mode and L-mode on MAST". In: *Journal of Physics: Conference Series* 123 (July 2008), p. 012005. DOI: 10.1088/1742-6596/123/1/012005 (cit. on pp. 47, 51, 88).

[126] H. Meyer et al. "L–H transition and pedestal studies on MAST". In: *Nuclear Fusion* 51.11 (2011), p. 113011 (cit. on p. 47).

[127] T. Estrada et al. "Sheared flows and transition to improved confinement regime in the TJ-II stellarator". In: *Plasma Physics and Controlled Fusion* 51.12 (Nov. 2009), p. 124015. ISSN: 0741-3335. DOI: 10.1088/0741-3335/51/12/124015 (cit. on pp. 47–49, 55, 57).

[128] T. Estrada et al. "Experimental observation of coupling between turbulence and sheared flows during L-H transitions in a toroidal plasma". In: *Europhysics Letters* 92.3 (Nov. 2010), p. 35001. ISSN: 0295-5075. DOI: 10.1209/0295-5075/92/35001 (cit. on p. 49).

[129] G. D. Conway et al. "Mean and Oscillating Plasma Flows and Turbulence Interactions across the L-H Confinement Transition". In: *Physical Review Letters* 106.6 (Feb. 2011), p. 065001. DOI: 10.1103/PhysRevLett.106.065001 (cit. on p. 49).

[130] L. Schmitz et al. "Role of Zonal Flow Predator-Prey Oscillations in Triggering the Transition to H-Mode Confinement". In: *Physical Review Letters* 108.15 (Apr. 2012), p. 155002. DOI: 10.1103/PhysRevLett.108.155002 (cit. on p. 49).

[131] K. Miki et al. "Spatio-temporal evolution of the L $\rightarrow$ I $\rightarrow$ H transition". In: *Physics of Plasmas* 19.9 (Sept. 2012), p. 092306. ISSN: 1070-664X. DOI: 10.1063/1.4753931 (cit. on p. 49).

[132] M. Cavedon et al. "Interplay between turbulence, neoclassical and zonal flows during the transition from low to high confinement mode at ASDEX Upgrade". In: *Nuclear Fusion* 57.1 (Oct. 17, 2016), p. 014002. DOI: 10.1088/0029-5515/57/1/014002 (cit. on p. 49).

[133] G. Birkenmeier et al. "Magnetic structure and frequency scaling of limit-cycle oscillations close to L- to H-mode transitions". In: *Nuclear Fusion* 56.8 (July 20, 2016), p. 086009. DOI: 10.1088/0029-5515/56/8/086009 (cit. on p. 49).

[134] T. N. Carlstrom et al. "Evidence for the role of velocity shear on the L-H transition in DIII-D". In: *Plasma Physics and Controlled Fusion* 44.5 (Apr. 2002), A333. ISSN: 0741-3335. DOI: 10.1088/0741-3335/44/5A/335 (cit. on pp. 50, 57, 88).

[135] C. Fenzi et al. "Effect of ion ∇B drift direction on density fluctuation poloidal flow and flow shear". In: *Physics of Plasmas* 12.6 (May 2005), p. 062307. ISSN: 1070-664X. DOI: 10.1063/1.1915349 (cit. on pp. 50, 57, 88).

[136] G. R. Mckee et al. "Turbulence imaging and applications using beam emission spectroscopy on DIII-D (invited)". In: *Review of Scientific Instruments* 74.3 (Mar. 2003), pp. 2014–2019. ISSN: 0034-6748. DOI: 10.1063/1.1535248. eprint: https://pubs.aip.org/aip/rsi/article-pdf/74/3/2014/19083449/2014_1_online.pdf (cit. on pp. 50, 56).

[137] J. Schirmer et al. "The radial electric field and its associated shear in the ASDEX Upgrade tokamak". In: *Nuclear Fusion* 46.9 (Aug. 2006), S780. ISSN: 0029-5515. DOI: 10.1088/0029-5515/46/9/S13 (cit. on pp. 51, 55, 57, 87, 88, 92, 99, 131).

[138] C. A. De Meijere et al. “Complete multi-field characterization of the geodesic acoustic mode in the TCV tokamak”. en. In: *Plasma Physics and Controlled Fusion* 56.7 (June 2014), p. 072001. ISSN: 0741-3335. DOI: 10.1088/0741-3335/56/7/072001 (cit. on pp. 53, 62).

[139] P. Molina Cabrera et al. “V-band Doppler backscattering diagnostic in the TCV tokamak”. In: *Review of Scientific Instruments* 89.8 (2018), p. 083503 (cit. on pp. 53, 67, 68).

[140] B. P. Duval et al. “Bulk plasma rotation in the TCV tokamak in the absence of external momentum input”. en. In: *Plasma Physics and Controlled Fusion* 49.12B (Nov. 2007), B195. ISSN: 0741-3335. DOI: 10.1088/0741-3335/49/12B/S18 (cit. on p. 53).

[141] C. Marini. “Poloidal CX visible light plasma rotation diagnostics in TCV”. en. PhD thesis. Lausanne: EPFL, 2017. DOI: 10.5075/epfl-thesis-8031. URL: https://infoscience.epfl.ch/handle/20.500.14299/142172 (cit. on pp. 53, 70, 72, 74).

[142] Sascha Rienäcker et al. “Survey of the edge radial electric field in L-mode TCV plasmas using Doppler backscattering”. In: *Plasma Physics and Controlled Fusion* 67.6 (2025), p. 065003 (cit. on p. 54).

[143] M. Hirsch et al. “Doppler reflectometry for the investigation of propagating density perturbations”. In: *Plasma Physics and Controlled Fusion* 43.12 (Oct. 2001), p. 1641. ISSN: 0741-3335. DOI: 10.1088/0741-3335/43/12/302 (cit. on pp. 54, 55).

[144] G. D. Conway et al. “Plasma rotation profile measurements using Doppler reflectometry”. In: *Plasma Physics and Controlled Fusion* 46.6 (Apr. 27, 2004), pp. 951–970. DOI: 10.1088/0741-3335/46/6/003 (cit. on pp. 54, 110).

[145] P. Hennequin et al. “Fluctuation spectra and velocity profile from Doppler backscattering on Tore Supra”. In: *Nuclear Fusion* 46.9 (Aug. 17, 2006), S771–S779. DOI: 10.1088/0029-5515/46/9/s12 (cit. on pp. 54, 56–58, 61, 62).

[146] Laure Vermare et al. “Impact of collisionality on fluctuation characteristics of micro-turbulence”. In: *Physics of Plasmas* 18.1 (2011), p. 012306 (cit. on pp. 54, 57, 96).

[147] J. Schirmer et al. “Radial correlation length measurements on ASDEX Upgrade using correlation Doppler reflectometry”. en. In: *Plasma Physics and Controlled Fusion* 49.7 (June 2007), p. 1019. ISSN: 0741-3335. DOI: 10.1088/0741-3335/49/7/006 (cit. on p. 55).

[148] P A Schneider et al. “Overview of the isotope effects in the ASDEX Upgrade tokamak”. In: *Plasma Physics and Controlled Fusion* 63.6 (May 7, 2021), p. 064006. DOI: 10.1088/1361-6587/abf540 (cit. on p. 55).

[149] O Panico et al. “Indirect evidence of avalanche-like transport in TCV plasmas backed by 1D nonlinear simulations”. In: *50th EPS Conference on Plasma Physics*. Poster contribution. July 2024. URL: https://cea.hal.science/cea-04723573 (cit. on pp. 55, 167).

[150] J. R. Pinzón et al. “Experimental investigation of the tilt angle of turbulent structures in the core of fusion plasmas”. In: *Nuclear Fusion* 59.7 (June 2019), p. 074002. DOI: 10.1088/1741-4326/ab227e (cit. on p. 55).

[151] J. R. Pinzón et al. “Measurement of the tilt angle of turbulent structures in magnetically confined plasmas using Doppler reflectometry”. en. In: *Plasma Physics and Controlled Fusion* 61.10 (Sept. 2019), p. 105009. ISSN: 0741-3335. DOI: 10.1088/1361-6587/ab394d (cit. on p. 55).

[152] Elisée Trier. “Champ électrique radial dans les plasmas de tokamak non axi-symétrique: étude par réflectométrie Doppler”. PhD thesis. Ecole Polytechnique X, 2010 (cit. on p. 56).

[153] A. Casati et al. “Turbulence in the TORE SUPRA Tokamak: Measurements and Validation of Nonlinear Simulations”. In: *Physical review letters* 102.16 (2009), p. 165005 (cit. on p. 56).

[154] P. Hennequin et al. “k spectra in Tore Supra : experiments, theory and modelling”. In: *Workshop on Electric Fields, Turbulence and Self-Organisation in Magnetised Plasmas (EFTSOMP)*. Oral contribution. July 2011 (cit. on p. 56).

[155] Frank Jenko et al. “Electron temperature gradient driven turbulence”. In: *Physics of plasmas* 7.5 (2000), pp. 1904–1910 (cit. on pp. 56, 149, 187).

[156] O. Krutkin et al. “Gyrokinetic simulations of the core turbulence in the reference JT-60SA scenario”. In: *Nuclear Fusion* 66.1 (Dec. 2025), p. 016043. DOI: 10.1088/1741-4326/ae248f (cit. on p. 56).

[157] E. Mazzucato. “Microwave reflectometry for magnetically confined plasmas”. In: *Review of Scientific Instruments* 69.6 (1998), pp. 2201–2217 (cit. on p. 56).

[158] L. Vermare. “Flow and phase velocity of turbulence in magnetized fusion plasmas”. In: *16th International Reflectometry Workshop*. Oral contribution. May 2024. URL: https://event.ipp-

hgw.mpg.de/event/954/contributions/1874/attachments/1076/1713/IRW16_LV.pdf (cit. on p. 57).

[159] A. Krämer-Flecken et al. "Observation and characterisation of trapped electron modes in Wendelstein 7-X". In: *Plasma Physics and Controlled Fusion* 67.2 (2025), p. 025014 (cit. on p. 57).

[160] F. Orlacchio et al. "Interpreting scale-dependent velocity measurements from DBS on WEST tokamak". In: *29th Joint EU-US Transport Task Force Meeting*. Poster contribution. Sept. 2025. URL: https://ttf2025.ek.hun-ren.hu/wp-content/uploads/2025/09/Abstract-booklet-TTF-2025.pdf (cit. on pp. 57, 167).

[161] E. Holzhauer and J. H. Massig. "An analysis of optical mixing in plasma scattering experiments". In: *Plasma Physics* 20.9 (Sept. 1978), p. 867. DOI: 10.1088/0032-1028/20/9/002 (cit. on p. 58).

[162] V. V. Bulanin and M. V. Yafanov. "Spatial and spectral resolution of the plasma Doppler reflectometry". In: *Plasma Physics Reports* 32.1 (2006), pp. 47–55 (cit. on p. 58).

[163] G. D. Conway et al. "Assessment of Doppler reflectometry accuracy using full-wave codes with comparison to beam-tracing and analytic expressions". In: *Plasma Physics and Controlled Fusion* 67.10 (2025), p. 105024 (cit. on pp. 58, 65).

[164] E. Blanco and T. Estrada. "Study of Doppler reflectometry capability to determine the perpendicular velocity and the k-spectrum of the density fluctuations using a 2D full-wave code". In: *Plasma Physics and Controlled Fusion* 50.9 (July 2008), p. 095011. ISSN: 0741-3335. DOI: 10.1088/0741-3335/50/9/095011 (cit. on p. 58).

[165] T. Happel et al. "Comparison of detailed experimental wavenumber spectra with gyrokinetic simulation aided by two-dimensional full-wave simulations". In: *Plasma Physics and Controlled Fusion* 59.5 (Mar. 2017), p. 054009. ISSN: 0741-3335. DOI: 10.1088/1361-6587/aa645b (cit. on pp. 58, 110).

[166] P. Hennequin et al. "Doppler backscattering system for measuring fluctuations and their perpendicular velocity on Tore Supra". In: *Review of Scientific Instruments* 75.10 (Oct. 7, 2004), pp. 3881–3883. DOI: 10.1063/1.1787920 (cit. on pp. 59, 60).

[167] R. Sabot et al. "Single sideband modulator, a key component of Tore-Supra heterodyne reflectometers". In: *Review of Scientific Instruments* 75.8 (Aug. 2004), pp. 2656–2659. ISSN: 0034-6748. DOI: 10.1063/1.1777379. eprint: https://pubs.aip.org/aip/rsi/article-pdf/75/8/2656/19240276/2656_1_online.pdf. URL: https://doi.org/10.1063/1.1777379 (cit. on pp. 59, 60).

[168] Laure Vermare et al. "Detection of geodesic acoustic mode oscillations, using multiple signal classification analysis of Doppler backscattering signal on Tore Supra". In: *Nuclear Fusion* 52.6 (2012), p. 063008 (cit. on pp. 61, 62, 98).

[169] Anna Medvedeva et al. "Density profile and turbulence evolution during LH transition studied with the ultra-fast swept reflectometer on ASDEX Upgrade". In: *Plasma Physics and Controlled Fusion* 59.12 (2017), p. 125014 (cit. on p. 61).

[170] P. Hennequin et al. "Analysis of density fluctuation frequency spectra in Tore Supra as a tool for studying plasma motion and transport properties". In: *Proc. 26th EPS Conf. on Plasma Physics (P3.006)*. 1999. URL: https://info.fusion.ciemat.es/OCS/EPS1999/web/pdf/p3006.pdf (cit. on pp. 61, 62).

[171] Ralph Schmidt. "Multiple emitter location and signal parameter estimation". In: *IEEE transactions on antennas and propagation* 34.3 (1986), pp. 276–280 (cit. on p. 62).

[172] A. Storelli et al. "Comprehensive comparisons of geodesic acoustic mode characteristics and dynamics between Tore Supra experiments and gyrokinetic simulations". In: *Physics of Plasmas* 22 (June 2015), p. 062508. DOI: 10.1063/1.4922845 (cit. on p. 62).

[173] Alexandre Storelli. "Study of the turbulent transport in the Tore Supra tokamak : observation of stationary perpendicular flows and of the geodesic acoustic mode". PhD thesis. Apr. 2015 (cit. on pp. 62, 65).

[174] C. Honoré et al. "Quasi-optical Gaussian beam tracing to evaluate Doppler backscattering conditions". In: *Nuclear Fusion* 46.9 (Aug. 2006), S809. ISSN: 0029-5515. DOI: 10.1088/0029-5515/46/9/S16 (cit. on p. 64).

[175] Hans-Jürgen Hartfuss and Thomas Geist. *Fusion Plasma Diagnostics with mm-waves: an introduction*. John Wiley & Sons, 2013 (cit. on p. 64).

[176] P. Molina Cabrera et al. "V-band nanosecond-scale pulse reflectometer diagnostic in the TCV tokamak". In: *Review of Scientific Instruments* 90.12 (Dec. 2019). ISSN: 1089-7623. DOI: 10.1063/1.5094850 (cit. on pp. 65, 67, 167).

[177] J-M Moret et al. “Tokamak equilibrium reconstruction code LIUQE and its real time implementation”. In: *Fusion Engineering and Design* 91 (2015), pp. 1–15 (cit. on p. 65).
[178] P. Blanchard et al. “Thomson scattering measurements in the divertor region of the TCV Tokamak plasmas”. en. In: *Journal of Instrumentation* 14.10 (Oct. 2019), p. C10038. ISSN: 1748-0221. DOI: 10.1088/1748-0221/14/10/C10038. URL: https://dx.doi.org/10.1088/1748-0221/14/10/C10038 (cit. on pp. 65, 68).
[179] E. Stefanikova et al. “Fitting of the Thomson scattering density and temperature profiles on the COMPASS tokamak”. In: *Review of Scientific Instruments* 87.11 (Aug. 2016), 11E536. ISSN: 0034-6748. DOI: 10.1063/1.4961554 (cit. on p. 65).
[180] M. Ugoletti et al. “Role of radiation re-absorption in the thermal helium beam diagnostic”. In: *Review of Scientific Instruments* 95.8 (Aug. 2024), p. 083530. ISSN: 0034-6748. DOI: 10.1063/5.0217220 (cit. on pp. 67, 150, 167).
[181] F. Bagnato et al. “Study of correlations between LOC/SOC transition, intrinsic toroidal rotation reversal and TEM/ITG bifurcation with different working gases in TCV”. In: *Nuclear Fusion* 63.5 (2023), p. 056006 (cit. on p. 70).
[182] M. Cavedon et al. “Separatrix ion to electron temperature ratio in the TCV and ASDEX Upgrade tokamaks”. In: *Nuclear Fusion* 65.10 (Sept. 2025), p. 106007. DOI: 10.1088/1741-4326/adfdfc (cit. on p. 70).
[183] N. Offeddu et al. “Gas puff imaging on the TCV tokamak”. In: *Review of Scientific Instruments* 93.12 (Dec. 2022), p. 123504. ISSN: 0034-6748. DOI: 10.1063/5.0126398 (cit. on pp. 70, 167).
[184] N. Offeddu et al. “Analysis techniques for blob properties from gas puff imaging data”. In: *Review of Scientific Instruments* 94.3 (2023) (cit. on p. 71).
[185] Ian H Hutchinson. “Principles of plasma diagnostics”. In: *Plasma Physics and Controlled Fusion* 44.12 (2002), pp. 2603–2603 (cit. on p. 71).
[186] S. Barry. “The extension of the FIR interferometer of TCV to a polarimeter and measurements of the Faraday rotation caused by the poloidal magnetic field”. PhD thesis. EPFL, 1999 (cit. on p. 71).
[187] A. Lebschy et al. “Measurement of the complete core plasma flow across the LOC–SOC transition at ASDEX Upgrade”. In: *Nuclear Fusion* 58.2 (2017), p. 026013 (cit. on p. 74).
[188] A. Bortolon et al. “Indirect measurement of poloidal rotation using inboard–outboard asymmetry of toroidal rotation and comparison with neoclassical predictions”. In: *Nuclear Fusion* 53.2 (Jan. 2013), p. 023002. ISSN: 0029-5515. DOI: 10.1088/0029-5515/53/2/023002 (cit. on p. 74).
[189] E. A. Belli and J. Candy. “Kinetic calculation of neoclassical transport including self-consistent electron and impurity dynamics”. en. In: *Plasma Physics and Controlled Fusion* 50.9 (July 2008), p. 095010. ISSN: 0741-3335. DOI: 10.1088/0741-3335/50/9/095010 (cit. on p. 74).
[190] EA Belli and J Candy. “Full linearized Fokker–Planck collisions in neoclassical transport simulations”. In: *Plasma physics and controlled fusion* 54.1 (2011), p. 015015 (cit. on p. 74).
[191] K. Höfler et al. “Poloidally resolved measurements of the perpendicular propagation velocity of density fluctuations in ASDEX Upgrade L-mode plasmas”. In: *Plasma Physics and Controlled Fusion* 63.3 (Jan. 2021), p. 035020. ISSN: 0741-3335. DOI: 10.1088/1361-6587/abd896 (cit. on pp. 76, 78).
[192] G. Conway et al. “Recent progress in modelling the resolution and localization of Doppler reflectometry measurements”. In: *14th International Reflectometry Workshop for Fusion Plasma Diagnostics*. 2019 (cit. on p. 77).
[193] A. Krämer-Flecken et al. “Poloidal rotation asymmetry and relation to turbulence”. In: *Proc. of the 39th EPS Conf. and 16th Int. Congress on Plasma Physics*. Vol. 36. 2012, p–P5 (cit. on pp. 78, 167).
[194] L. Vermare et al. “Poloidal asymmetries of flows in the Tore Supra tokamak”. In: *Physics of Plasmas* 25.2 (Feb. 2018), p. 020704. ISSN: 1070-664X. DOI: 10.1063/1.5022122 (cit. on pp. 78, 167).
[195] T. Estrada et al. “Turbulence and perpendicular plasma flow asymmetries measured at TJ-II plasmas”. In: *Nuclear Fusion* 59.7 (2019), p. 076021 (cit. on pp. 78, 167).
[196] A. Bortolon et al. “Observation of spontaneous toroidal rotation inversion in ohmically heated tokamak plasmas”. In: *Physical Review Letters* 97.23 (2006), p. 235003 (cit. on pp. 80, 95).

[197] B. P. Duval et al. "Spontaneous L-mode plasma rotation scaling in the TCV tokamaka)". In: *Physics of Plasmas* 15.5 (Apr. 2008), p. 056113. ISSN: 1070-664X. DOI: 10.1063/1.2841528 (cit. on pp. 80, 95, 116).

[198] M. Peret. "Pushing the physics of edge transport barriers towards the wall : how do boundary conditions impact confinement transitions in tokamaks?" PhD thesis. Institut Polytechnique de Paris, Feb. 2022. URL: https://theses.hal.science/tel-03681704 (cit. on p. 80).

[199] C. Silva et al. "Er measurements in JET L-mode plasmas for a wide range of densities—from the low-recycling regime up to the density limit". In: *Nuclear Fusion* 65.3 (Feb. 2025), p. 036042. DOI: 10.1088/1741-4326/adb762 (cit. on pp. 80, 116).

[200] A.H. Kritz et al. "Ray tracing study of electron cyclotron heating in toroidal geometry". In: *Heating in Toroidal Plasmas 1982*. Ed. by C. Gormezano, G.G. Leotta, and E. Sindoni. Pergamon, 1982, pp. 707–723. ISBN: 978-1-4832-8428-6. DOI: https://doi.org/10.1016/B978-1-4832-8428-6.50081-3. URL: https://www.sciencedirect.com/science/article/pii/B9781483284286500813 (cit. on pp. 80, 120).

[201] B. LaBombard et al. "Transport-driven scrape-off layer flows and the x-point dependence of the L-H power threshold in Alcator C-Mod". In: *Physics of Plasmas* 12.5 (May 2005), p. 056111. DOI: 10.1063/1.1876294 (cit. on pp. 86–88, 99, 131, 165).

[202] B. Labombard et al. "Transport-driven Scrape-Off-Layer flows and the boundary conditions imposed at the magnetic separatrix in a tokamak plasma". In: *Nuclear Fusion* 44.10 (Sept. 2004), p. 1047. ISSN: 0029-5515. DOI: 10.1088/0029-5515/44/10/001 (cit. on pp. 87, 88, 99, 131, 165).

[203] A. Y. Aydemir. "An intrinsic source of radial electric field and edge flows in tokamaks". en. In: *Nuclear Fusion* 49.6 (Apr. 2009), p. 065001. ISSN: 0029-5515. DOI: 10.1088/0029-5515/49/6/065001 (cit. on p. 87).

[204] O. Grover et al. "Reduced model for H-mode sustainment in unfavorable ∇B drift configuration in ASDEX Upgrade". In: *Nuclear Fusion* 64.5 (Mar. 2024), p. 056020. DOI: 10.1088/1741-4326/ad326b (cit. on pp. 87, 90, 129, 131, 133, 166).

[205] F. Wagner et al. "Experimental evidence for neoclassical ion transport effects in the H-transition of ASDEX". In: *Nuclear Fusion* 25.10 (Oct. 1985), p. 1490. ISSN: 0029-5515. DOI: 10.1088/0029-5515/25/10/013 (cit. on p. 87).

[206] T. N. Carlstrom et al. "Experimental survey of the L-H transition conditions in the DIII-D tokamak". In: *Plasma Physics and Controlled Fusion* 36.7 (July 1994), A147. ISSN: 0741-3335. DOI: 10.1088/0741-3335/36/7A/019 (cit. on p. 87).

[207] A. E. Hubbard et al. "Local variables affecting H-mode threshold on Alcator C-Mod". In: *Plasma Physics and Controlled Fusion* 40.5 (May 1998), p. 689. ISSN: 0741-3335. DOI: 10.1088/0741-3335/40/5/024 (cit. on p. 87).

[208] F. Ryter et al. "H-Mode operating regimes and confinement in ASDEX-Upgrade". In: *Physica Scripta* 51.5 (May 1995), p. 643. ISSN: 1402-4896. DOI: 10.1088/0031-8949/51/5/017 (cit. on p. 87).

[209] L. Chen et al. "Effect of ∇ B drift on the H-mode power threshold in upper single null plasmas with ITER-like tungsten divertor on EAST". In: *Physics of Plasmas* 25.7 (July 2018), p. 072504. ISSN: 1070-664X. DOI: 10.1063/1.5033983 (cit. on p. 87).

[210] B. Labombard et al. "Critical gradients and plasma flows in the edge plasma of Alcator C-Moda)". In: *Physics of Plasmas* 15.5 (Feb. 2008), p. 056106. ISSN: 1070-664X. DOI: 10.1063/1.2838246 (cit. on pp. 87, 99, 131).

[211] J. P. Gunn et al. "Evidence for a poloidally localized enhancement of radial transport in the scrape-off layer of the Tore Supra tokamak". In: *Journal of Nuclear Materials* 363-365 (June 2007), pp. 484–490. DOI: 10.1016/j.jnucmat.2007.01.195 (cit. on p. 88).

[212] P. Hennequin et al. "The effect of SOL flows on edge and core radial electric field and rotation in Tore Supra". In: *37th EPS Conference on Plasma Physics P1.1040*. 2010 (cit. on pp. 88, 89, 96, 100, 101, 132).

[213] Nobuyuki Asakura. "Understanding the SOL flow in L-mode plasma on divertor tokamaks, and its influence on the plasma transport". In: *Journal of Nuclear Materials* 363-365 (2007). Plasma-Surface Interactions-17, pp. 41–51. ISSN: 0022-3115. DOI: 10.1016/j.jnucmat.2006.12.029. URL: https://www.sciencedirect.com/science/article/pii/S0022311506006325 (cit. on p. 88).

[214] H. Meyer et al. "H-mode physics of near double null plasmas in MAST and its applications to other tokamaks". In: *Nuclear Fusion* 46.1 (2006), p. 64. ISSN: 0029-5515. DOI: 10.1088/0029-5515/46/1/008 (cit. on p. 88).

[215] R. Varennes. "Flow drive in tokamak plasmas: competition and synergies between turbulence and neoclassical effects". PhD thesis. Aix-Marseile Université, France, Dec. 2022. URL: https://hal.science/tel-03820772 (cit. on pp. 89, 100).

[216] R. Varennes et al. "Safety factor influence on the edge E × B velocity establishment in tokamak plasmas". en. In: *Plasma Physics and Controlled Fusion* 66.2 (Dec. 2023), p. 025003. ISSN: 0741-3335. DOI: 10.1088/1361-6587/ad1653 (cit. on p. 89).

[217] M. Peret et al. "On the interplay between interchange turbulence and sheared flows". In: *Physics of Plasmas* 29.7 (July 2022), p. 072306. ISSN: 1070-664X. DOI: 10.1063/5.0086992 (cit. on pp. 90, 131, 133).

[218] P. Manz et al. "Magnetic configuration effects on the Reynolds stress in the plasma edge". In: *Physics of Plasmas* 25.7 (2018) (cit. on pp. 90, 131, 133, 166).

[219] W. Zholobenko et al. "The role of neutral gas in validated global edge turbulence simulations". In: *Nuclear Fusion* 61.11 (Oct. 2021), p. 116015. DOI: 10.1088/1741-4326/ac1e61 (cit. on p. 90).

[220] I. Cziegler et al. "Turbulence Nonlinearities Shed Light on Geometric Asymmetry in Tokamak Confinement Transitions". In: *Physical Review Letters* 118.10 (Mar. 2017), p. 105003. DOI: 10.1103/PhysRevLett.118.105003 (cit. on pp. 90, 100).

[221] B. J. Frei et al. "First-Principles Explanation of the Drift Configuration Dependence of the Radial Electric Field and High-Confinement Access in Tokamaks". In: (). In preparation. (cit. on pp. 90, 126, 127, 129, 131, 132, 166).

[222] Dominik Michels et al. "GENE-X: A full-f gyrokinetic turbulence code based on the flux-coordinate independent approach". In: *Computer Physics Communications* 264 (2021), p. 107986 (cit. on pp. 90, 125).

[223] Matthias Wiesenberger et al. "Reproducibility, accuracy and performance of the Feltor code and library on parallel computer architectures". In: *Computer Physics Communications* 238 (2019), pp. 145–156 (cit. on p. 91).

[224] Raul Gerru Miguelañez. "Study of the origin of the electric field in toroidal magnetized plasmas". PhD thesis. Department of Physics, Technical University of Denmark, 2022 (cit. on pp. 91, 100).

[225] P Ricci et al. "Simulation of plasma turbulence in scrape-off layer conditions: the GBS code, simulation results and code validation". In: *Plasma Physics and Controlled Fusion* 54.12 (Nov. 2012), p. 124047. DOI: 10.1088/0741-3335/54/12/124047. URL: https://doi.org/10.1088/0741-3335/54/12/124047 (cit. on p. 91).

[226] B. De Lucca et al. "Electromagnetic suppression of drift-wave turbulence and the L-H transition". In: *TSVV1 Progress Workshop*. Oral contribution. Oct. 2025 (cit. on pp. 91, 125).

[227] P. Cano-Megias et al. "Experimental study of the impact of ion orbit losses on the edge radial electric field at the ASDEX Upgrade tokamak". In: *47th EPS Conference on Plasma Physics*. European Physical Society. 2021 (cit. on p. 91).

[228] L. Vermare et al. "Radial electric field profile and geodesic acoustic modes in tokamak plasmas". In: *29th Joint EU-US Transport Task Force Meeting*. Poster contribution. Sept. 2025. URL: https://ttf2025.ek.hun-ren.hu/wp-content/uploads/2025/09/Abstract-booklet-TTF-2025.pdf (cit. on pp. 99, 132, 166).

[229] R.A. Pitts et al. "Parallel SOL flow on TCV". In: *Journal of Nuclear Materials* 363-365 (2007). Plasma-Surface Interactions-17, pp. 505–510. ISSN: 0022-3115. DOI: https://doi.org/10.1016/j.jnucmat.2006.12.065. URL: https://www.sciencedirect.com/science/article/pii/S0022311506006404 (cit. on p. 99).

[230] S. Rienäcker et al. "Linking Edge Flows to the Magnetic Geometry Asymmetry in Tokamaks". In: *50th EPS Conference on Plasma Physics (P4.047), Salamanca, Spain*. July 2024, P4–047. URL: https://hal.science/hal-04677735 (cit. on p. 105).

[231] Y. Camenen et al. "Experimental Evidence of Momentum Transport Induced by an Up-Down Asymmetric Magnetic Equilibrium in Toroidal Plasmas". In: *Physical Review Letters* 105.13 (Sept. 2010), p. 135003. DOI: 10.1103/PhysRevLett.105.135003 (cit. on p. 107).

[232] Molina Cabrera et al. "W-band tunable, multi-channel, frequency comb Doppler backscattering diagnostic in the ASDEX-Upgrade tokamak". In: *Review of Scientific Instruments* 94.8 (2023) (cit. on p. 110).

[233] R. Fischer et al. “Integrated Data Analysis of Profile Diagnostics at ASDEX Upgrade”. In: *Fusion Science and Technology* 58.2 (2010), pp. 675–684. DOI: 10.13182/FST10-110. eprint: https://doi.org/10.13182/FST10-110. URL: https://doi.org/10.13182/FST10-110 (cit. on p. 110).

[234] B. Lipschultz et al. “Marfe: an edge plasma phenomenon”. In: *Nuclear Fusion* 24.8 (Aug. 1984), p. 977. DOI: 10.1088/0029-5515/24/8/002. URL: https://doi.org/10.1088/0029-5515/24/8/002 (cit. on p. 110).

[235] M. Cavedon et al. “The radial localization of the transition from low to high confinement mode in the ASDEX Upgrade tokamak”. en. In: *Plasma Physics and Controlled Fusion* 66.2 (Jan. 2024), p. 025011. ISSN: 0741-3335. DOI: 10.1088/1361-6587/ad1ae3 (cit. on p. 119).

[236] B. J. Frei et al. “Spectrally accelerated edge and scrape-off layer gyrokinetic turbulence simulations”. In: *Computer Physics Communications* 316 (2025), p. 109817. ISSN: 0010-4655. DOI: 10.1016/j.cpc.2025.109817. URL: https://www.sciencedirect.com/science/article/pii/S0010465525003194 (cit. on pp. 125, 126).

[237] B. J. Frei. Private communication. 2026 (cit. on p. 126).

[238] Alessandro Marinoni, O. Sauter, and S. Coda. “A brief history of negative triangularity tokamak plasmas”. In: *Reviews of Modern Plasma Physics* 5.1 (2021), p. 6 (cit. on p. 135).

[239] M. Kikuchi et al. “L-mode-edge negative triangularity tokamak reactor”. In: *Nuclear Fusion* 59.5 (2019), p. 056017 (cit. on p. 135).

[240] Eleonora Viezzer et al. “Prospects of core–edge integrated no-ELM and small-ELM scenarios for future fusion devices”. In: *Nuclear Materials and Energy* 34 (2023), p. 101308 (cit. on p. 135).

[241] T. Happel et al. “Overview of initial negative triangularity plasma studies on the ASDEX Upgrade tokamak”. In: *Nuclear Fusion* 63.1 (Nov. 24, 2022), p. 016002. DOI: 10.1088/1741-4326/ac8563 (cit. on pp. 135–137).

[242] Carlos Paz-Soldan et al. “Simultaneous access to high normalized density, current, pressure, and confinement in strongly-shaped diverted negative triangularity plasmas”. In: *Nuclear Fusion* 64.9 (2024), p. 094002 (cit. on p. 135).

[243] A. Balestri et al. “Experiments and gyrokinetic simulations of TCV plasmas with negative triangularity in view of DTT operations”. In: *Plasma Physics and Controlled Fusion* 66.6 (May 2024), p. 065031. DOI: 10.1088/1361-6587/ad4674 (cit. on pp. 135, 136).

[244] B. Vanovac et al. “Pedestal properties of negative triangularity discharges in ASDEX Upgrade”. In: *Plasma Physics and Controlled Fusion* 66.11 (Sept. 2024), p. 115005. DOI: 10.1088/1361-6587/ad76d7 (cit. on pp. 136, 137).

[245] A. Merle, O. Sauter, and S. Yu Medvedev. “Pedestal properties of H-modes with negative triangularity using the EPED-CH model”. In: *Plasma Physics and Controlled Fusion* 59.10 (2017), p. 104001 (cit. on p. 136).

[246] S Saarelma et al. “Ballooning instability preventing the H-mode access in plasmas with negative triangularity shape on the DIII–D tokamak”. In: *Plasma Physics and Controlled Fusion* 63.10 (Sept. 8, 2021), p. 105006. DOI: 10.1088/1361-6587/ac1ea4 (cit. on p. 136).

[247] A. O. Nelson, C. Paz-Soldan, and S. Saarelma. “Prospects for H-mode inhibition in negative triangularity tokamak reactor plasmas”. In: *Nuclear Fusion* 62.9 (Aug. 2022), p. 096020. ISSN: 0029-5515. DOI: 10.1088/1741-4326/ac8064 (cit. on p. 136).

[248] M. Fontana et al. “The effect of triangularity on fluctuations in a tokamak plasma”. In: *Nuclear Fusion* 58.2 (2017), p. 024002 (cit. on pp. 136, 162).

[249] Zhouji Huang, Stefano Coda, et al. “Dependence of density fluctuations on shape and collisionality in positive-and negative-triangularity tokamak plasmas”. In: *Plasma Physics and Controlled Fusion* 61.1 (2018), p. 014021 (cit. on pp. 136, 162).

[250] M. Fontana et al. “Effects of collisionality and Te/Ti on fluctuations in positive and negative δ tokamak plasmas”. In: *Nuclear Fusion* 60.1 (Oct. 2019), p. 016006. DOI: 10.1088/1741-4326/ab4d75 (cit. on pp. 136, 149, 162).

[251] Woonghee Han et al. “Suppression of first-wall interaction in negative triangularity plasmas on TCV”. In: *Nuclear Fusion* 61.3 (2021), p. 034003 (cit. on pp. 136, 162).

[252] O. Krutkin et al. “Validation of short-pulse reflectometry turbulence measurements with a synthetic diagnostic”. In: *Nuclear Fusion* 64.2 (Jan. 2024), p. 026010. DOI: 10.1088/1741-4326/ad15b1 (cit. on pp. 136, 162, 167).

[253] Samuel David Stewart et al. “Experimental characterization of turbulence properties in negative triangularity DIII-D plasmas”. In: *Plasma Physics and Controlled Fusion* 67.2 (2025), p. 025032 (cit. on pp. 136, 137, 162).
[254] Alessandro Marinoni et al. “The effect of plasma triangularity on turbulent transport: modeling TCV experiments by linear and non-linear gyrokinetic simulations”. In: *Plasma Physics and Controlled Fusion* 51.5 (2009), p. 055016 (cit. on pp. 136, 149, 162).
[255] G. Merlo et al. “Nonlocal effects in negative triangularity TCV plasmas”. In: *Plasma Physics and Controlled Fusion* 63.4 (2021), p. 044001 (cit. on pp. 136, 149, 162).
[256] Gabriele Merlo et al. “On the effect of negative triangularity on ion temperature gradient turbulence in tokamaks”. In: *Physics of Plasmas* 30.10 (Oct. 2023), p. 102302. ISSN: 1070-664X. DOI: 10.1063/5.0167292 (cit. on pp. 136, 149, 162).
[257] Giovanni Di Giannatale et al. “System size scaling of triangularity effects on global temperature gradient-driven gyrokinetic simulations”. In: *Plasma Physics and Controlled Fusion* 66.9 (July 2024), p. 095003. DOI: 10.1088/1361-6587/ad5df9 (cit. on pp. 136, 149, 162).
[258] A. Balestri et al. “Physical insights from the aspect ratio dependence of turbulence in negative triangularity plasmas”. In: *Plasma Physics and Controlled Fusion* 66.7 (May 2024), p. 075012. DOI: 10.1088/1361-6587/ad4d1d (cit. on pp. 136, 149, 162).
[259] Xavier Garbet et al. “Effect of shaping on Trapped Electron Mode stability: an analytical model”. In: *Nuclear Fusion* (2024) (cit. on pp. 136, 149, 162).
[260] P. Ulbl et al. “Simulations of edge and SOL turbulence in diverted negative and positive triangularity plasmas”. In: *Nuclear Fusion* 65.10 (Sept. 2025), p. 106004. DOI: 10.1088/1741-4326/adfd70 (cit. on pp. 136, 137, 149, 162).
[261] O. Sauter et al. “On the non-stiffness of edge transport in L-mode tokamak plasmas”. In: *Physics of Plasmas* 21.5 (2014) (cit. on p. 136).
[262] Rameswar Singh, Patrick H. Diamond, and A. O. Nelson. “Geometric dependencies of the mean E× B shearing rate in negative triangularity tokamaks”. In: *Nuclear Fusion* 63.12 (2023), p. 126053 (cit. on p. 136).
[263] Colin Chrystal et al. “Effect of rotation on negative triangularity plasmas in DIII-D”. In: *Plasma Physics and Controlled Fusion* 66.10 (2024), p. 105004 (cit. on pp. 136, 162, 165).
[264] L. Schmitz. “Effective edge transport barriers supported by intrinsic rotation shear in DIII-D negative triangularity plasmas”. Abstract submitted for the 30th IAEA Fusion Energy Conference. 2025. URL: https://conferences.iaea.org/event/392/contributions/36026/attachments/19999/34055/Schmitz-EX-C.pdf (cit. on pp. 137, 162, 165).
[265] Filippo Bagnato et al. “Study of impurity C transport and plasma rotation in negative triangularity on the TCV tokamak”. In: *Plasma Physics and Controlled Fusion* 66.7 (2024), p. 075019 (cit. on pp. 137, 154, 161).
[266] G. J. Kramer et al. “The formation of an radial edge electric field due to finite ion orbit width effects is the possible root cause of the H-mode edge”. In: *Nuclear Fusion* 64.10 (2024), p. 106035 (cit. on p. 137).
[267] M. Bécoulet et al. “Non-linear gyro-kinetic Ion Temperature Gradient (ITG) and Trapped Electron Modes (TEM) turbulence modelling in X-point geometry in negative and positive triangularity shapes.” In: *29th Joint EU-US Transport Task Force Meeting, Budapest, Hungary*. Oral contribution. Sept. 2025 (cit. on pp. 137, 163, 165).
[268] L. De Gianni et al. “Analysis of trapped electron modes in negative triangularity plasmas”. In: *13th Festival de Théorie, Aix-en-Provence, France*. Oral contribution. June 2025. URL: https://festival-theorie.org/festival-de-theorie-2025-2/ (cit. on pp. 137, 163, 165).
[269] B. J. Frei and P. Ulbl. Private communication. 2025 (cit. on pp. 137, 163, 165).
[270] S. Rienäcker et al. “Edge radial electric field in positive and negative triangularity plasmas in the TCV tokamak”. In: *Nuclear Fusion* 66.1 (Nov. 2025), p. 014002. DOI: 10.1088/1741-4326/ae19fd (cit. on p. 138).
[271] Zhouji Huang. “Experimental study of plasma turbulence in the TCV tokamak”. PhD thesis. Swiss Federal Institute of Technology EPFL, 2017 (cit. on pp. 149, 162).
[272] S. Coda et al. “Optimization of shape for confinement in negative triangularity diverted tokamak plasmas”. In: *49th EPS Conference on Plasma Physics* (cit. on pp. 152, 161).

[273] R.I. Morgan et al. “Triangularity dependence of the divertor heat flux profile and SOL filamentary turbulence on TCV”. In: *Nuclear Fusion* 65.10 (Sept. 2025), p. 106030. DOI: 10.1088/1741-4326/ae034e (cit. on p. 162).

[274] M. Ugoletti. “Study of plasma-edge turbulence reduction in negative triangularity plasmas using Thermal Helium Beam diagnostic in the TCV Tokamak”. Poster contribution, manuscript in preparation. Oct. 2025. URL: https://conferences.iaea.org/event/392/papers/36298/files/13736-Manuscript_Ugoletti%20FEC%202025_FORMATTED.pdf (cit. on p. 162).

[275] Gabriele Merlo and Frank Jenko. “Interplay between magnetic shear and triangularity in ion temperature gradient and trapped electron mode dominated plasmas”. In: *Journal of Plasma Physics* 89.1 (2023), p. 905890104 (cit. on p. 162).

[276] Rameswar Singh and P. H. Diamond. “Zonal flow screening in negative triangularity tokamaks”. In: *Nuclear Fusion* 62.12 (2022), p. 126073 (cit. on p. 165).

Appendix A: Supplementary comparisons between radial force balance DBS

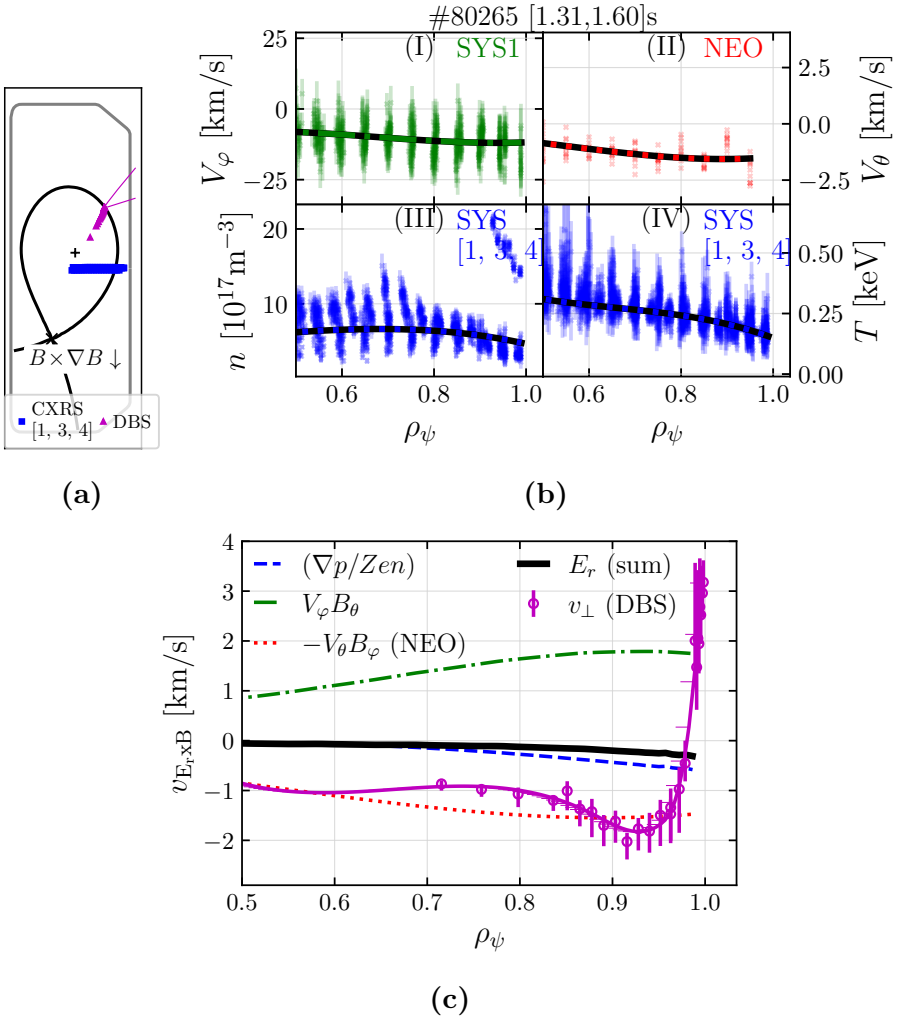

Figure A.1: *Comparison between DBS and radial force balance for C^{6+}, similar to Fig. 3.15, for a different, LSN scenario, with 850 kW of auxiliary ECRH. (a) Equilibrium reconstruction of the considered scenario, showing the DBS and CXRS-SYS(1,3,4) probing regions. (b) Spline fits to the CXRS data (I,III,IV) and to the V_θ results from NEO (II). (c) Radial force balance terms overplotted with the DBS $v_\perp$ profile.*

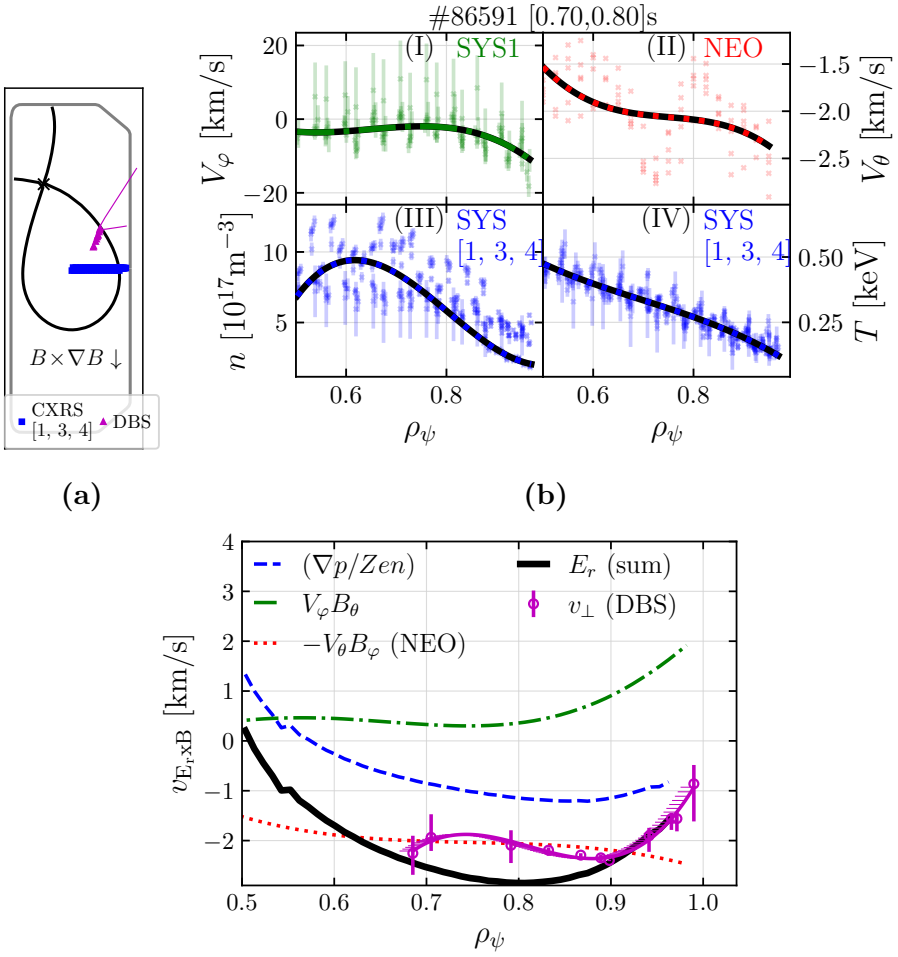

Figure A.2: *Same representation as Fig. A.1 for an Ohmic USN Ohmic scenario.*

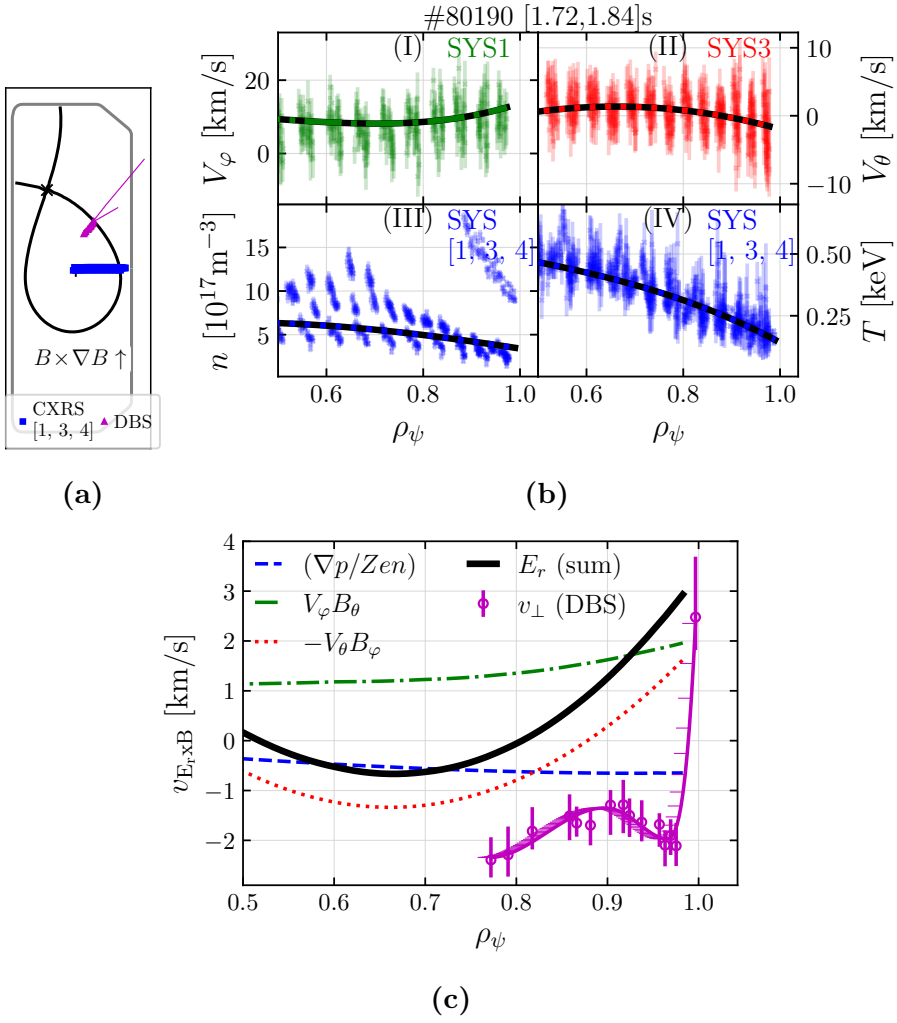

Figure A.3: *Result of an equivalent analysis to the one shown in Fig. 3.15, except that V_θ is taken from the CXRS (SYS3) measurements instead of NEO calculations. This tends to "bend" E_r towards positive values at the edge, in clear disagreement with the expected shape and the DBS measurements, highlighting the need to replace V_θ by a neoclassical estimate.*

Appendix B: Definition of triangularity

We distinguish between bottom, top, and average triangularities, defined respectively as follows (see Fig. B.1):

$$\delta_{\text{bot}} = (R_{\text{geo}} - R_{\text{bot}})/a \tag{B.1}$$

$$\delta_{\text{top}} = (R_{\text{geo}} - R_{\text{top}})/a \tag{B.2}$$

$$\delta = (\delta_{\text{bot}} + \delta_{\text{top}})/2\,, \tag{B.3}$$

where the geometric major radius $R_{\text{geo}} = (R_{\text{out}} + R_{\text{in}})/2$ and the plasma minor radius $a = (R_{\text{out}} - R_{\text{in}})/2$ have been introduced to ease notations. Note how the magnitude of δ

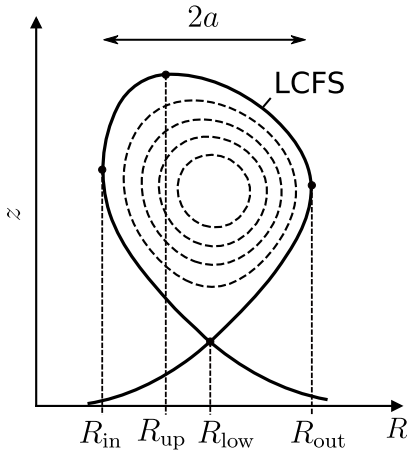

Figure B.1: *Poloidal cross-section of a shaped plasma, showing the notations used in defining the triangularity parameter.*

quickly vanishes towards the core as the flux-surfaces become more circular. In this work, triangularity implicitly refers to its value at the LCFS.

Appendix C: Results of linear GENE simulations in NT and PT

To assess the dominant type of instability in the NT/PT discharges compared in Sec. 5.2.4, a linear gyrokinetic analysis was performed using the GENE code [155], modelling the present scenarios on a flux-tube corresponding to $\rho_\psi = 0.9$. The results of these simulations are displayed in Fig. C.1; The linear growth rate γ (a) and the associated frequency ω (b) display little difference between NT and PT. Moreover, the sign of ω is negative,

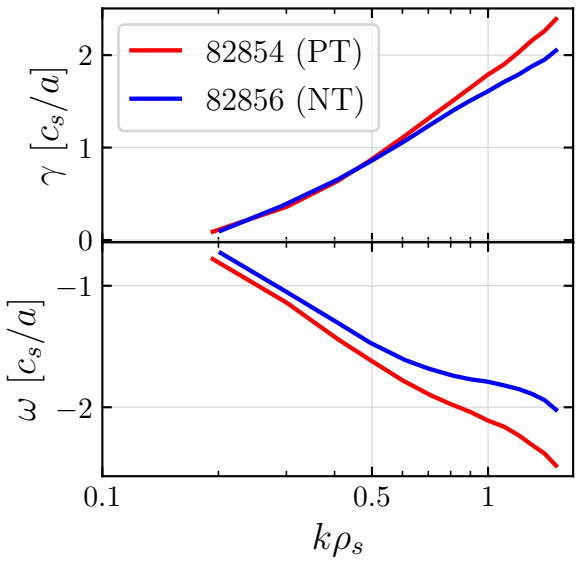

Figure C.1: *(a) Normalized rowth rates γ and (b) frequencies as a function of the normalized perpendicular scale $k_\perp \rho_s$, for NT and PT discharges with matched kinetic profiles. The negative ω correspond to propagation in the electron diamagnetic direction, suggesting the dominance of TEMs (as common in TCV).*

which corresponds to a propagation in the electron diamagnetic direction. At these ion scales, it can be attributed to trapped electron modes (TEMs), which are often found to be the dominant instability type in TCV.

ECOLE
DOCTORALE

Titre : Influence de la géométrie magnétique sur le champ électrique radial au bord des plasmas de tokamaks

Mots clés : fusion par confinement magnétique, tokamak, champ électrique radial, turbulence, cisaillement de vitesse

Résumé : La réduction de la turbulence dans les plasmas de fusion par confinement magnétique est un objectif majeur de la recherche dans ce domaine, car le transport de chaleur et de particules qui en résulte détermine largement la qualité du confinement – et donc les performances ainsi que le coût des futurs réacteurs à fusion. Les écoulements plasma cisaillés jouent un rôle central dans la régulation de ce transport turbulent. Ils permettent notamment la formation de barrières de transport associées aux régimes de confinement amélioré. Même en « mode L » (Low confinement mode), les plasmas de tokamak présentent typiquement une couche de cisaillement $E_r \times B$ située au bord du plasma, correspondant à un « puits » du champ électrique radial (E_r). Cependant, une compréhension approfondie du rôle de ce puits de E_r dans les propriétés de confinement en mode L et dans l'accès à des régimes de confinement améliorés fait encore défaut. De plus, la sensibilité de E_r aux conditions plasma demeure mal comprise et difficile à reproduire à l'aide des modèles ou outils numériques existants. Cette thèse étudie expérimentalement ces sensibilités afin d'aider à discriminer les mécanismes dominants à l'origine de E_r et de clarifier leur rôle dans l'amélioration du confinement. Les expériences sont menées principalement sur le tokamak TCV, en utilisant un diagnostic de rétrodiffusion Doppler (DBS) récemment installé pour caractériser le profil de E_r au bord du plasma. À l'aide de scans systématiques dans des décharges soigneusement accordées, ce travail met en évidence l'impact de la configuration de dérive magnétique et de la forme du plasma (triangularité) sur le profil de E_r. Dans l'ensemble, les résultats soutiennent l'existence d'un lien entre le cisaillement de E_r au bord et l'influence de la géométrie magnétique sur les propriétés de confinement. Combinées à de récentes simulations premiers principes, ces observations soulignent l'importance de la génération d'écoulement induite par la turbulence pour expliquer la sensibilité de E_r à la géométrie magnétique.

Title : Magnetic Geometry Impact on the Edge Radial Electric Field in Tokamaks

Keywords : magnetic confinement fusion, tokamak, radial electric field, turbulence, flow shear

Abstract : Mitigating plasma turbulence is a major objective of magnetic confinement fusion research, as the resulting transport of heat and particles largely determines confinement quality—and thus, the performance and cost of future fusion power plants. Sheared plasma flows play a central role in regulating turbulent transport, enabling, in particular, the formation of transport barriers associated with high confinement regimes. Even in low confinement mode (L-mode), tokamak plasmas typically exhibit, at the edge of the confined region, a narrow $E_r \times B$ shear layer corresponding to a negative radial electric field (E_r) "well". However, a deep understanding of the role of this E_r well in setting L-mode confinement properties and in providing access to higher confinement regimes is still lacking. In addition, the sensitivities of E_r to plasma conditions remain poorly understood and difficult to capture using existing models or numerical tools. This PhD thesis investigates these sensitivities experimentally to help disentangle the dominant E_r drives in L-mode and clarify their role in confinement improvement or transitions. Experiments are primarily conducted on the TCV tokamak, using a newly installed Doppler backscattering (DBS) diagnostic to characterize the edge E_r profile. Systematic parameter scans are performed in carefully matched discharges to isolate the impact of magnetic drift configuration and plasma shaping (specifically, triangularity) on the mean E_r and other edge profiles. Overall, the findings support a link between edge E_r shear and the influence of magnetic geometry on confinement properties. Combined with recent first-principles simulations, the observations point to the importance of turbulence-driven flow generation in explaining sensitivities of E_r to magnetic geometry.

Institut Polytechnique de Paris
91120 Palaiseau, France